GDAŃSK UNIVERSITY OF TECHNOLOGY

FACULTY OF APPLIED PHYSICS AND MATHEMATICS

FTiMS PG

The author of the PhD dissertation: Ewa Erdmann

Scientific discipline: Physics

DOCTORAL DISSERTATION

Title of PhD dissertation: Theoretical studies of fragmentation processes of neutral and ionized furan molecule

Title of PhD dissertation (in Polish): Teoretyczne badania procesów rozpadu neutralnej i zjonizowanej cząsteczki furanu

Supervisor	Auxiliary supervisor
signature	signature
prof. dr hab Józef E. Sienkiewicz, prof. zw. PG	dr inż. Marta Łabuda

Gdańsk, 2019

Preface

Since working on my bachelor's thesis, my academic interests revolved around processes induced by collisions with ions. This curiosity stemmed from my background of physics in medicine, which I studied as a specialization at Gdańsk University of Technology. I find the physics of ion interactions with molecules very interesting mainly due to their advantageous application in radiation therapy. During my PhD studies my efforts focused on exploring the complex dynamics of excited systems with many degrees of freedom. With the increased understanding of topics in molecular physics, I became more interested in effective theoretical methodologies of modelling the molecular rearrangement and fragmentation processes.

My work substantially benefits from the collaboration between research groups initiated through the COST XLIC (XUV/X-ray light and fast ions for ultrafast chemistry) action, namely: the group of Prof. Manuel Alcamí from the Autonomous University of Madrid, Spain, the group of Dr. Paola Bolognesi from Italian National Research Council, Rome, Italy and the group of Dr. Patrick Rousseau from University of Caen, France. The research problem studied in this work formulated during my first Short-Term Scientific Mission at the Autonomous University of Madrid (AUM) in February of 2015, funded by the XLIC program. Subsequently, I was given the opportunity of two more scientific stays at the AUM (in 2016 and 2017) to obtain, review and interpret the theoretical results.

I was engaged in writing the manuscript of this thesis from April 2018 to February 2019. In the meantime, I had the opportunity of visiting ARIBE, the low-energy ion beam facility of GANIL (Grand Accélérateur National d'Ions Lourds) in Caen, France at the time when the experiment of ion collisions with furan molecules has been performed.

I would like to take this opportunity and kindly thank those, who have helped and supported me during the course of my work. To Dr. Marta Łabuda, I am extremely grateful for her guidance, kindness and unwavering support. Without her experience and attention to detail this thesis would not have been possible.

I would also like to extend my gratitude to Prof. Józef E. Sienkiewicz, for giving me the opportunity of working in his group and supporting me throughout my studies.

My time spent in Madrid has always been a great learning experience, so I kindly thank Prof. Manuel Alcamí for hosting me in his group and allowing me to learn from prominent researchers.

I am also very grateful to Dr. Sergio Díaz Tendero. I valued greatly his welcoming attitude and ability to provide me with many ideas on how to solve a single problem.

I would like to express my thanks to Dr. Néstor F. Aguirre for a great deal of scientific and technical support. I very much appreciate the amount of time and effort he devoted to sharing his knowledge and expertise with me.

iv

I would also like to thank Dr. Paola Bolognesi and Dr. Patrick Rousseau for performing the experiments, providing the measured data and concurrently enhancing the quality of this thesis.

Last but not least, to my family that supported me with love and encouragement - thank you.

Contents

Chapter 1

Introduction

Despite the current existence of very accurate quantum chemical methods and rapid increase in the available computer power, full theoretical description of the chemical reactivity remains a difficult problem to study. On the other hand, novel light sources with XUV/X-ray attosecond pulses allow for excellent control of numerous processes and imaging of ultrafast electronic and nuclear dynamics. Still, investigations of molecular fragmentation remain complicated due to the multiplicity of active degrees of freedom. Among all possible fragmentation pathways and products, it is necessary to uncover those that are relevant to understanding the physics of the problem.

The main aim of this thesis is to investigate and understand the fragmentation process of a furan molecule with complementary theoretical methodologies. Depending on the initial charge state, the furan molecule is expected to decompose in a various ways. An additional objective is to propose and test a theoretical procedure that will provide information on the studied process and, at the same time, will be universal if applied to other systems. Moreover, as one of the steps, the present work adopts a statistical method, which is currently being developed. Due to scarce number of its applications, it is crucial to extend the scope of studied systems. Finally, direct quantitative comparison of the theoretically calculated observables with the recently obtained experimental results can provide systematic means of evaluating the accuracy and applicability of the new methodology.

The essence of this work resides in elucidating how the amount and distribution of the internal energy influences the fragmentation yields, regardless of the way it was deposited. It has been previously shown that excitation of the target is much faster than the time scale of the fragmentation. Redistribution of the excitation energy among internal degrees of freedom takes much longer time than the excitation itself. Hence, it is possible to study the fragmentation problem separately from the excitation. Then, comparison with experimental studies using electron beams, synchrotron radiation and ions as primary sources is feasible. So far, experimental measurements of furan interactions with electrons [1], [2] and synchrotron radiation [3] have already been performed. However, to the author's knowledge, this is the first presentation of the ion-induced fragmentation of furan. The newly performed experiments provide great opportunity to asses the chosen theoretical procedure and complement theoretical results.

The furan molecule has been chosen as a target for a few reasons: (1) widespread applications and model structure of the furan molecule (explained later in section 2) make it an interesting research subject; (2) furan comprises of nine atoms, which means that the application of proposed theoretical methods to such system requires sensible computational cost; (3)

the new statistical approach has been previously applied to homo-atomic clusters and hetero-atomic linear systems, but has never been used to the investigation of a hetero-atomic ring molecule. Therefore, furan is a good choice for testing and improving the method; and finally (4) an extensive amount of research focused on the decomposition of the neutral furan, however, there are a few studies on the fragmentation of the singly ionized furan and only one on doubly ionized furan (only experimental). In particular, an essential role of few-particle furan cation breakups, not studied before, has been highlighted in a recent paper by Dampc *et al* [2].

The presented objectives will be achieved by a theoretical procedure comprising of three computational approaches: (1) *ab initio* Molecular Dynamics simulations describing the evolution of the system following deposition of the energy; (2) exploration of the Potential Energy Surface (PES) comprising of optimized reactants, intermediate and products at high level of theory; (3) statistical calculations employing the Microcanonical Metropolis Monte Carlo (M_3C) method. In other words, considerations of three aspects of the studied process: dynamical, energetic and entropic are expected to create a full picture of the fragmentation mechanism.
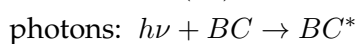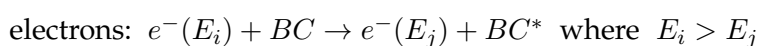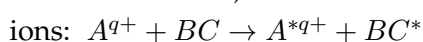
The text of this thesis is organized as follows: next subsection of Chapter 1 introduces the physical grounds of the fragmentation process. Chapter 2 explores some general information about the furan molecule and current state of knowledge with regard to the furan fragmentation. Next, in Chapter 3 the theoretical framework applied in this work is presented. Following Chapter 4 contains computational details of the performed calculations. Chapter 5 presents obtained results, discussion and comparison with previous theoretical works and experimental measurements. Finally, Chapter 6 concludes with summary of the results and a forward look on the further research directions.

1.1 Fragmentation mechanism

The molecular fragmentation process can be induced in various ways, a few of which will be briefly discussed in this section. In a neutral state, fragmentation of a molecule is possible through a process of pyrolysis, meaning thermal decomposition into smaller fragments carried out at elevated temperatures (generally above 400°C) in the absence of oxygen. Depending on the temperature and residence time, pyrolysis processes are typically classified as slow, moderate or fast. Another way of distinguishing the type of pyrolysis relies on the expected effect. The goal of applied pyrolysis is synthesis of certain compounds through thermal decomposition. Typical chemicals taken as a starting point include fossil fuels, biomass, wastes or polymers. Studies in applied pyrolysis investigate relationships between pyrolysis conditions and product properties, which can be subsequently characterized with such experimental methods like gas chromatography mass spectrometry, Fourier transform infrared spectrometry and nuclear magnetic resonance [4]. On the other hand, the purpose of analytical pyrolysis is characterization of the analyte through thermally induced degradation. This technique investigates chemical compositions and decomposition pathways of different materials. In practice, pyrolysis is used in many industrial applications such as conversion of oils to lighter products in the manufacture of fuels and chemical recycling of waste [5].
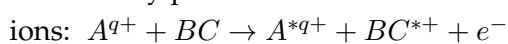
Further description of possible physical processes will be limited to the regime of low-energy interactions, because this energy range is of interest to the present work. As it was mentioned earlier, interaction of ionizing radiation (photons, electron beams, ion beams) with matter can cause variety of possible processes. Gas phase collision experiments help to elucidate the very first steps of this complicated chain of events by providing well-defined laboratory conditions. On the molecular scale, radiation damage results from deposition of the energy during the collision that leads to production of excited and/or ionized states and in the case of sufficient excess energy to fragmentation through different competing pathways. Schematically, typical collisional processes of different projectiles (A^{q+}, e^-, $h\nu$) with a molecule represented as BC can be written as

Excitation occurs when deposited energy is distributed among internal degrees of freedom and leads to population of higher rovibrational and/or electronic levels (here denoted with an asterisk *)

ions: $A^{q+} + BC \rightarrow A^{*q+} + BC^*$

electrons: $e^-(E_i) + BC \rightarrow e^-(E_j) + BC^*$ where $E_i > E_j$

photons: $h\nu + BC \rightarrow BC^*$

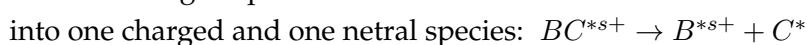**Ionization** takes place when absorbed energy exceeds the ionization potential of the molecule. As a results, a molecule looses electron(s), which can interact further in what is known as a secondary process

ions: $A^{q+} + BC \rightarrow A^{*q+} + BC^{*+} + e^-$

electrons: $e^- + BC \rightarrow 2e^- + BC^{*+}$

photons: $h\nu + BC \rightarrow e^- + BC^{*+}$

Charge transfer implies electron capture by the projectile and consequential acquisition of a positive charge by the target molecule

ions: $A^{q+} + BC \rightarrow A^{*(q-r)+} + BC^{*r+}$
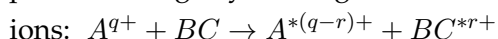
Fragmentation takes place when deposited energy is sufficient to break chemical bonds

into two charged species: $BC^{*s+} \rightarrow B^{*u+} + C^{*(s-u)+}$

into one charged and one netral species: $BC^{*s+} \rightarrow B^{*s+} + C^*$

If the fragmentation is statistical, its extent depends dramatically on the internal energy of the parent ion [6]. This implies that, prior to fragmentation, the internal excitation is completely randomized among all accessible internal degrees of freedom of the fragmenting ion. A portion of the excess internal energy is released in the relative translation of produced fragments. This energy, named kinetic energy release (KER), provides valuable information about the initial structures of the species involved and the energetics of the reaction. Its values depend on the details of the potential energy surface. The existence of reverse activation barrier, associated with the preceding isomerization, gives large KERs. Moreover, in the case of the fragmentation of multiply charged ions, large KERs result from the Coulomb repulsion between the charged fragments. KER distribution can be observed experimentally in the form of metastable peaks commonly present in mass spectra due ions dissociating in a field-free region of a mass spectrometer.

For a certain type of processes, a quantity that specifies the probability of its occurrence is known as a cross-section. In experimental studies of fragmentation and ionization, their values can be obtained by peak integration of spectra as a function of the projectile's velocity [7]. Based on this approach, theoretical investigation of charge transfer induced by collisions of carbon ions with uracil [8] showed evidence that processes of charge transfer and fragmentation are complementary.

Chapter 2

Furan molecule

The aim of this chapter is to present general characteristics of the furan molecule and explore studies that have already investigated fragmentation of the furan molecule. Then, a clear reference in the results section will be possible, allowing for a comprehensible comparison and emphasis on the novelty of results presented in this thesis.
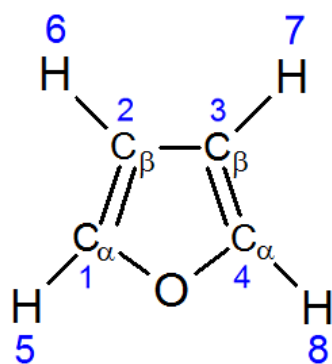

FIGURE 2.1 The structural formula of furan with labelling of atoms.

Furan is a five-membered heterocyclic molecule of formula H_4C_4O (see Figure 2.1) with an oxygen atom in the ring. The identification of the carbon atoms bonded with the oxygen by α subscripts and carbons connected only to other carbons by β subscripts simplifies the further analysis by the use of symmetry properties. The aromatic character of furan results from one of the oxygen atom's lone pairs of electrons being delocalized into the ring. This leads to $4n + 2$ aromatic system according to the Hückel's rule. Consequently, furan shows planar geometry and high reactivity in the sense of electrophilic substitution.

The geometry of the ground state furan belongs to the C_{2v} symmetry point group. Overall, furan molecule contains 36 electrons occupying 18 orbitals. Figure 2.2 shows two of the outermost π orbitals: HOMO ($1a_2$) and HOMO-1 ($2b_1$). The first ionization energy of furan has been previously determined in the multiphoton ionization experiment as 8.886 eV [9]. The appearance energies of the doubly ionized furan have been measured in the electron impact
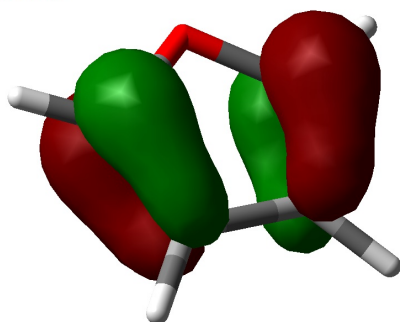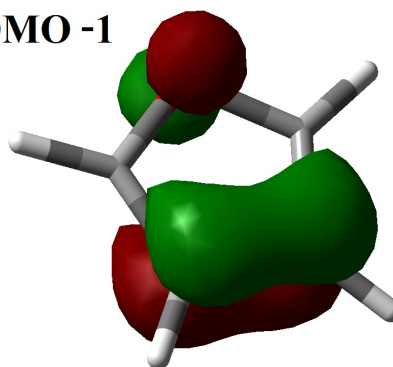

FIGURE 2.2 Two outermost orbitals of furan. Calculated at HF/6-311G(d,p) level of theory. Isosurface value is 0.08.

experiment at 25.7 eV [10] and in the photoionization experiment at 25.8 eV [11]. Theoretical value of the Vertical Ionization Potential (VIP) can be calculated from the energy difference between the ionized and neutral molecules at the equilibrium geometry of the neutral state. At the B3LYP/6-311++G(d,p) level of theory the value of the first VIP is equal to 8.93 eV and the second VIP is 25.82 eV, showing great comparison with the experimental values.

Abundance of research concerning furan stems from its various applications in pharmaceutical industry, organic synthesis and combustion chemistry, among others. Furan and its derivatives display a potential role in the second-generation biofuel production as their energy density is comparable to that of gasoline [12]. Understanding its thermal decomposition plays a role in clean coal combustion due to furan being one of the basic structure units of coal [13]. Moreover, furan and furan analogues are starting points of many reactions. Wide range of applications in the medicinal chemistry results from furan's broad availability and easy functionalization [14]. Finally, major amounts of furan have been found in tobacco smoke [15] and heat treated foods [16], so its cancerogenic and toxic effects have been an objective of numerous studies.

More recently, a renewed interest in the furan molecule is due to its model structure that resembles the building block of the DNA's backbone - deoxyribose sugar. Furan can be seen as a simplified tetrahydrofuran with reduced number of hydrogens. Tetrahydrofuran, on the other hand, is often taken as an analogue of the deoxyribose. Thus, furan is a second step approximation to the DNA chain element. Investigations regarding effects of the ionizing radiation on the biological tissue span over decades of extensive and notable research. Double-strand breaks of the DNA chain play a major role in the cell death because they are exceptionally difficult to repair [17]. Ionizing radiation causes numerous types of damage to the DNA, but double-strand breaks are the most biologically effective [18]. Moreover, it has been recently shown that on the molecular level the source of significant DNA damage is due to secondary particles and not the primary radiation itself [19]. Those particles include mostly low-energy electrons [20], but also radicals [21] as well as singly and multiply charged ions [7], [8]. To this day, numerous theoretical and experimental investigations are devoted to extending our understanding of how radiation modifies a biological system.

2.1   Fragmentation of neutral furan

Numerous studies can be found in the literature on the pyrolysis of furan from both the experimental and the theoretical perspectives. The first investigation on the very low pressure furan pyrolysis over the temperatures of 1050-1270 K has been published in 1985 by Grela *et al* [22]. The only two products that have been measured were CO and H_4C_3. A year later, Lifshitz *et al* [23] applied a single pulse shock tube technique over the temperatures of 1050-1460 K. As a result, they proposed furan pyrolysis to be a two-channel process of decomposition to CO/H_3CCCH and HCCH/H_2CCO. However, they were unable to detect ketene (H_2CCO), probably due to its high reactivity toward water that was absored on the walls of the shock tube. Then, in 1991, Organ and Mackie [24] extended the understanding of furan pyrolysis by application of the time-resolved infrared absorption spectrometry together with single pulse

shock tube method over the temperatures of 1100-1700 K. Similarly to Lifshitz *et al*, they obtained CO, H_4C_3, H_2C_2 as major products, but were able to detect H_2CCO as well. Additionally, they proposed a third minor channel of furan decomposition to be HCO/H_3C_3. However, this channel has been determined as unlikely by Fulle *et al* [25] in the combined experiment of the time-of-flight (TOF) and the shock tubes techniques. The absence of the third channel was explained by the high heat of that reaction in comparison with the other two channels. Fulle *et al* suggested that the observation of HCO and H_3C_3 might have resulted from the dissociation of the primary products or impurity initiation. All four groups suggested the rate determining step to be the CO scission and production of the intermediate open-chain biradical, which rapidly fragments to various products.

In 1998, Liu *et al* [26] published the first quantum chemical study of the unimolecular decomposition of furan. The calculations were carried out using density functional theory (B3LYP) for optimization of the geometries and the QCISD(T) method for the energies. They investigated three decomposition pathways and concluded that CO and H_3CCCH should be the major products of furan pyrolysis with HCCH and H_2CCO being distinguishable, but contributing to a minor extend. They proposed that the most favourable mechanism of obtaining channel CO/H_3CCCH relies on the 2,1 H shift, ring opening, two more hydrogen transfers and $C_\beta(3)$–$C_\alpha(4)$ bond cleavage resulting in fragmentation. Production of channel $HCCH/H_2CCO$, on the other hand, implies 1,2 H shift and concerted $C_\alpha(1)$–O and $C_\beta(2)$–$C_\beta(3)$ bonds fission.

The first experimental observation of channel HCO/H_3C_3 taking place directly from furan has been published by Sorkhabi *et al* [27]. By the use of photofragment translational spectroscopy at 196 nm with tunable vacuum ultraviolet probe, they provided evidence of an anisotropic angular distribution, indicating a swift dissociation process characteristic for radical channels such as HCO/H_3C_3. Moreover, they concluded that this channel likely occurs on an electronically excited PES, due to higher energies provided in the photodissociation experiment compared to that of pyrolysis. The mechanism of producing channel HCO/H_3C_3 has been proposed to consist of ring scission, followed by a 2,3 hydrogen transfer and a $C_\beta(3)$–$C_\alpha(4)$ bond cleavage. The concerted mechanism of obtaining this channel has been identified as unlikely on the basis of measured translational energy of produced fragments.

The most extensive theoretical investigation of furan unimolecular decomposition with high level *ab initio* quantum chemistry (calculated at CASSCF, CASPT2 and G2-(MP2) levels of theory) and kinetic modelling methods has been performed by Sendt *et al* [28]. Unlike Liu *et al* [26], this study contains calculation of rate parameters that allow for a comparison with experimental studies. The crucial conclusion has been made that instead of C–O or C–H bond cleavages being the first steps, the 1,2-H transfers leading to cyclic carbenes initiate production of the observed species. Their calculations indicate two parallel channels: CO/H_3CCCH and $HCCH/H_2CCO$, former being the dominant one. Direct ring cleavage, on both singlet and triplet PES, has been found to be much too energetic to contribute appreciably to the furan thermal decomposition. Similarly, the high activation energy required to produce channel HCO/H_3C_3 ruled out this mechanism as a way of obtaining H_3C_3. Instead, H_3C_3 radicals have been suggested to arise from secondary decomposition of H_4C_3.

The first experimental study showing that H_3C_3 radicals are produced also in the thermal

decomposition has been published in 2009 by Vasillou *et al* [29]. There, it has been shown with the use of the high-temperature supersonic nozzle technique combined with IR spectroscopy that these radical species are produced from furan at a higher temperature of 1550 $\pm$100K. The work of Vasillou *et al* [29] has been complemented by *ab initio* electronic structure calculations that further confirm that all of the furan fragmentation processes occur after rearrangement to either the α-carbene or β-carbene.

Combustion of furan in premixed furan/oxygen/argon flames has been studied by Tian *et al* [30] with tunable synchrotron VUV photoionization and molecular-beam mass spectrometry. Consumption of furan under different flames conditions has been investigated. Therein, it has been concluded that in the temperature range characteristic to pyrolysis the model of furan combustion fits best with the predictions of Sendt *et al* [28]. Moreover, they concluded that the hydrogen abstraction and decomposition of resulting furyl radicals may play a crucial role under high temperatures.

In 2013, Urness *et al* [31] performed the pyrolysis experiment of furan over the temperatures of 1200-1600 K in a microreactor. To confirm the most probable pathway of unimolecular decomposition, they measured branching ratios of intermediate species as a function of temperature with the tunable synchrotron radiation photoionization mass spectrometry. Specifically, they measured branching ratios of β-carbene to α-carbene and propargyl radical to propyne ([H_2CCH]/[H_3CCCH]). It has been shown that 80% to 90% decomposition of furan proceeds through production of β-carbene. Moreover, no evidence of propargyl radicals has been found in the temperature range of 1200-1500 K. For higher temperatures, at most 10% of formyl allene ($H_2CCCHCHO$) fragments to channel H_2CCH/CO/H, as most of this intermediate fragments to CO/H_3CCCH. These results confirmed the skeleton fragmentation to channel HCO/H_3C_3 as an unlikely process.

The most recent study of furan pyrolysis over the temperature range of 1100 to 1600 K has been performed by Cheng *et al* in 2017 [32]. Their results are consistent with the conclusions of previous pyrolysis studies that furan mainly decomposes to CO and H_3CCCH. Moreover, on the basis of the mole fraction profiles and measured formation temperatures of H_3C_3, authors concluded that the mechanism of producing propargyl radicals occurs through secondary fragmentation of propyne. Authors highlighted the importance of understanding the production mechanism of propargyl radicals due to their significant role as precursors of large aromatics formation in the pyrolysis of furan.

Summary of the experimentally observed fragmentation channels is presented in Table 2.1.

TABLE 2.1 Neutral furan fragmentation channels.

	$\rightarrow$	$CO + H_4C_3$	[22]–[25], [27], [29]–[32]
Furan	$\rightarrow$	$H_2C_2 + H_2C_2O$	[23]–[25], [27], [29]–[32]
	$\rightarrow$	$HCO + H_3C_3$	[24], [27], [29]
	$\rightarrow$	$H + CO + H_3C_3$	[31], [32]

2.2 Fragmentation of charged furan

Previous studies of ionization and subsequent fragmentation of furan molecules have been studied using various experimental techniques, such as charge-exchange mass spectrometry [33], [34], electron impact [2], [35]–[37], photoelectron-photoion coincidence (PEPICO) spectroscopy [11], [38], [39] and multiphoton mass spectrometry [40], [41].

The first study determining the charge-exchange mass spectra in collisions of furan molecules with wide range of reagent ions has been published in 1971 by Derrick *et al* [33]. They concluded that for primary ions of 11-12 eV of recombination energy three main channels were $H_4C_3^+$/CO, $H_2C_2O^+$/H_2C_2 and $H_3C_3^+$/HCO. At higher energies, channels $H_3C_4O^+$/H and HCO^+/H_3C_3 have been observed as well. Later, in 1980, Tedder *et al* [34] employed the same experimental technique, and extended the understanding of ionized furan fragmentation by reporting Appearance Energies (AEs) of the three most abundant ions.

The earliest work on decomposition of furan upon electron impact has been performed by Williams *et al* in 1968 [35]. The mass spectrum of furan has been measured at beam energy of 18 eV and reported three charged fragments: $H_3C_3^+$, $H_4C_3^+$ and $H_2C_2O^+$. Moreover, mass spectrum of deuterium labeled furan led to the conclusion that either hydrogen randomization does not take place in furan prior to fragmentation, or occurs slowly compared to the rate of fragmentation. Then, in 1979, Holmes and Terlouw [36] reported the 70 eV electron beam Collisional Activation spectrum of furan ions, which consisted of three main peaks corresponding to $H_4C_3^+$, $H_3C_3^+$ and $H_2C_3^+$ with Relative Abundances (RA) of 20%, 100% and 29%, respectively. On the basis of the obtained kinetic energy distribution, wide range of kinetic energies released upon CO loss from furan cation was the evidence of substantial energy required to reach the transition state prior to fragmentation. Moreover, the shape of the kinetic energy distribution implied that production of more than one isomer of $H_4C_3^+$ is possible. Three years later, Burgers *et al* [37] reported collisional activation mass spectra for various $H_4C_4O^+$ ions and wider range of mass over charge ratios. For furan cation fragmentation, additional observation has been made of HCO^+ and $H_4C_3O^+$ fragments, among others. More recently in 2015, ionization and fragmentation of furan has been studied by Dampc *et al* [2]. Cation mass spectrum at electron energy of 100 eV and absolute total and partial ionization cross sections at energy range of 5–150 eV were measured. With comparable intensity two ionic species dominate the mass spectrum: $H_3C_3^+$ (Relative Abundance (RA) = 100%) and $H_4C_4O^+$ (RA = 94%). Intensities of remaining ions did not exceed 15%, highest of which were fragments $H_4C_3^+$ (RA = 15%) and HCO^+ (RA = 12%). Authors highlighted the need for *ab initio* calculations that could provide more insight into such high abundance of $H_3C_3^+$. Moreover, Appearance Energies of various charged fragments have been determined. Those values will be later compared with energy barriers calculated in this work. Due to high AEs of some ionic fragments the possibility of multiple-step fragmentation has been pointed out. Moreover, the formation mechanism of the most abundant fragmentation products has been proposed as simultaneous cleavage of two bonds, the $C_\alpha(1)$-O and the $C_\beta(3)$–$C_\alpha(4)$ or $C_\beta(2)$–$C_\beta(3)$. This statement can be verified by the calculations performed in this work.

In 1980, Willet and Bear were the first to apply threshold PEPICO technique to study the

dissociation of state-selected furan ions [38]. AEs of four fragments: $H_4C_3^+$, $H_2C_2O^+$, $H_3C_3^+$ and HCO^+ have been reported. Furan ion has been found to be metastable. Identical rates for production of ions $H_4C_3^+$ and $H_2C_2O^+$ indicated that channels producing these fragments have been found to be in competition in the energy range of 11.5-13 eV. Moreover, on the basis of rate and kinetic energy release data authors argued that in the near threshold region $H_4C_3^+$ ion was the most likely produced in the allene from ($H_2CCCH_2^+$). Also, it has been suggested that fragmentation to $H_2C_2O^+$ and $H_3C_3^+$ proceeds through one transition state, without additional isomerization. A need for further studies explaining increasing rate of $H_3C_3^+$ have been expressed in this study. Further investigations of photoabsorption, photoelectron and photoion spectroscopy have been performed in 1998 by Rennie *et al* [11] and extended in 2001 by threshold-PEPICO measurements [39]. In [11] TOF mass spectrum has been reported at the photon energy of 27.2 eV. Moreover, normalised intensities of sixteen fragment ions as a function of the photon energy have been measured in the photon energy range 12-26 eV and their AEs have been presented. In addition, *ab initio* calculations have been performed for fragmentation pathways to channels $H_2CCC_2^+$/CO and H_3CCCH^+/CO, concluding that production of $H_4C_3^+$ ion in the allene form is more favourable. For higher photon energies, production mechanism of the $H_2C_4O^+$ ion has been explained as sequential loss of two hydrogen atoms. Moreover, metastable route of $H_3C_3^+ \rightarrow H_3C_2^+ \rightarrow HC_3^+$ has been suggested. More insight into furan cation fragmentation has been provided by the threshold PEPICO measurement [39]. On the basis of fitting of the RRKM/QET calculations with the experimental data, authors deduced barrier heights for channels $H_4C_3^+$/CO, $H_2C_2O^+$/H_2C_2 and $H_3C_3^+$/HCO as 2.75 eV, 2.88 eV and 3.05 eV, respectively. Moreover, measurements of the breakdown curves have been extended to the photon energy of 12-30 eV. In the energy range of 14-20 eV $H_3C_3^+$ has been found to be the most prominent fragment. Their RRKM/QET calculations did not account for sequential process, but authors suggested that this ion could have been produced from $H_4C_3^+$, provided it carried sufficient energy for further fragmentation. Ion $H_2C_3^+$ has been suggested to most likely result from channel $H_2C_3^+$/H_2CO. Authors emphasize possible high values of the kinetic shift in higher energy channels due to the slow onset at threshold.

In a very recent study of unimolecular dissociative photoionization mechanism of furfural (furan-2-carbaldehyde) [42] it has been suggested that the furan breakdown diagram is contained within the one obtained for furfural. Authors calculated potential energy surface of fragmentation of furan cation to three channels: $H_4C_3^+$/CO, $H_2C_2O^+$/H_2C_2 and HCO^+/H_3C_3 at the CBS-QB3 level of theory. However, the presence of $H_3C_3^+$ ions has been attributed to direct fragmentation of furfural.

Fragmentation of furan cation has been also studied with the infrared multiphoton dissociation technique by Wu *et al* [40], where intensities of fragments $H_4C_3^+$ and $H_2C_2O^+$ as a function of laser power have been reported. Authors concluded that although it has been previously suggested that these fragments proceed through a common transition state, their results indicate that this is not the case and stepwise photoexcitation leads to prompt fragmentation producing mostly $H_4C_3^+$. Moreover, in the study of resonance enhanced multiphoton ionization combined with TOF mass spectrometry by Ridley *et al* [41] the mass spectra of furan at different laser wavelengths (308-363 nm) have been reported. Therein, it has been concluded

that the extent of fragmentation has been determined by the laser wavelength reaching or exceeding the ionization potential of the orbitals attributed to the C-C, C-O, and C-H bonds and that there should be resonant intermediate states for efficient ionization.

The only investigation available in the literature of furan fragmentation following double ionization has been performed by Pešić *et al* [3]. This study employed the momentum-resolved coincidence ion spectroscopy and reported the kinetic energy distribution and momentum correlation between coincident ions. The abundance of detected small fragments results from K-shell ionization induced by 548 eV photons. Inner-shell excitations lead to high probability of four- or five-body reactions. Interestingly, authors were able to assign observed fragmentation channels as concerted, secondary decay, or deferred based on the measured momentum correlations and the constructed model. However, comparison between the present study and the results of Pešić *et al* [3] is inadequate as this work investigates fragmentation channels after valence-shell ionization, which results in larger-mass fragments.

In summary, the abundance of research has already focused on the fragmentation of charged furan, but there still remains a few unclear issues: (1) the high intensity of fragment $H_3C_3^+$ has not been supported by theory, (2) only two-body fragmentation has been previously theoretically investigated, but already at 13 eV sequential fragmentation can play a role in decomposition of furan cation, (3) no *ab initio* investigation on the fragmentation of doubly ionized furan has been performed. The comparison only with the results by Rennie *et al* [11], [39] and Dampc *et al* [2] will be made in the later chapter due to their recent and detailed quality.

Chapter 3

Theoretical methods

Quantum chemistry methods enable investigation of molecular systems by approximating the solution to the fundamental equation of quantum mechanics, the Schrödinger equation. Its exact analytic solution is only possible for small subset of physical systems. In practice, approximations must be applied, which naturally decrease the accuracy of the obtained result. The computational complexity of a selected method often substantially limits the range of possible applications. However, with advances made in development of theoretical methods and increase in availability of supercomputing resources, more and more complex systems are feasible to study with great accuracy.

The goal of this chapter is to formulate essential framework of three theoretical methodologies applied in this work. On the basis of following sections, their complementary character is emphasized as well as their role in describing the process of interest - fragmentation. Firstly, the fundamental approximation of the electronic structure theory: the Born-Oppenheimer approximation is presented. Next section introduces density functional theory as a powerful tool to solve the time-independent Schrödinger equation. Then, as a way elucidating the dynamical evolution of the system, a family of *ab initio* Molecular Dynamics methods is presented. Final section describes a recently developed, statistical technique based on the Metropolis Monte Carlo algorithm of the microcanonical ensemble.

Theoretical considerations presented in this chapter employ atomic units, i.e. by definition $m_e = \hbar = e_0 = 4\pi\varepsilon_0 = 1$. Such approach is very convenient, especially due to a simple form of the resulting molecular Hamiltonian.

3.1   Born-Oppenheimer approximation

The starting point of solving stationary, quantum chemical molecular problems is a time-independent Schrödinger equation given by

$$\hat{H}\Psi_k(\boldsymbol{r}, \boldsymbol{R}) = E_k^{tot}\Psi_k(\boldsymbol{r}, \boldsymbol{R}), \tag{3.1}$$

where Hamiltonian $\hat{H}$ operates on the wave function Ψ_k of the kth eigenstate and produces the total energy eigenvalue E_k^{tot}.

A non-relativistic Hamiltonian written in atomic units for a system of N_n nuclei (characterized by their position vector $\boldsymbol{R}$, mass M and atomic number Z) and N_e electrons (characterized by their position vector $\boldsymbol{r}$) consists of kinetic energy and electrostatic interactions and is given

by

$$\hat{H} = \sum_{A=1}^{N_n} -\frac{1}{2M_A}\nabla_A^2 + \sum_{i=1}^{N_e} -\frac{1}{2}\nabla_i^2 - \sum_{A=1}^{N_n}\sum_{i=1}^{N_e} \frac{Z_A}{|\boldsymbol{R}_A - \boldsymbol{r}_i|} + \sum_{A<B}^{N_n} \frac{Z_A Z_B}{|\boldsymbol{R}_A - \boldsymbol{R}_B|} + \sum_{i<j}^{N_e} \frac{1}{|\boldsymbol{r}_i - \boldsymbol{r}_j|}, \quad (3.2)$$

where nuclei are numbered by the A subscript and electrons by the i subscript. Eq. 3.2 can be rewritten in a more compact way as

$$\hat{H} = \hat{T}_n(\boldsymbol{R}) + \hat{T}_e(\boldsymbol{r}) + \hat{V}_{en}(\boldsymbol{r}, \boldsymbol{R}) + \hat{V}_{nn}(\boldsymbol{R}) + \hat{V}_{ee}(\boldsymbol{r}), \quad (3.3)$$

where $\hat{T}_n$ is the operator of nuclear kinetic energy, $\hat{T}_e$ is the operator of electronic kinetic energy, $\hat{V}_{en}$ is the operator of electron-nucleus interaction, $\hat{V}_{nn}$ is the operator of nucleus-nucleus interaction and $\hat{V}_{ee}$ is the operator of electron-electron interaction.

When examining the non-relativistic Hamiltonian, it can be seen that the explicit separation of nuclear and electronic coordinates is prevented by the electron-nucleus interaction $\hat{V}_{en}(\boldsymbol{r}, \boldsymbol{R})$ that depends on both nuclear and electronic coordinates. In 1927, Born and Oppenheimer introduced a fundamental *ansatz* for the decomposition of the total wave function [43]. They postulated that decoupling of fast electronic and slow nuclear motions is approximately correct and the total wave function can be separated into electronic and nuclear parts as

$$\Psi(\boldsymbol{r}, \boldsymbol{R}) \approx \Phi(\boldsymbol{r}; \boldsymbol{R})\chi(\boldsymbol{R}), \quad (3.4)$$

where Φ denotes the electronic wave function and χ is the nuclear wave function. As a consequence, solving the molecular Schrödinger equation becomes a two step problem. First, the electronic Schrödinger equation

$$\hat{H}_e\Phi_k(\boldsymbol{r}; \boldsymbol{R}) = E_k(\boldsymbol{R})\Phi_k(\boldsymbol{r}; \boldsymbol{R}) \quad (3.5)$$

must be solved. Here, $\hat{H}_e$ denotes the electronic Hamiltonian given by

$$\hat{H}_e = \hat{T}_e + \hat{V}_{en} + \hat{V}_{nn} + \hat{V}_{ee}. \quad (3.6)$$

As the electronic wave function $\Phi_k(\boldsymbol{r}; \boldsymbol{R})$ only parametrically depends on $\{\boldsymbol{R}\}$, it can be calculated at fixed positions of nuclei. Computing $E_k(\boldsymbol{R})$ for a range of nuclear coordinates leads to the potential energy surface (PES) of the kth electronic state.

In the next step, the nuclear Schrödinger equation

$$\hat{H}_n\chi_j(\boldsymbol{R}) = E_k^{tot}\chi_k(\boldsymbol{R}), \quad (3.7)$$

where the nuclear Hamiltonian $\hat{H}_n$

$$\hat{H}_n = \hat{T}_n + E_k(\boldsymbol{R}) \quad (3.8)$$

must be solved for a selected kth electronic state. Such approach indicates that the nuclei move in the field produced by the electrons and nuclei themselves.

In order to show the adequacy of the Born-Oppenheimer approximation, this work follows the derivation shown in [44]. When introducing the postulated product of electronic and nuclear wave functions to the time-independent Schrödinger equation one obtains

$$\hat{H}\Phi\chi = \left[\hat{T}_n + \hat{T}_e + \hat{V}_{en} + \hat{V}_{nn} + \hat{V}_{ee}\right]\Phi\chi = \tag{3.9}$$

$$= \sum_{A=1}^{N_n} -\frac{1}{2M_A}\nabla_A^2[\Phi\chi] + \left[\hat{T}_e + \hat{V}_{en} + \hat{V}_{nn} + \hat{V}_{ee}\right]\Phi\chi. \tag{3.10}$$

The *laplacian* ∇_A^2 acting on product $\Phi\chi$ gives

$$\nabla_A^2[\Phi\chi] = \chi\nabla_A^2\Phi + 2(\nabla_A\Phi\nabla_A\chi) + \Phi\nabla_A^2\chi. \tag{3.11}$$

Hence, eq. 3.10 can be written as

$$\hat{H}\Phi\chi = \sum_{A=1}^{N_n} -\frac{1}{2M_A}\left[\chi\nabla_A^2\Phi + 2(\nabla_A\Phi\nabla_A\chi) + \Phi\nabla_A^2\chi\right] + \\ + \left[\hat{T}_e + \hat{V}_{en} + \hat{V}_{nn} + \hat{V}_{ee}\right]\Phi\chi. \tag{3.12}$$

If one denotes the sum of terms with derivatives of the electronic wave function ($\nabla_A\Phi$) as B

$$B = \sum_{A=1}^{N_n} -\frac{1}{2M_A}\left[\chi\nabla_A^2\Phi + 2(\nabla_A\Phi\nabla_A\chi)\right] \tag{3.13}$$

and takes Φ out of the remaining sum term, then eq. 3.12 becomes

$$\hat{H}\Phi\chi = B + \Phi\underbrace{\sum_{A=1}^{N_n} -\frac{1}{2M_A}\nabla_A^2\chi}_{\hat{T}_N\chi} + \left[\hat{T}_e + \hat{V}_{en} + \hat{V}_{nn} + \hat{V}_{ee}\right]\Phi\chi. \tag{3.14}$$

Introducing $\hat{T}_N\chi$ into eq. 3.14 results in

$$\hat{H}\Phi\chi = B + \Phi\hat{T}_N\chi + \underbrace{\left[\hat{T}_e + \hat{V}_{en} + \hat{V}_{nn} + \hat{V}_{ee}\right]\Phi}_{E\Phi}\chi. \tag{3.15}$$

Next, substituting the highlighted term in eq. 3.15 with the right hand side of the electronic Schrödinger equation gives

$$\hat{H}\Phi\chi = B + \Phi\hat{T}_N\chi + E\Phi\chi = \tag{3.16}$$

$$= B + \Phi\underbrace{\left[\hat{T}_N + E\right]\chi}_{E^{tot}\chi}. \tag{3.17}$$

Lastly, introducing the right hand side of the nuclear Schrödinger equation leads to the final formula

$$\hat{H}\Phi\chi = B + E^{tot}\Phi\chi. \tag{3.18}$$

From eq. 3.18 it is clear that the representation of the total wave function as a product of electronic and nuclear functions is not exact, as this approach omits the terms included in the sum B. These neglected terms, named non-adiabatic coupling terms, contain derivatives of the electronic wave function with respect to the nuclear positions. Those values are considered relatively small for molecules close to the equilibrium, because they couple different electronic states according to the nuclear motion. If an average value of the non-adiabatic coupling for a selected kth electronic state

$$\sum_{A=1}^{N_n} -\frac{1}{2M_A}\left[\langle\Phi_k|\nabla_A^2|\Phi_k\rangle + 2\langle\Phi_k|\nabla_A|\Phi_k\rangle\nabla_A\right] \tag{3.19}$$

is added to the nuclear Hamiltonian, then the *adiabatic* approach is considered.

From a physical perspective, Born-Oppenheimer and adiabatic approximations result from nuclei being several thousand times heavier than the electrons (mass of a proton is ~ 1836.15 times larger than mass of an electron [44]). The Born-Oppenheimer approximation implies that the electrons adjust instantaneously to the changes in the nuclear positions. On the other hand, the adiabatic correction depends on the masses of the nuclei and hence, gives different values for different isotopes. This results in a shift of the energies (small when compared to significant isotopic effects on vibrational and rotational energy levels).

Finally, there exist situations when Born-Oppenheimer and adiabatic approximations do not hold. Those include regions of the PES when different electronic states approach each other and produce avoided crossings. It has been shown [43] that the Born-Oppenheimer approximation works until the separation between electronic states is at least two orders greater than the difference between rovibrational energy levels. Nevertheless, present work does consider non-adiabatic phenomena.

3.2   Density Functional Theory

In quantum mechanics, finding a physical observable $\hat{O}$ of a system in the kth eigenstate corresponds to calculating its expectation value $O_k = \langle\Phi_k|\hat{O}|\Phi_k\rangle$, where the kth wave function is known. The drawback of such approach is that the number of parameters required to accurately approximate the wave function increases exponentially with number of electrons in the studied system. Additionally, the amount of information that the wave function of such system contains often exceeds the complexity of investigated properties (such as single values of energy and dipole moments or functions of a few variables such as one-particle probability density). In this context, Density Functional Theory (DFT) reduces the intricate problem of solving the many body Schrödinger equation by replacing the wave function formalism with the ground state density. The basic framework of DFT significant to the present work is presented in following sections.

3.2.1 Hohenberg-Kohn theorems

In 1964, Hohenberg and Kohn published the first theoretical considerations giving rise to the nowadays very extensive field of DFT [45]. Therein, authors considered a system of N interacting electrons moving under the influence of an external potential $v(\boldsymbol{r})$ and mutual Coulomb repulsion. In agreement with the Born-Oppenheimer approximation described earlier, positions of nuclei are fixed. Such system is described by the electronic Schrödinger equation (eq. 3.6). For the purpose of clear presentation of the method in this section, one rewrites the electronic Hamiltonian $\hat{H}_e$ as a sum of kinetic energy operator $\hat{T}$, potential operator $\hat{V}$ and electron-electron Coulomb interaction operator $\hat{W}$, as follows

$$\hat{H}_e = \hat{T} + \hat{V} + \hat{W} = \sum_{i=1}^{N} -\frac{1}{2}\nabla_i^2 + \sum_{i=1}^{N} v(\boldsymbol{r}_i) + \sum_{i<j}^{N} \frac{1}{|\boldsymbol{r}_i - \boldsymbol{r}_j|}, \tag{3.20}$$

where the Coulomb interaction of nuclei is included in the external potential $v(\boldsymbol{r}_i)$. The one-particle probability density of such system in an electronic ground state is given by

$$n_0(\boldsymbol{r}) = N \sum_{\sigma_1 \ldots \sigma_N} \int d\boldsymbol{x}_2 \ldots \int d\boldsymbol{x}_N |\Phi_0(\boldsymbol{r}, \sigma_1, \boldsymbol{x}_2, \ldots, \boldsymbol{x}_N)|^2, \tag{3.21}$$

where variable $\boldsymbol{x}_i$ denotes space coordinates and spin state of the ith electron ($\boldsymbol{x}_i \equiv (\boldsymbol{r}_i, \sigma_i)$). It can be clearly seen that the ground state density $n_0(\boldsymbol{r})$ is a functional of the potential $v(\boldsymbol{r})$ because it is obtained from the wave function governed by the Schrödinger equation. Hohenberg and Kohn showed for the first time that the opposite is also true. The first Hohenberg-Kohn theorem for a nondegenerate system reads:

HK theorem 1 *The external potential $v_0(\boldsymbol{r})$ of the many-body ground state system (and hence the total ground state energy E_0) is a unique functional of the ground state density $n_0(\boldsymbol{r})$.*

The proof relies on showing that the opposite assumption leads to a contradictory result, i.e. it is impossible that two different potentials produce the same wave function and by analogy two different ground state wave functions cannot give the same density. As a conclusion, given the ground state density, reconstruction of the molecular Hamiltonian is straightforward and hence all properties of the system can be derived.

Moreover, in [45] Hohenberg and Kohn also presented a way of minimizing the total energy functional

$$E_{v_0}[n] = \langle \Phi[n]|\hat{T} + \hat{V}_0 + \hat{W}|\Phi[n]\rangle \tag{3.22}$$

when considering the ground state potential operator $\hat{V}_0$ following the Rayleigh-Ritz principle. The second Hohenberg-Kohn theorem reads:

HK theorem 2 *The ground state energy $E_{v_0}[n]$ can be found with the use of ground state density $n_0(\boldsymbol{r})$ according to the variational principle:*

$$\begin{aligned} E_{v_0}[n] &> E_0 \text{ for } n(\boldsymbol{r}) \neq n_0(\boldsymbol{r}) \\ E_{v_0}[n] &= E_0 \text{ for } n(\boldsymbol{r}) = n_0(\boldsymbol{r}) \end{aligned} \tag{3.23}$$

In other words, the density that minimizes the total energy is the exact ground state density. Since the total number of electrons in the system is fixed and can be calculated from

$$N = \int n(\boldsymbol{r})d^3r, \tag{3.24}$$

such constrained minimization of the energy is possible using the Lagrange multipliers (λ) method. Given the Lagrangian

$$\mathcal{L}[n] = E_{v_0}[n] - \lambda \left[\int n(\boldsymbol{r})d^3r - N \right], \tag{3.25}$$

according to the principle of stationary action, solving the resulting Euler equation

$$\frac{\delta \mathcal{L}[n]}{\delta n(\boldsymbol{r})} = \frac{\delta E_{v_0}[n]}{\delta n(\boldsymbol{r})} - \lambda = 0 \tag{3.26}$$

should give the exact ground state density $n_0(\boldsymbol{r})$ without solving the Schrödinger equation. Rewriting equation 3.22 as

$$E_{v_0}[n] = \langle \Phi[n]|\hat{T} + \hat{W}|\Phi[n]\rangle + \int d^3r n(\boldsymbol{r})v_0(\boldsymbol{r}) = \tag{3.27}$$

$$= F[n] + \int d^3r n(\boldsymbol{r})v_0(\boldsymbol{r}) \tag{3.28}$$

introduces the universal functional $F[n]$ for the system of N electrons that is irrespective of the external potential. This leads to a new form of eq. 3.26, as follows

$$\frac{\delta F[n]}{\delta n(\boldsymbol{r})} + v_0(\boldsymbol{r}) = \lambda. \tag{3.29}$$

The biggest advantage of DFT arises from reduction of the dimensionality of the electronic many-body problem. As the wave function formalism refers to $3N$ variables, electronic density is a function of only three spatial variables. Still, a difficulty remains in finding the appropriate expression for the unknown functional $F[n]$. The following section presents a practical method of finding the ground state density.

3.2.2   Kohn-Sham equations

A practical scheme for carrying out DFT calculations analogous to the Hartree-Fock procedure, but containing the effects of exchange and correlation was published in 1965 by Kohn and Sham [46]. It is known that for the systems of N non-interacting particles, the ground state wave function Φ_s takes the form of a single Slater determinant

$$\Phi_s(\boldsymbol{x}_1, \ldots, \boldsymbol{x}_N) = \frac{1}{\sqrt{N!}} \begin{vmatrix} \phi_1(\boldsymbol{r}_1) & \phi_2(\boldsymbol{r}_1) & \ldots & \phi_N(\boldsymbol{r}_1) \\ \phi_1(\boldsymbol{r}_2) & \phi_2(\boldsymbol{r}_2) & \ldots & \phi_N(\boldsymbol{r}_2) \\ \vdots & \vdots & & \vdots \\ \phi_1(\boldsymbol{r}_N) & \phi_2(\boldsymbol{r}_N) & \ldots & \phi_N(\boldsymbol{r}_N) \end{vmatrix}, \tag{3.30}$$

where each one-particle orbital $\phi_i(\boldsymbol{r})$ satisfies the Schrödinger equation

$$\left(-\frac{\nabla^2}{2} + \upsilon_s(\boldsymbol{r})\right)\phi_i(\boldsymbol{r}) = \varepsilon_i\phi_i(\boldsymbol{r}). \tag{3.31}$$

The Hamiltonian in eq. 3.31 consists of the kinetic energy term and the effective potential of a non-interacting system $\upsilon_s(\boldsymbol{r})$. Acting on the ith orbital ϕ_i it produces the orbital energy ε_i. At the same time, the Euler equation of the non-interacting system is given by

$$\frac{\delta T_s[n]}{\delta n(\boldsymbol{r})} + \upsilon_s(\boldsymbol{r}) = \lambda, \tag{3.32}$$

where T_s is the kinetic energy functional in the absence of electron-electron interactions. Kohn and Sham applied the effective one-particle orbital technique, which transformed DFT into a problem feasible to solve. Their approach started with rewriting eq. 3.28 as

$$E[n] = T_s[n] + \int d^3r\, n(\boldsymbol{r})\upsilon(\boldsymbol{r}) + \frac{1}{2}\int d^3r\int d^3r'\frac{n(\boldsymbol{r})n(\boldsymbol{r}')}{|\boldsymbol{r} - \boldsymbol{r}'|} + E_{xc}[n], \tag{3.33}$$

where E_{xc} is an exchange-correlation (xc) energy functional given by

$$E_{xc}[n] = T[n] - T_s[n] + W[n] - \frac{1}{2}\int d^3r\int d^3r'\frac{n(\boldsymbol{r})n(\boldsymbol{r}')}{|\boldsymbol{r} - \boldsymbol{r}'|}. \tag{3.34}$$

All terms of eq. 3.33 can be derived explicitly besides the xc energy functional. The corresponding Euler equation with the new form of the total energy functional now becomes

$$\frac{\delta T_s[n]}{\delta n(\boldsymbol{r})} + \upsilon(\boldsymbol{r}) + \int d^3r'\frac{n(\boldsymbol{r}')}{|\boldsymbol{r} - \boldsymbol{r}'|} + \frac{\delta E_{xc}}{\delta n(\boldsymbol{r})} = \lambda. \tag{3.35}$$

Comparing eq. 3.32 and 3.35 leads to conclusion that the mathematical problems are identical if

$$\upsilon_s[n](\boldsymbol{r}) = \upsilon(\boldsymbol{r}) + \int d^3r'\frac{n(\boldsymbol{r}')}{|\boldsymbol{r} - \boldsymbol{r}'|} + \upsilon_{xc}[n](\boldsymbol{r}), \tag{3.36}$$

where υ_{xc} denotes the xc potential

$$\upsilon_{xc}(\boldsymbol{r}) = \frac{\delta E_{xc}}{\delta n(\boldsymbol{r})}. \tag{3.37}$$

Plugging the new effective potential $\upsilon_s[n]$ to the Schrödinger equation for the system of non-interacting particles (eq. 3.31) enables finding the ground state density of the interacting system, as follows

$$\left(-\frac{\nabla^2}{2} + \upsilon_s[n](\boldsymbol{r})\right)\phi_i(\boldsymbol{r}) = \varepsilon_i\phi_i(\boldsymbol{r}). \tag{3.38}$$

Then, the ground state density n_0 becomes a sum over N non-interacting lowest occupied orbitals

$$n_0(\boldsymbol{r}) = \sum_{i=1}^{N}|\phi_i(\boldsymbol{r})|^2. \tag{3.39}$$

Equations 3.36 - 3.39 are labeled as Kohn-Sham (KS) equations. Similarly to the Hartree-Fock theory, KS equations are solved iteratively until self-consistency is obtained. This technique presents a big advantage over wave function based electron correlation methods, because the KS approach to DFT calculations results in lower computational cost (compared to that of the HF calculations). However, solving the many-body problem is still hindered by the missing expression for the xc energy functional.

3.2.3   Approximate functionals

Basing on the former description, DFT can be seen as a formally exact theory if the exact exchange-correlation functional is known. Unfortunately, this is true only for the case of a uniform electron gas, so for the molecular systems approximations must be applied. Although as seen in [47], the xc energy contributes to a minor extend to the total energy, it is relevant when establishing the binding energy of matter. After 50 years of research performed on DFT, abundance of approximate energy functionals can be found in the literature.

Local Density Approximation

The first approximation, named Local Density Approximation (LDA), was introduced by Kohn and Sham already in 1965 [48]. It relies on the assumption that the xc energy density (xc energy per unit of volume) of an infinitesimal volume element can be approximated by the xc energy density of a system with uniform density $\bar{n}$. At a position $\boldsymbol{r}$ the value of density $\bar{n}$ is evaluated as the value of the local density $n(\boldsymbol{r})$. Then, for the inhomogeneous system, the xc energy E_{xc}^{LDA} takes the form of an integral over xc energy density in a homogeneous electron gas e_{xc}^h that is determined at the local density, as follows

$$E_{xc}^{LDA}[n] = \int d^3r \; e_{xc}^h(\bar{n}) \Big|_{\bar{n}=n(\boldsymbol{r})}. \tag{3.40}$$

Corresponding exchange correlation potential is given by

$$v_{xc}^{LDA}(\boldsymbol{r}) = \frac{de_{xc}^h(\bar{n})}{d\bar{n}} \Big|_{\bar{n}=n(\boldsymbol{r})}. \tag{3.41}$$

The xc energy density $e_{xc}^h(n)$ consists of two terms: one corresponding to the exchange ($e_X^h(n)$) and one to correlation ($e_C^h(n)$). The exchange part can be determined analytically from theory of the homogeneous electron gas, however, there is no exactly known expression for the correlation part. The approximated values come from accurate numerical calculations, such as quantum Monte Carlo simulations [49]. On the basis of such results, high-precision representations of the electron gas correlation energy have been developed [50], [51].

Evidently, LDA succeeds for nonuniform systems with slowly varying density. Hence, for the LDA to hold, the local density variations should satisfy the condition

$$\frac{|\nabla n(\boldsymbol{r})|}{n(\boldsymbol{r})} \ll k_F(n), \tag{3.42}$$

where $k_F(n)$ indicates Fermi wave vector. In practice, there are many energetic and structural properties that the LDA approximation is able to reproduce within few percent of the experimental values. Those include total ground state energies (1-5%), equilibrium distances ($\sim$3%) and vibrational frequencies (few percent) [47]. The main drawback of the LDA approach results from incorrect asymptotic behaviour (v_{xc}^{LDA} approaches zero too fast). As a result, KS eigenvalues calculated with the LDA approach are too low in magnitude and the highest occupied molecular orbital energies differ significantly from the ionization energies. However, the LDA approximation works well for computing the total energies because underestimation of the correlation is compensated by the overestimation of the exchange effects.

Gradient Expansion Approximation

Improvement of the LDA approximation is possible through consideration of dependence of the energy density on the gradient of the local density. If condition 3.42 holds, reduced density gradients can be introduced to the energy density as small expansion series. Reduced density gradient takes the form of [47]

$$s(\boldsymbol{r}) = \frac{\nabla n(\boldsymbol{r})}{2n(\boldsymbol{r})k_F(\boldsymbol{r})}. \tag{3.43}$$

A general formula for the xc energy functional according to Gradient Expansion Approximation (GEA) is given by

$$E_{xc}^{GEA}[n] = \int d^3r \left(e_{xc}^h \left(n(\boldsymbol{r}) \right) + C_{xc}^2(n)s^2 + \dots \right), \tag{3.44}$$

where $C_{xc}^2(n)$ is the second order term of the gradient expansion series. In the last years much effort has been invested in deriving mathematical expressions for higher order terms that reproduce as many of the exact properties as possible. The most widely used Generalized Gradient Approximation (GGA) functionals are the exchange functional of Becke E_X^{B88} [52], the correlation energy functional introduced by Lee, Yang and Parr E_c^{LYP} [53] and PBE functional of Perdew E^{PEB} [54]. Generally, total ground state energies and spectroscopic constants show improvement when calculated with the GGA functionals.

Hybrid functionals

With the advancements in construction of the GGAs, another idea allowed for surpassing the accuracy of the Gradient Expansion Approximation. The next level of refinement is possible via introduction of portion of exact exchange energy from the Hartree–Fock theory:

$$E_X^{exact}(\boldsymbol{r}) = -\sum_{i<j}^{N} \int d^3r \int d^3r' \frac{\phi_i^\star(\boldsymbol{r}')\phi_j(\boldsymbol{r}')\phi_i(\boldsymbol{r})\phi_j^\star(\boldsymbol{r})}{|\boldsymbol{r}-\boldsymbol{r}'|} \tag{3.45}$$

and mixing it with fractions of standard LDA and GGA functionals. Hybrid functionals are generally constructed according to the following formula

$$E_{xc}^{hybrid} = aE_X^{exact} + (1-a)E_X^{GGA} + E_C^{GGA}. \tag{3.46}$$

Nowadays, the most widely used hybrid functional named B3LYP consists of

$$E_{xc}^{B3LYP} = (1-a)E_X^{LDA} + aE_X^{exact} + bE_X^{B88} + cE_C^{LYP} + (1-c)E_C^{LDA}, \tag{3.47}$$

where a=0.20, b=0.72 and c=0.81. Other hybrid functionals include PBE0 [55] and B98 [56].

Performance of the B3LYP functional has been extensively studied and according to [47] it has been applied to around 80% of all studies using DFT. Some benchmark data can be found in [57]–[59]. In [59] it has been shown that the B3LYP functional is an accurate choice for the investigations of oxygen containing organic systems, such as furan, the object of the present work. Particularly, those studies commented on calculating heats of formation and isomerization energies. In combination with basis sets that include dispersion corrections, the B3LYP functional gives mean absolute error values of around 1.9 kcal/mol (0.08 eV) for determination of the isomerization energies.

With the abundance of available options in the literature, the selection of the correct density functional may seem like a challenge. However, large sets of benchmark calculations provide systematic insight into errors in calculation of several physical properties. Provided their careful examination, making the right choice for the system in question in numerous instances can be easily resolved.

3.3   Molecular Potential Energy Surface

Previous sections introduced the concept of a Potential Energy Surface and the method of calculating values of the energy. The potential energy of a non-linear molecular system comprising of N atoms is a multidimensional function of $3N$-6 internal coordinates. Consequently, visualization of the entire PES is impossible except for systems with one or two internal coordinates. However, in a polyatomic system, it is possible to select certain parts of the PES, such as relationship between the energy and distance between two atoms (1D Potential Energy Curve, Figure 3.1 **a)**) or energy dependence of simultaneous changes of two internal coordinates (2D Potential Energy Surface, Figure 3.1 **b)**).

Points on the PES that are especially interesting for understanding the behaviour of molecular systems are stationary points, i.e. minima and saddle points. In a minimum energy configuration the system remains in a stable state, as any change in the geometry results in higher energy. One PES may posses numerous minima with the lowest minimum named global minimum. The relative populations of various equilibrium structures, i.e. thermodynamical properties, can be determined on the basis of the shape of the PES. For example, a broad minimum (point **A** in the Figure 3.1 **a)**) is expected to be more highly populated than a deeper, but more narrow minimum (point **C** in the Figure 3.1 **a)**) due to vibrational energy levels being more spread out and consequently less accessible [60]. Transition from one minimum to another
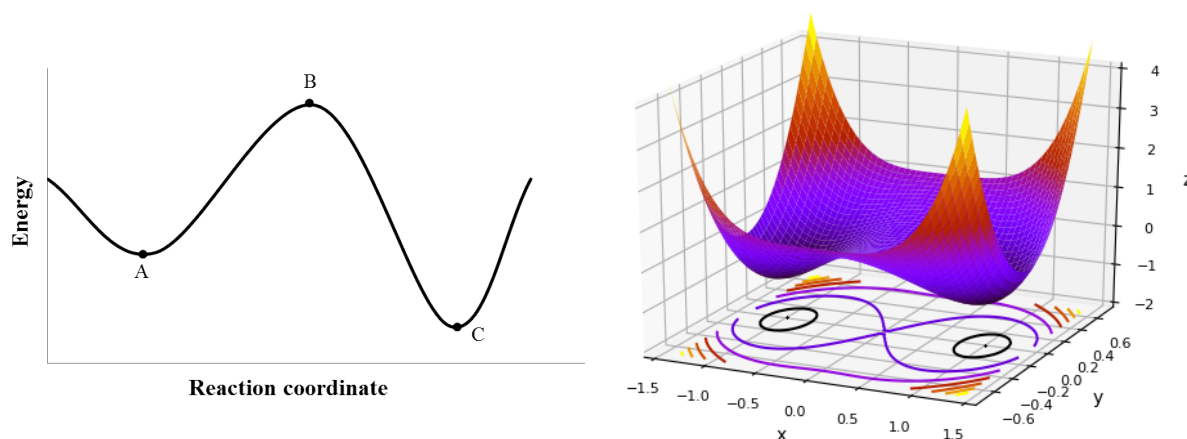
FIGURE 3.1 Panel **a)**: schematic energy curve. Panel **b)**: surface of a function $f(x, y) = x^4 + 4x^2y^2 - 2x^2 + 2y^2$ with one saddle point at (0,0) and two minima at (1,0) and (0,1). Adapted from [60].

occurs through a saddle point (point **B** in the Figure 3.1 **a)**), corresponding to a transition structure, which is the highest point on a reaction pathway (a path between two minima). Two adjacent minima can be taken as reactants and products of a specific reaction. Those structures may correspond to many configurations involved in different processes, such as two conformers of a single molecule or two molecules involved in a bimolecular reaction. Then, a transition structure provides information about the changes in geometry and variations in energy during a reaction. Kinetic studies of transition structures provide information about conversion rates from reactants to products. Moreover, during the fragmentation reactions, reverse activation barriers (E(**B**) - E(**C**) in Figure 3.1 **a)**) indicate the energy that is converted to relative kinetic energy of produced fragments.

As the first derivatives of the energy function at a stationary point are zero, it is necessary to calculate the second derivatives in order to distinguish between a minimum and a saddle point. Then, a structure with all positive second derivatives is a minimum and a configuration with only one negative eigenvalue in the matrix of second derivatives is a saddle point. Energy minimisation problems of quantum mechanics predominantly use numerical methods that approximate the true minima and saddle points. The default optimization method of the Gaussian software package [61] employed in this work is the Berny algorithm using GEDIIS [62]. The GEDIIS abbreviation stands for Geometry Optimization Using Energy-Represented Direct Inversion in the Iterative Subspace. This algorithm relies on a least-squares minimization scheme and due to enforced interpolation results in enhanced stability and generally smooth convergence behaviour [62].

After determination of a transition structure, it is necessary to make sure that the studied configuration indeed follows a particular reaction pathway. A way to do so relies on the steepest descent minimisation algorithm that produces the Intrinsic Reaction Coordinate (IRC) - the approximation to the minimum energy path that connects a transition structure with the equilibrium geometry. The first steps of reaching each minimum are derived from the eigenvector associated with the imaginary frequency of the transition structure.

3.4   *Ab initio* Molecular Dynamics

Next approach to studying the fragmentation process is a dynamical treatment using *ab initio* Molecular Dynamics (MD). This methodology unifies first-principle electronic structure theory with the framework of classical dynamics. Contrary to the fully classical MD, where the interatomic potentials are parametrized, predefined functions of the coordinates, *ab initio* MD methods rely on computing the forces acting on the nuclei "on the fly" from the electronic structure calculations. By that means, the electronic variables are active degrees of freedom as the MD trajectory evolves. Such methodology proves essential in systems where electronic rearrangement causes changes in the nature of bonding and induces chemical reactions, as in the processes under study in this work.

Similarly to the classical MD, *ab initio* MD employs generalized Lagrangian formulation with a Lagrangian $\mathcal{L}$ defined as the total kinetic energy minus potential energy of the system. Given the Lagrangian of the studied system, corresponding equations of motion are obtained from Euler-Lagrange equations:

$$\frac{d}{dt}\frac{\partial \mathcal{L}}{\partial \dot{\boldsymbol{R}}_I} = \frac{\partial \mathcal{L}}{\partial \boldsymbol{R}_I}, \tag{3.48}$$

$$\frac{d}{dt}\frac{\delta \mathcal{L}}{\delta \langle \dot{\phi}_i|} = \frac{\delta \mathcal{L}}{\delta \langle \phi_i|}, \tag{3.49}$$

for the nuclear coordinates $\boldsymbol{R}_I$ (3.48) and the orbitals ϕ_i (3.49). Here, and in the following discussion, the dot over a variable symbol indicates time derivative. Typically, resulting equations of motion are integrated numerically using gradient-based methods such as velocity Verlet [63] or fourth order Runge-Kutta [64] algorithms. In essence, the type of methods described below relies on solving the time-independent, stationary Schrödinger equation for electrons together with solving the motion of nuclei according to classical mechanics. Methods described in this section only refer to the ground state dynamics and employ DFT as a method of calculating electronic structure.

3.4.1   Born-Oppenheimer Molecular Dynamics

The Born-Oppenheimer approximation of decoupling nuclear and electronic degrees of freedom is also applied to the time dependent problem. According to the Born-Oppenheimer Molecular Dynamics (BOMD), the electronic structure calculations are converged at every time step under the constraint that orbitals are orthonormal, i.e. $\langle \phi_i | \phi_j \rangle = \delta_{ij}$. Consequently, the Lagrangian is equal to

$$\mathcal{L}_{BO} = \underbrace{\sum_I \frac{1}{2}M_I \dot{\boldsymbol{R}}_I^2}_{\text{kinetic energy}} - \underbrace{\min_{\{\phi_i\}}\{\langle \Phi_0 | H_e^{KS} | \Phi_0 \rangle\}}_{\text{potential energy}} + \underbrace{\sum_{i,j} \Lambda_{ij}(\langle \phi_i | \phi_j \rangle - \delta_{ij})}_{\text{constraint for orthonormality}}, \tag{3.50}$$

where Λ_{ij} builds a matrix of Lagrangian multipliers required for the constrained solution. Introducing this Lagrangian to the Euler-Lagrange equations results in the following equations

of motion

$$M_I \ddot{\boldsymbol{R}}_I(t) = -\nabla_I \min_{\{\phi_i\}} \{\langle \Phi_0 | \hat{H}_e^{KS} | \Phi_0 \rangle\}, \qquad (3.51)$$

$$0 = -H_e^{KS}\phi_i + \sum_j \Lambda_{ij}\phi_j, \qquad (3.52)$$

for the system in the electronic ground state. Nevertheless, the BOMD scheme is easily applicable to a particular electronic excited state $\Phi_k, k > 0$. Previously mentioned gradient-based methods are employed to propagate the nuclear degrees of freedom by calculating gradients of the energy, i.e. forces acting on the nuclei. For each nuclear configuration electronic Schrödinger equation is solved. Above equations already imply the Kohn-Sham density functional theory described before by the application of the KS one-particle Hamiltonian H_e^{KS} (eq. 3.38).

Such approach to molecular dynamics presents one very significant advantage. Due to the adiabatic separation and minimization of the potential energy at every time step, there exists no constraint on the maximum values of the integration time step coming from the electronic motion. An adequate time step is determined by the nuclear degrees of freedom only. On the other hand, due to the need of converging the wave function at every instance of time, BOMD calculations are computationally expensive (even easily converged system require around 8-12 self-consistent field steps [65]).

3.4.2 Extended Lagrangian methods

The high computational cost of self-consistent optimization at every time step of the BOMD limits the feasible size of the studied system and accessible simulation time. As the adopted time step causes small changes in the wave functions, the orbitals might as well be treated by the appropriate equations of motion. In this sense, a more computationally efficient approach to the molecular dynamics calculations was firstly developed by Car and Parinello and published in 1985 [66]. They proposed extending the Lagrangian with kinetic energy of fictitious particles that serve a purpose of the dynamical simulated annealing:

$$\mathcal{L}_{CP} = \underbrace{\sum_I \frac{1}{2} M_I \dot{\boldsymbol{R}}_I^2 + \sum_i \mu \langle \dot{\phi}_i | \dot{\phi}_i \rangle}_{\text{kinetic energy}} - \underbrace{\langle \Phi_0 | H_e^{KS} | \Phi_0 \rangle}_{\text{potential energy}} + \underbrace{\sum_{i,j} \Lambda_{ij} (\langle \phi_i | \phi_j \rangle - \delta_{ij})}_{\text{constraint for orthonormality}}, \qquad (3.53)$$

where again orthonormality of orbitals is imposed by the Lagrange multipliers Λ_{ij}. The new dynamical variable μ introduces the fictitious dynamics of the wave function. As a result, both the electronic and nuclear degrees of freedom are propagated at the same time. The resulting CPMD equations of motion are

$$M_I \ddot{\boldsymbol{R}}_I(t) = -\nabla_I \langle \Phi_0 | H_e^{KS} | \Phi_0 \rangle, \qquad (3.54)$$

$$\mu \ddot{\phi}_i(t) = -H_e^{KS}\phi_i + \sum_j \Lambda_{ij}\phi_j. \qquad (3.55)$$

Typically to Car-Parinello Molecular Dynamics (CPMD), a plane wave expansion is chosen to represent the orbitals. Such basis allows for an easy calculation of the integrals using fast Fourier transform methods, but shows disadvantages in reproducing the high electron density and cusps near the nuclei. Ultimately, propagation of the orbital coefficients leads to $\mathcal{O}(N^3)$ computational scaling with the system size.

The challenge of the CPMD approach remains in the correct definition of the inertia parameter μ of the electronic degrees of freedom, so that the electronic subsystem remains "cold", i.e. is close to the associated Born-Oppenheimer PES. Adiabatic separation has been extensively discussed in [67]. Therein, it has been shown that the highest phonon frequency ω_n^{max} has to be much smaller than the lowest electronic frequency ω_e^{min} for the correct CPMD simulation. The highest phonon frequency depends entirely on the physics of the system and the lowest electronic frequency ω_e^{min} is given by

$$\omega_e^{min} \propto \left(\frac{E_{gap}}{\mu} \right)^{1/2}, \tag{3.56}$$

where E_{gap} denotes the energy difference between the highest occupied and lowest unoccupied molecular orbitals, which depends on the physical system as well. Hence, it can be seen that the only variable that allows one to control the adiabaticity is the fictitious mass μ. As presented in [67], adequate values of μ for large-gap systems range from 500 to 1000 a.u., allowing for a time step between 0.1 and 0.25 fs. To summarize, provided that fictitious mass μ is small enough, CPMD simulations guarantee negligible errors in conservation of the total energy.

In 2001, a modification to the CPMD theory has been introduced by Schlegel *et al* [68]–[70]. In the new approach named, Atom-centered Density Matrix Propagation (ADMP), the authors proposed propagating the one-particle density matrix instead of orbital coefficients and using atom-centered Gaussian basis functions rather than plane waves. Generally, to achieve desired accuracy in reproducing the orbitals, a large plane wave basis set is needed. Using Gaussian basis functions presents two significant benefits: it ensures better reproduction of the high electron density regions and, as Gaussians are atom-centered, they adopt to the nuclear motion. Due to transition to the density matrix propagation formalism the following discussion employs the matrix forms for the representation of the phase space $\{\{\boldsymbol{R}, \boldsymbol{M}, \boldsymbol{V}\}, \{\boldsymbol{P}, \mu, \boldsymbol{W}\}\}$.

Then, the Lagrangian of the ADMP approach is given by

$$\mathcal{L}_{ADMP} = \frac{1}{2}Tr\left[\boldsymbol{V}^T\boldsymbol{M}\boldsymbol{V}\right] + \frac{1}{2}\mu Tr\left[\boldsymbol{W}\boldsymbol{W}\right] - E(\boldsymbol{R}, \boldsymbol{P}) - Tr[\boldsymbol{\Lambda}(\boldsymbol{P}\boldsymbol{P} - \boldsymbol{P})], \tag{3.57}$$

where $\boldsymbol{R}$, $\boldsymbol{M}$ and $\boldsymbol{V}$ are the nuclear positions, masses and velocities, respectively. The electronic degrees of freedom are described by the one-particle density matrix $\boldsymbol{P}$ (defined as $\sum_{i=1}^{N_e} |\phi_i\rangle\langle\phi_i|$), density matrix velocity $\boldsymbol{W}$ and fictitious mass μ. Here, Lagrangian multiplier matrix introduces a constraint on the idempotency of the density matrix (resulting from description of a pure state) and on the total number of electrons. Applying Lagrangian $\mathcal{L}_{ADMP}$ to the Euler-Lagrange equations leads to the following ADMP equations of motion

$$\boldsymbol{M}\frac{d^2\boldsymbol{R}}{dt^2} = -\left.\frac{\partial E(\boldsymbol{R}, \boldsymbol{P})}{\partial \boldsymbol{R}}\right|_{\boldsymbol{P}}, \tag{3.58}$$

$$\mu \frac{d^2 \boldsymbol{P}}{dt^2} = - \left[\left. \frac{\partial E(\boldsymbol{R}, \boldsymbol{P})}{\partial \boldsymbol{P}} \right|_{\boldsymbol{R}} + \boldsymbol{\Lambda P} + \boldsymbol{P \Lambda} - \boldsymbol{\Lambda} \right], \tag{3.59}$$

for the nuclear and electronic degrees of freedom, respectively. Solution of eq. 3.59 gives dynamics of the one-particle density matrix in the orthonormal basis. In practice, the forces acting on the nuclei and density matrices are derived using the McWeeny density matrix purification transformation [71] in the expression for the energy.

As in the case of CPMD simulations, the fictitious mass μ should act as a parameter of the adiabatic control. Analysis of its influence on the adiabaticity has been investigated in [72]. This study relied on assessment of the commutator of Fock and density matrices, which in the BOMD approach is equal to zero. The authors concluded that, indeed, as the fictitious mass is proportional to the mentioned commutator, its magnitude determines the lower limit for deviations from the Born-Oppenheimer PES.

In summary, alterations introduced by the ADMP method decrease significantly the computational cost of the dynamical calculations by ensuring linear scaling of computational time with the increasing system size.

3.4.3 Time integration algorithm

After establishing the equations of motion the next step of solving a dynamical problem is to decide on the method of their numerical integration. Present work employs the ADMP technique, so the integration algorithm implemented for this method will be presented in the following section, namely the velocity Verlet algorithm [63]. This method relies on expanding position r of a particle of mass m around time t in a Taylor series as

$$r(t + \Delta t) = r(t) + V(t)\Delta t + \frac{f(t)}{2m}\Delta t^2 + \mathcal{O}(\Delta t^4), \tag{3.60}$$

where V and f denote velocity and force, respectively. Expanding the velocity in the same manner and applying the expansion of the force gives the following formula for the velocity at time $t + \Delta t$

$$V(t + \Delta t) = V(t) + \frac{f(t) + f(t + \Delta t)}{2m}\Delta t. \tag{3.61}$$

This variant of the Verlet algorithm leads to convenient expressions for positions and velocities computed at equal times. In this form, obtaining new velocities requires preceding calculations of positions and forces at times t and $t + \Delta t$. However, the most commonly used iterative procedure of the velocity Verlet algorithm avoids storing forces at two instances of time [73]. It comprises of following steps:

1. Given $V(t)$ and $f(t)$, computing velocity at half-time step as $V(t + \frac{1}{2}\Delta t) = V(t) + \frac{f(t)}{2m}\Delta t$.

2. Computing position at time $t + \Delta t$ as $r(t + \Delta t) = r(t) + V(t + \frac{1}{2}\Delta t)\Delta t$.

3. Evaluating force at time $t + \Delta t$ from the interaction potential with the use of $r(t + \Delta t)$.

4. Computing velocity at time $t + \Delta t$ as $V(t + \Delta t) = V(t + \frac{1}{2}\Delta t) + \frac{f(t+\Delta t)}{2m}\Delta t$.

The velocity Verlet algorithm is preferable for iterations of constrained dynamics, such as ADMP. Applying above approach to the ADMP equations of motion leads to the following formula for propagation of the density matrix

$$\boldsymbol{P}_{(t+\Delta t)} = \boldsymbol{P}_{(t)} + \boldsymbol{W}_{(t)}\Delta t - \frac{\Delta t^2}{2\mu}\left[\left.\frac{\partial E(\boldsymbol{R}_{(t)}, \boldsymbol{P}_{(t)})}{\partial \boldsymbol{P}_{(t)}}\right|_{\boldsymbol{R}_{(t)}} + \boldsymbol{\Lambda}_{(t)}\boldsymbol{P}_{(t)} + \boldsymbol{P}_{(t)}\boldsymbol{\Lambda}_{(t)} - \boldsymbol{\Lambda}_{(t)}\right]. \quad (3.62)$$

Density matrix velocities are calculated using

$$\boldsymbol{W}_{(t+\frac{1}{2}\Delta t)} = \boldsymbol{W}_{(t)} - \frac{\Delta t}{2\mu}\left[\left.\frac{\partial E(\boldsymbol{R}_{(t)}, \boldsymbol{P}_{(t)})}{\partial \boldsymbol{P}_{(t)}}\right|_{\boldsymbol{R}_{(t)}} + \boldsymbol{\Lambda}_{(t)}\boldsymbol{P}_{(t)} + \boldsymbol{P}_{(t)}\boldsymbol{\Lambda}_{(t)} - \boldsymbol{\Lambda}_{(t)}\right] \quad (3.63)$$

$$= \frac{\boldsymbol{P}_{(t+\Delta t)} - \boldsymbol{P}_{(t)}}{\Delta t}, \quad (3.64)$$

and

$$\boldsymbol{W}_{(t+\Delta t)} = \boldsymbol{W}_{(t+\frac{1}{2}\Delta t)} - \frac{\Delta t}{2\mu}\left[\left.\frac{\partial E(\boldsymbol{R}_{(t+\Delta t)}, \boldsymbol{P}_{(t+\Delta t)})}{\partial \boldsymbol{P}_{(t+\Delta t)}}\right|_{\boldsymbol{R}_{(t+\Delta t)}}\right.$$
$$\left. + \boldsymbol{\Lambda}_{(t+\Delta t)}\boldsymbol{P}_{(t+\Delta t)} + \boldsymbol{P}_{(t+\Delta t)}\boldsymbol{\Lambda}_{(t+\Delta t)} - \boldsymbol{\Lambda}_{(t+\Delta t)}\right]. \quad (3.65)$$

Aforementioned propagation of the density matrix requires computation of the Lagrange multipliers matrix at each time step. The ADMP method works under the idempotency constraint $\boldsymbol{P}^2 = \boldsymbol{P}$ and the time derivative of the idempotency constraint $\boldsymbol{WP} + \boldsymbol{PW} = \boldsymbol{W}$. According to these conditions, given the density matrix at time step t ($\boldsymbol{P}_{(t)}$), idempotent $\boldsymbol{P}_{(t+\Delta t)}$ is obtained by iteratively solving for the idempotency constraint. Then, given values of $\boldsymbol{P}_{(t)}$, $\boldsymbol{P}_{(t+\Delta t)}$, $\boldsymbol{W}_{(t)}$ and $\boldsymbol{W}_{(t+\frac{1}{2}\Delta t)}$, idempotent density matrix velocity $\boldsymbol{W}_{(t+\Delta t)}$ can be found by iteratively solving for the time derivative of the idempotency constraint.

Similarly to the propagation of the electronic degrees of freedom, for the nuclear positions one obtains

$$\boldsymbol{R}_{(t+\Delta t)} = \boldsymbol{R}_{(t)} + \boldsymbol{V}_{(t)}\Delta t - \frac{\Delta t^2}{2}\boldsymbol{M}^{-1}\left[\left.\frac{\partial E(\boldsymbol{R}_{(t)}, \boldsymbol{P}_{(t)})}{\partial \boldsymbol{R}_{(t)}}\right|_{\boldsymbol{P}_{(t)}}\right] \quad (3.66)$$

and for the nuclear velocities

$$\boldsymbol{V}_{(t+\frac{1}{2}\Delta t)} = \boldsymbol{V}_{(t)} - \frac{\Delta t}{2}\boldsymbol{M}^{-1}\left[\left.\frac{\partial E(\boldsymbol{R}_{(t)}, \boldsymbol{P}_{(t)})}{\partial \boldsymbol{R}_{(t)}}\right|_{\boldsymbol{P}_{(t)}}\right] \quad (3.67)$$

$$= \frac{\boldsymbol{R}_{(t+\Delta t)} - \boldsymbol{R}_{(t)}}{\Delta t}, \quad (3.68)$$

and

$$\boldsymbol{V}_{(t+\Delta t)} = \boldsymbol{V}_{(t+\frac{1}{2}\Delta t)} - \frac{\Delta t}{2}\boldsymbol{M}^{-1}\left[\left.\frac{\partial E(\boldsymbol{R}_{(t+\Delta t)}, \boldsymbol{P}_{(t+\Delta t)})}{\partial \boldsymbol{R}_{(t+\Delta t)}}\right|_{\boldsymbol{P}_{(t+\Delta t)}}\right]. \quad (3.69)$$

There are no constraints for the nuclear motion, as the idempotency depends only on the electronic coordinates.

In practice, initial configurations of $\boldsymbol{R}_{(0)}$, $\boldsymbol{V}_{(0)}$ and $\boldsymbol{W}_{(0)}$ are known. At each time step the

density matrix is calculated with a cost equivalent to a one cycle of the self-consistent field approach. As previously described, values at consecutive time steps are derived from analytical gradients of energy and idempotency constraints.

Correct choice of the time step size ensures total energy conservation in the ADMP calculations. The requirement for small oscillations of the ADMP energy around the BO PES does not allow for as large time steps as the BOMD method. Good energy conservation of the ADMP method ($\sim 10^{-5}$ Hartree) has been found to result from time steps two times smaller when comparing to the BOMD [65]. Finally, according to [65], ADMP trajectories can be obtained 3-4 times faster than when using the BOMD approach.

3.5 Microcanonical Metropolis Monte Carlo

Third approach to studying the fragmentation process is a statistical treatment based on the assumption of the internal thermodynamic equilibrium. The method, named Microcanonical Metropolis Monte Carlo (M_3C), has been previously applied to several systems, such as: atomic metal clusters [74], neutral and singly charged carbon clusters [75]–[78] as well as singly charged acetylene [78]. The present work is the first attempt at investigation of decomposition of a heterocyclic molecule in a neutral and singly charged state using M_3C. In essence, the goal of the M_3C method is to describe the fragmentation process with a lower computational cost than required by the *ab initio* Molecular Dynamics without significant loss in accuracy.

In the following sections, a theoretical basis of the M_3C technique is presented, including general foundations of the method, interpretation of the final expression for the Density of States (DOS) and explanation of the stochastic sampling technique. Recently, a detailed theoretical description of the method has been published [78], presenting some improvements to the theory derived in [74] and [76]. The following is significantly based on these three studies.

3.5.1 Microcanonical ensemble

In statistical mechanics, a system can belong to a certain ensemble depending on the quantities defining it. Particularly, a system with fixed total energy belongs to a microcanonical ensemble. According to the Boltzmann's formula, the entropy S of such isolated system at equilibrium is given by:

$$S = k_B ln\Omega(E), \tag{3.70}$$

where k_B is the Boltzmann's constant and $\Omega(E)$ is the total DOS. The value of $\Omega(E)$ defines a number of accessible microstates with energy E that, according to the Laplace principle of indifference, are equally probable. In a microcanonical ensemble with conserved total linear P_0 and angular J_0 momenta, the formula for the Density of States is given by

$$\Omega(E, P_0, J_0) = \int d\mathbf{\Gamma}\delta[\mathcal{H}(\mathbf{\Gamma}) - E]\delta[\mathcal{J}(\mathbf{\Gamma}) - \mathcal{J}_0]\delta[\mathcal{P}(\mathbf{\Gamma}) - \mathcal{P}_0], \tag{3.71}$$

where $\int d\mathbf{\Gamma}$ is the integral over the phase space $\mathbf{\Gamma}$ (values of all possible position and momentum variables), δ denotes Dirac's delta function and $\mathcal{H}(\mathbf{\Gamma})$ is the Hamiltonian of the system.

Considering the second law of thermodynamics, thermodynamic equilibrium is obtained by reaching the state of maximum entropy. Hence, an accurate description of the DOS is the most significant step of the M$_3$C technique.

3.5.2 Approximation of the Density Of States

The M$_3$C method relies on factorization of the DOS into a product of several, easily integrable components. The system of coordinates is defined in a laboratory frame, in which $\mathcal{R}_i$ denotes the center of mass position of the ith fragment and $\boldsymbol{\theta}_i$ is the orientation of the fragment i with respect to its body-fix frame. Let n denote number of atoms in the studied system and N_c number of possible fragmentation channels. Firstly, through a convenient phase space channel decomposition, a $(3n \times N_c)$-dimensional problem becomes N_c uncoupled problems. The double well potential, taken as the pairwise interaction potential between fragments, allows for partition of the phase space into three regions according to the position of its local maximum and the asymptotic limit. Different interaction potentials are applied to channels that belong to either of the subspaces. As a result, the total DOS is given by a sum over possible channels such as

$$\Omega(E) = \sum_{j=1}^{N_c} \Omega_e(\boldsymbol{c}_j)\Omega_n(\boldsymbol{c}_j)\Omega_{\boldsymbol{c}_j}(E), \tag{3.72}$$

where $\Omega_e(\boldsymbol{c}_j)$ represents the electronic DOS, $\Omega_n(\boldsymbol{c}_j)$ denotes the combinatorial DOS and $\Omega_{\boldsymbol{c}_j}(E)$ is associated with the $\boldsymbol{c}_j$-th channel with the energy E. The electronic DOS introduces the electronic state degeneracy. If $N_f^{(j)}$ denotes number of fragments in channel $\boldsymbol{c}_j$ and $\boldsymbol{s}_i^{(j)}$ is the i-th fragment in channel $\boldsymbol{c}_j$, then

$$\Omega_e(\boldsymbol{c}_j) = \prod_{i=1}^{N_f^{(j)}} \Omega_e(\boldsymbol{s}_i^{(j)}) \tag{3.73}$$

represents the total electronic DOS. The number of accessible microstates is calculated using the symmetry of the electronic wave function of each fragment as follows:

$$\Omega_e(\boldsymbol{s}) = \begin{cases} (2S+1)(2L+1), & \text{if } \boldsymbol{s} \text{ is an atom} \\ (2S+1), & \text{if } \boldsymbol{s} \text{ is a linear molecule}(M_L = 0) \\ (2S+1)2\mid M_L \mid, & \text{if } \boldsymbol{s} \text{ is a linear molecule}(M_L \neq 0) \\ (2S+1)2D, & \text{if } \boldsymbol{s} \text{ is not a linear molecule} \end{cases} \tag{3.74}$$

Total spin S and total orbital angular momentum L quantum numbers specify values of $\Omega_e(\boldsymbol{s})$ for atoms. In the case of linear molecules, values of $\Omega_e(\boldsymbol{s})$ depend on the total spin and the component of L along the molecular axis: M_L. For nonlinear molecules, $\Omega_e(\boldsymbol{s})$ is calculated using the degeneracy of irreducible representation: D, which equals to 1 for states A and B, and 2,3,4,5 for states E,F,G,H, respectively.

Second component of the total DOS, named combinatorial DOS, introduces the Gibbs' correction factor for the possibility of identical fragments in channel c_j:

$$\Omega_n(\boldsymbol{c}_j) = \frac{1}{\prod_k \boldsymbol{m}(\boldsymbol{s}_k^{(j)})!} \delta \left\{ \sum_{i=1}^{N_f^{(j)}} \boldsymbol{s}_i^{(j)} - \boldsymbol{s}_0 \right\} \delta \left\{ \sum_{i=1}^{N_f^{(j)}} z_i^{(j)} - z_0 \right\}, \tag{3.75}$$

where $\boldsymbol{m}(\boldsymbol{s}_k^{(j)})$ denotes the number of times kth fragment appears in channel $\boldsymbol{c}_j$. Moreover, by including the Dirac's delta functions with the initial fragment identity $\boldsymbol{s}_0$ and the initial charge z_0, the composition and charge conservation rules are satisfied.

The remaining component of the total DOS in eq. 3.72 - $\Omega_{\boldsymbol{c}_j}(E)$ - represents the DOS of a fragmentation channel $\boldsymbol{c}_j$ with the energy E. The Hamiltonian model for a fragmentation channel is obtained by omitting the ro-vibrational couplings and consequently the vibrational contribution of each fragment can be integrated out from the total DOS, leading to

$$\Omega_{\boldsymbol{c}}(E) = \int \prod_{\mu=1}^{N_f} dE_{\nu\mu} \Omega_{\nu\mu}(\boldsymbol{c}, E_{\nu\mu}) \Lambda(\boldsymbol{c}, E - E_\nu), \tag{3.76}$$

where $\Omega_{\nu\mu}(\boldsymbol{c}, E_{\nu\mu})$ is the vibrational DOS of μth fragment and $\Lambda(\boldsymbol{c}, E)$ denotes the combined translational and rotational contributions to the density of states. Next, by assuming a classical harmonic approximation of the fragment's internal degrees of freedom, the vibrational DOS takes the form of the density of states for $f_{\nu\mu}$-dimensional harmonic oscillator, given by

$$\Omega_{\nu\mu}(\boldsymbol{c}, E) = \frac{E^{f_{\nu\mu}-1}}{\hbar^{f_{\nu\mu}} \Gamma(f_{\nu\mu})} \prod_{k=1}^{f_{\nu\mu}} \omega_{\mu k}^{-1}, \tag{3.77}$$

where Γ denotes Euler's gamma function, $f_{\nu\mu}$ is the number of internal vibrational degrees of freedom of μth fragment and $\omega_{\mu k}$ is the frequency of its kth vibrational mode.

The final component $\Lambda(\boldsymbol{c}, E)$ comprises integration of the rotational motion, which is hindered by the coupling of the system's angular momentum with the fragments' orbital rotation. Firstly, definition of the linear momenta of constituent fragments in the center of mass laboratory-oriented system enables fixing $\mathcal{P}_0 = 0$ and the constraint for the linear momentum in eq. 3.71 can be integrated out. However, this approach can not be applied to the constraint for the angular momentum. The M$_3$C method employs a technique proposed by Jellinek and Ly [79], which is based on representing the overall rotation of a nonrigid system as a rotation of a changing rigid body. This means that the tensor of inertia is adapted to the instantaneous position of fragments and the overall rotation and internal displacements can exchange energy. Consequently, the density of states for the translational and rotational motion takes the form of

$$\Lambda(\boldsymbol{c}, E) = \frac{(2\pi)^{s/2}}{\Gamma(s/2)} \left(\frac{1}{M} \prod_{\mu=1}^{N_f} m_\mu \right)^{3/2} \int \frac{d^{f_t}\boldsymbol{\mathcal{R}}}{(2\pi\hbar)^{f_t}} \frac{d^{f_r}\boldsymbol{\theta}}{(2\pi\hbar)^{f_r}} \tag{3.78}$$

$$\times det\boldsymbol{B}(\boldsymbol{\mathcal{R}}, \boldsymbol{\theta})^{1/2} [E - U(\boldsymbol{\mathcal{R}}) - E_{\mathcal{J}_0}(\boldsymbol{\mathcal{R}})]^{s/2-1},$$

where s is the total number of translational and rotational degrees of freedom ($s = f_t + f_r$), m_μ and M are the mass of μth fragment and total mass, respectively. Equation 3.78 includes the term $\boldsymbol{B}$, which results from integration of the angular momenta. Matrix $\boldsymbol{B}$ denotes the diagonal representation of the coupling matrix of inertia tensor, which initially includes effective inertia tensors for the μth fragment (diagonal terms) and the strength of interaction between different fragments (off-diagonal terms). The integrals in eq. 3.78 represent the spatial occupation and the angular part of the eigenrotation of the fragments. The complexity of these integrals requires application of a method of approximation for the calculation of the total DOS. The approach employed by the M₃C method is described in the following subsection.

3.5.3 Metropolis Monte Carlo Sampling

In practice, the Metropolis Monte Carlo procedure is used to integrate the configurational space in eq. 3.78 and sample the vibrational energy in eq. 3.77. In contrast to the regular Monte Carlo technique, the accessible states are not sampled uniformly, but the values of $\Omega(E)$ are the weighting factors leading to the most important parts of the phase space (here, region of maximum entropy). The M₃C method employs the Metropolis algorithm [80], which allows one to find this region through the following procedure:

Step 1 A random configuration of the state vector $\boldsymbol{\chi}_i$ for the given internal energy is chosen and corresponding DOS $\Omega'(\boldsymbol{\chi}_i)$ is calculated.

Step 2 A new state vector $\boldsymbol{\chi}_{i+1}$ is obtained through a small, random modification of the state variables and the new DOS $\Omega'(\boldsymbol{\chi}_{i+1})$ is computed.

Step 3 The acceptance ratio of the new configuration is obtained as

$$p(\boldsymbol{\chi}_i \longrightarrow \boldsymbol{\chi}_{i+1}) = min\left(1, \frac{\Omega'(\boldsymbol{\chi}_{i+1})}{\Omega'(\boldsymbol{\chi}_i)}\right). \tag{3.79}$$

Step 4 A random number $U_{(0,1)}$ is sampled from the uniform distribution.

Step 5 The new state vector is either accepted or rejected depending on the comparison with $U_{(0,1)}$. If $U_{(0,1)} \leq p$, the state $\boldsymbol{\chi}_{i+1}$ is accepted. Otherwise, the system returns to the initial state $\boldsymbol{\chi}_i$.

Steps **2** - **5** are repeated until the accepted modifications constitute 30-50% of all trials. Each transformation is followed by adjustment of the kinetic energy so that the total energy is conserved.

In the M₃C method, the abstract objects which modify the state vectors are called *reactors*. The system's state vector $\boldsymbol{\chi}$ denotes a phase space configuration determined by four variables: composition of the system $\boldsymbol{c}$ (includes number of fragments, their charge, geometry, electronic configuration and spin multiplicity), vibrational energy $\boldsymbol{E}_\nu$, Cartesian coordinates of the fragments' centres of mass $\boldsymbol{R}$ and their orientation in space $\boldsymbol{\theta}$. Following operations enable exploration of the state vectors space:

Vibrational reactor (V) relies on random sampling of the vibrational energy. The maximum possible value is limited by the lowest dissociation energy of involved fragments. Consequently, the vibrational DOS $\Omega_\nu(\boldsymbol{c}, E)$ is recalculated.

Rotational reactor (R) denotes random sampling of the fragments' orientation from the uniform distribution. This operation modifies the angular momentum couplings between different fragments and the inertia tensors.

Translational reactor (T) randomly samples new positions of each fragment, so that they fit in the reaction volume and do not overlap. As a result, the interacting potential between fragments is recomputed.

Structure reactor (S_n) changes the system's composition according to a random search tree of all fragments from the database. Possible values of n include $n = -1, 0, 1$, where n determines the change in number of fragments. This reactor requires recomputation of all quantities.

The resulting sequence of accepted state vectors is called the Markov Chain. In general, a sequence of several thousand reactors guarantees a sufficient exploration of the phase space and can be written in a following way: $\boldsymbol{\chi}_0 \xrightarrow{V} \boldsymbol{\chi}_1 \xrightarrow{R} \boldsymbol{\chi}_2 \xrightarrow{T} \boldsymbol{\chi}_3 \xrightarrow{S_1} \boldsymbol{\chi}_4 \xrightarrow{V} \cdots$

Eventually, the statistical expectation value of an observable f is approximated as an arithmetic average

$$\langle f \rangle = \frac{1}{N} \sum_{i=1}^{N} f(\boldsymbol{\chi}_i), \tag{3.80}$$

where N denotes total number of proposed changes of the state vector (both accepted and rejected). In order to account for the equilibration period of the system, the first 10% of generated state vectors is removed from the averaging procedure. This average is true within the ergodic hypothesis that the M$_3$C method assumes. The ergodic theorem states that when the system has infinite time to evolve, the statistical time average of a certain property becomes a space average. This approach is widely used in studies of stochastic processes and the entropy of dynamical systems [81]. For a specific internal energy, the obtained observables include fragmentation channel probabilities, components of the total energy and different contributions to the total DOS.

Chapter 4

Computational details

The approach applied in the present work consists of three theoretical methodologies, previously detailed in Chapter 3. These three methods have been chosen due to the fact that they provide complementary information about the fragmentation process. Following section specifies the technical aspects of the applied theoretical techniques.

4.1 *Ab initio* Molecular Dynamics

Firstly, *ab initio* Molecular Dynamics simulations enabled the identification of the most probable reaction mechanisms occurring for different internal energies. The calculations were carried out using the ADMP method with the B3LYP functional and 6-31G(d,p) basis set implemented in the Gaussian09 package [61]. The propagation time of the simulations has been limited to $t_{max} = 500$ fs for neutral and singly ionized furan and to $t_{max} = 300$ fs in the case of furan dication. Such duration of the simulations proved to be sufficient in observation of the separated fragmentation products. A time step of $\Delta t = 0.1$ fs ensured good separation between electronic and nuclear degrees of freedom. Moreover, fictitious mass of $\mu_e = 0.1$ amu has been chosen to guarantee conservation of the total energy. Modelling the experimental conditions of collision induced fragmentation is possible through taking the molecule optimized in the neutral state as input geometry in the dynamical simulations of ionized furan. This is in accordance with the Franck-Condon principle, stating that positions of the nuclei in the molecule experience no significant change under an electronic transition, such as ionization [82]. Therefore, either one or two electrons from the highest occupied molecular orbital were extracted and the excitation energy, varying from 5 to 30 eV in steps of 1 eV, was introduced into the system. Random distribution of the internal energy over all vibrational degrees of freedom and multiple simulations starting from the same structure made it possible to perform a statistical analysis of the fragmentation mechanism. For each internal energy of every charge state 150 calculations were run, leading to 3900 trajectories in total for each charge state. Dynamical calculations have been performed at the Centre of Informatics - Tricity Academic Supercomputer & networK (CI TASK). The CPU time of the simulations varied significantly depending on the initial distribution of velocities, however, on average, single trajectory of 500 fs run for about 48 hours (the average taken over 150 trajectories of 15 eV deposited to singly ionized furan).

The large amount of obtained data imposes the use of external programs, which efficiently parse the output files. A convenient choice are bash scripts that work quickly with the outputs stored at the computing servers. The data analysis was based on the following:

Step 1 Extraction of geometries and charge distributions from the last step of the Gaussian output files,

Step 2 Determination of the exit channel of every trajectory by assuming bonds to be broken when distance between atoms exceeded R = 2.5 Å,

Step 3 Counting and classification of final exit channels depending on the number of produced fragments for more comprehensible interpretation.

All MD output files were treated with the described procedure, which only provided the information about the final step of the simulation. It is equally important to have an idea of the mechanisms taking place during the simulations, so some trajectories were viewed using the MOLDEN visualization package [83]. Additionally, trajectories of the most abundant processes were treated with a script extracting geometries at consecutive time steps. As a consequence, intermediate processes were explored. In summary, the features that have been extracted from the MD include structures and charge distribution of fragments at a final time step, channels probabilities, type of observed processes and their average times and sequence of events in a specific group of processes.

4.2 Exploration of the Potential Energy Surface

As the lifetime of some reactions might be longer than 500 fs, it is necessary to carry out an investigation of structural and energetic features of the species participating in the observed processes. Hence, as a second step, exploration of the Potential Energy Surface has been performed. For this purpose, quantum chemistry calculations of reactants, intermediates, transition states and products were carried out. Geometry optimizations have been performed at the B3LYP/6-311++G(3df,2p) level of theory for the neutral molecule and B3LYP/6-311++G(d,p) for charged furan. This level of theory has been extensively applied to studies of hydrocarbons [84], [85] and heterocyclic molecules [86], [87] and proves to be an adequate choice for molecular and electronic structure calculations of furan. The harmonic vibrational frequencies and zero point energy corrections were predicted using the same level of theory. All minima are characterized by having positive harmonic vibrational frequencies and all transition states present only one imaginary frequency. In search for the geometries of transition states three approaches were interchangeably applied:

- optimization of the trial geometry,

- relaxed scans along the reaction coordinate,

- the Synchronous Transit-Guided Quasi-Newton method that requires reactants and products as input.

The first and the second method were used with similar frequency, however, `QST2` procedure failed most of the time. To check the correct connections of the critical points on the Potential Energy Surface, Intrinsic Reaction Coordinate (IRC) calculations have been performed for

successfully optimized transition states. Again, all quantum chemical calculations were carried out using Gaussian09 package [61] and computing resources provided by the Wrocław Centre for Networking and Supercomputing (WCSS) and CI TASK. The graphical interface used for visualization of molecular geometries was GaussView version 5.0.8 [88].

4.3   Microcanonical Metropolis Monte Carlo

Finally, simulations of the Microcanonical Metropolis Monte Carlo technique have been performed. Results presented in this work were obtained with the 2.0 version of the M_3C program. The source files were provided by Néstor F. Aguirre, the first author of [78], and installed on the computing cluster of CI TASK, Tryton. The M_3C method was employed to study fragmentation of only neutral and singly ionized furan, because it is not yet applicable to investigation of multiply charged molecules.

4.3.1   Input information

First, a database of all possible fragmentation products is necessary to perform the M_3C simulations. The M_3C interface with the Gaussian package allows for a stochastic search of isomers by optimization of fixed number of trial geometries. Consequently, 226 neutral and 243 singly ionized isomers were successfully optimized at the B3LYP/6-311++G(d,p) level of theory. All obtained geometries are presented in Appendix A. In a complete fragment database every isomer is characterized by: electronic energy, geometry in an xyz format, vibrational frequencies, symmetry of the wave function and molecular symmetry. All this information is required as an input of the M_3C simulation. Moreover, it is necessary to establish the lowest energy dissociation channel of every fragment in the database. This is done automatically through a tool implemented in the M_3C package, which samples the feasible dissociation channels and finishes with the one with the lowest energy.

4.3.2   Convergence search

Before performing any Monte Carlo calculation it is important to check the influence of the simulation parameters on the obtained results. Therefore, performance of the following parameters has been tested:

- system radius - R_{sys} - specifies the radius (in Å) of the available reaction volume,

- Markov Chain sequence - MC_{seq} - indicates the sequence of events acting on the studied system,

- number of events - N_{ev} - defines number of steps in the sampling procedure leading to the maximum entropy region. Single modification of the state vector by a reactor corresponds to one event,

- number of experiments - N_{exp} - number of performed Monte Carlo simulations. Each experiment starts with a randomly selected initial state vector χ_0. Final fragmentation

probabilities are averaged over all experiments and errors are calculated as standard deviations from the mean values.

In this section, the search for convergence of the M_3C simulations is described. To minimize the computational time of the trial simulations, the fragments database was limited to only the most important species. The adopted criteria of a successful simulation were the error values, calculated as a standard deviation from the mean value of a channel probability. Typically, a good Monte Carlo calculation is characterized by errors below 10%. In order to have a single criterion assessing the simulation's accuracy, the errors in channels were averaged according to the following formula

$$\sigma_{sim} = \frac{1}{J} \sum_{j=1}^{J} \sum_{c_j=1}^{C_j} \frac{\sigma_{c_j}}{C_j}, \tag{4.1}$$

where σ_{c_j} is the error in channel c for the jth energy scan. The value of C_j denotes total number of channels for the jth energy scan and J total number of performed energy scans (here 21).

Firstly, the R_{sys} parameter has been tested. The essential requirement is that the parent molecule and dissociation products should fit into the volume $V_R = \frac{4}{3}\pi R_{sys}^3$. In the previous M_3C application to investigation of fragmentation of carbon clusters [76] the authors suggested that $R_{sys} = N_T \cdot 1$Å and $R_{sys} = N_T \cdot 2$Å (N_T denotes total number of carbon atoms) provided practically the same results. As furan molecule consists of nine atoms, the values of R_{sys} = {10Å, 13Å, 15Å, 20Å} have been tested and as in [76] no significant changes have been observed. Consequently, the $R_{sys} = 13$ Å has been chosen for the future simulations. Optimization of the rest of simulation parameters is discussed separately for the neutral and ionized case.

For the neutral furan, the Markov Chain sequence and number of events were tested simultaneously while number of experiments was kept constant ($N_{exp} = 5$). Figure 4.1 shows the averaged error as a function of the number of events for different Markov Chain sequences. The notation used in the figure denotes following sequences:

$MC_{1/5S}$	5×(V,T,R),S:0,5×(V,T,R),S:-1:1
MC_{1S}	V,T,R,S:0,V,T,R,S:1:-1
MC_{5S}	V,T,R,5 × S:0,V,T,R,5× S:1:-1
$MC_{5,5S}$	5× S:0,V,T,R,5*S:0,V,T,R,10 × S:1:-1
MC_{10S}	V,T,R,10× S:0,V,T,R,10× S:1:-1
MC_{20S}	V,T,R,20× S:0,V,T,R,20× S:1:-1

The definition of each reactor is described in the section 3.5.3. The main difference between tested sequences is the amount and order of the S reactors (which have the highest computational cost). From Figure 4.1 it can be seen that with increasing number of S reactors the averaged error decreases until reaching 5 reactors in the MC sequence. Then, the simulation's accuracy stabilizes and does not substantially improve when more S reactors are added. Moreover, with the increasing number of events the averaged error reaches a plateau starting from around 800 000 events. Consequently, the values chosen for the next step of the convergence
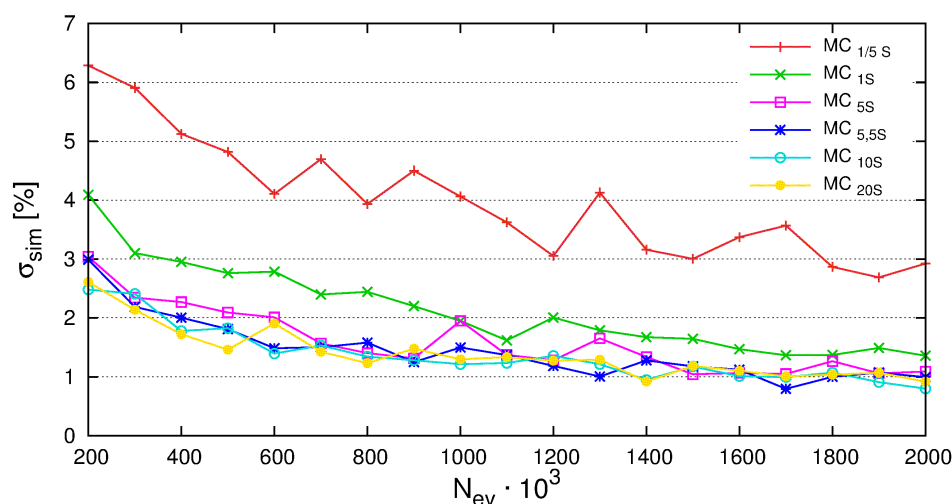
FIGURE 4.1 Results of optimization of the MC sequence and number of events of the M_3C simulation of neutral furan with $N_{exp} = 5$.
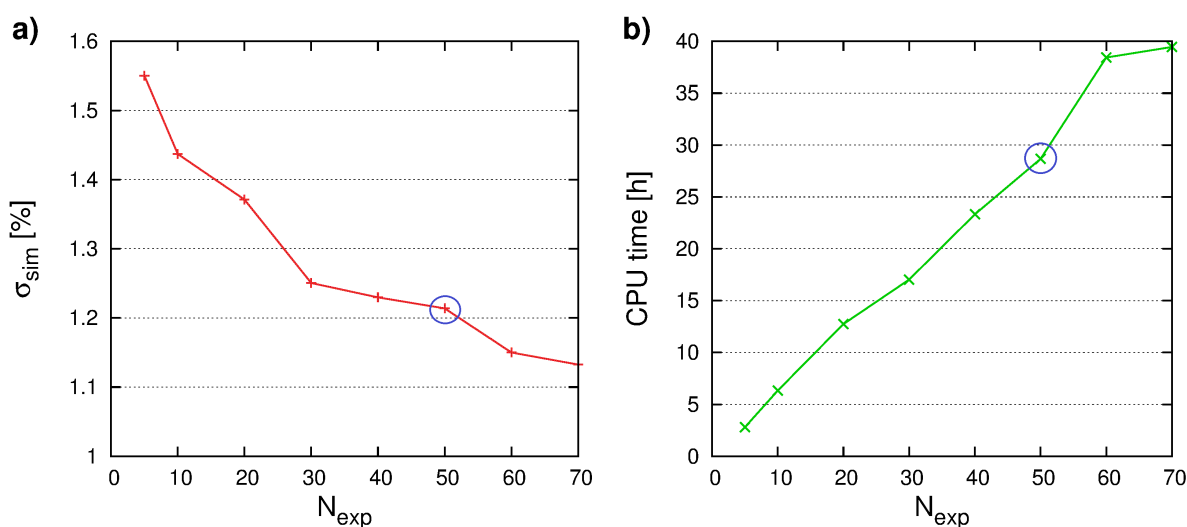
FIGURE 4.2 Panel **a)**: results of the optimization of the number of experiments of the M_3C simulation of neutral furan with MC_{5S} and $N_{ev} = 800\,000$. Panel **b)**: computational time of the respective simulations.

search are: $MC_{seq} = V, T, R, 5 \times S : 0, V, T, R, 5 \times S : 1 : -1$ and $N_{ev} = 800\,000$. Finally, the optimum number of experiments was tested. Figure 4.2 presents averaged errors as a function of the number of experiments together with the CPU times of the corresponding simulations. The number of experiments chosen for the final calculation was $N_{exp} = 50$. At this point, the averaged error value stabilizes at around 1.2% (highlighted with a blue circle in Figure 4.2) and the computational cost is justifiable.

The M_3C simulations of the singly ionized furan include an improvement to the phase space sampling method. The new technique, named SEQUENTIAL, differs from the RANDOM sampling in allowed transitions as steps in the Markov Chain sequence. SEQUENTIAL sampling removes S reactors that in a way are "unphysical". This modification works under the assumption that if the system has already lost a light fragment, it is unlikely that it will reattach to the

parent molecule and then recombine. As an example, a forbidden reaction under the SEQUEN-
TIAL sampling method would be the second transition in sequence: $H_4C_4O^+ \rightarrow H + H_3C_4O^+$
$\rightarrow C + H_4C_3O^+$. Consequently, the configurational space is sampled more efficiently and the
computational cost of calculations decreases. Again, the first step of the convergence search
was the simultaneous optimization of the Markov Chain sequence and number of events, while
number of experiments was kept constant ($N_{exp} = 100$). Figure 4.3 demonstrates decrease of
the averaged error until around $N_{ev} = 250\,000$. As a compromise between computational cost
and accuracy, MC_{1S} and MC_{5S} sequences with 200 000 number of events were chosen for sub-
sequent testing of the number of experiments. According to the results presented in Figure 4.4,
the optimum value of experiments for the M_3C simulation of singly ionized furan is $N_{exp} = 500$
with MC_{5S} (highlighted with a blue circle).
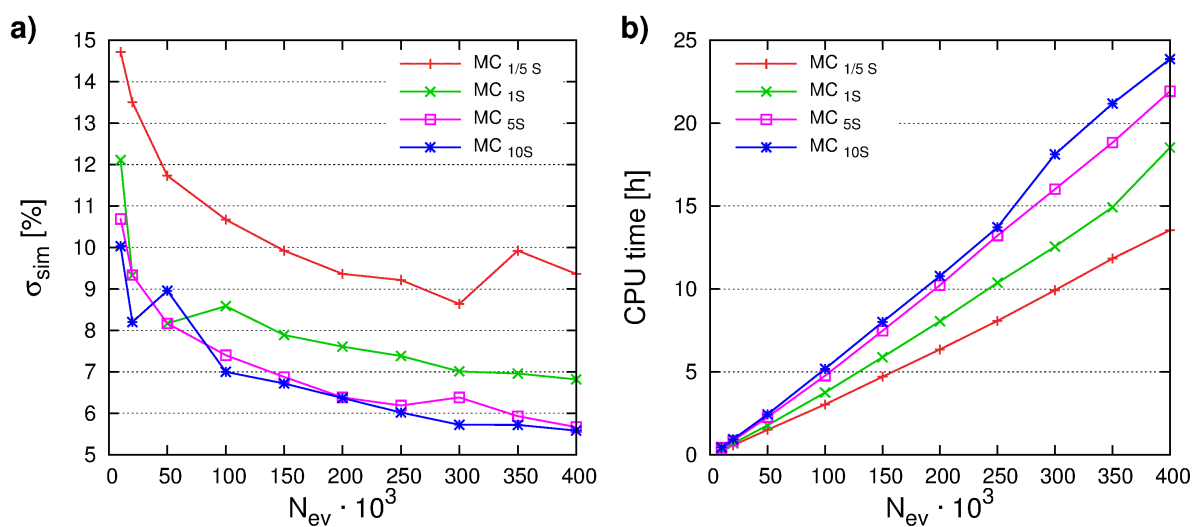
FIGURE 4.3 Panel **a)**: Results of optimization of the MC sequence and number of events of the M_3C simulation of
singly ionized furan. Panel **b)**: computational time of the respective simulations.
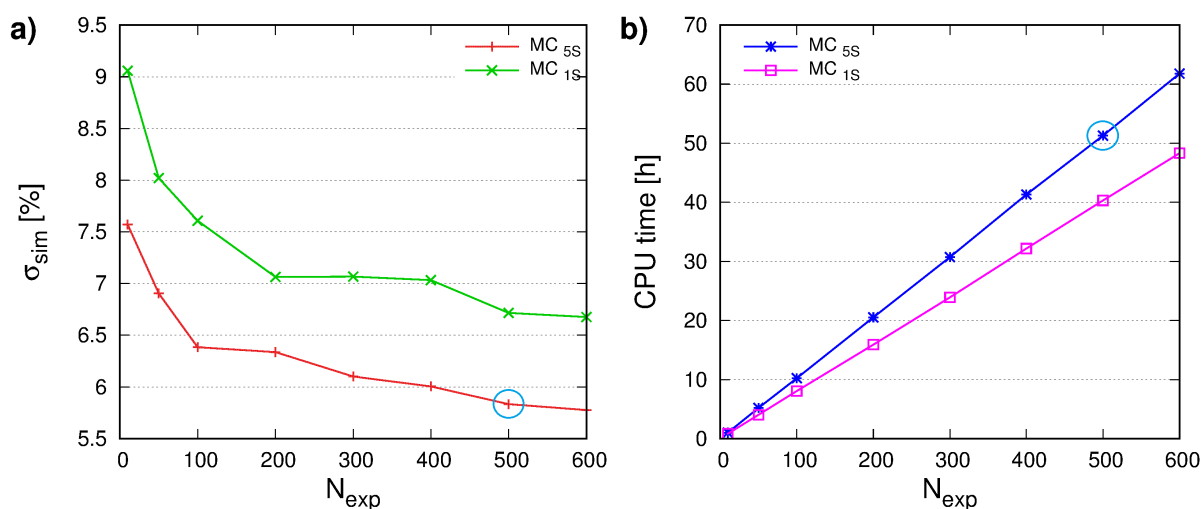
FIGURE 4.4 Panel **a)**: results of the optimization of the number of experiments of the M_3C simulation of singly
ionized furan with $N_{ev} = 200\,000$. Panel **b)**: computational time of the respective simulations.

In summary, parameters chosen for the final calculations are presented in Table 4.1. Both in the neutral and singly ionized case the energy was scanned up to 20 eV every 0.5 eV. As a result of the performed simulations, similarly to the ADMP method, a statistical distribution of all possible fragmentation channels as a function of the internal energy is obtained. Additional output information include possible reactions and the correlation between pairs of energy components.

TABLE 4.1 Final parameters of the M$_3$C simulations

Parameter	H$_4$C$_4$O	H$_4$C$_4$O$^+$
System Radius	13 Å	
Markov chain sequence	V,T,R,5×S:0,V,T,R,5×S:1:-1	
Number of experiments	50	500
Number of events	800 000	200 000
Sampling method	RANDOM	SEQUENTIAL

4.3.3 Fitting of the energy distribution function

As an output, the M$_3$C method provides fragmentation probabilities as a function of the internal energy. Direct comparison of the theoretical and experimental results is possible if the distribution of energy deposited during the collision is known. Such functions have been previously reported only for several systems. Those procedures relied either on coincidence measurement of the scattered negative ion and the fragmentation products [89] or combination of photon and ion experiments [90]. Theoretical determination of energy transfer is also possible by calculating the nuclear and electronic stopping powers [91] or evaluating the calculated transition amplitudes [92], [93]. However, basing on the semiempirical arguments, distribution of the deposited energy might as well result from fitting of an analytical function so that the errors between theoretical and measured branching ratios are minimized. This last approach is implemented in the M$_3$C software package and was applied in the present work. The employed fitting procedure is described below.

A branching ratio R_i of a channel i in a microcanonical ensemble is given by

$$R_i = \int_0^\infty f(E)P_i(E)dE \quad \text{for} \quad i = 1, 2, \ldots, I \tag{4.2}$$

where $f(E)$ is the normalized energy distribution function and $P_i(E)$ is the fragmentation probability of a channel i. The form of function $f(E)$ has been chosen so that it represent a Boltzmann distribution at higher temperatures. A Slater-type basis set ensures the required features of a one-maximum distribution and exponential decay at long range. Hence, the energy distribution function takes the form of

$$f(E) = \sum_{k=1}^K c_k B_k(E), \quad \text{where} \quad B_k(E) = B_{\{n_k,l_k\}}(E) = \frac{1}{l_k!}\left(\frac{1}{n_k}\right)^{l_k+1} E^{l_k} e^{-E/n_k}. \tag{4.3}$$

The normalization of the $f(E)$ function is satisfied by the constrains on the c_k coefficients: $\sum_{k=1}^{K} c_k = 1$ and basis set elements $B_k(E)$: $\int_0^\infty B_k(E)dE = 1$. Effectively, determination of the parameters c_k, n_k and l_k is the goal of the fitting procedure. The new form of the branching ratio R_i now reads

$$R_i = \sum_{k=1}^{K} c_k A_{ik}, \quad \text{where} \tag{4.4}$$

$$A_{ik} = \int_0^\infty B_k(E) P_i(E)dE \quad \text{for} \quad i = 1, 2, \ldots, I \quad \text{and} \quad k = 1, 2, \ldots, K. \tag{4.5}$$

This set of equations can not be uniquely solved, as it describes an overdetermined system (number of channels I is larger than the number of basis set elements K). Hence, a least squares method has been applied in order to minimize the sum of squared differences between theoretical R_i and experimental R_i^{exp} branching ratios, which reads

$$S = \sum_{i=1}^{I} \left[\sum_{k=1}^{K} c_k A_{ik} - R_i^{exp} \right]^2, \tag{4.6}$$

in a matrix form:

$$S = Tr[(\mathbf{Ac} - \mathbf{R}^{exp})^T (\mathbf{Ac} - \mathbf{R}^{exp})]. \tag{4.7}$$

If $\hat{\mathbf{c}}$ denotes the values of $\mathbf{c}$ that minimize the S, then

$$\frac{dS}{d\mathbf{c}}\bigg|_{\mathbf{c}=\hat{\mathbf{c}}} = 2\mathbf{A}^T (\mathbf{A}\hat{\mathbf{c}} - \mathbf{R}^{exp}) = 0. \tag{4.8}$$

Finally, the problem simplifies to the solution of

$$\mathbf{A}\hat{\mathbf{c}} = \mathbf{R}^{exp}, \quad \text{where} \quad \hat{\mathbf{c}} \geq \mathbf{0} \quad \text{and} \quad \hat{\mathbf{c}}^T \hat{\mathbf{c}} = 1. \tag{4.9}$$

In practice, equation 4.9 is transformed to

$$\left[\begin{pmatrix} \mathbf{I} & \mathbf{0} \\ \mathbf{0} & \eta \end{pmatrix} \begin{pmatrix} \mathbf{A} \\ 1 \end{pmatrix} \right] \begin{pmatrix} \hat{\mathbf{c}} \\ 0 \end{pmatrix} = \begin{pmatrix} \mathbf{I} & \mathbf{0} \\ \mathbf{0} & \eta \end{pmatrix} \begin{pmatrix} \mathbf{R}^{exp} \\ 1 \end{pmatrix}, \tag{4.10}$$

where $\mathbf{I}$ is the identity matrix of size $I \times K$ and η is a real number that is set to 10^8 in this particular calculation. The transformation to eq. 4.10 allows one to apply the standard Lawson and Hanson's algorithm [94] for solution of the least square problems.

As an example of the fitting procedure, Figure 4.5 presents the fitted energy distribution functions for collision of Ar^{11+} ions (panel **a)**) and electrons (panel **b)**) with singly ionized furan. Their interpretation and convolution with species probabilities are provided in the Chapter 5. Here, a difference can be noticed in the shape of obtained functions through inclusion of several basis set elements. The total energy distribution function of collision with Ar^{11+} exhibits a maximum at approx. 1 eV and a second node at 6 eV. However, the total energy distribution function of collision with electrons is a single maximum distribution with the peak

centred at approx. 4 eV. These results show that the applied fitting procedure is adequate for reproducing the experimental branching ratios of various kinds of collisional systems.
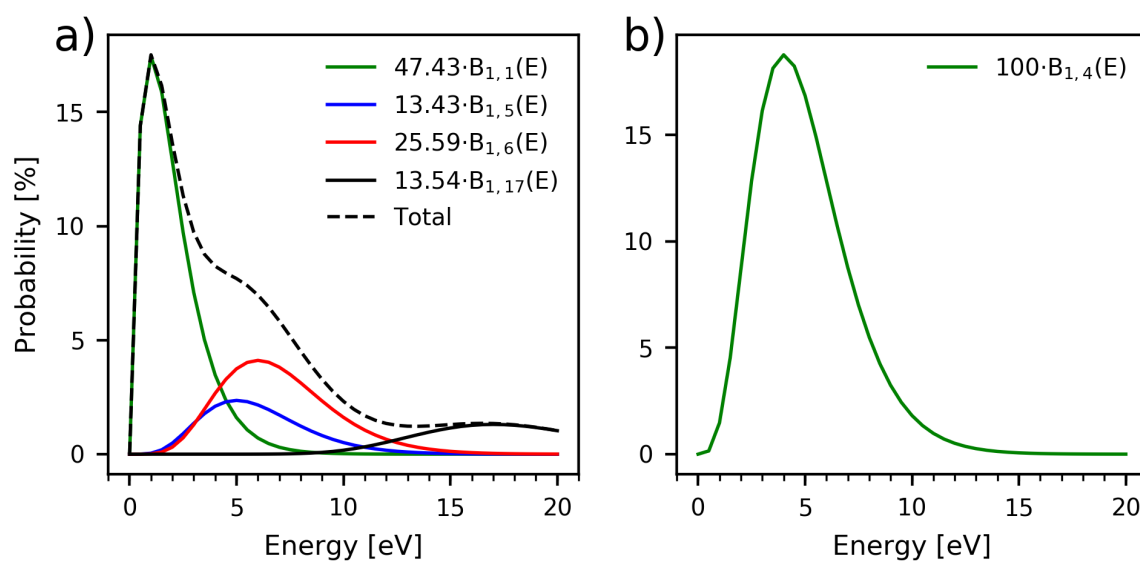
FIGURE 4.5 Results of the fitting to the experimental branching ratios measured for the collsion of singly ionized furan with **a)** Ar^{11+} ions and **b)** electrons.

Chapter 5

Results and discussion

5.1 Neutral furan

5.1.1 Molecular Dynamics

Results of the dynamical simulations of neutral furan are presented in Figures 5.1 - 5.3. Statistical analysis of the obtained trajectories (3900 overall) allowed to identify the most abundant processes presented in Figure 5.1 **a)**. The following description of the observed processes is divided into four groups of possible mechanisms: (1) isomerization, (2) fragmentation, (3) H/H$_2$
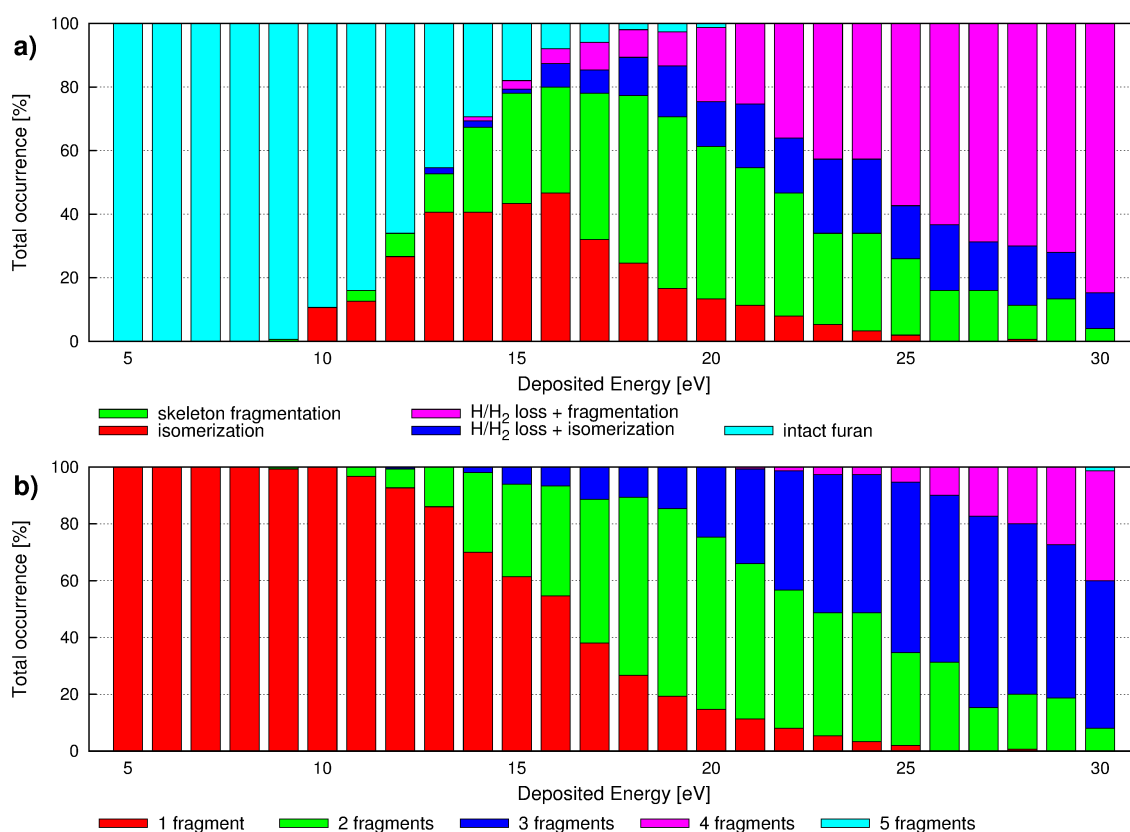
FIGURE 5.1 Results of the ADMP simulations of neutral furan: total occurrence of **a)** observed processes **b)** number of fragments as a function of internal energy.

loss + isomerization and (4) H/H_2 loss + fragmentation. The first process to appear is isomerization at 9 eV and it remains a dominant process until the energy of 16 eV. Secondly, we can observe skeleton fragmentation starting at 10 eV and becoming a dominant process between the energies of 17 and 23 eV. Channels that include H and H_2 loss followed by isomerization both start at the energy of 13 eV and reach maximum probability at 24 eV and 19 eV, respectively. Finally, since the energy of 22 eV H/H_2 loss followed by fragmentation become the dominant processes. Figure 5.1 **b)** presents produced number of fragments depending on the energy applied to the system. It can be noticed that, as expected, for lowest energies furan molecule does not decompose. Two-body fragmentation is the dominant process for the energy range 17-23 eV. Afterwards, three-body fragmentation channels prevails.
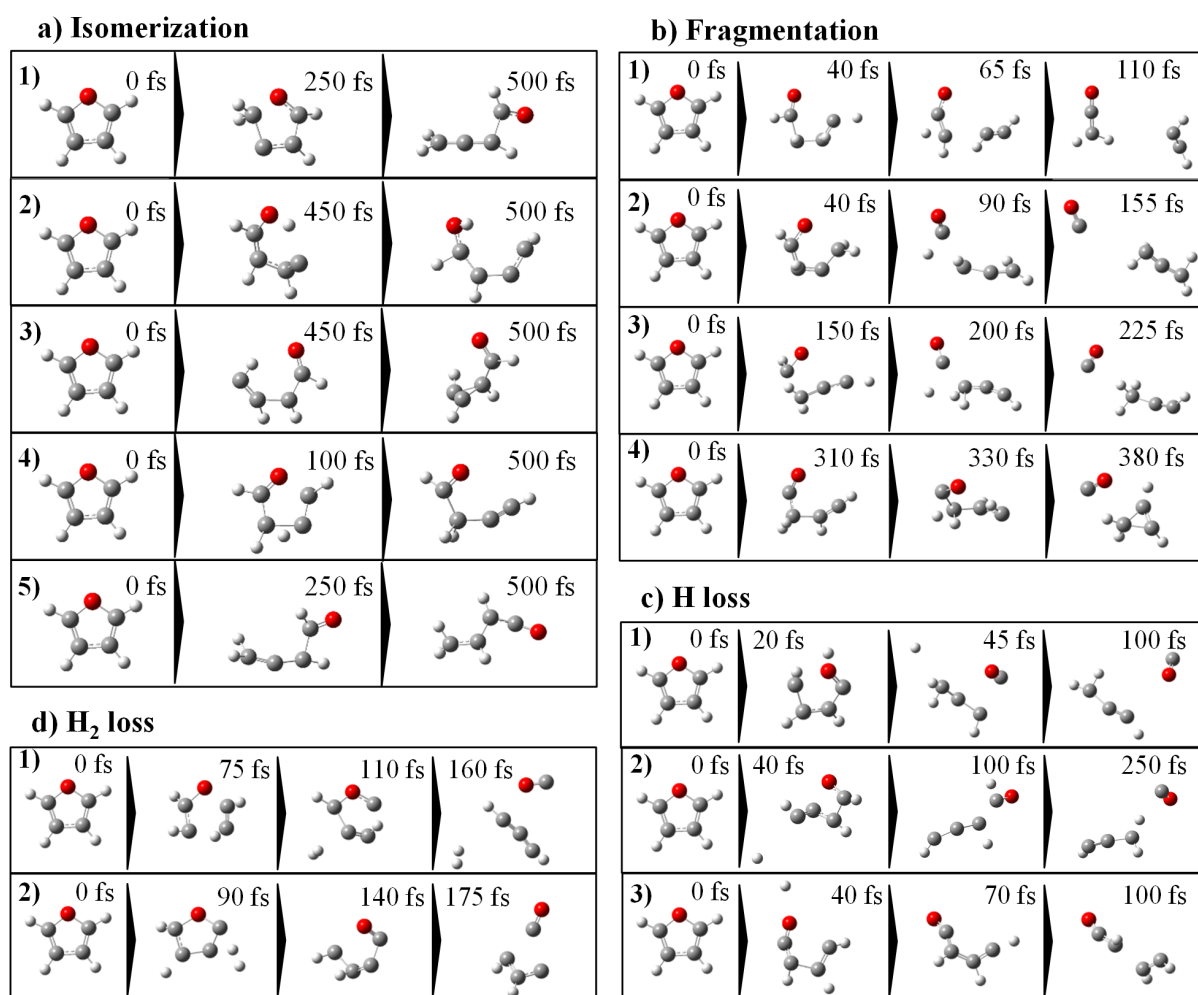
FIGURE 5.2 Results of the ADMP simulations of neutral furan: snapshots of the most significant trajectories.

In the case of furan, an **isomerization** process can indicate either ring opening, hydrogen transfer to neighbouring atom or rotation of the dihedral angle and breaking of the planar symmetry of the molecule. The panel **a)** in Figure 5.2 presents five furan isomers that dominate the MD and how they evolve in time. Their order corresponds to how abundant they were throughout the entire energy range, from the most (panel **1)**) to least (panel **5)**) observed. These exemplifying snapshots show that the required rearrangements take place late in the
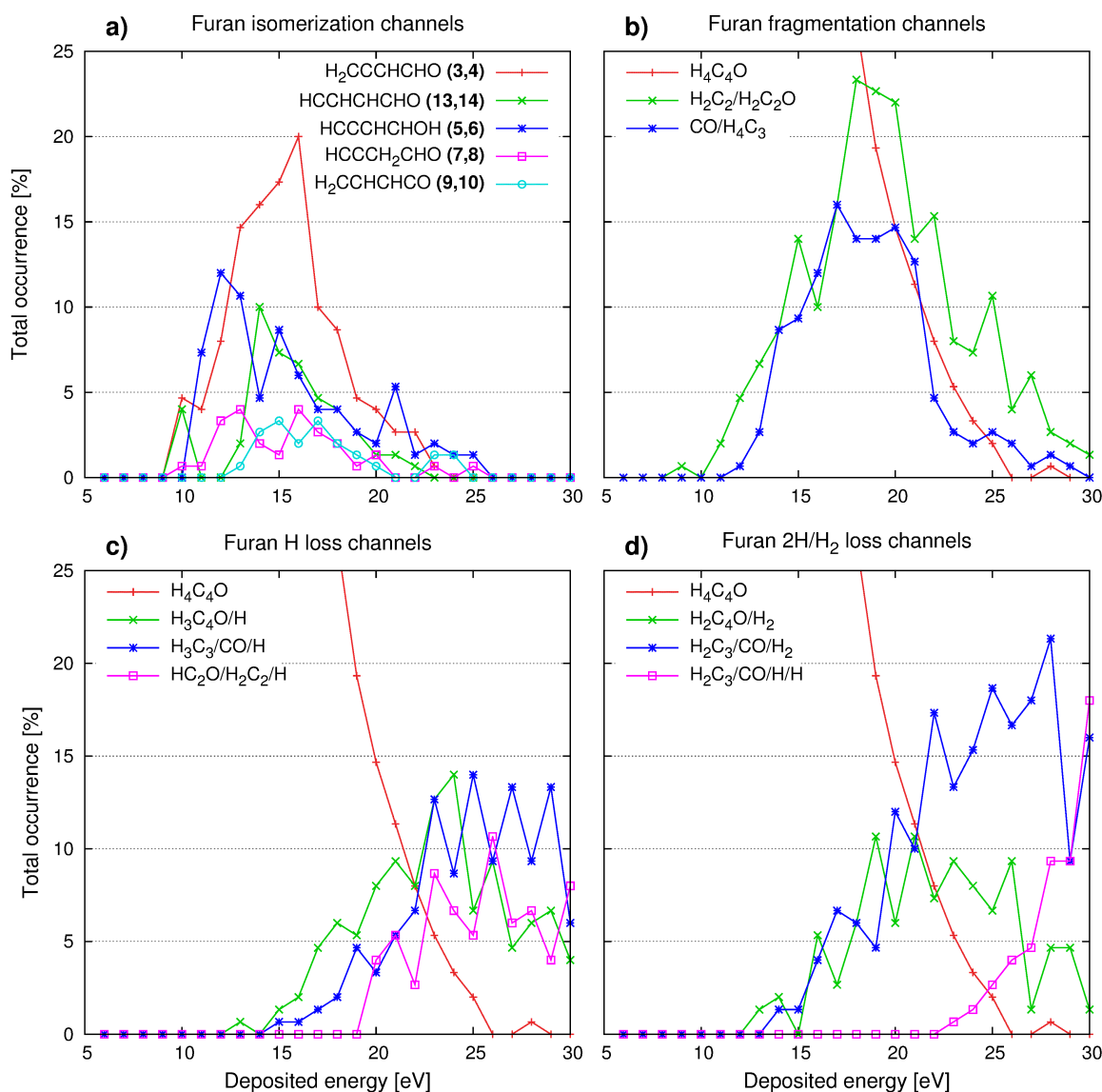
FIGURE 5.3 Results of the ADMP simulations of neutral furan: Most important channels as a function of internal energy. Only channels that appeared at least 10% at a certain point in the energy range are presented. Numbers in brackets of the panel **a)** indicate numbering of isomers in the Potential Energy Surface exploration.

dynamics and if the system was given more simulation time it could potentially evolve until fragmentation. As it is shown in Figure 5.3 **a)**, the most prevalent furan isomer corresponds to formyl-allene structure that can be achieved by 1,2 hydrogen transfer ($H_2C=C=CH-CHO$, 177 trajectories in total). Next most abundant isomer - alkyne-alcohol - is produced by H transfer to the oxygen atom ($HC\equiv C-CH-CH-OH$, 110 trajectories). Third most populated isomerization channel can be seen as cyclopropene substituted by a CHO group (67 trajectories). This isomer does not include hydrogen transfer, but relies on ring opening and cyclization of three carbon atoms. The following isomers are a formyl-alkyne ($HC\equiv C-CH_2-CHO$, 36 trajectories), achieved by 2,3 H transfer and a structure $H_2C=CH-CH=C=O$ (28 trajectories), achieved by two subsequent hydrogen transfers. It is worth pointing out that decreasing probability of isomerization at higher energies does not reflect reduced relevance of the isomerization process.

This mechanism remains valid, but simply occurs earlier in the dynamics and at t=500 fs is already followed by fragmentation.

Channels marked as **skeleton fragmentation** involve cleavage of C-O and C-C bonds, usually after prior isomerization, but does not allow H/H$_2$ loss. In significant majority of considered trajectories C-O bond is the first to break. The panel **b)** in Figure 5.2 presents illustrative time evolution of two most populated fragmentation channels: HCCH + H$_2$CCO (**1)**) and CO + H$_4$C$_3$ (**2)-4)**). Production of exit channel HCCH + H$_2$CCO starts with C-O bond break and is followed by simultaneous 1,2 H transfer and C-C break. As it can be noticed from panel **b)** of Figure 5.3, fragmentation into acetylene (HCCH) and ethenone (H$_2$CCO) appears first in the dynamical simulations and is the most abundant mechanism of furan decomposition into two fragments. Channel CO + H$_4$C$_3$ can be obtained in a few different ways, depending on the final isomer of H$_4$C$_3$. The most populated channels comprise either two 2,1 H transfers leading to allene (H$_2$CCCH$_2$) or 3,2 and 1,2 H transfer leading to propyne (H$_3$CCCH). Least populated channel produces cyclopropene (H$_2$CCHCH) and requires cyclization and one H transfer. The total numbers of trajectories producing mentioned isomers of H$_4$C$_3$ are 96, 44 and 35, respectively.

Third observed process was found to be **H/H$_2$ loss** followed by **isomerization**. As presented in panel **c)** of Figure 5.3, single H loss and subsequent isomerization appears early in the energy range, however, it has to be stressed again that the remaining H$_3$C$_4$O species might fragment, given more time to evolve. A competition between H$_\alpha$ and H$_\beta$ elimination can be noticed, however, majority of the cases of single hydrogen loss occurs from α position (91 vs 73 trajectories, respectively). Channels of H$_2$ loss are also highly observed. Particularly, significant prevalence of H$_2$ loss from α and β positions of one side of the furan ring can be noticed. The frequency of H$_2$ loss in a decreasing order is: adjacent H$_\alpha$ and H$_\beta$ (64%) > opposite H$_\alpha$ and H$_\beta$ (15%) > two H$_\alpha$ (11%) > two H$_\beta$ (10%).

The most abundant three-body fragmentation channel has been found to produce fragments H$_2$C$_3$, CO and H$_2$ and at the same time to exhibit second highest total occurrence throughout all energies. H$_2$ loss from adjacent α and β positions remains the most abundant configuration of molecular hydrogen loss with the total occurrence being: adjacent H$_\alpha$ and H$_\beta$ (61%) > two H$_\alpha$ (18%) > opposite H$_\alpha$ and H$_\beta$ (13%) > two H$_\beta$ (8%). The most important channels of H loss appear after the channel of H$_2$ loss, first at 15 eV producing H$_2$C$_3$, CO and H and later at 20 eV producing HC$_2$O, H$_2$C$_2$ and H. Snapshots of mentioned channels in panel **c)** of Figure 5.2 show that H loss takes place at around 20-40 fs. Subsequently, it can be followed by H transfer (decomposition to H$_3$C$_3$/CO/H) or can directly fragment (decomposition to HC$_2$O/H$_2$C$_2$/H). Alike in the process of H loss followed by isomerization, hydrogen is mainly eliminated from α position (66% of trajectories).

5.1.2   Potential Energy Surface

Complementary information on relative stability of structures obtained in the MD and their reaction pathways are required to understand production yields of important exit channels.

Moreover, exploration of Potential Energy Surface enables extending the dynamical simulations of trajectories that could still undergo some processes, but were limited by the simulation time. Calculated pathways, presenting minima and transition structures optimized at the B3LYP/6-311++G(3df,2p) level of theory, are displayed in Figures 5.4 - 5.7. Correspondingly to the discussion of MD results, description of PES follows a similar scheme. Isomerization of the system prior to the fragmentation is considered first, followed by explanation of the skeleton fragmentation, H loss and finally H_2 loss. Previous theoretical studies [26], [28] focused on isomerization and fragmentation processes, however, hydrogen elimination as well as multi-fragmentation have never been studied before.

Search for possible furan isomers was mainly based on the mechanisms observed in the Molecular Dynamics simulations. Depending on the first step of the process, five **isomerization** pathways (p1-p5), shown in Figure 5.4, can be distinguished. The lowest energy barrier is associated with 1,2 H migration to form cyclic α-carbene (**1**) – a structure with two unshared electrons localized on the same C_α atom. Second pathway - p2 - corresponds to 2,1 H transfer to form β-carbene (**2**). It is worth pointing out that no carbene structures were found at the end of MD simulations, the reason being the known short lived and highly reactive character of carbenes. Structure **2** can further isomerize to formyl-allene (**3** and **4**) through elongation of the C-O bond. This molecule can also be obtained directly from furan by concerted H transfer and ring opening (p2'), but requires overcoming a higher energy barrier. Low barrier for obtaining formyl-allene is consistent with high abundance of this isomer in MD calculations (177 trajectories).

Further hydrogen migration from C_α(4) to oxygen atom with a transition structure located at 2.66 eV gives structure **5**, the second most populated isomer in MD simulations (110 trajectories). Alternatively, from formyl-allene (**4**) a higher energy barrier of 3.14 eV was found for 1,4 H transfer leading to stable structures **9** and **10**, the lowest populated isomers in MD.

Third pathway - p3 - connects furan and structures **7** and **8** by 2,3 H transfer through the highest energy barrier computed for direct transition from furan, viz. 3.74 eV. On the other hand, structure **8** can be also obtained from formyl-allene (**4**), however the energy barrier for such isomerization is higher (3.83 eV) and more steps of rearrangement are required. The fourth pathway - p4 - is associated with the ring opening by cleavage of the C-O bond and implies energy barrier of 3.52 eV. Obtained minima **13** and **14** correspond to isomers of the third most populated channel (67 trajectories). Pathway p5 also starts with cleavage of the C-O bond, but the calculated transition structure is located 0.08 eV higher than the first TS of p4 and yields unstable isomers, not found in the MD.
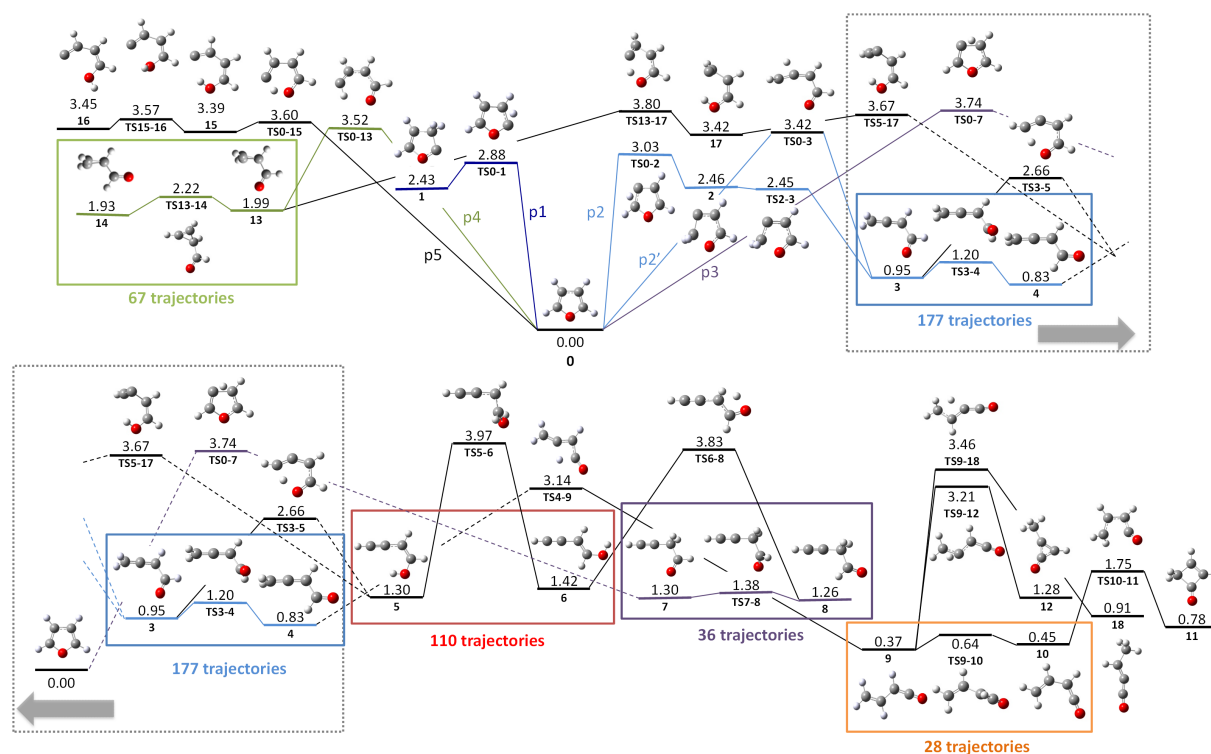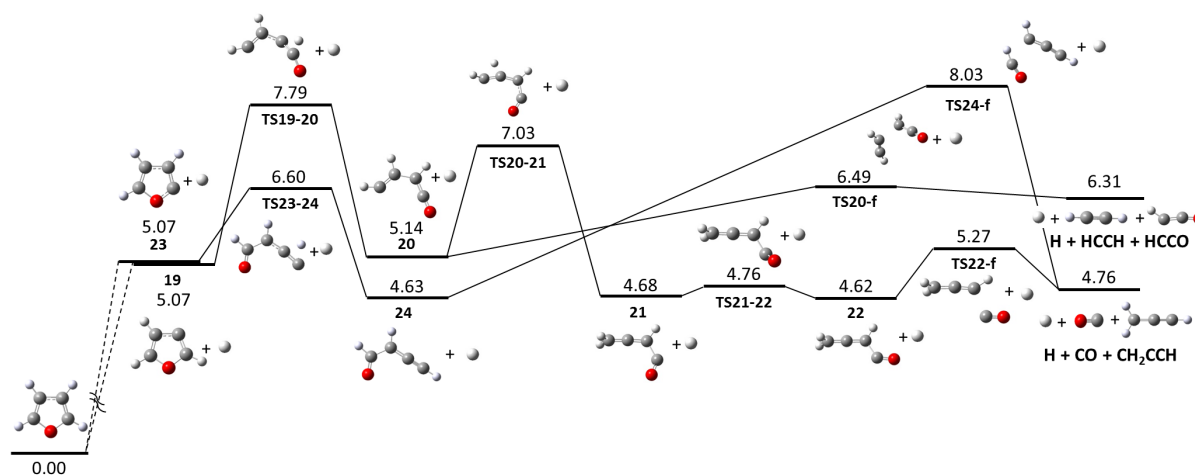
FIGURE 5.4 Potential Energy Surface for the isomerization process. Energies calculated at B3LYP/6-311++G(3df,2p) level of theory are given in eV relative to furan. Zero point energy (ZPE) corrections are included. Transition structures are named with regard to the minima they connect. The total number of trajectories obtained in the MD is indicated for five families of isomers.

TABLE 5.1 Comparison of ADMP and PES exploration results for the isomerization process.

Isomer	Total number of trajectories	Structure	Energy barrier [eV]	Number of TS	Energy barrier [eV] [28]
$H_2C=C=CH-CHO$	177	**3** and **4**	3.03	2	2.99
$HC\equiv C-CH-CH-OH$	110	**5** and **6**	3.03	3	-
$cyc(HC=CH-CH)-CHO$	67	**13** and **14**	3.52	1	-
$HC\equiv C-CH_2-CHO$	36	**7** and **8**	3.74	1	3.69
$H_2C=CH-CH=C=O$	28	**9** and **10**	3.14	4	4.41^a

^{a}different path to obtain this isomer

As an isomerization summary and a link between dynamical results and exploration of PES for this process, Table 5.1 presents total occurrence in MD, lowest energy barrier and number of steps (transitions states) required to reach the most important furan isomers. It can be seen that the lowest energy barrier is associated with the highest number of trajectories. Moreover, although producing structures **9** and **10** requires overcoming second lowest energy barrier, their occurrence in MD is least abundant because of several steps required to reach these isomers.

Figure 5.5 demonstrates possible pathways of **fragmentation** into two channels: HCCH + H_2CCO and CO + H_4C_3. From α-carbene (**1**) exist two possibilities of fragmentation by either concerted C-O and C_β-C_β or C-O and C_α-C_β bond cleavages. Barriers calculated for these reactions are 3.55 and 4.40 eV, respectively. The same channels can be obtained by C_α-C_β or C_β-C_β bond cleavage of more stable structure **7**, however these mechanisms show higher energy barriers of 4.30 and 6.55 eV, respectively. Third possibility of fragmentation was found from structure **4** by either direct decomposition to CO + H_2CCCH_2 or two-step hydrogen migration and C_α-C_β bond cleavage to CO + H_3CCCH. As presented in Figure 5.5 **b)**, fragmentation can also occur from cyclic isomer cyc(HC=CH−CH)−CHO (**13**). Single bond cleavage, but higher barrier (5.51 eV) was found to produce of H_4C_3 in a cyclic form (cyclopropene). Second cyclic isomer of H_4C_3 (cyclopropylidene) can be obtained by more steps, but presents lower energy barrier (4.52 eV).
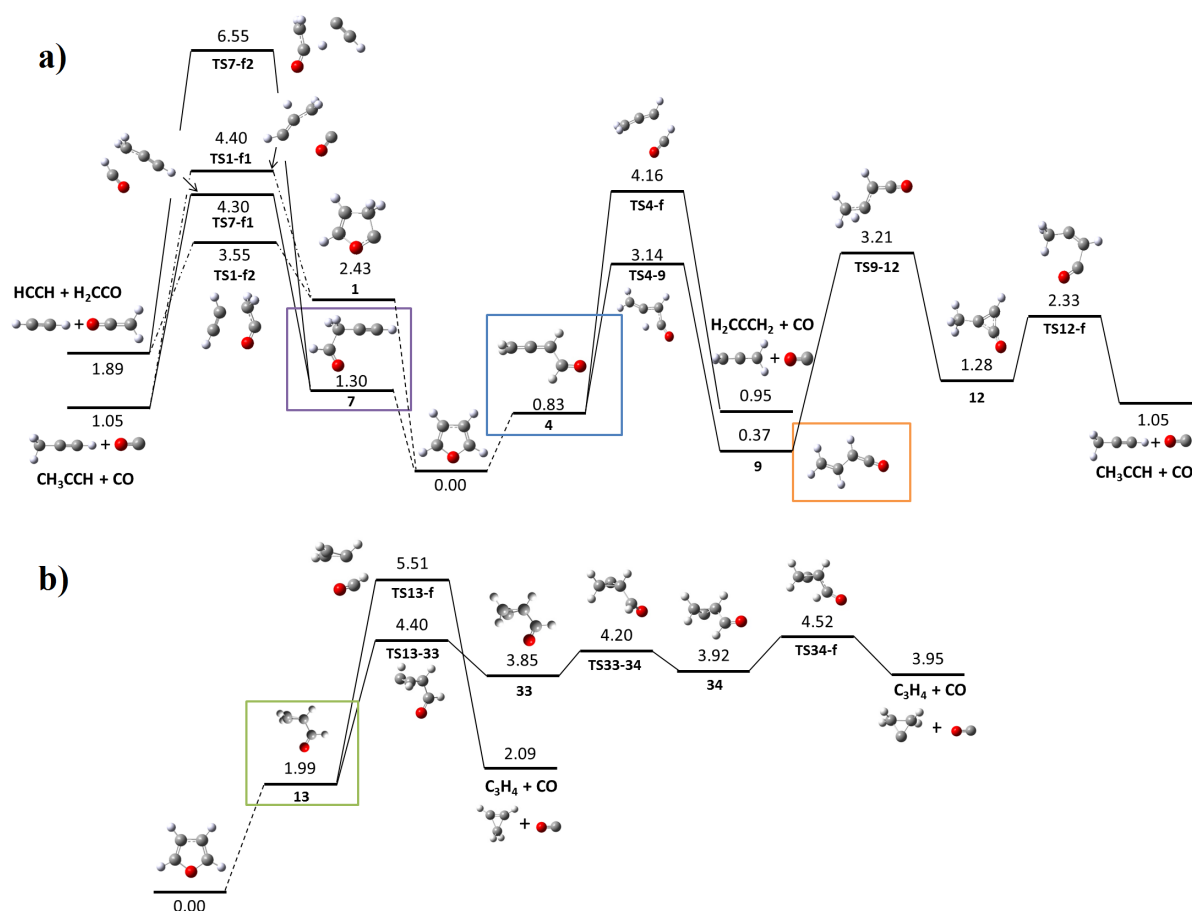
FIGURE 5.5 Potential Energy Surface for the skeleton fragmentation. Energies calculated at B3LYP/6-311++G(3df,2p) level of theory are given in eV relative to furan. Zero point energy corrections are included.

TABLE 5.2 Comparison of ADMP and PES exploration results for the fragmentation process.

Fragmentation channel	Total number of trajectories	Energy of the exit channel	Energy barrier	Number of TS
HCCH + H$_2$CCO	198	1.89	3.55	2
CO + H$_2$CCCH$_2$	96	0.95	4.16	3/4
CO + H$_3$CCCH	44	1.05	3.14	6
CO + cyc(HCCHCH$_2$)	35	2.09	5.51	2
CO + cyc(H$_2$CCCH$_2$)	-	3.95	4.52	4

From the Table 5.2, summarizing results of the fragmentation process, it can clearly be seen that channel HCCH + H$_2$CCO presents the optimum combination of the second lowest energy barrier and only two steps of rearrangement required before decomposition. However, absolute abundance of channel CO + H$_4$C$_3$ closely follows that of channel HCCH + H$_2$CCO with total occurrence of 175. As discussed in the section of MD results, three isomeric forms of H$_4$C$_3$ have been distinguished. Their relative stability follows an adequate order as the one obtained by ADMP method and not the one determined by the exploration of reaction paths and energy barriers. It is worth pointing out that with enough internal energy to overcome the barriers, statistical distribution of products should prevail over the differences in energy barriers, meaning that MD should present more quantitatively reliable results.

FIGURE 5.6 Potential Energy Surface for the hydrogen loss. Energies calculated at B3LYP/6-311++G(3df,2p) level of theory are given in eV relative to furan. ZPE corrections are included.

As shown in Figure 5.6, energy barriers for **hydrogen elimination** from both positions are of equal height (5.07 eV). Resulting α-furyl and β-furyl structures (**23** and **19**) present practically unchanged geometry to that of furan. The maximum variation in geometrical parameters appeared after H$_\alpha$ loss and led to decrease of C$_\alpha$-O bond length by 0.03 Å as well as decrease in C$_\alpha$-C$_\beta$-C$_\beta$ angle and increase in O-C$_\alpha$-C$_\beta$ angle by approx. 3°. The unpaired electron of these radicals occupies a π type orbital. Further isomerization after H loss can either proceed

through cleavage of the $C_\alpha(4)$-O bond of the α-furyl or $C_\alpha(1)$-O of the β-furyl concerted with H transfer to the carbon from which hydrogen was previously eliminated, leading to structures **24** and **20**. Then, subsequent isomerization from structure **20** by 2,1 H transfer gives structure **21** and rotation of the dihedral angle O-C_α-C_β-C_β leads to structure **22**.

Following H loss, two possible fragmentation channels: H + HCCH + HCCO and H + CO + H_2CCCH were found, latter being more stable. CO and H_2CCCH can be obtained after both H_α or H_β loss by either 1,2 hydrogen transfer of structure **24** or elongation of the $C_\alpha(4)$-$C_\beta(3)$ bond of structure **22**. Energy barriers calculated for these mechanism are 8.03 eV and 7.79 eV, respectively. Break of the planar geometry of structure **20** by rotation around C_β-C_β bond can lead to products HCCH and HCCO. Following H_β elimination first step of H migration was found to be rate determining. The system will, however, more probably relax to channel H + HCCH + HCCO.
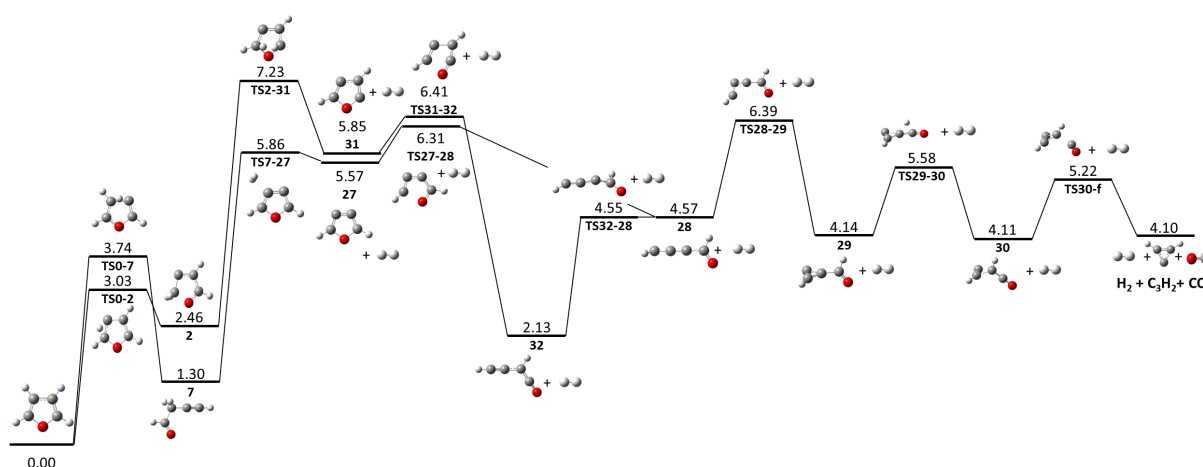
FIGURE 5.7 Potential Energy Surface for the molecular hydrogen loss from two α, two β and opposite α and β positions. Energies calculated at B3LYP/6-311++G(3df,2p) level of theory are given in eV relative to furan. ZPE corrections are included.

During exploration of Potential Energy Surface all possible positions of **H_2 loss** have been studied. Figures 5.7 and 5.8 present pathways for this process. Although the energy barrier for emission of H_2 from two β positions is the lowest (5.86 eV), such low occurrence of this channel in the dynamical simulations can be explained by deterring properties of the stable structure **7**. Reaching the transition structure for the loss of two β hydrogens from structure **7** would additionally require closing of the furan ring. Second and third lowest energy barriers were found for the loss of two adjacent hydrogens in α and β positions. These pathways imply either production of β-carbene (**2**) and H_2 loss from $C_\alpha(4)$ or production of α-carbene (**1**) and H_2 loss from $C_\beta(3)$, with barriers of 6.17 eV and 6.30 eV, respectively, both leading to structure **25**. From there, subsequent ring opening gives structure **26**. Common mechanism, exhibiting the highest energy barrier of 7.23 eV, was found for the elimination of H_2 from opposite sides of the furan ring and two α positions giving structure **31**. Further stabilization of the system can additionally occur after ring opening to structure **32**.

Reaction pathways following H_2 loss present a lower energy barrier than any channel of decomposition observed after H loss. The only three-body **fragmentation followed by H_2**

loss observed in the dynamical simulation produced CO and H_2C_3. Consequently, this single process was investigated. The most energetically favorable fragmentation takes place after the elimination of two H_β with barrier of 6.39 eV, but as it was previously pointed out, such reaction can be stopped at stable structure **7** and requires succeeding ring formation. Thus, the most probable mechanism of fragmentation takes place after loss of adjacent hydrogens from α and β positions due to low energy barrier (6.79 eV) and few steps of rearrangement. Such conclusion is consistent with the ADMP results.
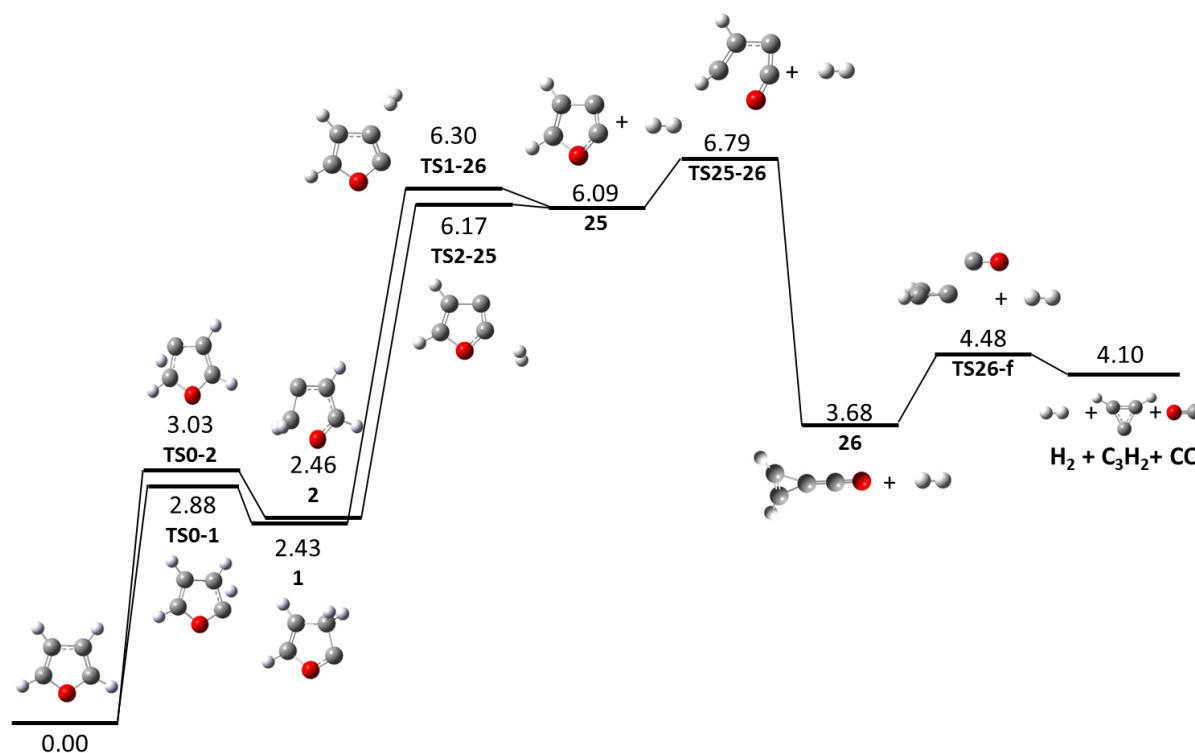
FIGURE 5.8 Potential Energy Surface for the molecular hydrogen loss from the adjacent α and β positions. Energies calculated at B3LYP/6-311++G(3df,2p) level of theory are given in eV relative to furan.

5.1.3 Statistical method

A complementary information about the fragmentation process can be provided by the M_3C methodology. The database of possible fragments included 226 isomers corresponding to 44 different chemical formulas. Their geometries are presented in Annex 1. The final parameters used to obtain the results discussed in this section are given in Table 5.3.

TABLE 5.3 Parameters of the M_3C simulation of neutral furan

System Radius	13 Å
Markov chain sequence	V,T,R,5×S:0,V,T,R,5×S:1:-1
Number of experiments	50
Number of events	800 000
Sampling method	RANDOM
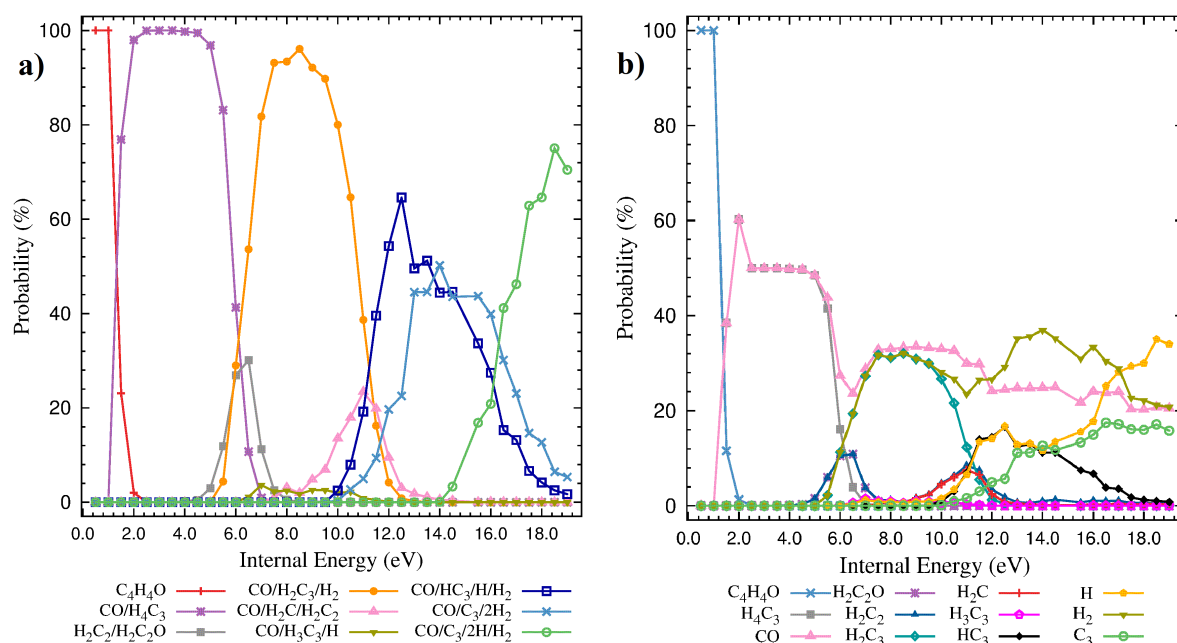
FIGURE 5.9 Results of M$_3$C calculations of neutral furan: **a)** channels and **b)** species probabilities as a function of the internal energy.

Figure 5.9 presents results obtained with the M$_3$C method, channels (panel **a)**) and species (panel **b)**) distributions as a function of the internal energy. The first channel that can be observed is CO/H$_4$C$_3$. For the energy range between 1 and 4.5 eV, it is the only fragmentation channel with probability of 100%. A second channel H$_2$C$_2$/H$_2$C$_2$O appears at 5 eV and reaches maximum probability of 30% at 6.5 eV. Both channels are dominant in the dynamical simulations at intermediate energies, but the H$_2$C$_2$/H$_2$C$_2$O presents higher total occurrence. No direct comparison of the probabilities for specific internal energies can be made due to each method's consideration of time. The ADMP method allows to investigate the very first steps of the fragmentation process and in the M$_3$C complete redistribution of the excitation energy over all fragments is assumed in the infinite time limit. Hence, it can be expected that longer simulation times of ADMP calculations would lead to enhanced probability of the CO/H$_4$C$_3$ channel. Figure 5.9 **b)** shows that the main fragment observed throughout all energies is CO. This species is a product of all but one presented fragmentation channels, which is coherent with the exploration of PES, showing that exit channels are more stable when CO is produced.

The first three-body channel to appear in the energy range was found to be CO/H$_2$C$_3$/H$_2$. It dominates since 6.5 until 11 eV with a maximum at 8.5 eV. Moreover, the fact that the total energy of products: H$_2$C$_3$, CO and H$_2$ is lower than any channel of single H loss can explain minor significance of this process in two- and three-body fragmentation channels obtained by the M$_3$C method. At higher energies also four- and five-body channels involving either atomic and molecular hydrogen loss can be noticed. The dominant ones are: CO/HC$_3$/H$_2$/H, CO/C$_3$/H$_2$/H$_2$, and CO/C$_3$/H$_2$/H/H. These channels, although highly stable and entropically favorable, do not appear in the ADMP simulations since not enough energy is deposited into the system and time evolution is not enough to observe such mechanisms. They were also

not considered in our previous discussion of the PES since they present high-energy barriers (at least of 10 eV).

5.1.4 Comparison with thermal decomposition experiments

Previously discussed importance of two-body fragmentation channels: CO/H_4C_3 and H_2C_2/H_2C_2O is consistent with the experimental measurements of furan pyrolysis [22]–[25], [27], [29]–[32], [95], where it has been shown that these are the most observed unimolecular decomposition reactions. The most probable mechanisms of obtaining these products occur through the formation of highly reactive carbenes, as it was confirmed in this work. Multifragmentation processes have not been an objective of any experimental study. However, in a theoretical investigation by Sendt *et al* [28] it was proposed that H loss from propyne (H_3CCCH) is a mechanism producing channel $CO/H_3C_3/H$. Propargyl radicals (H_3C_3) were observed as a thermal decomposition products by Sorkhabi *et al* [27] and Vasiliou *et al* [29], where it was indicated that these species are direct products of furan decomposition. However, none of the methods applied in this work pointed out to such reaction. The H_3C_3 fragment is rather produced in channel $CO/H_3C_3/H$. Contrary to the conclusion of Sendt, the mechanism of producing this channel relies on H loss taking place directly from furan rather than from propyne. Moreover, present results show that H_2 loss and subsequent fragmentation to CO and H_2C_3 should be a highly observed three-body fragmentation channel for higher energies applied into the system.

5.2 Singly ionized furan

5.2.1 Molecular Dynamics

Results of the dynamical simulations of singly ionized furan are presented in Figures 5.10 - 5.14. As in the case of the neutral molecule, four types of processes can be distinguished. The amount of internal energy required to observe them is shifted to lower values in comparison with the neutral furan. As it is shown in Figure 5.10 **a)**, furan cation remains intact until the energy of 8 eV. Since then, the first isomerization takes place and can be ultimately observed at the energy of 25 eV. Skeleton fragmentation occurs for all energies starting from 9 eV and dominates for the energy range between 16 and 20 eV. Next, H/H_2 loss followed by isomerization starts at 13 eV. The major process since 20 eV was found to be H/H_2 loss followed by fragmentation. Figure 5.10 **b)** presents number of fragments produced at different internal energies. It can be noticed that two body fragmentation dominates for midrange energies from 16 to 21 eV and three body fragmentation is the most abundant for higher energies between 22 and 28 eV. Decomposition to four fragments starts at 19 eV and is the most frequent at 29 eV. Finally, the calculations show that five body fragmentation is a minor process with maximum occurrence of 7 % at 30 eV.
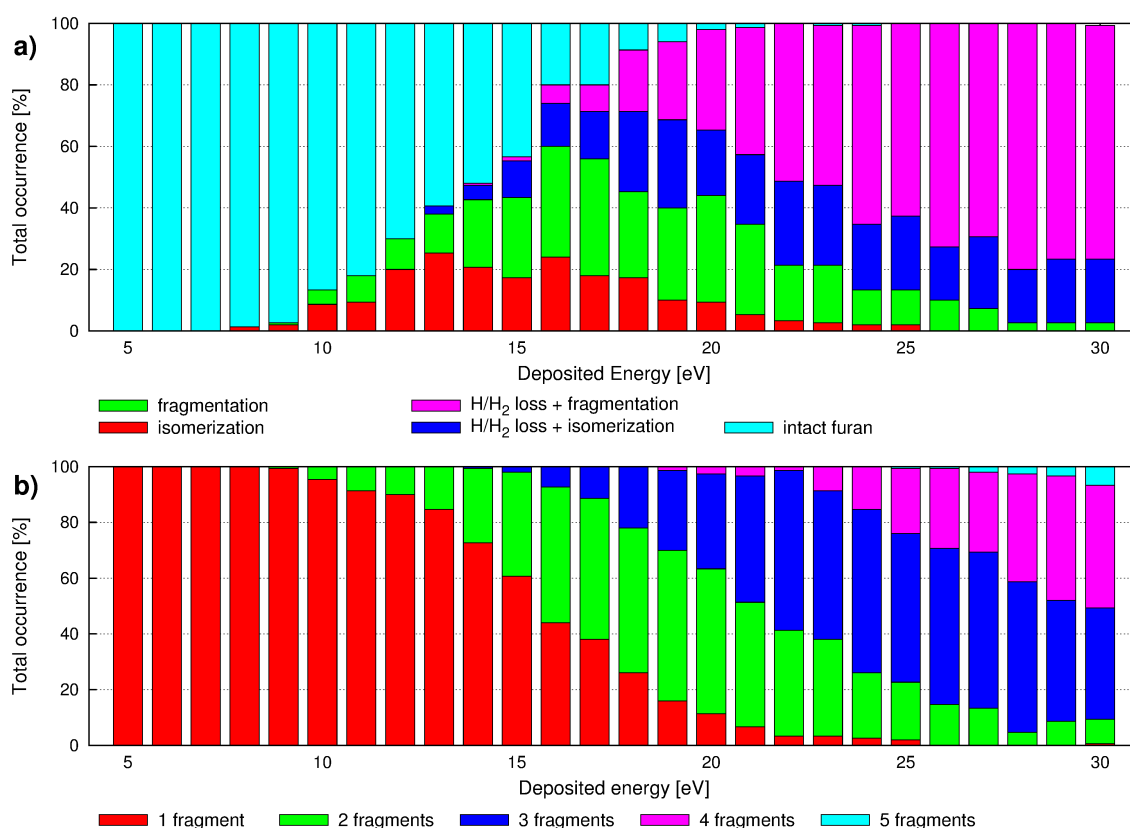
FIGURE 5.10 Results of the ADMP simulations of singly ionized furan: total occurrence of **a)** observed processes **b)** number of fragments as a function of the internal energy.
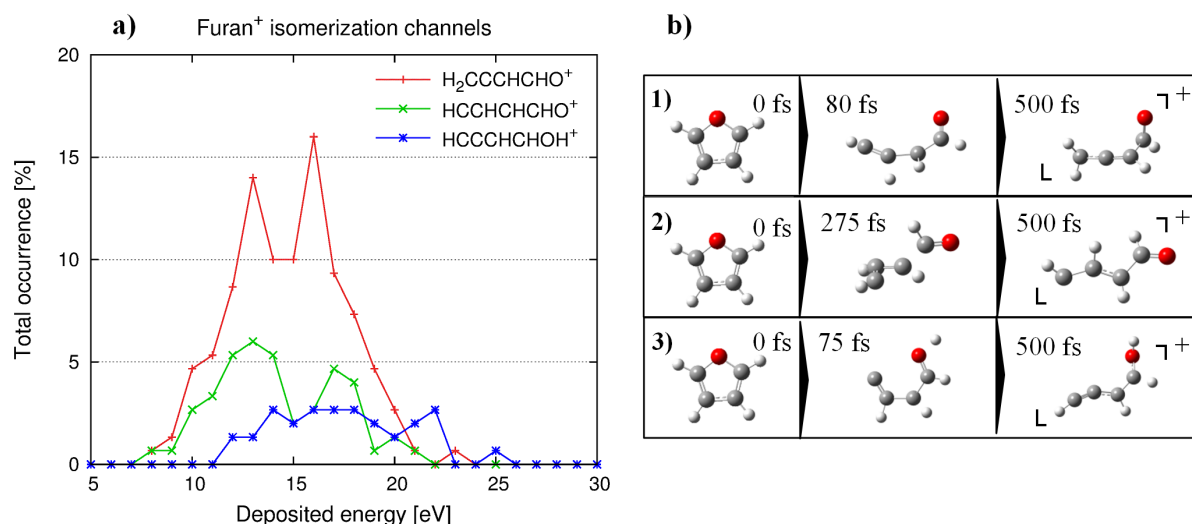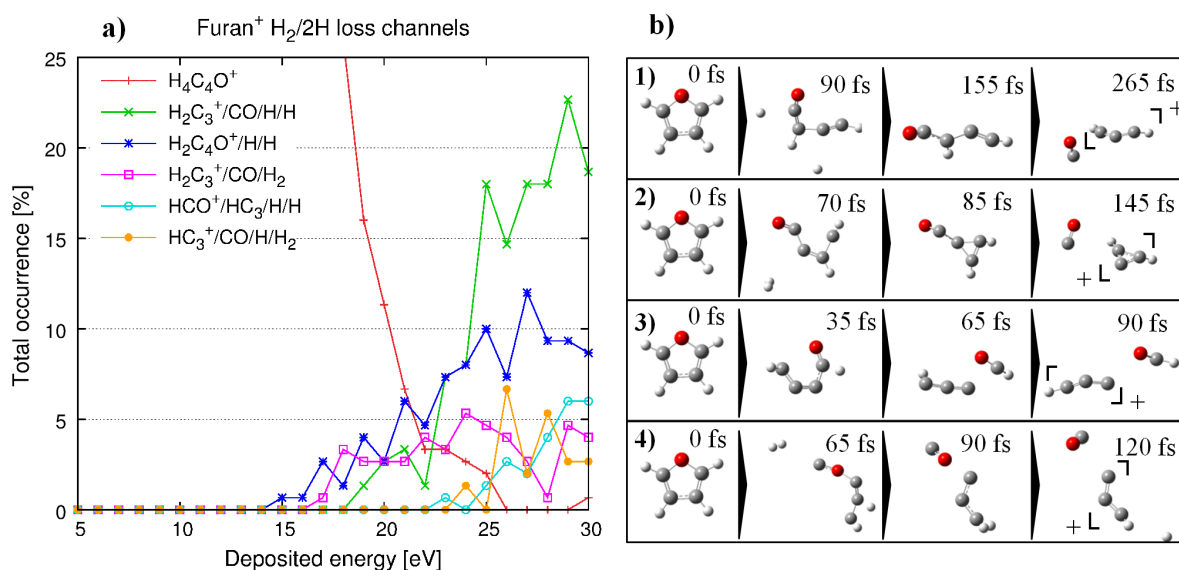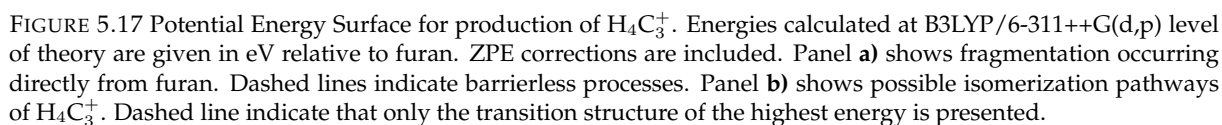
FIGURE 5.11 Results of the ADMP simulations of singly ionized furan: **a)** total occurrence of isomerization channels **b)** snapshots of trajectories leading to channels from the left panel.

Starting with the **isomerization** process, only three distinctive structures were found at the final step of the simulations. The panel **a)** of Figure 5.11 shows their abundances and panel **b)** exemplifies their evolution in time. The first isomerization channel corresponds to 2,1 H transfer to form $H_2C=C=CH-CHO^+$ (145 trajectories in total). The second most populated channel, with 43 trajectories overall, implies opening of the furan ring and break of the planar symmetry of the molecule without any hydrogen transfer. Lastly, hydrogen migration to the oxygen atom was observed 36 times. The panel **a)** of Figure 5.11 shows distinct prevalence of 2,1 H migration until the energy of 21 eV, when hydrogen transfer to oxygen becomes more abundant.
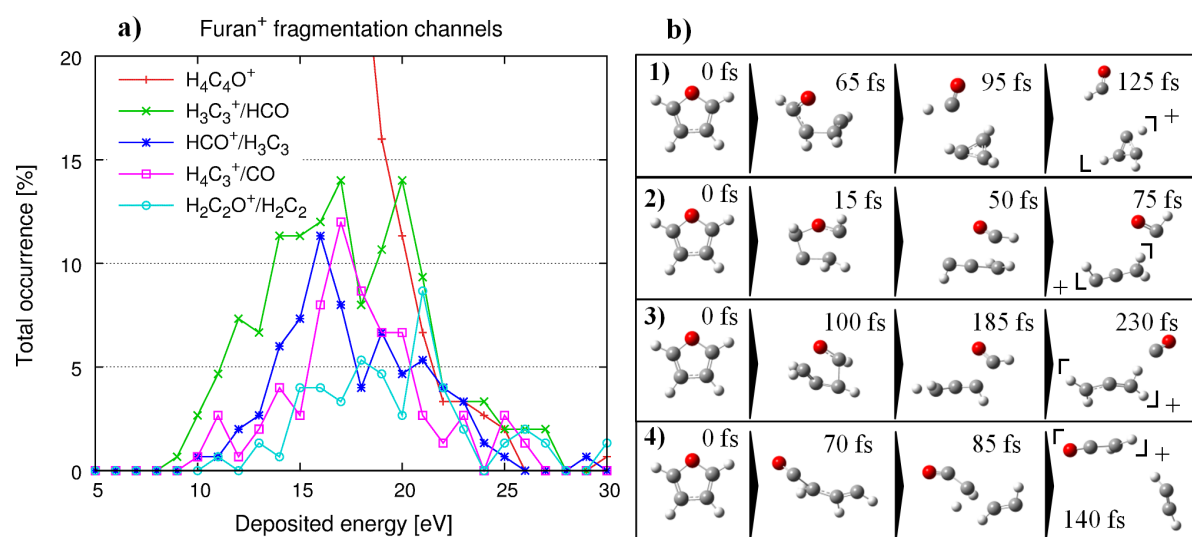
FIGURE 5.12 Results of the ADMP simulations of singly ionized furan: **a)** total occurrence of fragmentation channels **b)** snapshots of trajectories leading to channels from the left panel. Only channels that appeared at least 5% at a certain point in the energy range are presented.

Compared to the neutral molecule, dynamical simulations of singly ionized furan produced more variations of **skeleton fragmentation**, as four major channels were found: $H_3C_3^+$/HCO, HCO^+/H_3C_3, $H_4C_3^+$/CO and $H_2C_2O^+$/H_2C_2, listing from the most to the least populated. The panel **b)** of Figure 5.12 shows that the first and the most abundant fragmentation mechanism does not impose hydrogen migration, but follows ring opening and later cyclization of three carbon atoms, producing cyclopropenium cation c-$H_3C_3^+$. The second most populated channel produces the same species, but charge is located on the HCO^+ fragment and H_3C_3 is formed in a linear configuration. In this mechanism, 2,3 H transfer takes place as a first step, followed by C-O and C_α-C_β bond cleavages. In the third channel of skeleton fragmentation, species $H_4C_3^+$ can be obtained in four possible isomers. To find out which configuration of $H_4C_3^+$ is the most abundant, 98 trajectories producing channel $H_4C_3^+$ + CO were examined. The total occurrence of mentioned species was found to be: allene ($H_2CCCH_2^+$) - 59 trajectories, cyclopropene (c-H_2CCHCH^+) - 28 trajectories, vinylmethylene (H_2CCHCH^+) - 6 trajectories and propyne (H_3CCCH^+) - 5 trajectories. Lastly, production of $H_2C_2O^+$ and H_2C_2 proceeds through ring opening, 1,2 H transfer and C_β-C_β bond cleavage. From panel **a)** of Figure 5.12 it can be noticed that channel $H_3C_3^+$/HCO, besides being the most abundant among skeleton fragmentation, is also the first to appear in the energy range. Channels HCO^+/H_3C_3 and $H_4C_3^+$/CO present similar character, but maximum value of producing $H_4C_3^+$ is shifted by 1 eV to higher energies.
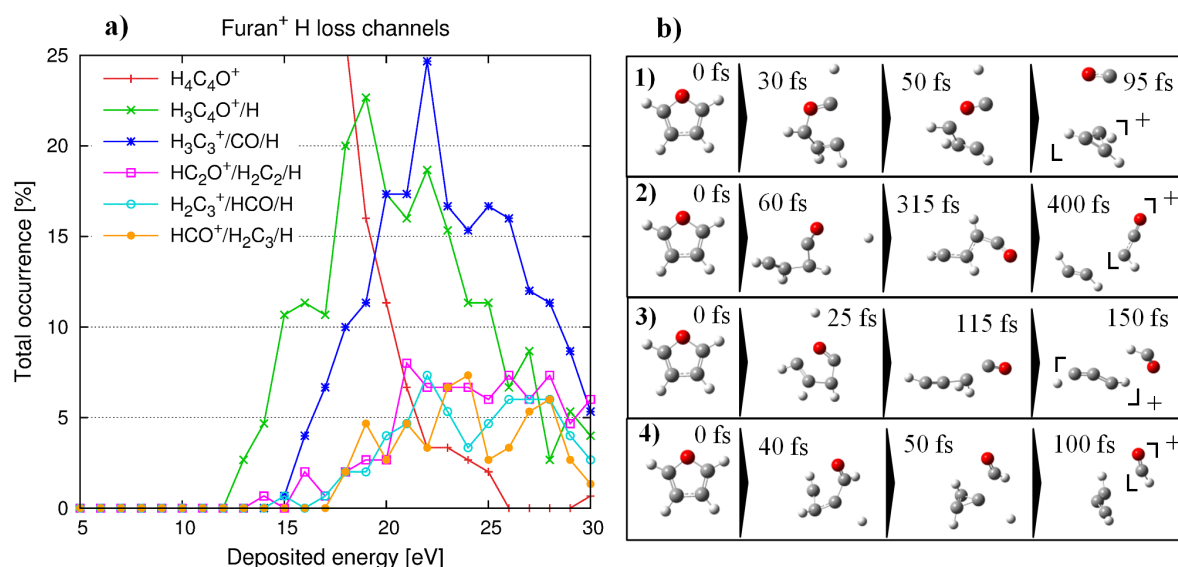
FIGURE 5.13 Results of the ADMP simulations of singly ionized furan: **a)** total occurrence of H loss channels **b)** snapshots of trajectories leading to channels from the left panel. Only channels that appeared at least 5% at a certain point in the energy range are presented.

Third process that can be observed is **H loss**. Firstly, ejection of the hydrogen atom can be followed by isomerization. Position of the eliminated hydrogen(s) was again subject of the statistical analysis. It was found that H_α was lost in 56% of the considered trajectories giving H and $H_3C_4O^+$. As it can be seen in panel **a)** of Figure 5.13, this channel is dominant until the energy of 20 eV. Since then, decomposition of the remaining fragment after H loss starts to
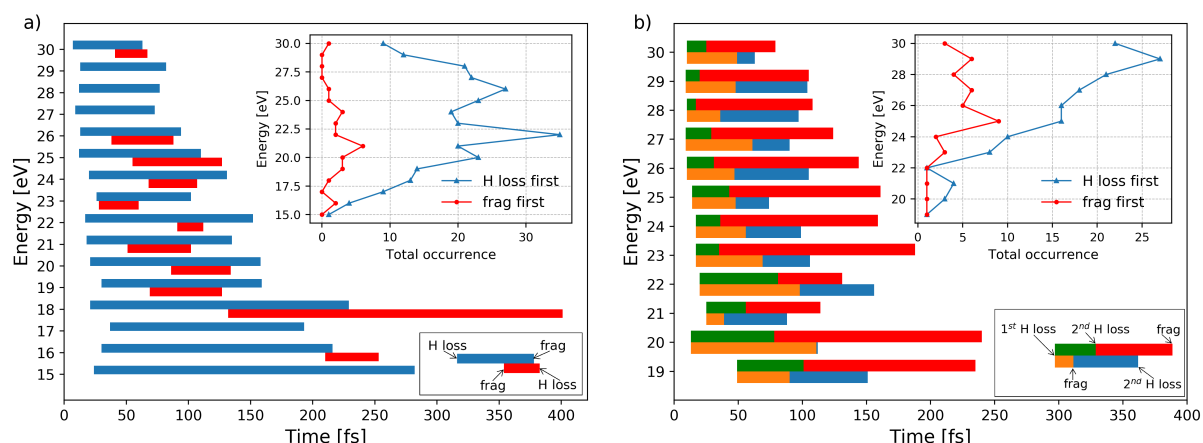
FIGURE 5.14 Average time scales of sequential events leading to **a)** $H_3C_3^+$/CO/H and **b)** $H_2C_3^+$/CO/H/H. Borders of bars represent when, for different energies, on average either H loss or fragmentation take place. Inset plots show abundance of different processes.

prevail. First panel of Figure 5.13 **c)** shows the most abundant mechanism leading to production of fragments $H_3C_3^+$, CO and H by H_α loss and subsequent ring rupture. This mechanism relies on H loss from α position in substantial majority of trajectories (82 %). As shown in Figure 5.13 **a)**, $H_3C_3^+$/CO/H is the most abundant channel for the middle energy range (20 - 25 eV). The sequence of events (H loss $\rightarrow$ fragmentation or fragmentation $\rightarrow$ H loss) has been studied in order to recognize the most probable mechanism. From Figure 5.14 **a)** it can be seen that hydrogen atom is mainly ejected from $H_4C_4O^+$ and not from the previously fragmented species. Moreover, the width of blue bars, representing the average time the system requires to decompose after initial H loss, decreases with increasing energy. Fragmentation before H loss was a minor process with only 25 occurrences in total (in comparison with 272 for H loss $\rightarrow$ fragmentation). However, if the fragmentation occurred as a first step, the intermediate channel was mainly found to be $H_3C_3^+$/HCO (17 trajectories) and the least frequent was $H_4C_3^+$/CO (8 trajectories).

The final major process was found to be the **H_2/2H loss**. As shown in panel **a)** of Figure 5.15, the elimination of two hydrogen atoms appears first at the energy of 16 eV and slowly increases until reaching maximum probability of 12 % for the energy of 27 eV. The frequency of 2H loss in a decreasing order is: adjacent H_α and H_β (34%) > opposite H_α and H_β (33%) > two H_α (26%) > two H_β (7%). Subsequently, the **H_2/2H loss** followed by fragmentation can be observed. This mechanism is complex and a lot of different channels of this character were found. However, one channel of the highest importance can be clearly distinguished. The first panel of Figure 5.15 **b)** shows the most abundant mechanism of obtaining fragments $H_2C_3^+$, CO and 2H by opposite H_α and H_β loss and subsequent C_α-C_β bond cleavage. The frequency of 2H loss in this channel in a decreasing order is: opposite H_α and H_β (44%) > two H_α (27%) > adjacent H_α and H_β (25%) > two H_β (4%). Panel **a)** of Figure 5.15 shows that production of $H_2C_3^+$, CO and 2H is the most numerous for the highest considered energies (26 - 30 eV). Again, time scale of this process and its transitional steps, presented in Figure 5.14 **b)**, can help to elucidate actual production mechanism of this channel. It can be seen that sequence of

FIGURE 5.15 Results of the ADMP simulations of singly ionized furan: **a)** total occurrence of H_2/2H loss channels **b)** snapshots of trajectories leading to channels from the left panel. Only channels that appeared at least 5% at a certain point in the energy range are presented.

events producing channel $H_2C_3^+$/CO/H/H is mainly 1st H loss $\rightarrow 2^{nd}$ H loss $\rightarrow$ fragmentation although on average it takes more time for this channel to be produced. Decomposition to this channel always starts with ejection of the first hydrogen in the time interval between 10 and 50 fs. Subsequently, in most cases second hydrogen is eliminated and the remaining structure breaks. Conversely, when fragmentation takes place right after the first H loss intermediate channels of $H_3C_3^+$/CO/H (21 trajectories) or $H_2C_3^+$/HCO/H (19 trajectories) are produced. Less populated channels of discussed type never exceed the total occurrence of 10%, so their contribution to the fragmentation process of singly ionized furan are minor.

5.2.2 Potential Energy Surface

Further understanding of the fragmentation process is provided by the exploration of the Potential Energy Surface. Scheme 5.16 shows all calculated fragmentation pathways of furan cation and clarifies steps of obtaining three and four body fragmentation channels. Obtained energy profiles, presenting minima and transition structures optimized at B3LYP/6-311++G(d,p) level of theory, are presented in Figures 5.17 - 5.21. For the reasons of clarity and further comparison with the experimental results, exploration of PES of singly ionized furan is divided into sections, investigating production of specific species.

FIGURE 5.16 Calculated fragmentation pathways corresponding to channels obtained by Molecular Dynamics.

FIGURE 5.17 Potential Energy Surface for production of $H_4C_3^+$. Energies calculated at B3LYP/6-311++G(d,p) level of theory are given in eV relative to furan. ZPE corrections are included. Panel **a)** shows fragmentation occurring directly from furan. Dashed lines indicate barrierless processes. Panel **b)** shows possible isomerization pathways of $H_4C_3^+$. Dashed line indicate that only the transition structure of the highest energy is presented.

The formation of the $H_4C_3^+$ ion has been explored with consideration of four possible structures for this species, previously mentioned in the MD results. Resulting Potential Energy Surface is presented in panel **a)** of Figure 5.17. The lowest energy barrier, equal to 11.52 eV, has been found for production of allene ($H_2CCCH_2^+$) by consecutive 2,1 H transfer, ring opening, rotation around C_α-C_β bond and 1,2 H transfer concerted with C_α-C_β bond cleavage (**ts1**→**ts2**→**ts3**→**ts4**). A different pathway results in production of propyne (H_3CCCH^+), with energy barrier of 11.69 eV, when 1,4 H transfer (**ts5**) occurs instead of **ts4**. Fragmentation to allene through barrier higher than **ts1** only by 0.04 eV (11.56 eV - **ts6**) can also take place when sequence of hydrogen migration is reversed, i.e. when 1,2 H transfer, ring opening, 2,1 H transfer and C_α-C_β bond cleavage (**ts6**→**ts7**→**ts8**→**ts9**) occur in succession. If ring opening is concerted with 1,2 H transfer as a first step of this reaction, then the transition structure (**ts10**) is located at higher energy of 12.22 eV. Production of vinylmethylene (H_2CCHCH^+) is possible when a barrierless C_α-C_β bond fission takes place from **min7**. No pathway was found to produce cyclopropene (c-H_2CCHCH^+) directly from furan cation. However, if $H_4C_3^+$ species posses enough internal energy, they can interconvert after primary fragmentation. The isomerization of $H_4C_3^+$ is presented in the panel **b)** of Figure 5.17. It can be seen that vinylmethylene and cyclopropene might be sequentially obtained from allene through energy barriers of 11.73 and 11.59 eV, respectively. Consequently, cyclopropene ion can also be a product of furan cation fragmentation. On the other hand, isomerization from allene to propyne presents higher energy barrier (12.10 eV) than for direct fragmentation to propyne from furan cation (11.69 eV), which can be another reason for such low observation of this isomer in the MD simulations.
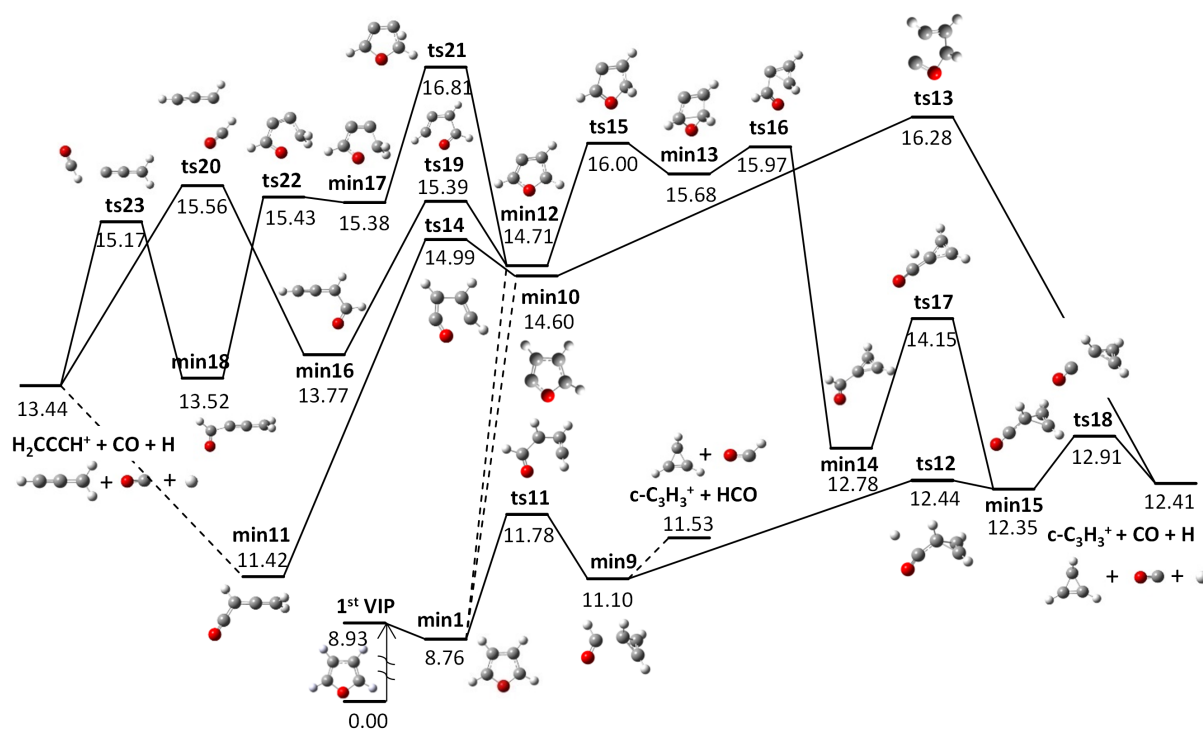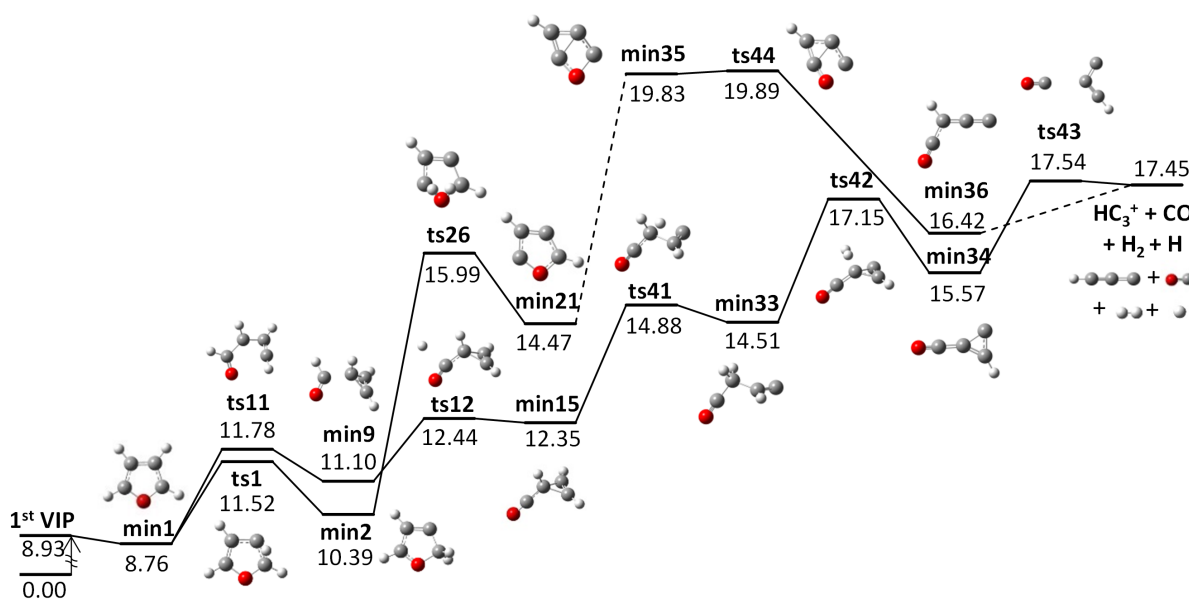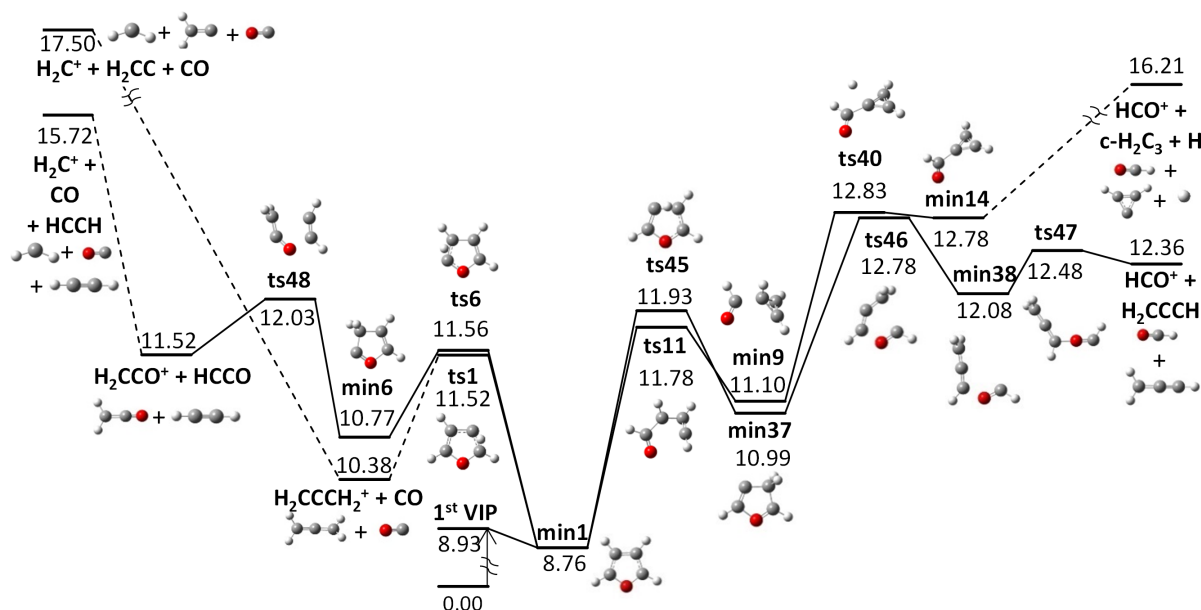

FIGURE 5.18 Potential Energy Surface for production of $H_3C_3^+$. Energies calculated at B3LYP/6-311++G(d,p) level of theory are given in eV relative to furan. ZPE corrections are included. Dashed line indicate barrierless transitions.

Possible ways of obtaining the $H_3C_3^+$ ion are presented in Figure 5.18. The cyclic isomer of $H_3C_3^+$ - cyclopropenium cation (c-$H_3C_3^+$) - requires the least amount of rearrangement to be produced. No hydrogen transfer is needed to obtain channel c-$H_3C_3^+$/HCO, only furan ring opening through a transition structure located at 11.78 eV (**ts11**). The mechanism follows a few steps, as fragmentation proceeds through formation of an ion-molecule complex in which the $C_\alpha \cdots C_\beta$ distance is equal to 1.68 Å (**min9**). The $H_3C_3^+$ ion can also be produced through channels involving H loss. As it was previously stated in the discussion of the MD results, the mechanism of producing channel $H_3C_3^+$/CO/H is based mainly on H loss $\rightarrow$ fragmentation sequence of events. Production of $H_3C_3^+$ through H loss exhibits higher energy barriers than the one for skeleton fragmentation, but the dynamical simulations show prevalence of this process for middle energies. H_α can be ejected directly from furan cation or from an isomer of furan cation. The least amount of energy (**ts12** - 12.44 eV) is required to eliminate hydrogen from **min9**. Subsequent C_α-C_β bond cleavage proceeds through the lowest energy barrier for formation of channel c-$H_3C_3^+$/CO/H, located at 12.91 eV. Barriers for H_α and H_β elimination directly from furan cation were calculated to be 14.60 and 14.71 eV, respectively. Lower barrier for elimination of hydrogen from α position, resulting in production of α-furyl cation (**min10**), is consistent with majority of H_α loss observed in the MD calculations. Only one transition structure (**ts13** - 16.28 eV) is required to obtain fragmentation channel c-$H_3C_3^+$/CO/H from **min10**. Although production of c-$H_3C_3^+$ from β-furyl cation (**min12**) presents a lower reaction barrier (**ts15** - 16.00 eV), this mechanism is less probable because of several steps of isomerization are required to reach fragmentation. A linear configuration of $H_3C_3^+$ - a propargyl cation (H_2CCCH^+) - might be formed in two steps after concerted C-O bond fission and 2,1 H transfer of α-furyl cation (**ts14** - 14.99 eV) and consecutive, barrierless C_α-C_β bond cleavage of **min11**. This mechanism leads to the most energetically favourable pathway of obtaining H_2CCCH^+ ion. This isomer can be also obtained after H_β elimination through two different mechanisms, but their energy barriers are higher (16.81 or 15.56 eV) than the one calculated for fragmentation of α-furyl cation (14.99 eV).

The fragmentation pathways leading to formation of $H_2C_3^+$ ion are presented in Figure 5.19. This species can be produced in two isomeric forms: cyclic or linear, former being more stable by 0.09 eV. Two-body fragmentation implies the energy barrier of 13.43 eV and the series of 2,1 H transfer, 2,3 H transfer C_α-C_β bond cleavage and finally barrierless C-O bond fission (**ts1**$\rightarrow$**ts24**$\rightarrow$**ts25**). This mechanism is unlikely to occur because of as many as four steps and after reaching **min2** the system is expected to follow reaction path of $H_4C_3^+$/CO. Next, the energy barrier of 15.99 eV was calculated for H_2 loss from **min2**. Depending on which C-O bond cleaves, either **min23** or very stable **min22** are obtained. From **min23** a c-$H_2C_3^+$ ion is produced by C_α-C_β bond fission. Fragmentation to $HCCCH^+$ proceeds without barrier from **min22**. A cyclic isomer of $H_2C_3^+$ can be also formed from **min22** by C_α-C_β bond cleavage. The first step of obtaining channel $H_2C_3^+$/CO/H_2 (**ts26**) is common for production of both $H_2C_3^+$ isomers. Stability of **min22** indicate which species will be more populated. From this structure the lowest energy path leads to linear isomer of $H_2C_3^+$. A channel that presents significant occurrence for the highest considered energies of the dynamical simulation was four-body fragmentation channel: $H_2C_3^+$/CO/2H. Previous analysis of the MD results specified the preferable sequence

FIGURE 5.19 Potential Energy Surface for production of $H_2C_3^+$. Energies calculated at B3LYP/6-311++G(d,p) level of theory are given in eV relative to furan. ZPE corrections are included. Panel **a)** shows two- and three-body fragmentation channels. Panel **b)** shows four-body fragmentation channels. Dashed lines indicate barrierless transitions.

of events to be: 1st H loss $\rightarrow 2^{nd}$ H loss $\rightarrow$ fragmentation. Reaction pathways following this scheme are depicted in panel **b)** of Figure 5.19. It can be seen that, as expected, the least amount of energy is required to emit hydrogens first from **min9** (H_α) and then from **min15** (H_β) rather than directly from furan cation. If H_β is emitted first from **min9** the system proceeds through higher energy barrier with a transition structure at 19.39 eV (**ts39**). Elimination of hydrogens

from furan cation and later from furyl cations proceeds without barriers. The position of emitted hydrogens influences the stability of obtained structures. The least energy is required to eliminate two hydrogens from β position (**min24** - 19.03 eV). Subsequent C-O bond fission and concerted C_α-C_β bond cleavage with 1,2 H transfer lead to channel $HCCCH^+$/CO/2H. Next lowest isomer of $H_2C_4O^+$ was obtained after opposite H_α and H_β loss (**min26** - 19.24 eV). From there, by ring opening and H transfer, both isomers of $H_2C_3^+$ can be produced. Emission of two hydrogens from two α positions (**min28** - 19.29 eV) gave the third lowest geometry of $H_2C_4O^+$. Consecutive ring opening leads to fragmentation through a barrier of 19.81 eV. The least stable isomer of $H_2C_4O^+$ was found after loss of adjacent H_α and H_β (**min30** - 19.32 eV). The ring opening of **min30** implies 20.04 eV of energy for decomposition to c-$H_2C_3^+$/CO/2H. The preferable position of emitted hydrogens concluded from dynamical simulations was found to be opposite H_α and H_β. This observation together with the lowest calculated reaction pathway indicate **ts11** $\rightarrow$ **min9** $\rightarrow$ **ts12** $\rightarrow$ **min15** $\rightarrow$ **min27** to be the most probable mechanism of producing $H_2C_3^+$ ions through a four-body fragmentation. Moreover, energy barrier for channel involving loss of molecular hydrogen is lower than for loss of two single hydrogen atoms. However, the reason for such low occurrence of this channel in the MD might be difficult spatial distribution for forming **ts26**.

FIGURE 5.20 Potential Energy Surface for production of HC_3^+. Energies calculated at B3LYP/6-311++G(d,p) level of theory are given in eV relative to furan. ZPE corrections are included. Dashed lines indicate barrierless transitions.

The only channel observed in the dynamical simulations producing ion HC_3^+ was found to be four body fragmentation to HC_3^+/CO/H/H_2. Figure 5.20 presents two calculated reaction pathways leading to formation of HC_3^+. As concluded from the MD, with comparable probability the sequence of events of producing this channel can either be H loss $\rightarrow$ H_2 loss $\rightarrow$ fragmentation or H_2 loss $\rightarrow$ H loss $\rightarrow$ fragmentation. This channel was observed only in 31 trajectories of the dynamical simulations, so exploration of Potential Energy Surface is vital for identifying the most probable mechanism. The lowest energy pathway was found to start

with H loss from **min9** as a first step. Further hydrogen migration produces **min33**, from which a transition structure for H_2 elimination was calculated at 17.15 eV. Cleavage of C_α-C_β bond leads to the highest transition structure for this mechanism located at 17.54 eV. As previously mentioned in the section of fragmentation to $H_2C_3^+$, hydrogen molecule can be ejected after previous isomerization to **min2**. Subsequent barrierless H loss from **min21** produces unstable **min35**, which under ring opening and C_α-C_β bond fission leads to the fragmentation through an energy barrier of 19.89 eV. Therefore, most probable mechanism of obtaining ion HC_3^+ proceeds through H loss, followed by H_2 loss and finally fragmentation of the HC_4O^+ ion.

FIGURE 5.21 Potential Energy Surface for production of HCO^+, $H_2C_2O^+$ and H_2C^+. Energies calculated at B3LYP/6-311++G(d,p) level of theory are given in eV relative to furan. ZPE corrections are included. Dashed lines indicate barrierless transitions or that only the transition structure of the highest energy is presented.

Potential Energy Surface producing remaining significant ions are presented in Figure 5.21. A species that can only be obtained by skeleton fragmentation was found to be ketene cation ($H_2C_2O^+$). Mechanism of decomposition to $H_2C_2O^+$ proceeds through 1,2 hydrogen transfer and concerted fission of C-O and C_β-C_β bonds. The calculated energy barrier was located at 12.03 eV (**ts48**). A fragment that was not observed in the dynamical simulations, but was identified by previous experimental studies [2], [11], [39] is methylene ion (H_2C^+). Possible mechanisms of producing H_2C^+ involve further decomposition of ketene cation, requiring 13.72 eV of energy or decomposition of allene cation, leading to higher energy barrier for production of H_2C^+ located at 17.50 eV. The last identified species, highly observed in the dynamical simulations coming from two- and three-body fragmentation channels, is formyl cation (HCO^+). Firstly, 2,3 H transfer and consecutive ring rupture lead to formation of HCO^+ and propargyl radical as a neutral species. The highest transition structure for this mechanism was located at 12.78 eV (**ts46**). Formyl cation might as well be produced after H loss from **min9** and subsequent C_α-C_β bond cleavage of **min14**. This three-body fragmentation channel requires 16.21 eV of deposited energy to occur.

To summarize, possible furan cation fragmentation pathways to nine charged species have been proposed. Exploration of PES enabled identification of the most probable decomposition mechanisms. Based on the obtained fragmentation pathways, the most abundant charged fragment is expected to be $H_3C_3^+$ due to low energy barriers, a simple production mechanism and numerous plausible channels forming this species. The $H_4C_3^+$ fragment is expected to be produced mostly in the allene isomeric form. For higher energies, a $H_2C_3^+$ ion can be produced as a results of four-body fragmentation involving elimination of two atomic hydrogens. Loss of hydrogen was found to be an important process. Interestingly, hydrogen elimination occurs from the $H_4C_4O^+$ molecule rather than from the already fragmented species.

5.2.3 Statistical method

More insight into the fragmentation of the furan cation can be provided by the Microcanonical Metropolis Monte Carlo method. The database of neutral fragments used for the M_3C calculations of the neutral furan consisted of 226 neutral isomers. In order to perform the M_3C calculation of the furan cation, 243 singly ionized isomers have been added to the data set. Appendix 1 presents their geometries. A different sampling method, named SEQUENTIAL, has been applied in the case of the ionized molecule. Again, detailed benchmark of the input parameters have been performed (Chapter 4.3.2 Convergence search). Table 5.4 summarizes the final parameters used to obtain results presented in Figures 5.22 - 5.27.

TABLE 5.4 Parameters of the M_3C simulation of singly ionized furan

System Radius	13 Å
Markov chain sequence	V,T,R,5×S:0,V,T,R,5×S:1:-1
Number of experiments	500
Number of events	200 000
Sampling method	SEQUENTIAL

As it can be seen in Figure 5.22, using SEQUENTIAL sampling method results in more channels being observed in comparison with the fragmentation of neutral molecule. Decomposition of the singly ionized furan starts with channel $H_4C_3^+$/CO at 2 eV of internal energy. Next channels to appear are H_2/$H_2C_4O^+$, H/$H_3C_4O^+$ and, the least populated among two body fragmentation, $H_3C_3^+$/HCO. An internal energy increase to middle and high values results in production of many channels of the same type as observed in the dynamical simulations, such as $H_3C_3^+$/CO/H, $H_2C_3^+$/CO/H_2, HC_3^+/CO/H/H_2 as well as unobserved channels like HCO^+/C_3/H/H_2 and $H_2C_2^+$/HC/CO/H/H. Panel **b)** of Figure 5.22 shows that production of $H_4C_3^+$ dominates until the energy of 3.5 eV, when $H_3C_3^+$ begins to be the most abundant up to 10.5 eV. Error bars, corresponding to standard deviation of mean probabilities over all experiments, present values of around 15% for channels and 10% for species distributions. Among two-body fragmentation production of $H_4C_3^+$ was found to be the most probable. Species $H_3C_3^+$ dominate as a product of three-body decomposition channels and HC_3^+ is the most abundant fragment in the four-body fragmentation.
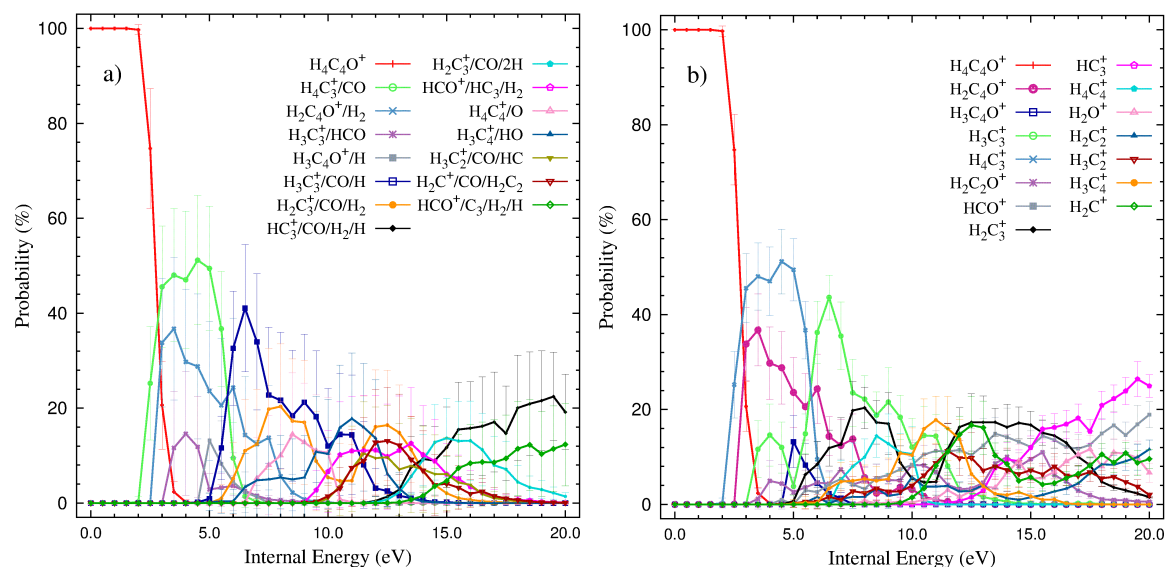
FIGURE 5.22 Results of M$_3$C calculations of singly ionized furan: **a)** channels and **b)** charged species probabilities as a function of the internal energy. Error bars correspond to standard deviations of the probabilities averaged over all experiments. Only channels/species with probabilities larger than 10% are shown.
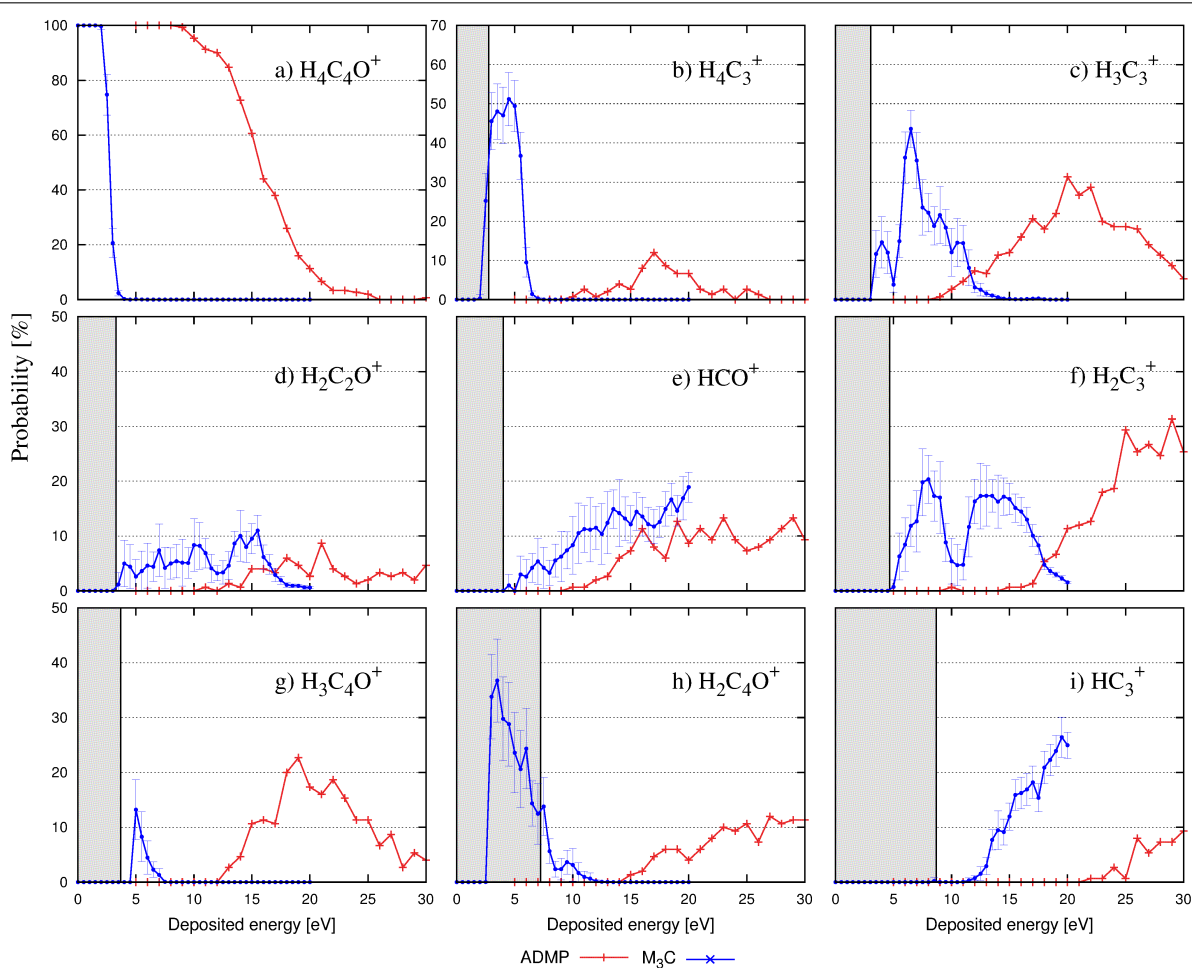
FIGURE 5.23 Comparison of significant species probabilities calculated by ADMP method (red) and M$_3$C (blue). Grey areas cover the energy range until the value of the lowest energy barrier for each fragment.

M$_3$C methodology considers only final minima on the PES and discards energy barriers. The effect of mentioned approach can be seen in Figure 5.23, where results of all three theoretical methods are included. In this figure, M$_3$C probabilities of specific species are plotted with its occurrences obtained by the ADMP method and grey blocks representing the height of calculated barriers. An assumption that the system holds enough energy to overcome all barriers can be untrue for depositions of lower energies into the system. In the case of furan cation, the undesirable feature is visible for fragments H$_4$C$_3^+$ and H$_2$C$_4$O$^+$, where M$_3$C species probabilities begin to occur before calculated energy barriers. The H$_4$C$_3^+$ ion starts to appear 1.09 eV before the barrier, but the shift is much more pronounced for the H$_2$C$_4$O$^+$ ion, which occurs 4.56 eV before the barrier. One way of getting around this problem is inclusion of barriers by increasing the energy of fragments H$_2$C$_4$O$^+$ and H$_4$C$_3^+$ by the respective barrier heights. This approach requires the assumption that vibrational frequencies of the respective transition structures don't vary considerably from the products. Then, the entropic contribution of the barrier is disregarded and only the energetic part is included in the calculation.

FIGURE 5.24 Simplified lowest reaction pathways for furan cation decomposition. Only critical points are shown.

A simplified version of fragmentation pathways in Figure 5.24 illustrates in red values of included barriers: 5.37 eV for the H$_2$C$_4$O$^+$ species, 1.14 eV for allene cation and 0.64 eV for propyne cation. This alteration leads to results presented in Figures 5.25 - 5.27. Firstly, it can be seen that in comparison with Figure 5.23, probabilities of fragments H$_2$C$_4$O$^+$ and H$_3$C$_4$O$^+$ decrease completely and anticipated increase of H$_3$C$_3^+$ probability occurs. Furan cation starts to dissociate around 3.5 eV. Figure 5.25 **a)** shows that H$_3$C$_3^+$ ion is first produced by the channel H$_3$C$_3^+$/HCO and from the energy of 5 eV channel H$_3$C$_3^+$/CO/H dominates. Moreover, H$_4$C$_3^+$/CO remains an important channel, but never exceeds probability for production of H$_3$C$_3^+$. From panel **b)** of Figure 5.25 it can be seen that H$_3$C$_3^+$ ion becomes now the most abundant charged fragment until 11 eV. A significant species observed for the energy range of 3.5 - 7 eV is H$_4$C$_3^+$ cation. Since the energy of 11 eV fragmentation process begins to be so abundant that it is difficult to determine unambiguously which fragments are the most prevalent. Highly observed species are H$_2$C$_3^+$, HC$_3^+$ and HCO$^+$. Figure 5.26 summarizes results of three methods applied in the present study. It can be noticed that no fragments appear before calculated energy barriers. The shift of ADMP breakdown curves to higher energy values compared with M$_3$C is caused by a different consideration of time by the theoretical methods. ADMP method considers time explicitly, however M$_3$C follows the ergodic hypothesis stating that time averages correspond to space averages in a microcanonical ensemble.
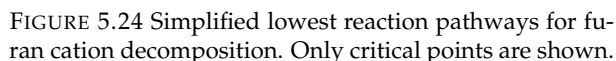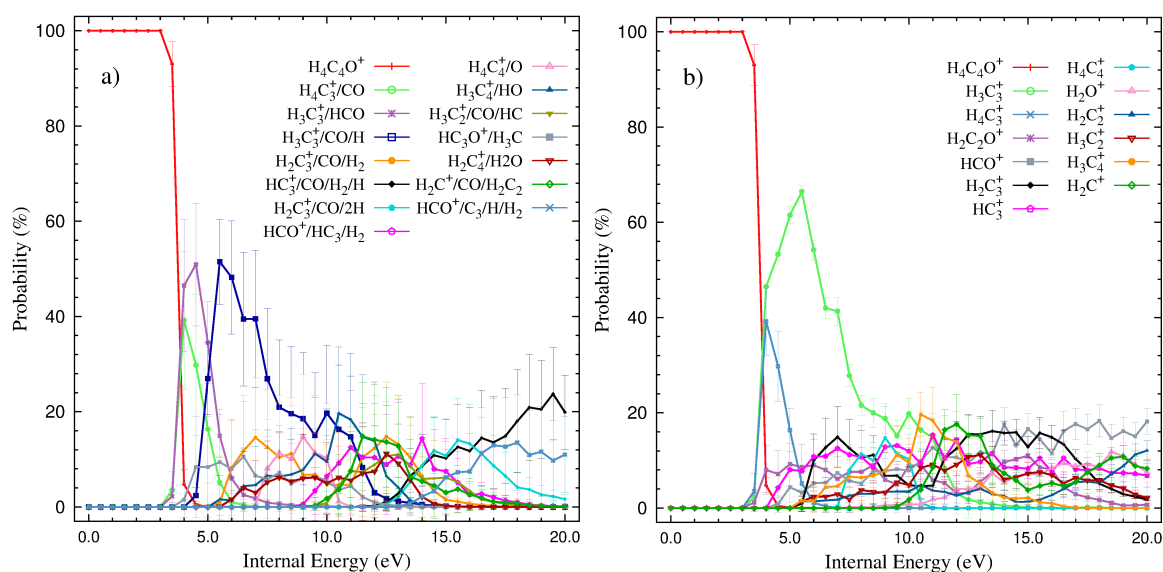
FIGURE 5.25 Results of M₃C calculations of singly ionized furan: **a)** channels and **b)** charged species probabilities as a function of the internal energy. Error bars correspond to standard deviations of the probabilities averaged over all experiments. Only channels/species with probabilities larger than 10% are shown.
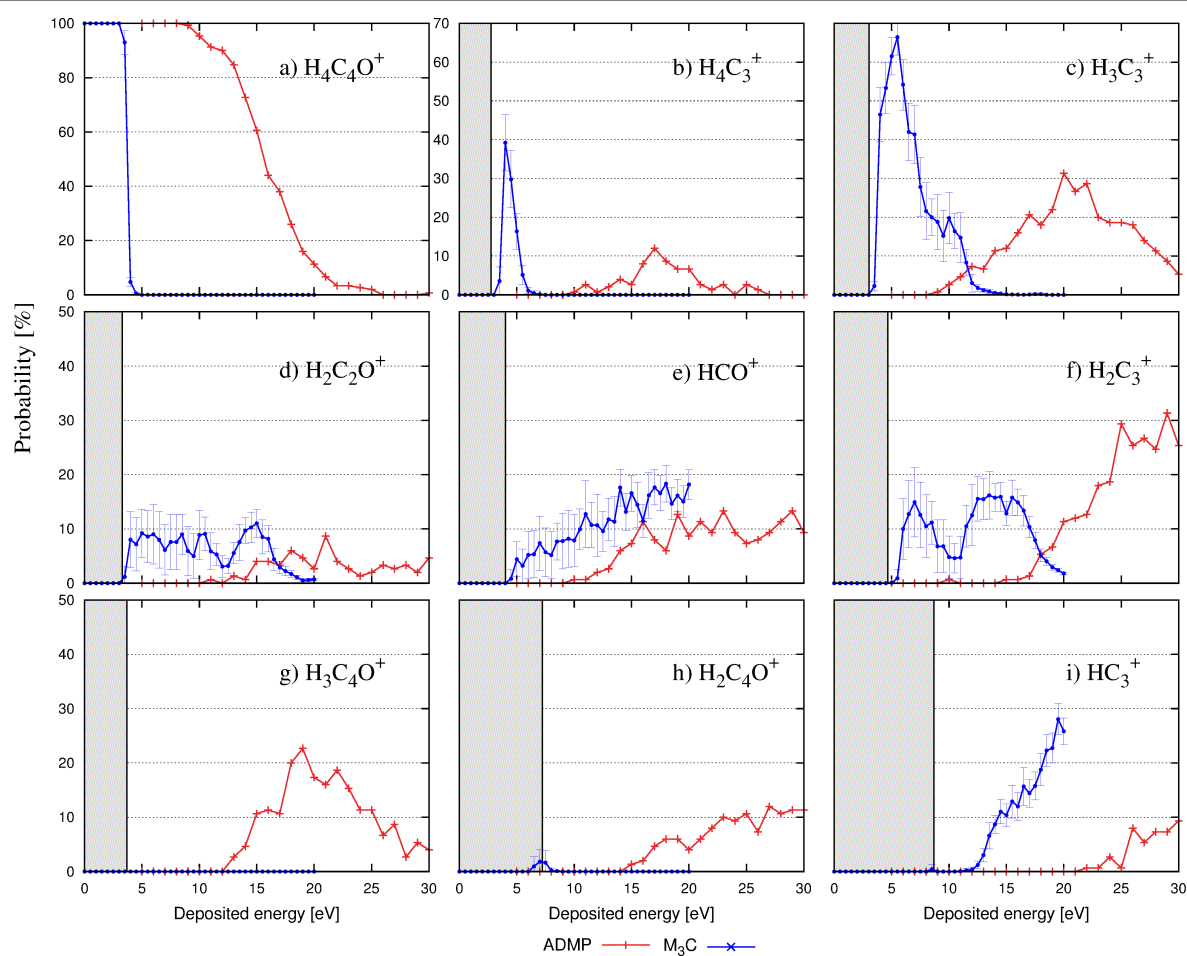
FIGURE 5.26 Comparison of significant species probabilities calculated by ADMP method (red) and M₃C (blue) after inclusion of barriers for fragments $H_2C_4O^+$ and $H_3C_4O^+$. Grey areas cover the energy range until the value of calculated barrier for each fragment.

Consequently, if the dynamical simulations could run until infinite time, in principle, ADMP and M_3C breakdown curves should overlap. Similar trends and maximum values can be observed for fragments $H_2C_2O^+$, HCO^+ and HC_3^+, but species $H_4C_3^+$, $H_3C_3^+$ and $H_2C_3^+$ present completely different features. Although M_3C probabilities of fragments $H_2C_4O^+$ and $H_3C_4O^+$ decrease completely, they are obtained by the ADMP method. Again, the reason of these discrepancies is limited simulation time of the molecular dynamics simulations. Hence, at some later point in time $H_2C_4O^+$ and $H_3C_4O^+$ are expected to decompose.
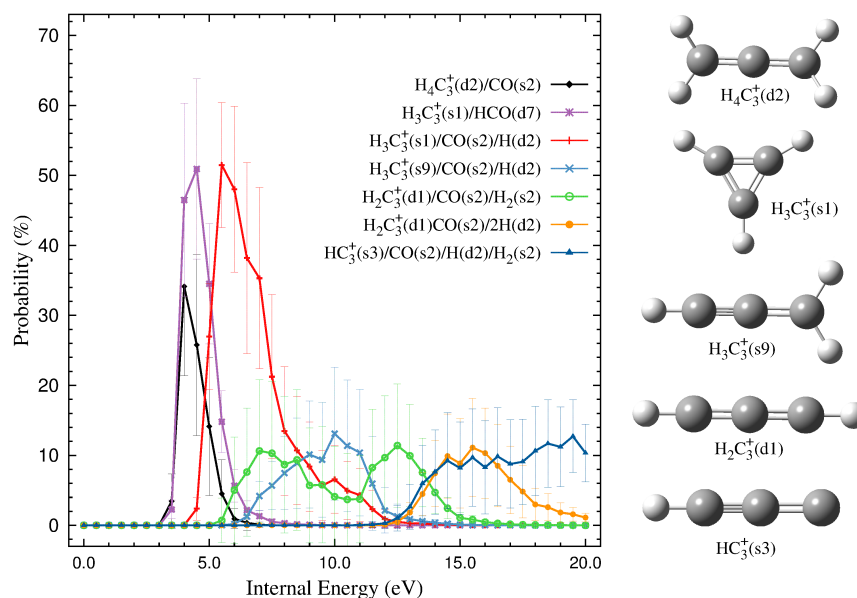
FIGURE 5.27 Results of M_3C calculations of singly ionized furan after inclusion of calculated energy barriers: detailed channels probabilities as a function of the internal energy.

Lastly, M_3C program provides an essential tool allowing to identify type of produced isomers. Figure 5.27 details channels probabilities producing ions $H_4C_3^+$, $H_3C_3^+$, $H_2C_3^+$ and HC_3^+. In accordance with PES exploration, $H_4C_3^+$ cation is mostly produced in allene form as well as HC_3^+ in linear configuration. However, not always the lowest energy isomer prevails. For the $H_3C_3^+$ cation, observation of cyclopropenium ion dominates initially, but since the energy of 9 eV a linear isomer - propargyl cation - becomes more abundant. Moreover, although cyclic isomer of $H_2C_3^+$ presents higher stability, a linear geometry is favoured as a product of fragmentation of furan cation.

5.2.4   Comparison with photon and ion collision experiments

Analogies between the results presented in preceding sections and previously performed experiments enable verification of the theoretical predictions and provide novel interpretation of the already measured data. A direct comparison can be made between measured ion Appearance Energies and calculated energy barriers for production of specific species. Previous electron impact ionization [2] and photoionization [11], [39] studies provide such results, given in Table 5.5.

TABLE 5.5 Lowest energy barriers of PES for selected charged fragments (in eV) compared with the AEs measurements of electron impact (EI), threshold photoelectron photoion coincidence (TPEPICO) and photoionization (PI) experiments.

m/z (fragment ion)	Channel	Lowest energy barrier	Dampc *et al* [2] EI	Rennie *et al* [39] TPEPICO	Rennie *et al* [11] PI
68 ($H_4C_4O^+$)		8.93	8.80 ± 0.10		
67 ($H_3C_4O^+$)	**min15$^+$**+H	12.44	12.80 ± 0.10		13.22
	α-furyl$^+$+H	14.60			
66 ($H_2C_4O^+$)	$H_2C_4O^+$+H+H	15.38	16.85 ± 0.10		17.32
	$H_2C_4O^+$+H_2	15.99			
42 ($H_2C_2O^+$)	$H_2C_2O^+$+H_2C_2	12.03	11.25 ± 0.10	11.80	11.8–11.9
40 ($H_4C_3^+$)	$H_2CCCH_2^+$+CO	11.52	11.45 ± 0.10	11.60	11.8–12.0
	c-H_2CCHCH^++CO	11.73			
39 ($H_3C_3^+$)	c-$H_3C_3^+$+HCO	11.78	12.60 ± 0.10	12.05	12.46
	c-$H_3C_3^+$+CO+H	12.91			
	H_2CCCH^++CO+H	14.99			
38 ($H_2C_3^+$)	$HCCCH^+$+H_2CO	13.43	12.85 ± 0.10	14.50	14.17
	$HCCCH^+$+CO+H_2	15.99			
	$HCCCH^+$+CO+2H	17.80			
	c-$H_2C_3^+$+CO+2H	18.07			
37 (HC_3^+)	HC_3^++CO+H_2 H	17.54	17.70 ± 0.15	18.25	18.31
29 (HCO^+)	HCO^++H_2CCCH	12.78	12.40 ± 0.20	13.00	12.84
	HCO^++c-H_2C_3+H	16.21			
14 (H_2C^+)	H_2C^++H_2CC+CO	15.72	17.35 ± 0.15	17.00	17.76
	H_2C^++HCCH+CO	17.50			

Calculated energy barriers should correspond to the dissociation onsets for specific species. Table 5.5 shows satisfactory agreement between the present computational results and experimental studies. Firstly, measured values of AEs for $H_3C_4O^+$ ion confirm that hydrogen is eliminated from $H_4C_4O^+$ isomer rather than directly from ionized furan. Moreover, studies of metastable transitions performed by Rennie *et al* [11] suggested that $H_2C_4O^+$ ion is produced by the sequential loss of two hydrogen atoms rather than by elimination of molecular hydrogen. Indeed, lower energy barrier was found for sequential H loss from furan cation, however measured AEs of $H_2C_4O^+$ remain around 1.5-2 eV higher than calculated values.

A barrier higher by 0.13-0.23 eV than measured photoionization AE was calculated for the production of ketene cation - $H_2C_2O^+$. However, barrier height for formation of $H_4C_3^+$ coincides perfectly with measured values. Willett and Baer [38] determined experimental rates for the production of $H_4C_3^+$ and $H_2C_2O^+$ from the total dissociation rates and PEPICO branching ratios. Their values were identical, suggesting the competition between these species and a

possibility of common transition structure. Present study indicates that different points on the PES are rate determining for $H_4C_3^+$ and $H_2C_2O^+$. However, a possibility of proceeding through a shared pathway arises from a very small difference between the lowest and the second lowest barriers for production of allene cation. The transition structure for 2,1 H transfer was located at 11.52 eV (**ts1**) and for 1,2 H transfer at 11.56 eV (**ts6**). A difference of only 0.04 eV and equal rates for the formation of $H_4C_3^+$ and $H_2C_2O^+$ can indicate that indeed 1,2 H transfer is the first step of producing these species. Furthermore, the kinetic energy release distribution for the loss of the CO fragment measured by Holmes and Terlouw [36] showed that a wide range of kinetic energies is released upon fragmentation. This result implies feasible participation of many isomeric structures of $H_4C_3^+$. Indeed, the dynamical simulations also show high abundance of cyclopropene (c-H_2CCHCH$^+$) cation.

The barrier height for production of $H_3C_3^+$ agrees best with TPEPICO studies and is 0.82 eV lower than measured after electron impact. Higher onset energy than observed for $H_4C_3^+$ and $H_2C_2O^+$ does not exclude high production rate of this ion. Dampc *et al* [2] reported that $H_3C_3^+$ ions are the most abundant products of electron induced dissociation. As shown in the section of PES exploration, simple formation mechanisms with loose transition structures can be the reason for such high occurrence of $H_3C_3^+$. Rennie *et al* [39] concluded from their TPEPICO experiment that by the energy of around 13 eV $H_3C_3^+$ becomes the most important fragment. They mentioned no experimental means of differentiating between direct and sequential processes, but the present study confirms that H loss channel producing $H_3C_3^+$ should open around 12.91 eV.

Calculated lowest energy barrier for production of $H_2C_3^+$ is located in between AEs measured by different techniques, so no clear conclusion can be made from comparison of these values. A discrepancy between thermodynamical threshold and measured AEs has been indicated by Rennie *et al* [39]. However, in their photoionization experiment [11] $H_2C_3^+$ has been prominent in the daughter ion spectra, suggesting a sequential process. Dynamical simulations of the present study suggest production of $H_2C_3^+$ cation after elimination of two hydrogen atoms, a process to which energy onset has been predicted at 17.80 eV. This is in perfect accord with an observation from [39] that a new channel to the $H_2C_3^+$ fragment opens between 17.6 and 18.0 eV. Although authors propose that $H_2C_3^+$ is produced by H loss from $H_3C_3^+$, this conclusion is not supported by the present study.

Good agreement can be noticed for the HC_3^+ ion. This comparison indicates that indeed H loss is followed by H_2 loss in forming HC_3^+, contrary to the proposal from [39] that this fragment is produced in channel $HC_3^+/HCO/H_2$. Additional notion against this suggestion is that channel $HCO^+/HC_3/H_2$ is more energetically favourable.

Measured AE aligns well with calculated lowest energy barrier for production of HCO^+, indicating that formyl cations are first produced in two-body fragmentation channel resulting in propargyl radicals as neutral species. A good agreement between lowest energy barrier of channel $H_2C^+/HCCH/CO$ and AE of H_2C^+ denotes that this ion is most likely produced in three body fragmentation, which requires 17.50 eV of internal energy.

It is worth pointing out that higher values of measured AEs than calculated ones can be expected due to the kinetic shift (the shift of the onset to an energy sufficient enough so that

the rate of decomposition exceeds some minimum value). Moreover, higher energy alternate processes generally show a slow onset at threshold, causing a significant kinetic shift [39]. Additionally, the applied theoretical method can be the source of some small discrepancies. As far as various computational methods are expected to give different absolute energies of optimized structures, values of relative energies should not essentially differ.
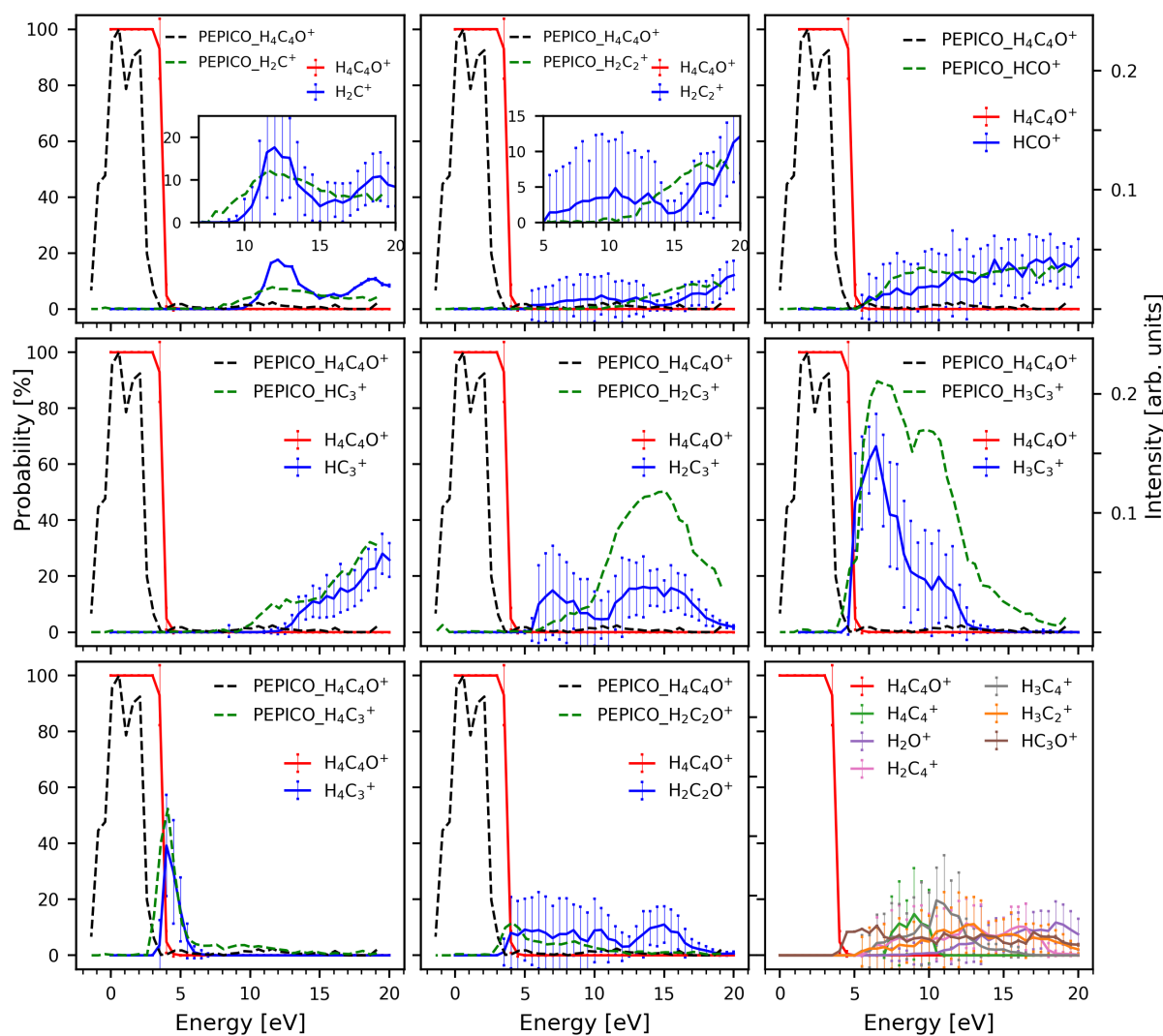
FIGURE 5.28 Comparison of breakdown curves calculated with M_3C and measured in the PEPICO experiment. Lowest right panel presents fragments that didn't appear in the PEPICO experiment, but were obtained by M_3C method with probability higher than 10%.

An extended theoretical investigation presented in this thesis, including three methodologies, might guide new experimental efforts. In particular, breakdown curves recorded by PEPICO technique over wide energy range can be directly compared with those predicted by the statistical theory of M_3C. The most recent experimental measurements have been performed by Paola Bolognesi and co-workers at the Elettra synchrotron radiation facility in Trieste, Italy [96]. Figure 5.28 shows comparison of the experimental data and the theoretical results for significant species. It can be noticed that the shape of the curves is correctly reproduced for all fragments besides H_2C^+ and $H_2C_3^+$. M_3C probabilities of these ions present two

distinct maxima, whereas the ones recorded by PEPICO show only one. As for differences in intensity, a decrease of about 30% can be observed for $H_3C_3^+$ between 5 and 11 eV. Despite this absolute discrepancy, both experimental and theoretical studies indicate that $H_3C_3^+$ is the most abundant species in the mentioned energy range. Moreover, detailed M_3C channels probabilities suggest that two peaks, which also occur in the PEPICO breakdown curve of $H_3C_3^+$, result from channels of H loss. First peak corresponds to production of c-$H_3C_3^+$ and the second one to production of H_2CCCH^+. A narrow breakdown curve with a maximum around 4 eV can be observed for fragmentation to $H_4C_3^+$ by both studies. M_3C probability for production of $H_2C_3^+$ originates from two channels: $H_2C_3^+$/CO/H_2 (lower energies) and $H_2C_3^+$/CO/2H (higher energies). A discrepancy between experimentally observed values for lower energies suggest that this fragment is rather produced in the channel of four body fragmentation. This is in accordance with the dynamical simulations showing that indeed majority of $H_2C_3^+$ is produced in channel of double atomic hydrogen loss. M_3C probability for production of HC_3^+ presents a good shape in comparison with PEPICO results. However, an underestimation in the intensity of around 10% can be noticed. Breakdown curves of HCO^+ overlap for energies from 12 to 20 eV, but differ between 6 and 12 eV. Moreover, M_3C probability for production of $H_2C_2^+$ starts to appear earlier by around 5 eV. Breakdown curves of $H_2C_2O^+$ overlap from the energy of 3 eV, but start to diverge at 12 eV, indicating that $H_2C_2O^+$ is produced in channel $H_2C_2O^+$/H_2C_2 (before 12 eV) rather than in $H_2C_2O^+$/HC_2/H (after 12 eV).

A source of occurring deviations can originate from a number of species obtained in the M_3C calculations that were not observed in PEPICO (lowest right panel of Figure 5.28). Their appearance reduces mostly the intensity of H_2C^+, $H_3C_3^+$ but also other species. It is possible that although fragments unrecorded by PEPICO are entropically favourable, they present a high energy barrier that M_3C does not account for.

Results obtained by the M_3C method may be also compared with experimental mass spectra. For this purpose it is necessary to determine energy distribution functions distinctive for every collisional system. The method of acquiring these functions is presented in Chapter 3, so here only the results of the fitting procedure are shown (Figure 5.29). Mass spectra detected after the production of singly ionized furan in the interaction with different ions (3 keV Ar^+, 48keV O^{3+}, 48keV O^{6+}, 165 keV Ar^{11+} and 565 keV Xe^{25+}) have been recently obtained by Patrick Rousseau and co-workers at ARIBE, the low-energy ion beam facility of GANIL (Grand Accélérateur National d'Ions Lourds) in Caen, France [97]. It has been previously shown [98], [99] that projectile charge state significantly influences energy deposition into the system. Generally, for higher charge states the collisions take place at larger impact parameters, leading to decrease in probability of energy transfer. Results presented in this work support these findings. Figure 5.29 exhibits energy deposition functions of various shapes and positions of peaks for different projectiles. Particularly, energy deposition functions of Ar^+, electrons and O^{3+} present only one peak with maxima at 6, 4, and 3.5 eV, respectively. Hence, it can be seen that with the increasing charge of the ions the highest peak shifts to the lower values of energy. Different distributions were found for O^{6+}, Ar^{11+} and Xe^{25+}, where two peaks (around 1 eV and 5 eV) and a flat region of probability for energies between 13 and 20 eV can be noticed. As far as collision with O^{6+} leads to a distinct peak of around 70 % at 5 eV, energy deposition

functions of Ar^{11+} and Xe^{25+} demonstrate only a small convex around 50 % and 30%, respectively. Presented features are reflected in the fact that multiply ionized projectiles give rise to less fragmentation products and higher intensity of the parent ion, however Ar^+, O^{3+} and electrons induce richer fragmentation.
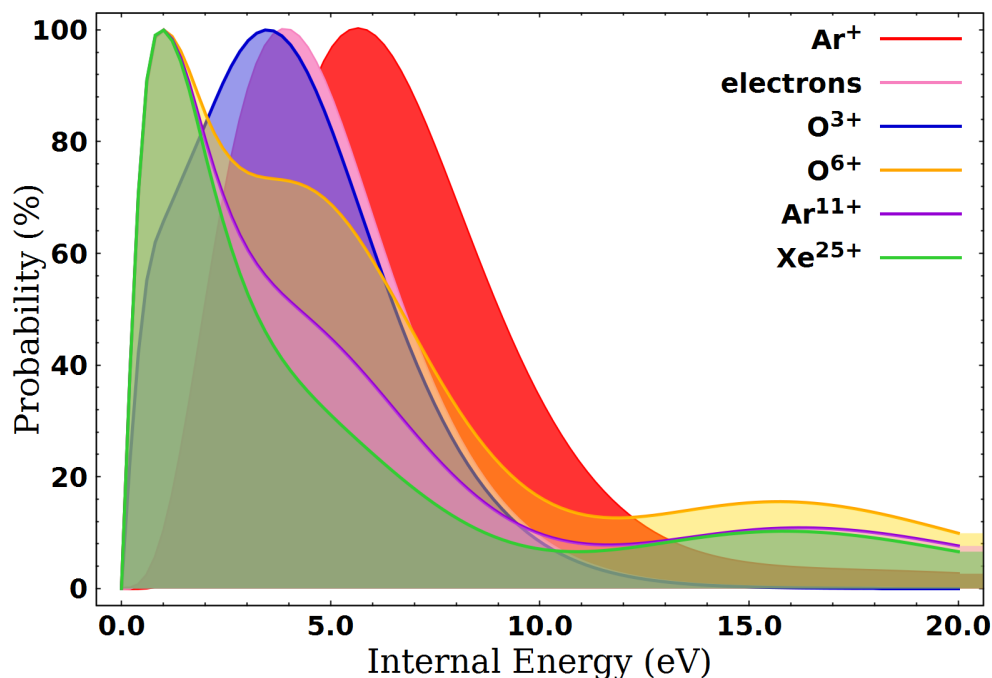
FIGURE 5.29 Fitted energy deposition functions for various projectiles.

Convolution of the M_3C probabilities with fitted deposited energy functions results in theoretical mass spectra presented in Figures 5.30 and 5.31. Firstly, as the statistical theory produces more abundant fragmentation due to the lack of barriers, obtained theoretical mass spectra often show peaks for fragments that were not observed in the experiments. In particular, overestimations of peaks can be noticed in m/z regions of 40-43 and 50-53. Furthermore, for Ar^+ and electrons, when fragment $H_3C_3^+$ presents the highest intensity, a peak corresponding to the parent ion is overestimated as well. Similarly to the case of photon induced fragmentation, $H_3C_3^+$ was the most significant decomposition product in the interaction with different ions. Figures 5.30 and 5.31 show that the weaker the fragmentation, the better the reproduction of the most important species: $H_3C_3^+$. The most noticeable underestimation can be observed for HC_3^+ and HCO^+. As a summary, a general observation in the discussion of theoretical and experimental mass spectra is that existing peaks of m/z below 39 ($H_3C_3^+$) are underestimated and peaks above that value are overestimated.
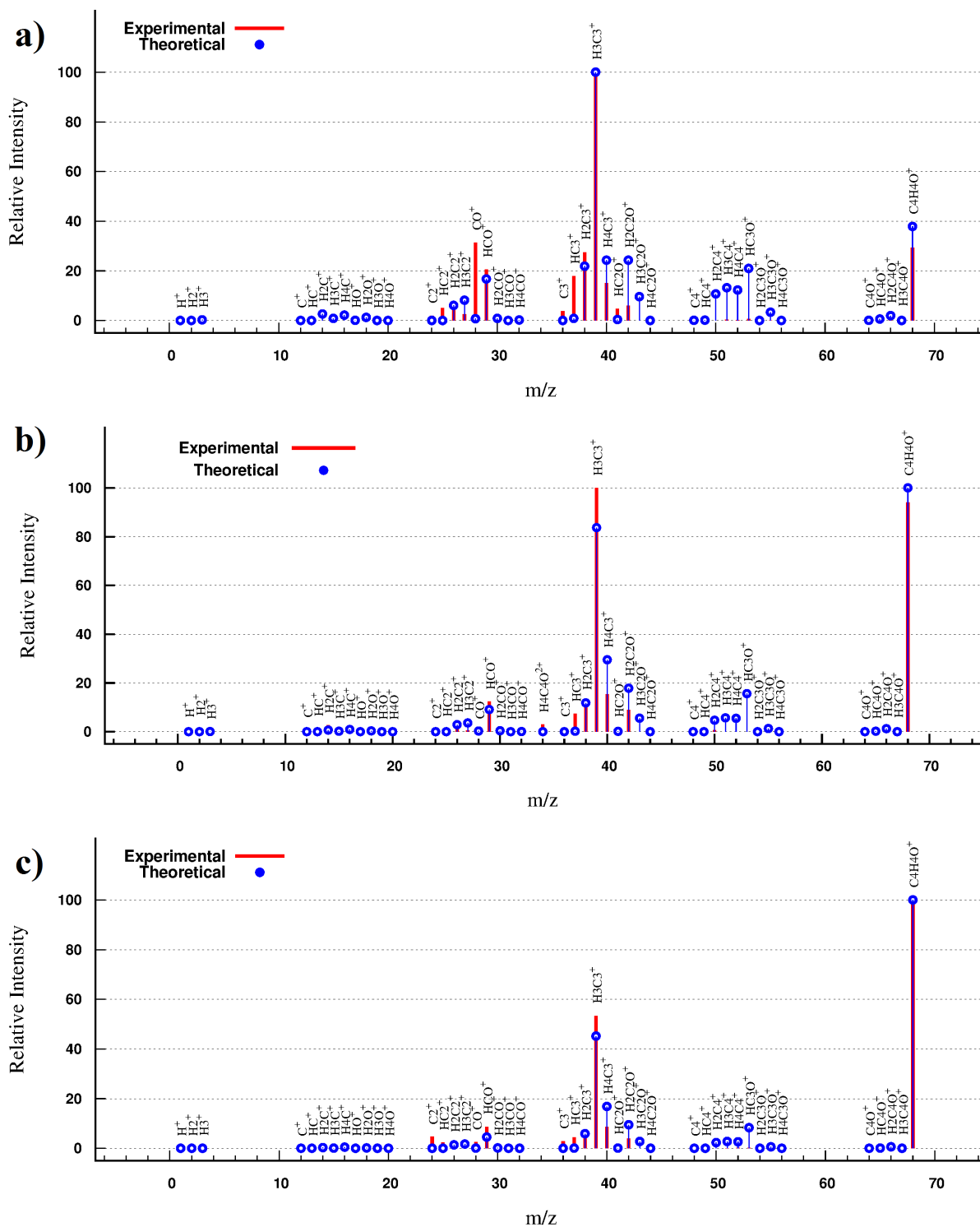
FIGURE 5.30 Comparison of theoretical and experimental mass spectra after collision with **a)** Ar^+ **b)** e^- **c)** O^{3+}.
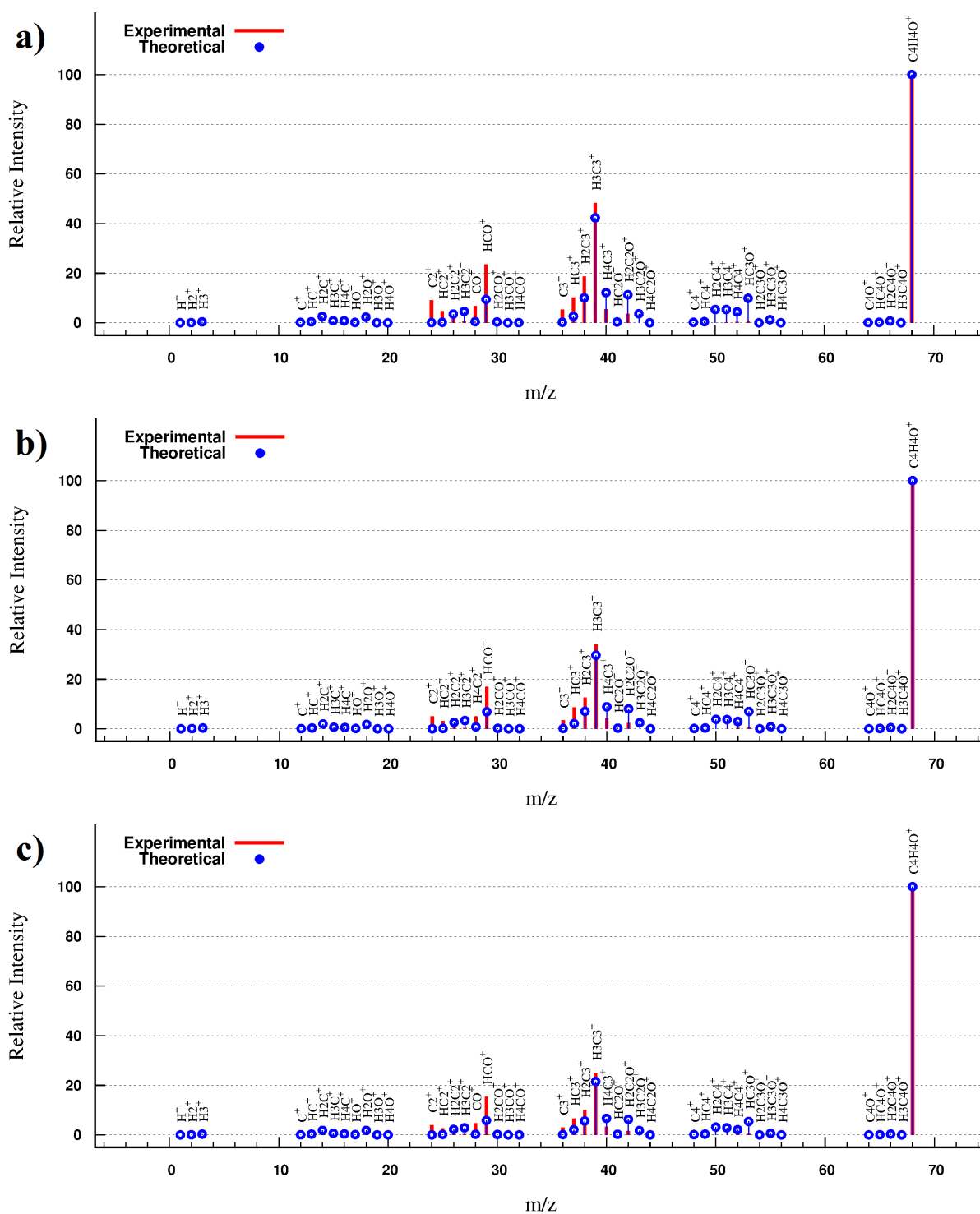
FIGURE 5.31 Comparison of theoretical and experimental mass spectra after collision with **a)** O^{6+} **b)** Ar^{11+} **c)** Xe^{25+}.

5.3   Doubly ionized furan

5.3.1   Molecular Dynamics

Results of the dynamical simulations of doubly ionized furan are presented in Figures 5.32 -
5.36. A different approach than for neutral and singly ionized molecule was required for clear
discussion of observed processes. Four possible mechanisms have been distinguished: (1) iso-
merization (2) skeleton fragmentation (3) H^+/H_2^+ loss and (4) H/H_2 loss. Their abundances are
presented in Figure 5.32 **a)**. Again, isomerization indicates intramolecular hydrogen migration
or cleavage of one of the C-O/C-C bonds. This process already appears for the first considered
energy of 5 eV and is lastly identified at 24 eV. Isomerization occurs for a wide energy range,
however, its abundance never exceeds 20%. Such outcome does not exclude isomerization tak-
ing place throughout the course of the simulation, but indicates that at the last time step (300
fs) observation of only this process is infrequent. Skeleton fragmentation denotes here that no
atomic or molecular hydrogen is ejected in neither neutral nor charged state. From the energy
of 10 eV until 20 eV, cleavage of the furan ring dominates. Third process, corresponding to
loss of an ionized hydrogen (H^+/H_2^+), prevails for energies between 21 and 30 eV. It is possible
that channels of this type also contain H or H_2 as fragments in a neutral state. Finally, fourth
family of observed processes implies neutral hydrogen loss, meaning that charge is localized
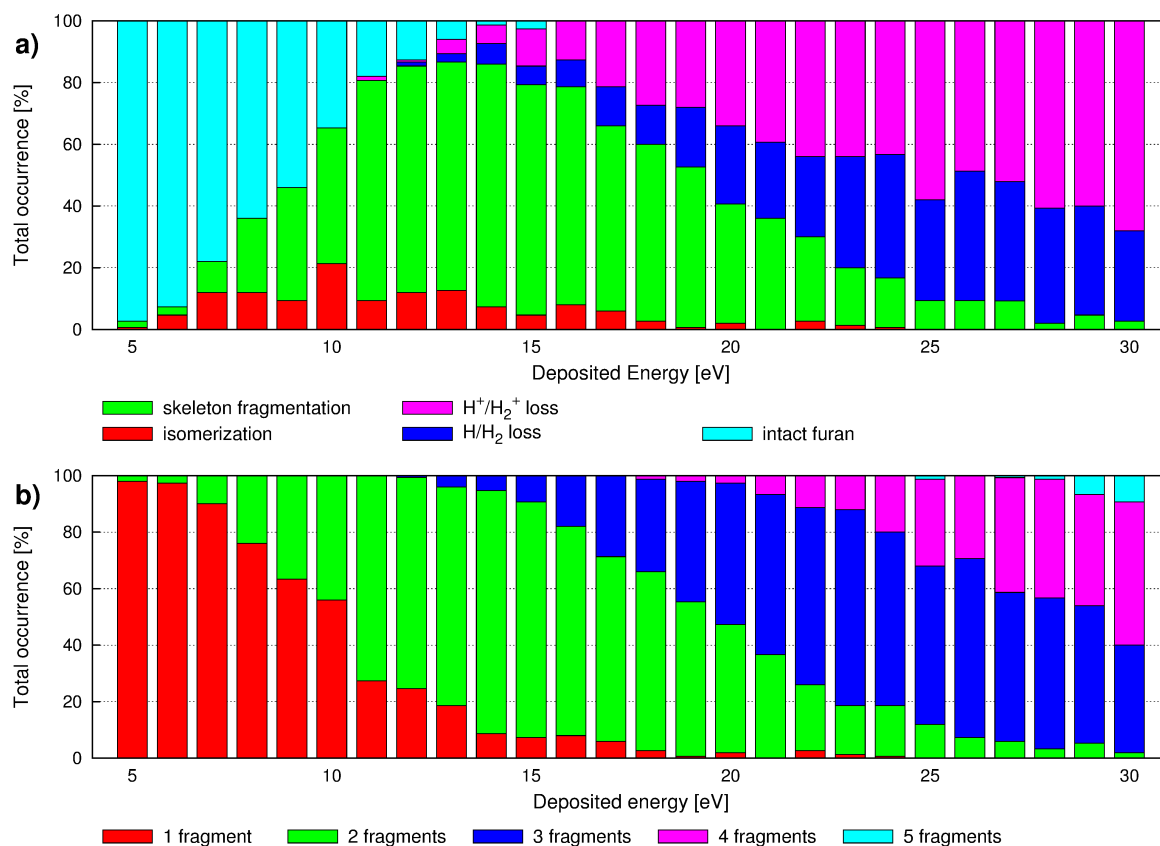
FIGURE 5.32 Results of the ADMP simulations of doubly ionized furan: total occurrence of **a)** observed processes
b) number of fragments as a function of internal energy.

on fragments containing C and/or O. This mechanism is never a dominant process, but since 14 eV its total occurrence increases until reaching maximum value of 42% for the energy of 26 eV. Figure 5.32 **b)** illustrates number of produced fragments as a function of the deposited energy. The occurrence of one fragment decreases until the energy of 26 eV. Two fragments can be observed for all considered energies with a maximum of 86% at 14 eV. Next, three body fragmentation occurs from 12 to 30 eV and is the most abundant process between 20 and 29 eV. At last considered energy of 30 eV four body fragmentation prevails. Production of five fragments was a minor process occurring from 27 eV with a maximum probability of 9% at 30 eV.
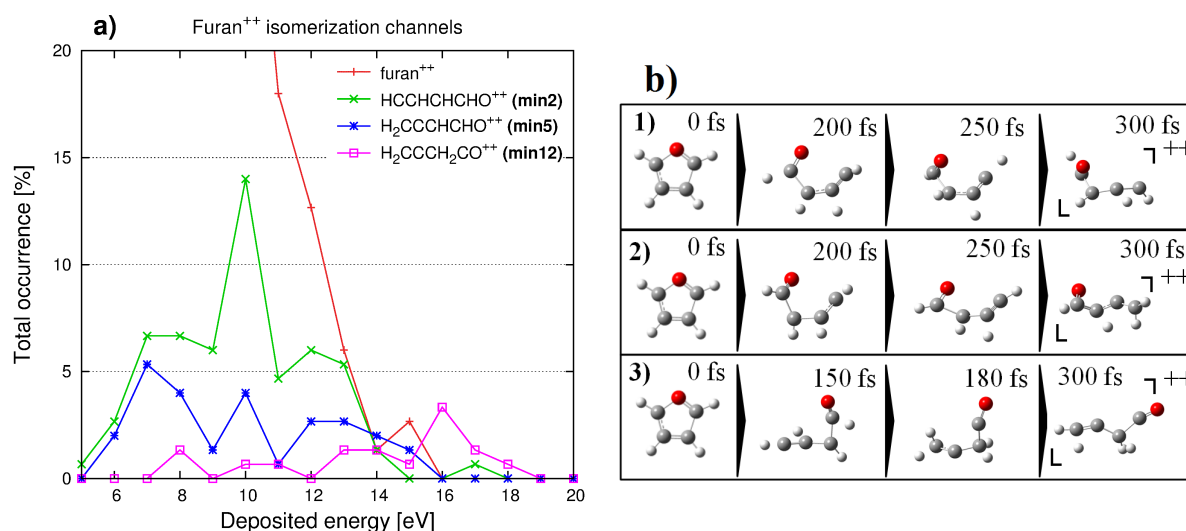
FIGURE 5.33 Results of the ADMP simulations of doubly ionized furan: **a)** total occurrence of the most abundant isomerization channels **b)** snapshots of trajectories leading to channels from the left panel.

The process requiring the least amount of internal energy was found to be isomerization, detailed in Figure 5.33. Three principal structures have been identified. Panel **a)** illustrates their occurrence as a function of the internal energy and panel **b)** shows possible production mechanisms of these isomers. The first and most populated structure is produced through ring opening by cleavage of the C-O bond and rotation around C_α-C_β bond. This mechanism is the most abundant from the energy of 5 until 13 eV. Second isomer implies ring opening by cleavage of the C-O bond as well, but is followed by a 2,1 H transfer. Finally, isomerization channel dominating for higher energies (between 16 and 19 eV) relies on cleavage of the C-O bond and concerted 1,2 and 2,1 H transfer occurring on the opposite sides of the furan ring.
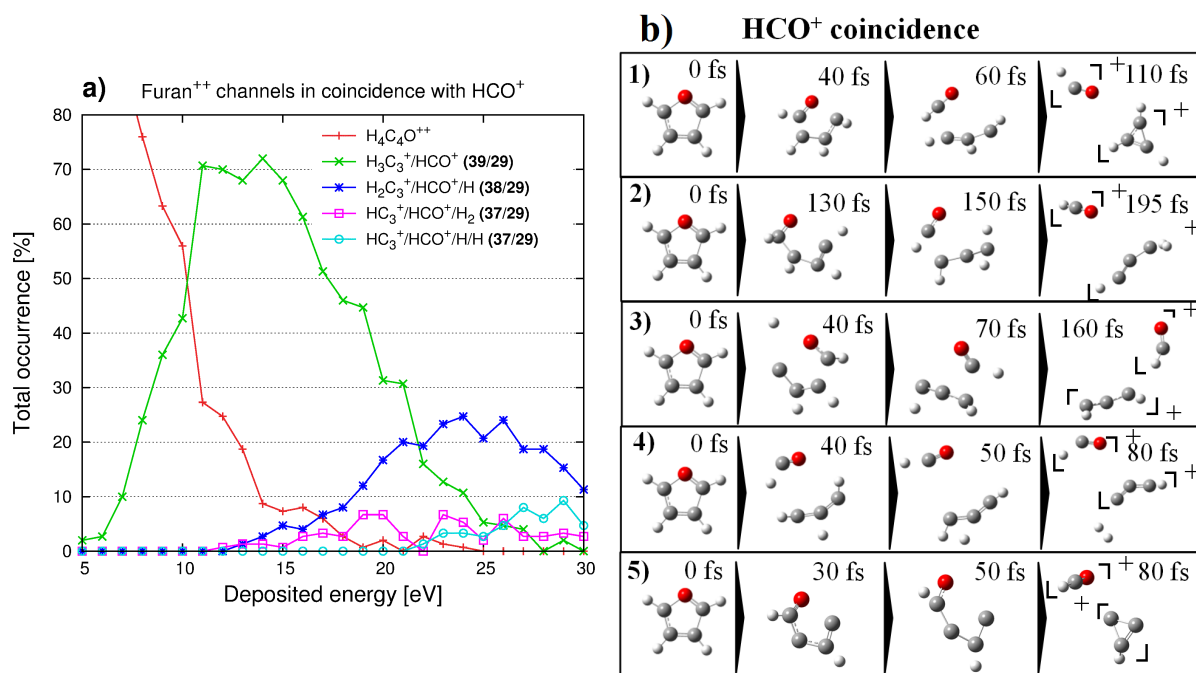
FIGURE 5.34 Results of the ADMP simulations of doubly ionized furan: **a)** total occurrence of channels in coincidence with HCO$^+$ **b)** snapshots of trajectories leading to channels from the left panel. Only channels that appeared at least 5% at a certain point in the energy range are presented.

Results of the dynamical simulations finishing with charged fragments HCO$^+$ and H$_n$C$_3^+$ (n = 3-1) are shown in Figure 5.34. Panel **a)** of Figure 5.34 demonstrates that two-body decomposition to H$_3$C$_3^+$ and HCO$^+$ is clearly the most abundant channel between energies of 11 and 21 eV and is also the only significant channel of skeleton fragmentation. Time evolution of trajectories containing decomposition to two possible configurations of H$_3$C$_3^+$ are shown in the first two panels of Figure 5.34 **b)**. Production of a cyclopropenium cation (c-H$_3$C$_3^+$) proceeds through ring opening by rupture of the C-O bond and subsequent C$_\alpha$-C$_\beta$ bond cleavage. An intermediate step of this mechanism corresponds to the most abundant channel of isomerization, indicating that if given more simulation time, trajectories finishing with HCCHCHCHO^{++} would increase the production yield of channel c-H$_3$C$_3^+$/HCO$^+$. Formation of propargyl cation (H$_2$CCCH$^+$) has been observed as well and is presented in the second panel of Figure 5.34 **b)**. This channel follows rearrangement to H$_2$CCCHCHO^{++} (second most populated isomer) by cleavage of the C$_\alpha$-C$_\beta$ bond. Hence again, longer simulation time should increase the abundance of channel H$_2$CCCH$^+$/HCO$^+$. Among skeleton fragmentation channels, c-H$_3$C$_3^+$/HCO$^+$ is expected to be the most abundant due to simple formation mechanism. However, the conclusion which isomer will prevail can only be confirmed by further exploration of the Potential Energy Surface of these reactions. Remaining channels, presented in Figure 5.34, rely on additional H/H$_2$ loss. The one exhibiting significant occurrence corresponds to formation of H$_2$C$_3^+$, HCO$^+$ and H. Statistical analysis of trajectories producing this channel indicates that α position is the preferable site for hydrogen loss (53% of observed cases). Possible mechanism of producing this channel, demonstrated in Figure 5.34 **b)**, proceeds through removal of hydrogen from α position, cleavages of C-O and subsequently C$_\alpha$-C$_\beta$ bonds.

The least populated channels, presented in Figure 5.34 **a)**, produce HC_3^+, HCO^+ as charged species and either hydrogen molecule or two atomic hydrogens. Of these two, $HC_3^+/HCO^+/H_2$ appears earlier in the energy range (at 12 eV) and is dominant until the energy of 24 eV. At 26 eV channel $HC_3^+/HCO^+/2H$ shows maximum probability, but its total occurrence never exceeds 10%. Snapshots of exemplifying trajectories indicate that production of HCO^+/H_2CCCH^+ is an intermediate step in channel $HC_3^+/HCO^+/H_2$ and H_2 is removed from propargyl cation. Four-body fragmentation to channel $HC_3^+/HCO^+/2H$ might proceed through two hydrogens being lost from adjacent α and β positions, C-O and C_α-C_β bond cleavages with cyclization of the HC_3^+ fragment.
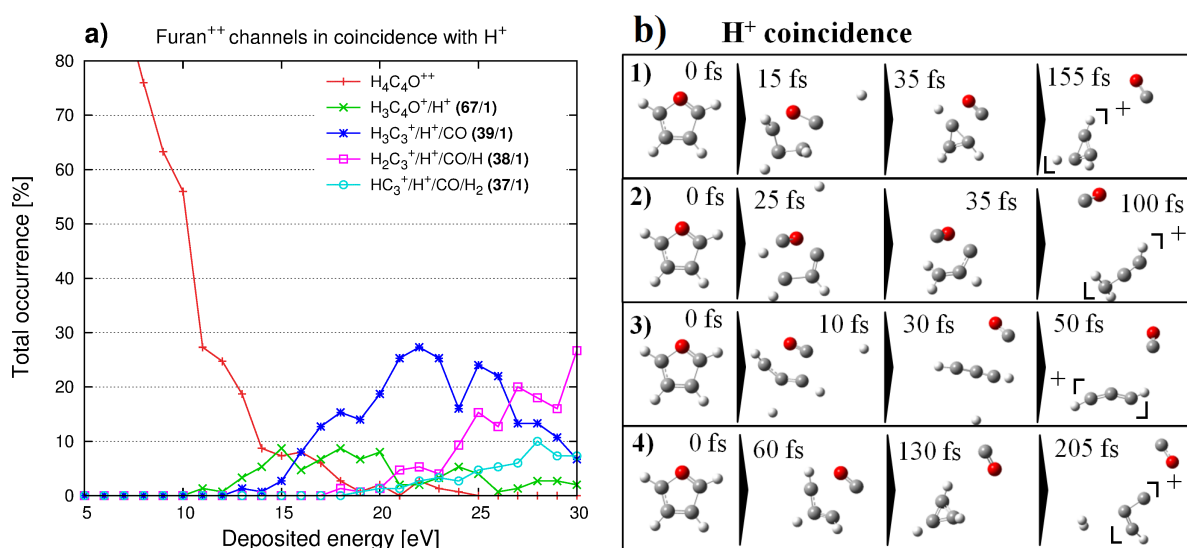
FIGURE 5.35 Results of ADMP simulations of doubly ionized furan: **a)** total occurrence of channels in coincidence with H^+ **b)** snapshots of trajectories leading to channels from the left panel. Only channels that appeared at least 5% at a certain point in the energy range are presented.

Second type of distinguished mechanisms, presented in Figure 5.35, consists of deprotonation. Loss of H^+ has been observed in coincidence with $H_3C_4O^+$ and with $H_nC_3^+$ (n = 3-1). Channel $H_3C_4O^+/H^+$ is the first to appear, but at the energy of 16 eV the dynamical simulations already show prevalence of the $H_3C_3^+/H^+/CO$, the most abundant channel of deprotonation over all energies. First two panels of Figure 5.35 **b)** illustrate possible production mechanisms, which rely on H_α^+ loss and subsequent C-O and C_α-C_β bond cleavages to produce c-$H_3C_3^+$ or 1,2 and 2,1 H transfers on the opposite sides of the ring, followed by C-O and C_α-C_β bond cleavages to produce H_2CCCH^+. Loss of H_α^+ prevails in substantial majority of calculated trajectories (81%). At the energy of 27 eV channel $H_2C_3^+/H^+/CO/H$ becomes the most abundant. Formation mechanism of this channel is presented in the third panel of Figure 5.35 **b)**. It can be seen that H^+ and H loss from adjacent α and β positions is followed by fragmentation. The least populated channel in Figure 5.35 **a)** reaches maximum total occurrence of 10% at the energy of 28 eV and produces HC_3^+, H^+, CO and H_2. Probable formation mechanism, presented in the last panel of Figure 5.35 **b)**, implies H^+ loss from α position, fragmentation to c-$H_3C_3^+/CO$ and finally H_2 loss from c-$H_3C_3^+$.
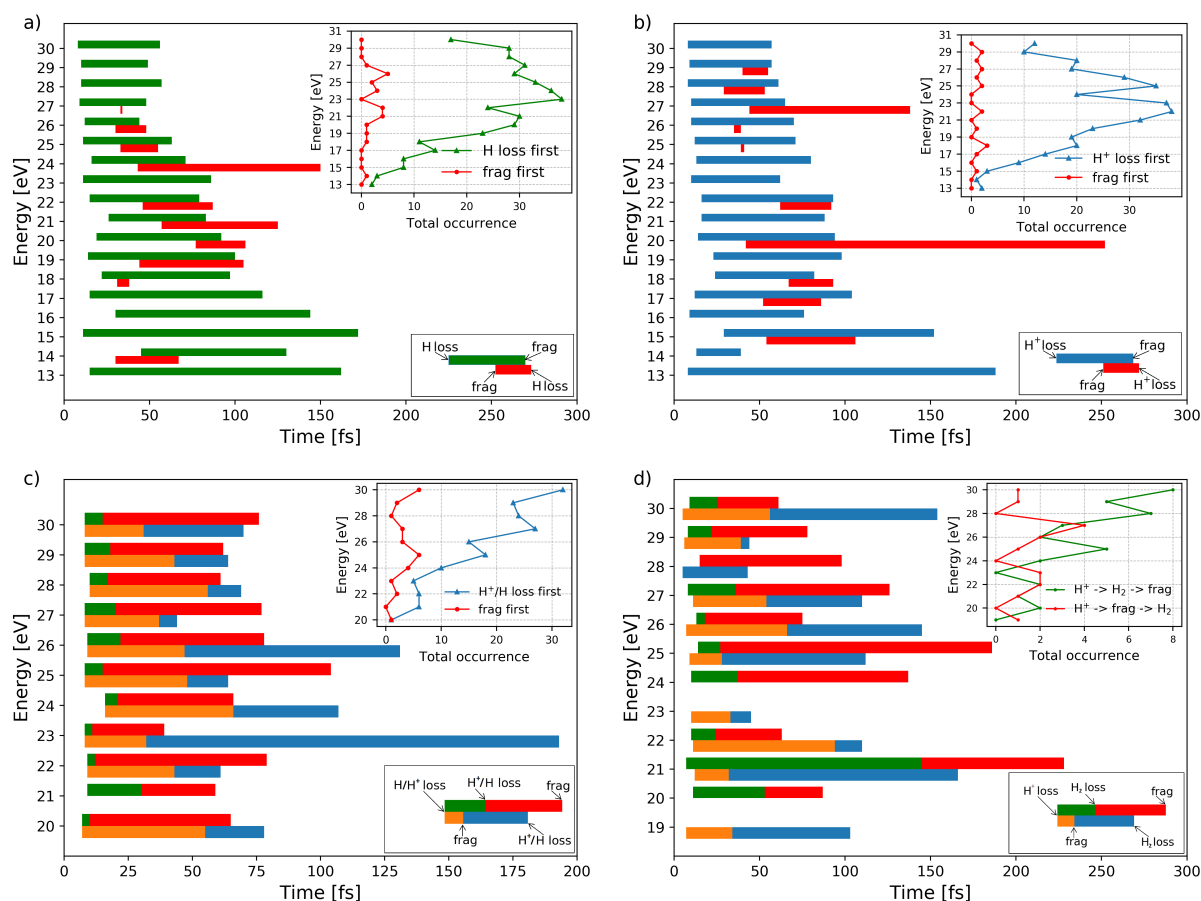
FIGURE 5.36 Results of the ADMP simulations of doubly ionized furan: average time scales of sequential events leading to channels that appeared at least 10% at a certain point in the energy range: **a)** $H_2C_3^+/HCO^+/H$, **b)** $H_3C_3^+/H^+/CO$, **c)** $H_2C_3^+/H^+/CO/H$ **d)** $HC_3^+/H^+/CO/H_2$. Borders of bars represent when, for different energies, on average either H, H^+, H_2 loss or fragmentation take place. Inset plots show abundance of different processes.

More insight into three- and four-body fragmentation processes can be obtained by investigation of the order of occurring events as the trajectory progresses. Results of such analysis are presented in Figure 5.36. From panel **a)** it can be noticed that in majority of trajectories producing channel $H_2C_3^+/HCO^+/H$ hydrogen loss is followed by fragmentation. Hydrogen atom is ejected around 10-30 fs and the time interval for fragmentation decreases with increasing energy. Moreover, analysis of the sequence of events of channel $H_3C_3^+/H^+/CO$ (panel **b)**) indicates clearly that H^+ loss takes place from $H_4C_4O^{++}$ and subsequently singly charged $H_3C_4O^+$ decomposes to $H_3C_3^+/CO$. As it is shown in Figure 5.36 **c)**, the most frequent sequence of events in channel $H_2C_3^+/H^+/CO/H$ is H^+/H loss $\rightarrow$ fragmentation. Interestingly, the increase of the internal energy does not affect when the first step of fragmentation takes place, which, on average, occurs at 9 fs. There is no way of differentiating whether H^+ or H is lost primarily based on the result of the dynamical simulations. Panel **d)** details two most populated sequences of events in channel $HC_3^+/H^+/CO/H_2$: H^+ loss $\rightarrow$ H_2 loss $\rightarrow$ fragmentation and H^+ loss $\rightarrow$ fragmentation $\rightarrow$ H_2 loss without evident distinction which process is more favourable. Further insight into production of these channels is necessary through exploration of the PES.

5.3.2 Potential Energy Surface

Following the analysis of the dynamical simulations, stability and mechanistic properties are investigated by exploration of the Potential Energy Surface. Figure 5.37 summarizes calculated pathways and groups them in types of observed process. This scheme demonstrates the most significant channels obtained in the MD, as well as additional plausible channels of two-body fragmentation. Optimized critical points on the fragmentation pathways of furan dication are presented in Figures 5.38 - 5.47. Energies, calculated at B3LYP/6-311++G(d,p) level of theory, are given in eV relative to neutral furan. ZPE corrections are included. For the reasons of clarity, complete pathways are shown even though some parts are duplicated in multiple figures (such as **ts3** $\rightarrow$ **ts6** in Figures 5.38 - 5.40 and 5.42).
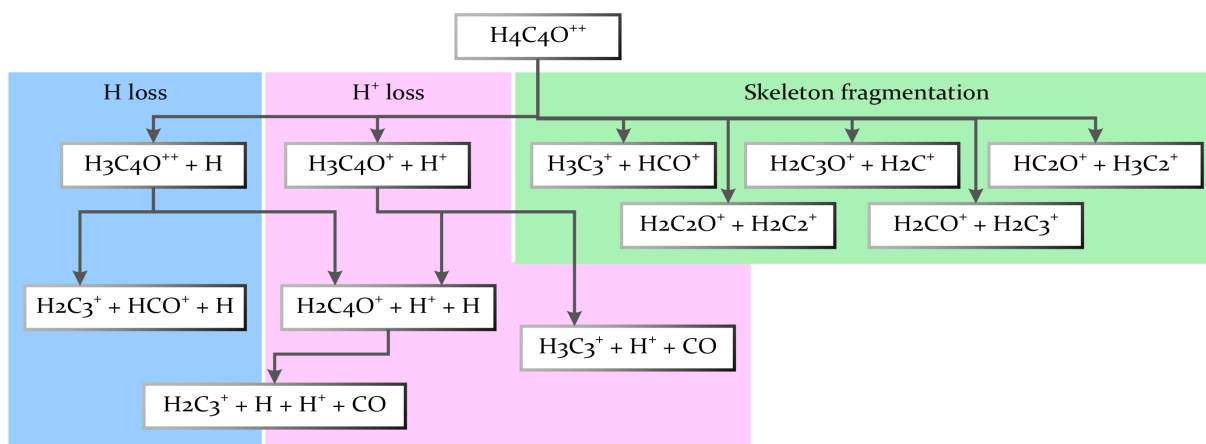
FIGURE 5.37 Calculated fragmentation pathways of furan dication.

Firstly, isomerization of the furan dication and subsequent decomposition to **two fragments** is illustrated in Figures 5.38 - 5.41. As it was previously pointed out, the only channel of skeleton fragmentation observed in the molecular dynamics with prominent probability was $H_3C_3^+/HCO^+$. The lowest energy pathway leading to production of c-$H_3C_3^+$ and HCO^+ (27.09 eV) implies ring opening by C-O bond cleavage and rotation around C_α-C_β bond (**ts1** $\rightarrow$ **ts2**). Propargyl cation, linear isomer of $H_3C_3^+$, can be obtained through 2,1 H transfer or 3,2 H transfer on the furan ring and subsequent C-O and C-C bond cleavages. The highest points of these reaction pathways are transition structures corresponding to hydrogen migration, which are equal to 28.49 eV (**ts3**) and 28.83 eV(**ts8**), respectively. Finally, production of the H_2CCHC^+ isomer is possible after 3,2 H transfer, 2,1 H transfer followed by C-O and C-C bond cleavages through an energy barrier of 28.83 eV. Hydrogen shift to the oxygen atom (**ts17** - 28.88 eV) can also lead to channel $H_3C_3^+/HCO^+$, however, it is less likely because of high energy barriers present in this mechanism. Moreover, exit channels obtained after hydrogen shift to oxygen are less stable. because produced fragment HOC^+ lies 1.60 eV higher in energy than formyl cation (HCO^+).
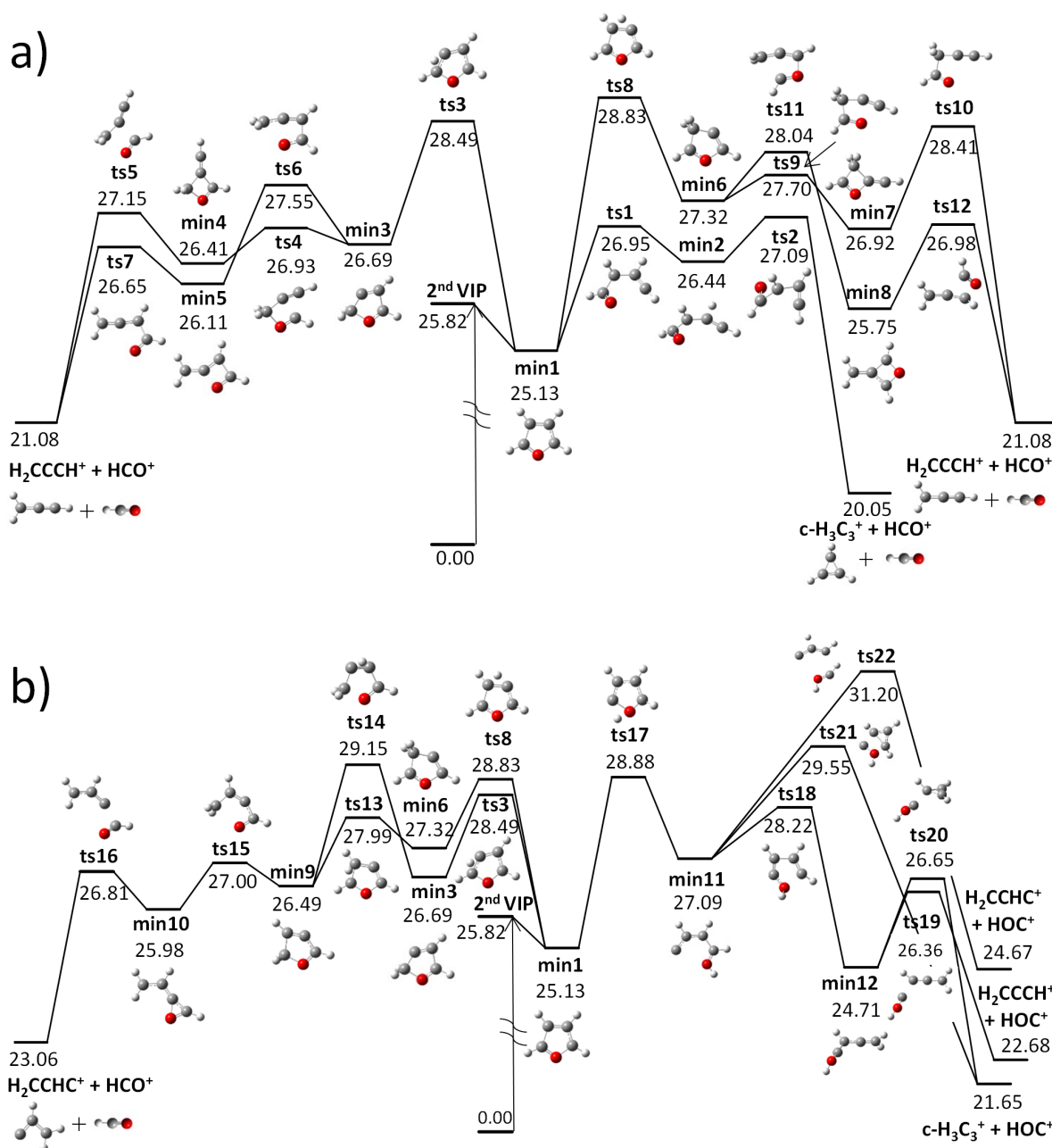
FIGURE 5.38 Potential Energy Surface for production of $H_3C_3^+$ and HCO^+ through skeleton fragmentation. Panel **a)** shows pathways producing linear and cyclic isomers of $H_3C_3^+$. Panel **b)** shows pathways producing H_2CCHC^+ isomer (left) and pathways following H migration to oxygen (right).
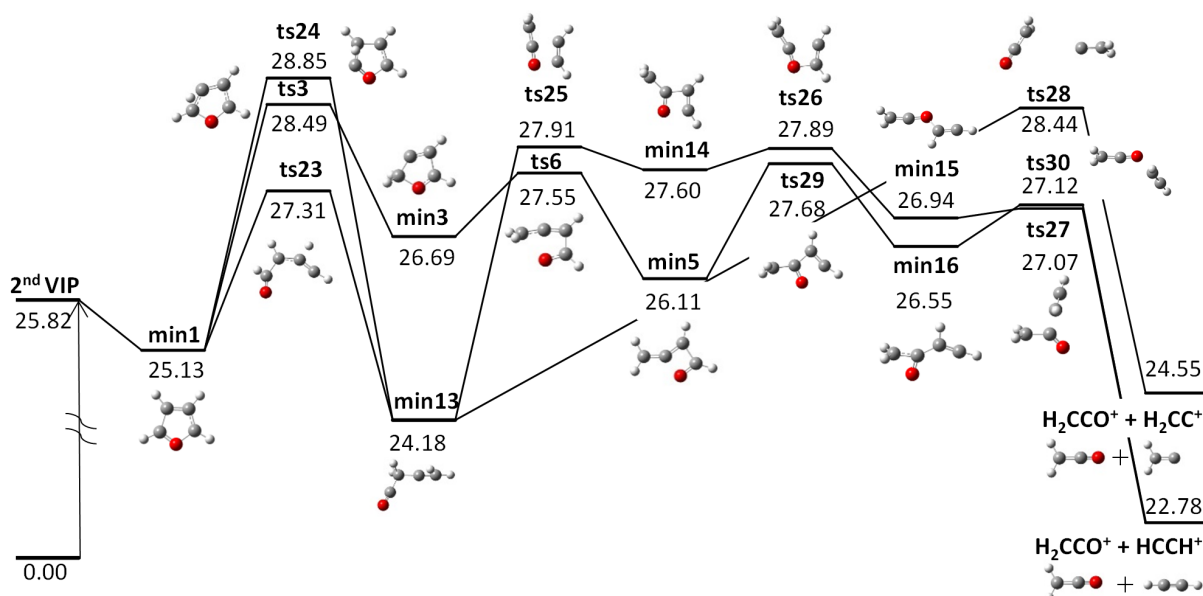
FIGURE 5.39 Potential Energy Surface for production of $H_2C_2O^+$ and $H_2C_2^+$ through skeleton fragmentation.
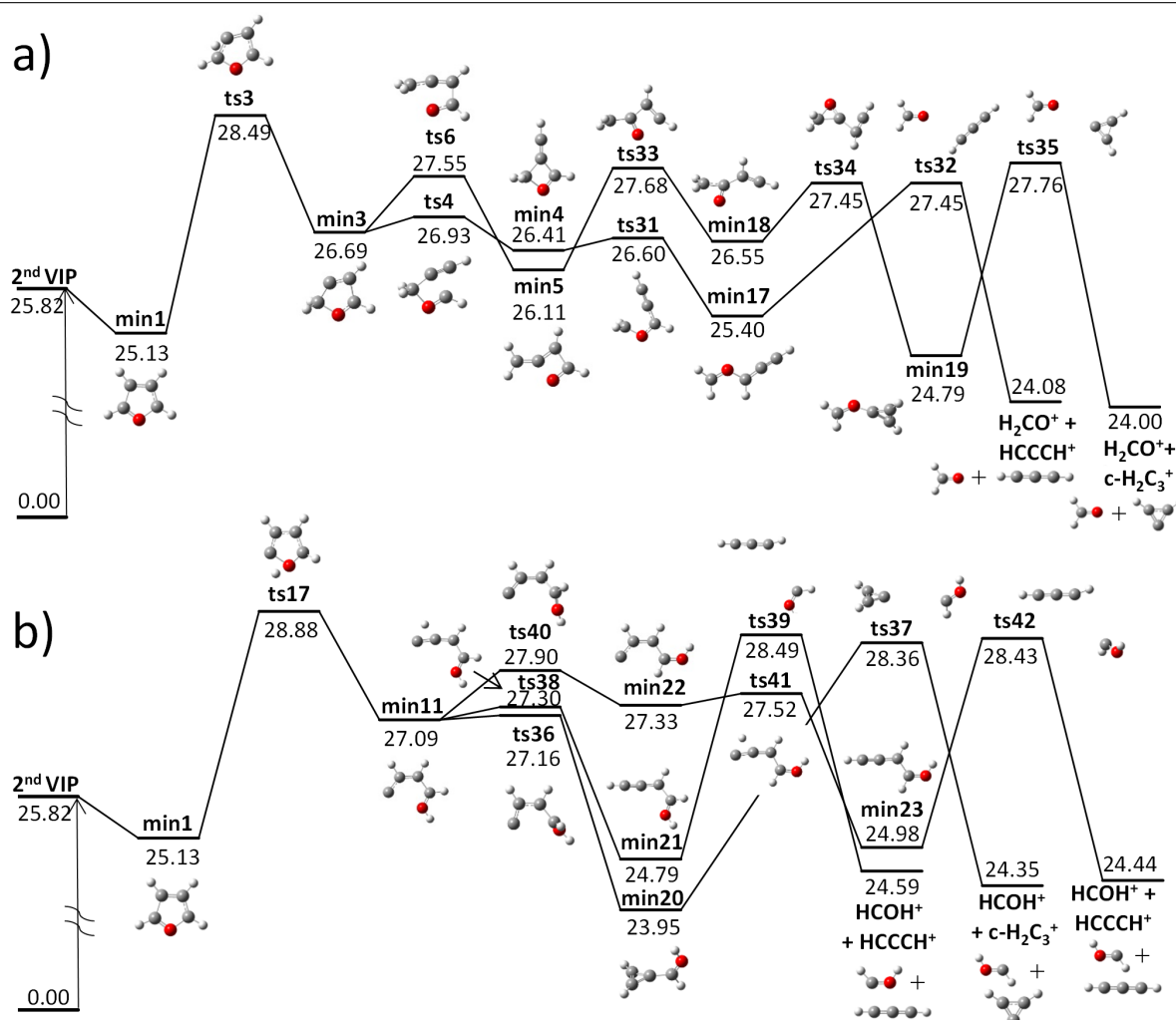
FIGURE 5.40 Potential Energy Surface for production of H_2CO^+ and $H_2C_3^+$ through skeleton fragmentation. Panel **a)** shows pathways following 2,1 H transfer. Panel **b)** shows pathways following H migration to oxygen.

Figure 5.39 exhibits mechanisms of skeleton fragmentation producing $H_2C_2O^+$ and $H_2C_2^+$. The lowest energy pathway relies on ring opening concerted with 1,2 H shift (**ts23**), C_β-C_β bond cleavage (**ts25** - highest point 27.91 eV) and temporary C-O rebonding (**ts26**). A higher energy pathway (by 0.58 eV) proceeds through 2,1 H shift, C-O bond cleavage, formation of the O-C_β bond and finally C_β-C_β bond cleavage leading to fragmentation. Lastly, exit channel producing less stable isomer of $H_2C_2^+$: H_2CC^+ is shown. This channel requires only one step from **min13** of concerted 3,4 H transfer and C_β-C_β bond cleavage to reach fragmentation (**ts28**-28.44 eV).

Potential Energy Surface of the channel producing H_2CO^+ and $H_2C_3^+$ is presented in Figure 5.40. After initial 2,1 H transfer, which is also the highest step on the PES, two pathways are possible. Starting from **min3**, the system can either proceed through C_α-C_β and C-O bond cleavage or C-O bond cleavage and formation of a structure with cyclic H_2C_3 group (**min19**). The first mechanism implies barrier of 27.76 eV (**ts35**) and leads to formation of $HCCCH^+$, whereas the highest point of second pathway is located at 27.45 eV (**ts32**) and produces c-$H_2C_3^+$. Pathway with a higher barrier (28.88 eV) corresponds to formation of H_2CO^+/$H_2C_3^+$ after H shift to oxygen presented in panel **b)**. From **min11** there are three options: (1) partial cyclization and C_α-C_β bond cleavage (**ts37** - 28.26 eV) leading to $HCOH^+$/c-$H_2C_3^+$, (2) dihedral rotation around C_α-C_β bond, 2,1 H transfer and C_α-C_β bond cleavage leading to $HCOH^+$/$HCCCH^+$ and (3) 2,1 H transfer and C_α-C_β bond cleavage also leading to $HCOH^+$/$HCCCH^+$. The energy barriers of mentioned pathways are 28.36 eV, 28.43 eV and 28.49 eV, respectively.
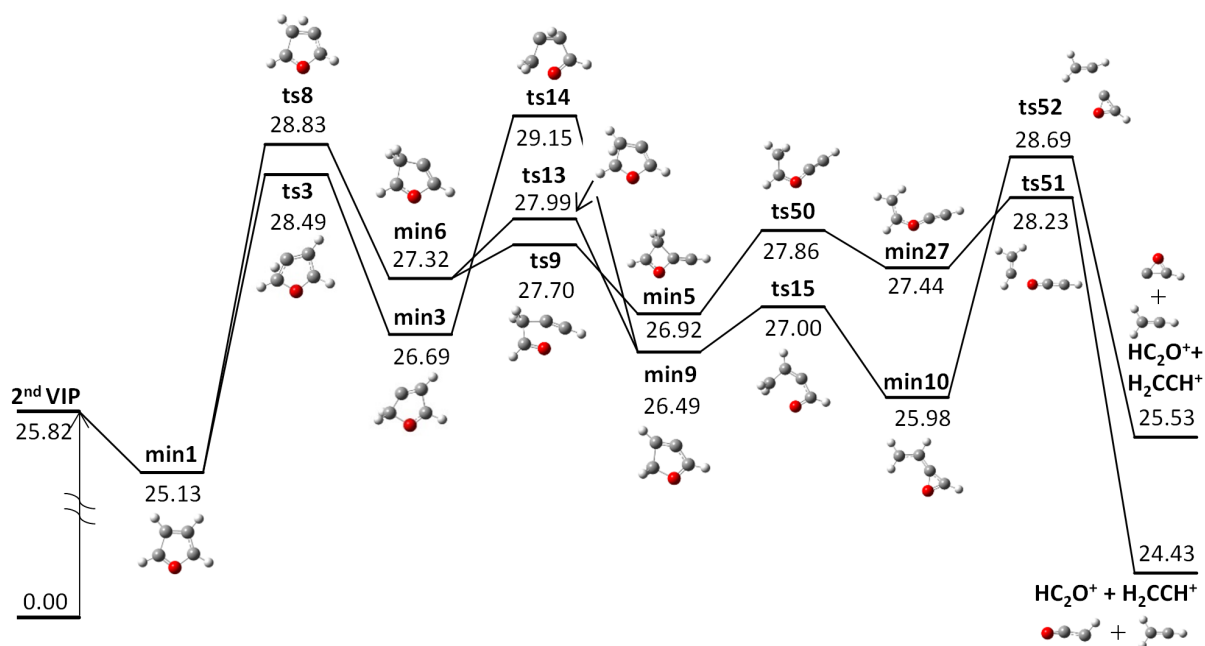
FIGURE 5.41 Potential Energy Surface for production of HC_2O^+ and $H_3C_2^+$ through skeleton fragmentation.

Fourth possibility of skeleton fragmentation is demonstrated in Figure 5.41 and shows decomposition to HC_2O^+ and $H_3C_2^+$. The most plausible fragmentation pathway follows initial 3,2 H transfer (**ts8** - 28.83 eV) by C-O bond cleavage, temporary C_α-C_β bond formation and C-O bond cleavage. This mechanism produces more stable, linear isomer of HC_2O^+. In a second mechanism, after **min6** a 2,1 H transfer and subsequent C-O and C_β-C_β bond cleavages take

place, leading to production of the cyclic isomer of HC_2O^+ that is less stable by 1.10 eV than the linear isomer of HC_2O^+.

FIGURE 5.42 Potential Energy Surface for channels $H_2C_3O^+/H_2C^+$ and $H_3C_2O^+/HC_2^+$ through skeleton fragmentation.

Last PES of skeleton fragmentation (Figure 5.42) shows production of two channels: $H_2C_3O^+/H_2C^+$ (right) and $H_3C_2O^+/HC_2^+$ (left). The lowest energy pathway leading to channel $H_2C_3O^+/H_2C^+$ relies on C_α-C_β bond cleavage of **min16** and overcoming an energy barrier of 29.38 eV. This mechanism leads also to the most stable isomer of $H_2C_3O^+$. Secondly, a higher energy barrier was found (**ts45** - 29.40 eV) for production of $H_2C_3O^+$ in a cyclic, less stable form. The only calculated pathway producing $H_3C_2O^+$ and HC_2^+ proceeds through 3,2 H transfer, concerted C_β-C_β bond cleavage and 1,2 H shift and finally C-O bond cleavage. The highest point of this pathway is located at 30.58 eV (**ts48**), making it unlikely to occur.
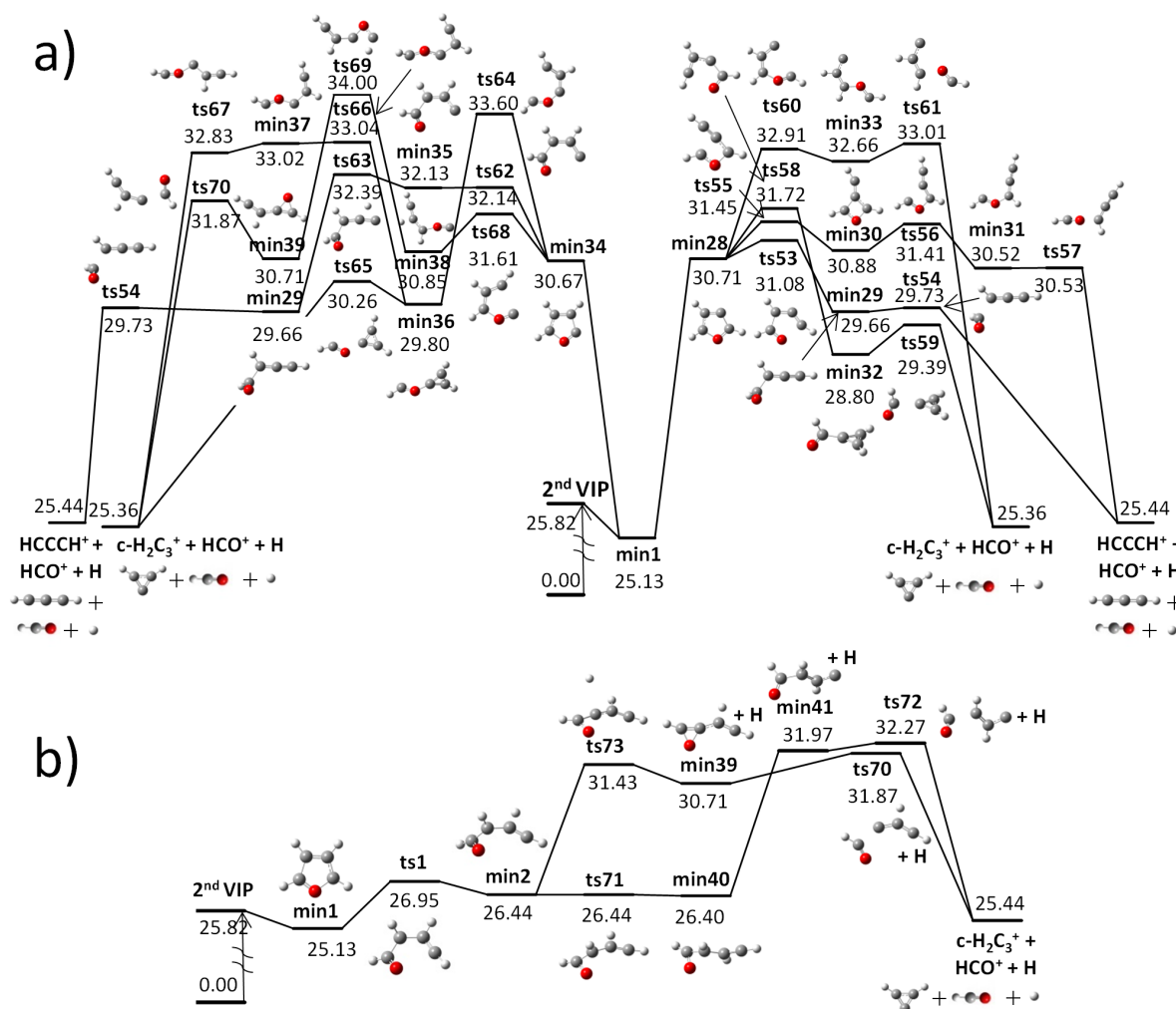
FIGURE 5.43 Potential Energy Surface for production of $H_2C_3^+$ and HCO^+ after H loss. Panel **a)** shows pathways following H loss directly from furan dication. Panel **b)** shows pathways following H loss from furan isomers (**min2** and **min40**).

Next process distinguished in the molecular dynamics simulations was H loss followed by fragmentation into two charged species. The first channel of this kind was found to produce: $H_2C_3^+$, HCO^+ and H. Panel **a)** of Figure 5.43 demonstrates eight possible fragmentation pathways after barrierless H_α (left) and H_β (right) loss. The lowest energy barrier is equal to 31.08 eV and involves H_β loss and subsequent C-O and C_α-C_β bond cleavages (**ts53** → **ts54**). Next pathway relies on H_β loss as well, however, the order is reversed because it proceeds through C_α-C_β bond cleavage as a first step followed by C-O bond fissions. Both mechanisms lead to formation of linear isomer of $H_2C_3^+$. This ion might also be produced in a cyclic form by overcoming a barrier of 31.72 eV (**ts58**). The highest energy barrier after H_β loss was calculated for fragmentation to c-$H_2C_3^+$/HCO^+/H through C_α-C_β and subsequent C-O bond cleavages (**ts61** - 33.01 eV). Although the loss of H_α leads to the remaining molecule being more stable than H_β loss does (by 0.04 eV), more energy is required to overcome barriers leading to fragmentation from this structure. The lowest energy barrier after H_α loss is already located at 32.39 eV and consists of C-O bond fission, 3,4 H transfer and C_α-C_β bond cleavage (**ts62** →

ts63 → ts54). In the panel b) of Figure 5.43, PES corresponding to H loss from isomers of furan dication is shown. It can be noticed that H_β loss from min2 proceeds through a barrier of 31.43 eV and if followed by C_α-C_β bond cleavage (ts70 - 31.87 eV) leads to production of channel c-$H_2C_3^+$/HCO^+/H. The same channel might be produced through a barrierless H_α loss from min40 and subsequent C_α-C_β bond fission. This reaction implies a barrier of 32.27 eV. In comparison with H loss directly from furan dication, H loss from isomeric structures requires more energy.
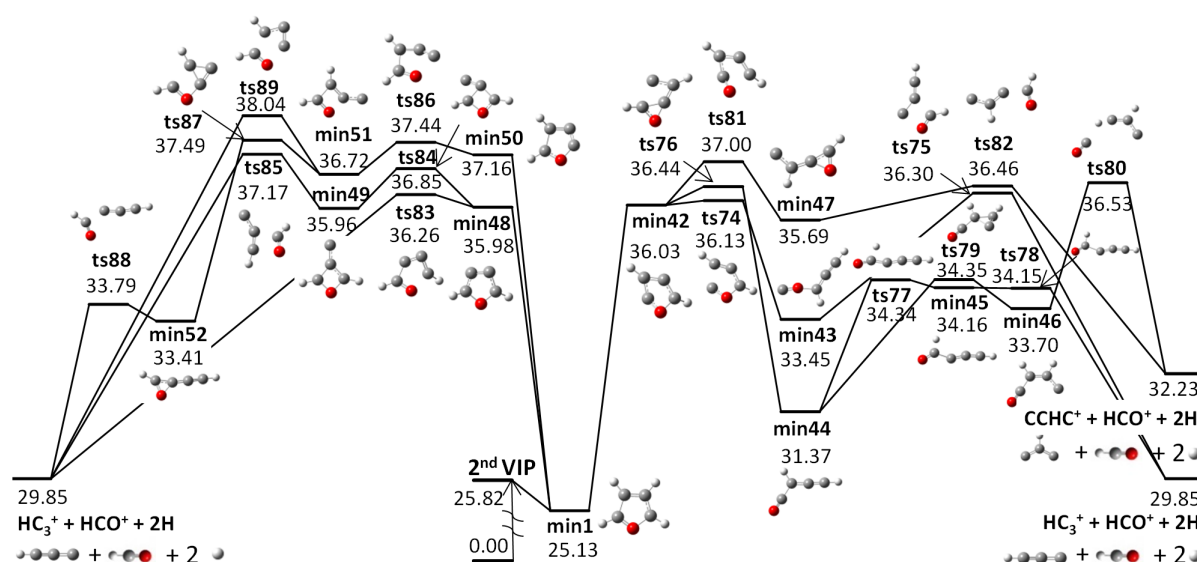
FIGURE 5.44 Potential Energy Surface for production of HC_3^+ and HCO^+ after two H loss.
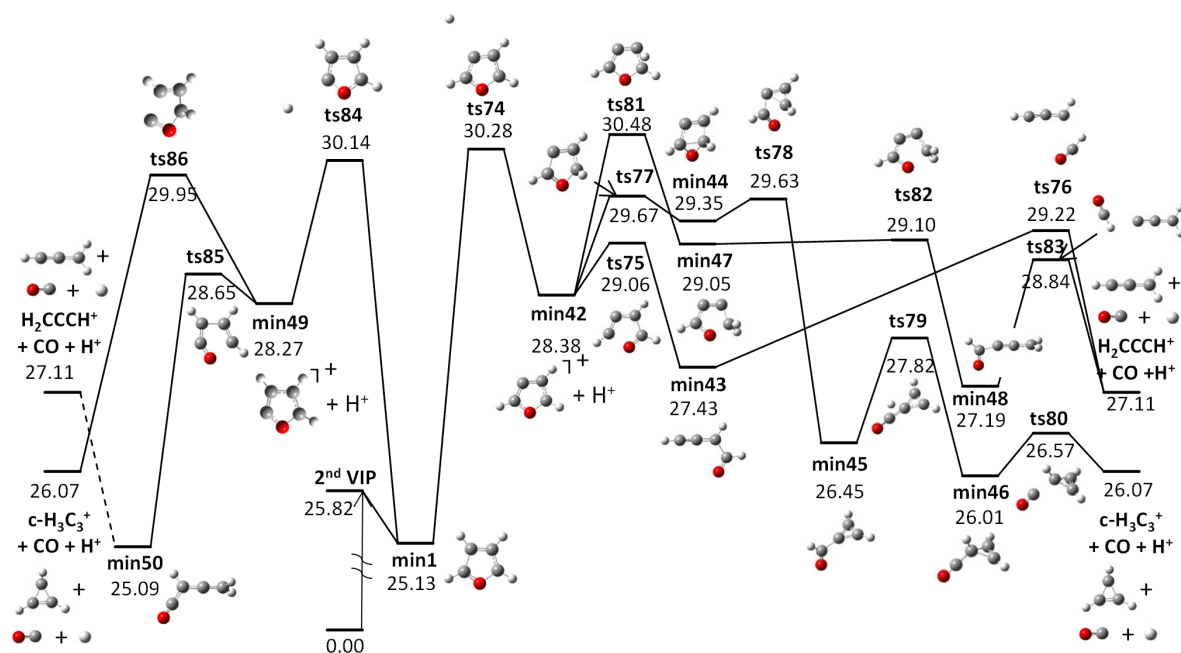
FIGURE 5.45 Potential Energy Surface for production of $H_3C_3^+$ and CO after H^+ loss directly from furan dication.

If enough energy is deposited into the system, loss of two atomic hydrogens might take place. In this respect, the MD simulations showed minor occurrence of channel producing HC_3^+, HCO^+ and 2H. Moreover, H loss proved to be the first step of the decomposition process. Figure 5.44 presents fragmentation pathways after two barrierless H losses, occurring directly from furan dication. The examined positions of hydrogens loss were: two H_β (**min48** - 35.98 eV), opposite H_α and H_β (**min42** - 36.03 eV), and adjacent H_α and H_β (**min50** - 37.16 eV). The lowest energy pathway consists of ejection of hydrogens from two β positions and one-step ring opening leading to fragmentation (**ts83** - 36.26 eV). An energy barrier higher only by 0.04 eV was calculated for an opposite H_α and H_β loss followed by C_α-C_β bond fission and ring reorganization (**ts75** - 36.30 eV). Three other pathways were obtained for **min42** decomposition, but they present higher barriers than the one mentioned before. Two of those mechanism lead to production of less stable isomer of HC_3^+ through energy barriers of 36.53 eV (**ts80**) and 37.00 eV (**ts81**). In the case of adjacent H_α and H_β loss, the multiple-step ring rupture implies the highest energy barrier of 37.49 eV (**ts87**).

A significant process observed in the MD consisted of deprotonation. When charge is localized on ejected hydrogen ion and the rest of the molecule remains singly ionized, possible skeleton fragmentation follows mechanisms described in the previous section of furan cation PES 5.2.2. However, contrary to H loss, H^+ loss is not a barrierless process. From Figure 5.45 it can be seen that loss of H_α^+ and H_β^+ exhibit barriers of 30.14 eV (**ts84**) and 30.28 eV (**ts74**), respectively. These transition structures are the highest points on the pathways leading to fragmentation, indicating that the remaining singly ionized system will easily decompose to channel $H_3C_3^+/H^+/CO$.
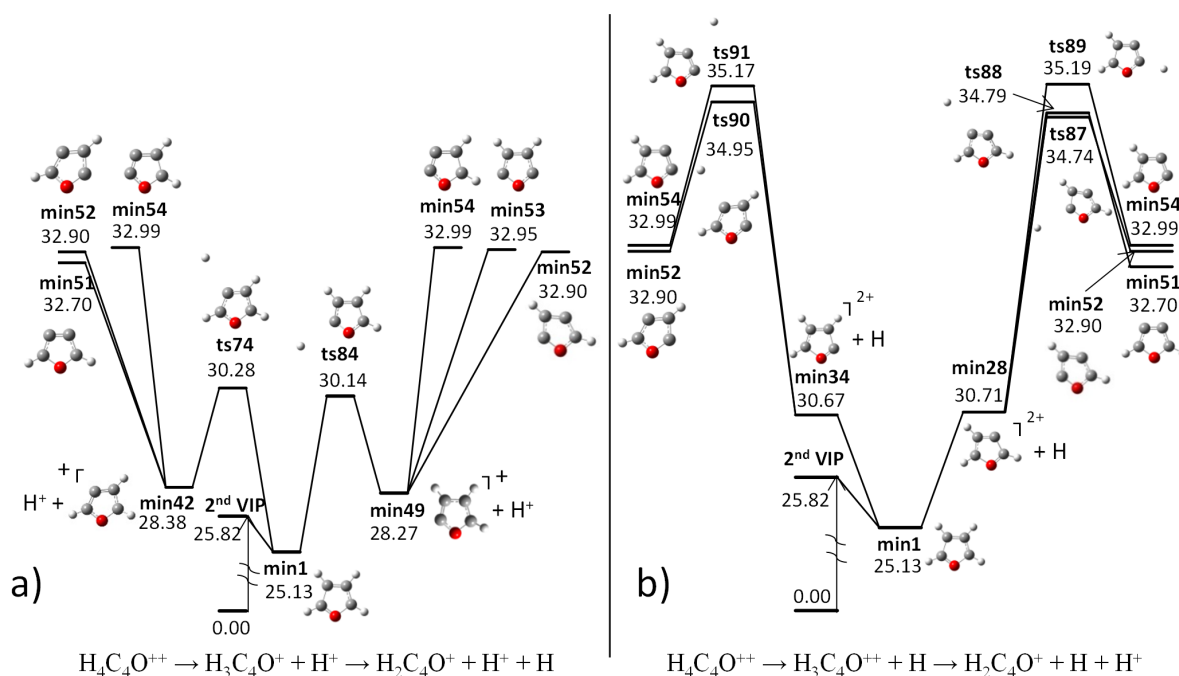
FIGURE 5.46 Potential Energy Surface for H^+ and H loss. Panel **a)** shows pathways of H^+ loss followed by the loss of H. Panel **b)** shows pathways of H loss followed by the loss of H^+.

Sequential loss of H and H^+ was also observed in the dynamical simulations. As charge distribution is only established at the end of the calculation, there is no way of concluding whether H or H^+ has been ejected first. However, optimization of critical structures can provide information about the preferable order of the H/H^+ loss. Energy profiles of this process have been investigated and are presented in Figure 5.46. It can be noticed that reaching exit channel $H_2C_4O^+/H^+/H$ requires around 33 eV of energy in the case of $H^+ \rightarrow H$ loss and more than 35 eV in the case of $H \rightarrow H^+$ loss.
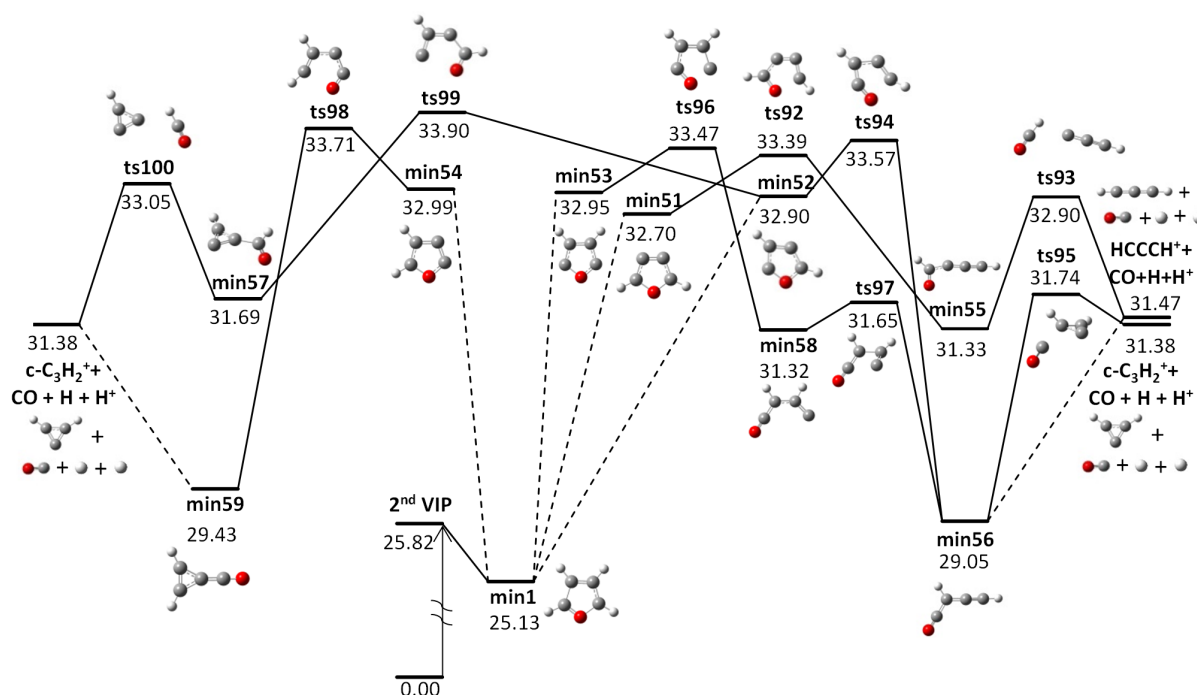
FIGURE 5.47 Potential Energy Surface for production of $H_2C_3^+$ and CO after sequential H^+ and H loss.

Finally, the process of consecutive H and H^+ loss can be followed by fragmentation. Again, decomposition of singly ionized $H_2C_4O^+$ has been previously explored in section 5.2.2. As presented in Figure 5.47, the lowest energy pathway proceeds through a barrier of 33.39 eV and consists of $H_\beta \rightarrow H_\beta^+$ loss from the furan dication ring and C-O and C_α-C_β bond cleavages.

In summary, altogether 66 fragmentation pathways have been studied. Table 5.6 summarizes the highest points on the lowest energy pathways associated with activation energy producing specific exit channels. In order to maintain the information about the width of the barriers, the table includes also the number of transition states comprising the reaction pathway.

TABLE 5.6 Summary of the exploration of the Potential Energy Surface of furan dication.

Exit Channel	Lowest energy barrier [eV]	Corresponding TS	Number of TS	Exit energy [eV]
$HCO^+/H_3C_3^+$	27.09	**ts2**	2	20.05 (c-$H_3C_3^+$)
	28.49	**ts3**	3	21.08 (l-$H_3C_3^+$)
$H_2C_2O^+/H_2C_2^+$	27.91	**ts25**	4	22.78
$H_2CO^+/H_2C_3^+$	28.49	**ts3**	4	24.00 (c-$H_2C_3^+$)
			5	24.08 (l-$H_2C_3^+$)
$HC_2O^+/H_3C_2^+$	28.83	**ts8**	4	24.43
$H_2C_3O^+/H_2C^+$	29.38	**ts47**	4	25.09
$H_3C_2O^+/HC_2^+$	30.58	**ts48**	3	25.92
$HCO^+/H_2C_3^+/H$	31.08	**ts53**	2	25.44 (l-$H_2C_3^+$)
	31.72	**ts58**	2	25.36 (c-$H_2C_3^+$)
$HCO^+/HC_3^+/2H$	36.13	**ts74**	3	29.85
$H_3C_3^+/H^+/CO$	30.14	**ts84**	2	26.07 (c-HC_3^+)
			2	27.11 (l-HC_3^+)
$H_2C_3^+/H^+/CO/H$	33.39	**ts92**	2	31.47 (l-$H_2C_3^+$)
	33.39	**ts96**	3	31.38 (c-$H_2C_3^+$)

5.3.3 Comparison with ion collision experiment

Coincidence time-of-flight (TOF) mass spectrometry has been employed to study the interaction of 46 keV O^{6+} ions with neutral furan. The experiment has been performed at ARIBE, the low-energy ion beam facility of GANIL in Caen, France. Detailed description of the experimental setup can be found in [100]. In this experiment, mechanism of the double ionization of the target relies on the capture of two valence electrons in a single ion-molecule collision. Subsequently, excess energy deposited into the system induces unimolecular decomposition. Figures 5.48-5.50 depict 2D histograms of the recorded ion pairs, in which the flight time of the slower ion (TOF 2) is plotted as a function of the flight time of the faster ion (TOF 1). After false coincidences (giving $m_1/q_1 + m_2/q_2 > 68$) subtracted out, the experiment recorded over 45000 events altogether. Quantum chemistry calculations, such as AIMD and exploration of PES, can help to elucidate evolution of the system upon collision, as well as suggest transient steps of reaching final fragmentation products.

Geometrical parameters of the measured correlation islands, such as shape, size and orientation, can be indicative of the mechanism of a specific dissociation channel. The dynamics of the fragmentation reactions have been discussed in [101] by means of the laws of energy and momentum conservation. Slopes of the correlation islands point out to the momenta of measured fragments and, hence, can provide information on the sequence of events. Firstly, two-body fragmentation produces an island of a narrow bar shape and slope of -1. Among the three-body fragmentation channels, producing two charged (A^+ and B^+, where $m_A < m_B$) and one neutral fragment (C), three processes can be differentiated:

deferred charge separation corresponding to reaction

$$ABC^{2+} \longrightarrow AB^{2+} + C \longrightarrow A^+ + B^+ + C$$
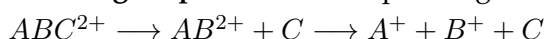
consists of ejection of neutral species from the parent ion followed by fragmentation of doubly ionized intermediate. The peak shape of this mechanism is a lozenge of slope -1. The peak's ends present a slope of m_B/m_A caused by a random momentum component associated with rotation of AB^{2+} to a random angle following ejection of C, but ahead of fragmentation. Additional evidence of this mechanism is the observation of an AB^{2+} peak in the mass spectrum.

secondary decay of primary fragments corresponding to reaction

$$ABC^{2+} \longrightarrow AC^+ + B^+ \longrightarrow A^+ + C + B^+$$
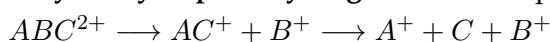
implies charge separation first and subsequent decay of the singly ionized species, taking place outside of the Coulomb zone. The resulting peak shape is a bar of slope $-(m_A + m_C)/m_A$ with horizontal ends. In this case, the deviation from -1 slope is associated with fragment C carrying some of the initial momentum of the intermediate AC^+. Hence, the width of the bar points out to the energy release in the secondary decay.

fast concerted dissociation corresponding to reaction

$$ABC^{2+} \longrightarrow A^+ + B^+ + C$$

results in a complex peaks shape. This mechanism relies on the simultaneous three-body dissociation, where, if present, an intermediate has no time to rotate ahead of fragmentation. The shape of the coincidence island can indicate the angle of ejection of fragment C relative to the line connecting A^+ and B^+. If this emission is close to perpendicular, an ovoid shape can be observed. Conversely, loss of C in a parallel direction produces a fan-shaped peak. In the case of concerted processes the peak slope are impossible to interpret due to variety of possible combinations of vector magnitude and orientation.

From the ion-ion TOF plot presented in Figure 5.48 four of the most significant correlation islands are identified. Each pattern has been assigned to a specific charged fragments pair and its measured relative intensity (RI) has been compared with calculated relative energy of the lowest-energy pathways in Table 5.7. With 17.06% of all counts, the major correlation island is clearly ion pair **29$^+$/39$^+$**, corresponding to HCO$^+$/H$_3$C$_3^+$ channel of skeleton fragmentation. As concluded from the MD simulations, this channel dominates in the range of internal energy between 5 and 13 eV. Moreover, exploration of the PES indicated that production of ions HCO$^+$ and H$_3$C$_3^+$ proceeds through the lowest energy barrier for furan dication decomposition. Both observations prompted a conclusion that fragmentation of furan dication induced by collisions with ions is dominated by the ring breakup. Furthermore, the experimental results point out to another, minor channel of two-body decomposition, ion pair **26$^+$/42$^+$**, corresponding to fragments H$_2$C$_2^+$/H$_2$C$_2$O$^+$. The activation barrier for this process equals to 27.91 eV, which is only 0.82 eV higher than the barrier for channel HCO$^+$/H$_3$C$_3^+$. However, such low intensity of island **26$^+$/42$^+$** can be explained by the multiple steps of isomerization required ahead of the fragmentation. Supporting of this conclusion are also results of the MD calculations, in which only 21 out of all 3900 trajectories finished in fragmentation to channel H$_2$C$_2^+$/H$_2$C$_2$O$^+$.
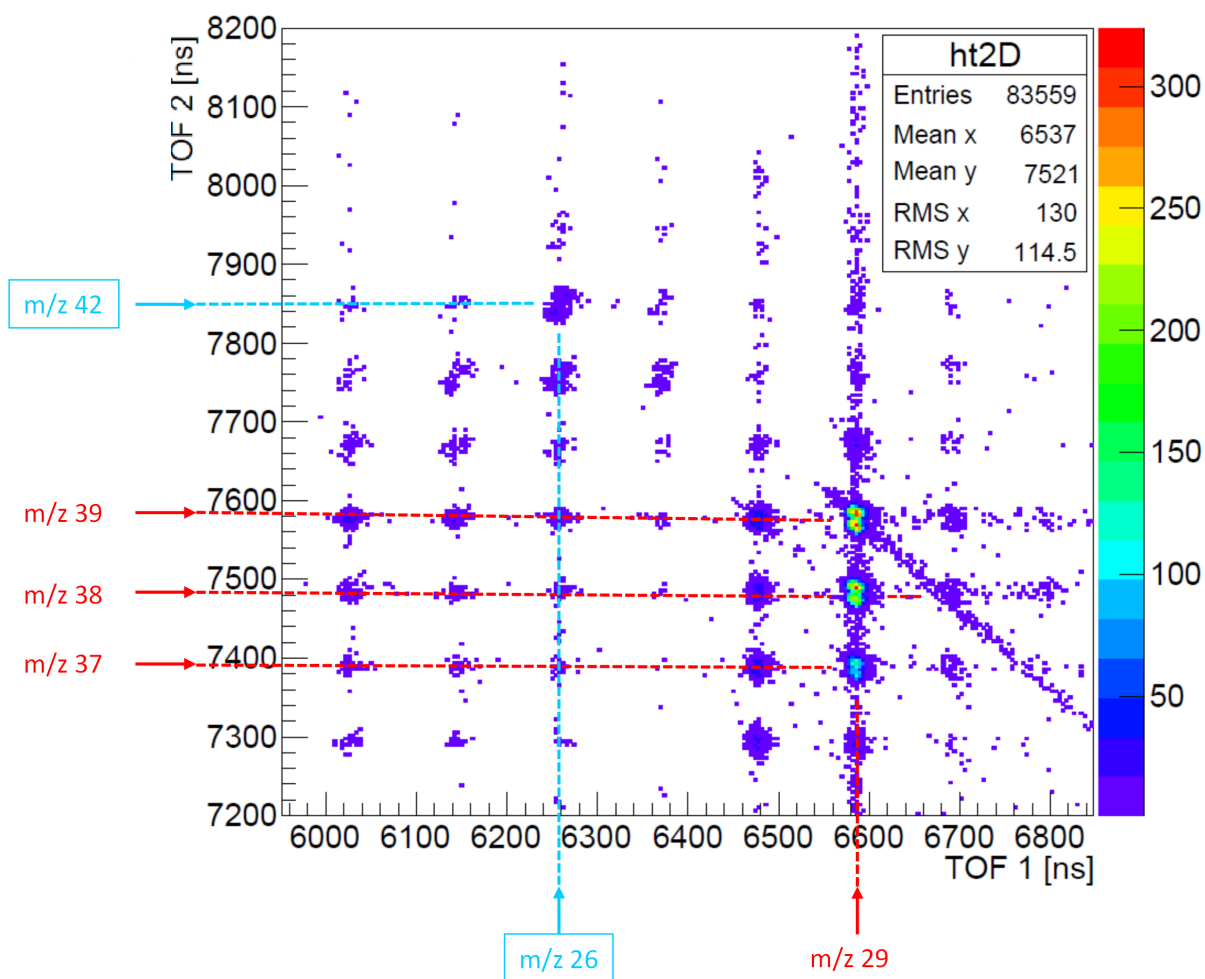
FIGURE 5.48 Coincidence map for the fragmentation of furan in collision with 46 keV O^{6+} ions. The most abundant coincidence islands are assigned to respective ion masses according to the formula: $TOF \propto \sqrt{\frac{m}{q}}$.

TABLE 5.7 Major coincidence islands are identified, assigned to respective fragmentation channels and compared with calculated energy barriers. Relative Intensities indicates total number of events in a square of side 1 amu centered on the respective TOF values, relative to all measured events and given in %.

Exit Channel	Ion pair m/z	Relative Intensity [%]	Lowest energy barrier [eV]	Corresponding TS
$HCO^+/H_3C_3^+$	$29^+/39^+$	17.06	27.09	ts2
$H_2C_2^+/H_2C_2O^+$	$26^+/42^+$	0.98	27.91	ts25
$HCO^+/H_2C_3^+/H$	$29^+/38^+$	14.60	31.08	ts53
$HCO^+/HC_3^+/2H$	$29^+/37^+$	6.17	36.13	ts74
$H_3C_3^+/H^+/CO$	$1^+/39^+$	1.01	30.14	ts84
$H_2C_3^+/H^+/CO/H$	$1^+/38^+$	0.61	33.39	ts92

Islands of the second and the third highest intensities are related to loss of neutral hydrogen, either single: ion pair $\mathbf{29^+/38^+}$ or double: ion pair $\mathbf{29^+/37^+}$. These channels have also been identified by the MD simulations as following in frequency after channel $\mathrm{HCO^+/H_3C_3^+}$ for the middle energies considered. Total measured RI of ion pair $\mathbf{29^+/38^+}$ is high and equals to 14.60%. The MD simulations indicated that the loss of hydrogen mostly takes place directly from parent ion and charge separation follows. This conclusion can be verified by the consideration of island $\mathbf{29^+/38^+}$, which, indeed shows the slope of -1. Total RI of measured coincidence island $\mathbf{29^+/37^+}$ is 6.17%. The dynamical simulations pointed out to the prevalence of double hydrogen atom loss rather than loss of hydrogen molecule. Moreover, it was found that this process occurs sequentially, directly from $\mathrm{H_4C_4O^{2+}}$.
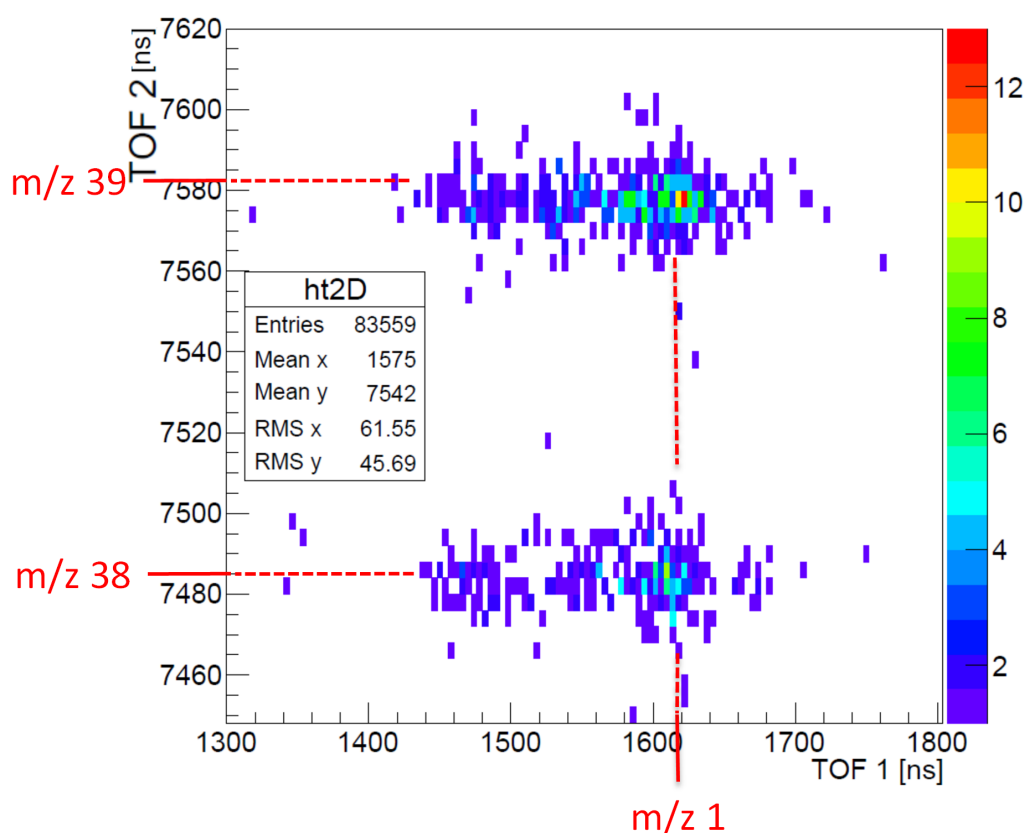
FIGURE 5.49 Zoom on the coincidence map for fragmentation of furan in collision with 46 keV $\mathrm{O^{6+}}$ ions involving correlation islands of deprotonation.

Channels of deprotonation have also been recorded. Figure 5.49 shows two patterns of fragments measured in coincidence with $\mathrm{H^+}$: correlation island $\mathbf{1^+/39^+}$ (corresponding to $\mathrm{H^+/H_3C_3^+}$) and $\mathbf{1^+/38^+}$ ($\mathrm{H^+/H_2C_3^+}$). Relative Intensities of these ion pars are 1.01% and 0.61%, respectively, which are low but not negligible. The possible explanation of such low abundance of this process in the measured spectrum is the soft character of collisions with $\mathrm{O^{6+}}$ ions. Indeed, the MD simulations showed that deprotonation briefly dominates over other mechanisms in the high energy region of 22 eV ($\mathrm{H_3C_3^+/H^+/CO}$) and also 30 eV ($\mathrm{H_2C_3^+/H^+/CO/H}$).
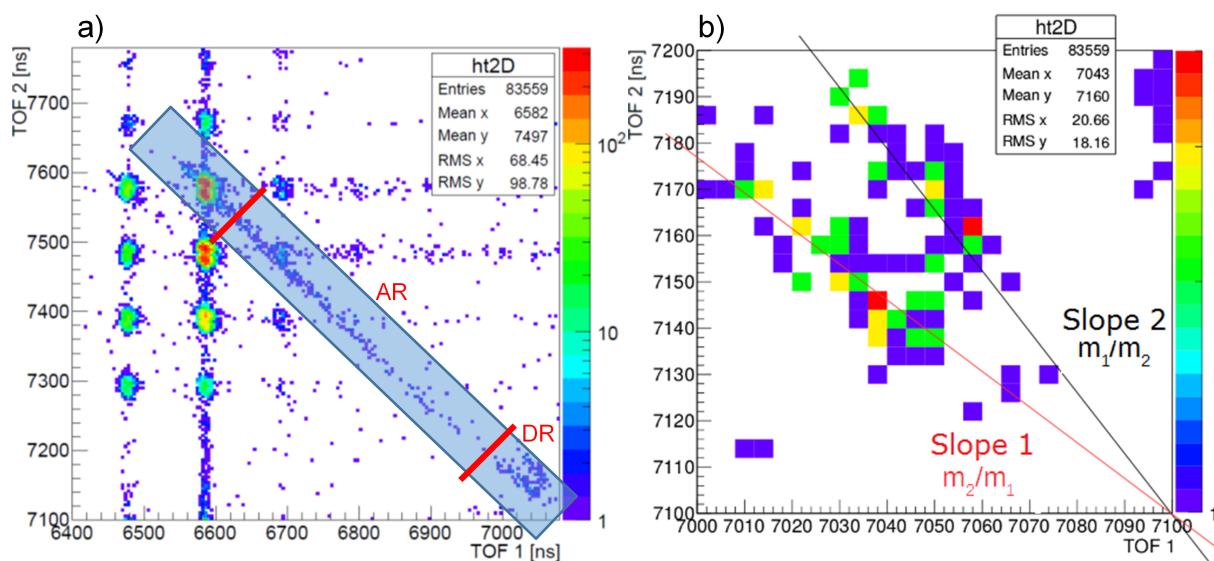
FIGURE 5.50 Coincidence map for fragmentation of furan in collision with 46 keV O^{6+} ions.

Finally, a long tail starting from the TOF values of ion pair **29^+/39^+** and extending to the TOF values of the parent dication has been measured (highlighted by a blue box in Figure 5.50). This feature indicates slow charge separation associated with the production of metastable $H_4C_4O^{2+}$. Indeed, PES of channel HCO^+/$H_3C_3^+$ demonstrates two transition structures and one minimum ahead of fragmentation, which correspond to ring breakup by rotation around C_α-C_β bond. Previous studies of lifetimes of metastable molecular doubly charged ions have been performed by Field and Eland [102]. In their work they provide a way of predicting mean lifetimes of metastable structures from the experimental mass spectra. However, more recently, the production of the metastable CO_2^{2+} has been investigated by Alagia *et al* [103]. Therein, it has been concluded that the mean lifetimes derived from obtained measurements are significantly influenced by the time observation window specific to each experiment and, hence, do not provide universal values.

The two areas of the metastable tail: "AR" and "DR" in Figure 5.50 **a)** point out to the delayed decay of the doubly charged ion taking place in different regions of the experimental setup. If the precursor dication undergoes fragmentation outside of the interaction volume, in the acceleration region, the measured TOFs fall into the area marked as "AR". The characteristic V shaped area "DR" comes from dissociation events occurring in the field-free drift region. Two arms of this shape should present slopes m_A/m_B and m_B/m_A, which correspond to 0.74 and 1.35 for the ion pair **29^+/39^+**, respectively. Their lengths are associated with the kinetic energy release of the dissociation. Measured slopes are equal to 0.76 and 1.29, indicating that indeed metastable $H_4C_4O^{2+}$ produces the ion pair **29^+/39^+**.

In conclusion, the complementary approach of two theoretical methods proved effective in the interpretation of the mechanism of the interaction of O^{6+} ions with the neutral furan. Direct ring fission, H and H^+ loss and deferred fragmentation have been experimentally observed and were supported by the theoretical results.

Chapter 6

Summary and perspective

The approach presented in this thesis combined three theoretical methodologies, allowing for a complete overview of the fragmentation process. Firstly, I performed molecular dynamics calculations, which provided details on the evolution of the system after deposition of various amounts energy. Consequently, a statistical analysis of the occurring mechanisms indicated the most prominent channels of fragmentation as a function of the internal energy. Secondly, I explored the potential energy surface considering the fragmentation mechanism and energetic dependence of the probable reaction pathways in a static manner. Finally, I employed a new statistical method based on the maximum entropy assumption, which provided breakdown curves with a substantially lower computational cost compared to the molecular dynamics simulations.

Although MD is the most computationally expensive approach, it complements the investigation of fragmentation processes with intermediate steps that might be difficult to determine only based on the chemical intuition. Another advantage of performing the MD simulations is the possibility of systematic investigation in a wide energy range. The same benefit characterizes the M_3C method, with the additional advantage of a lower computational cost. Moreover, *ab initio* MD calculations are limited by the choice of the total simulation time. Instead, the ergodic hypothesis of the statistical M_3C method replaces the consideration of time with the consideration of space and, consequently, provides the results as if the system had infinite time to evolve.

A drawback of the M_3C approach remains in the approximation of sudden fragmentation and disregard of the transition states constituting a reaction pathway. In my thesis the solution to this problem relied on a manual introduction of energy barriers previously determined by quantum chemistry calculations, a step that was rather time consuming. Alternatively, further developments of the M_3C program should focus on the search for less demanding procedures. Moreover, future M_3C applications will extend to multiply charged molecules, in which Coulomb explosion processes compete with mechanisms of decomposition to one, multiply charged and few neutral fragments. In such case energy barriers may play an even more significant role in the mechanism of fragmentation. As the main goal of the M_3C method is providing a general tool that can be applicable to a wide range of systems, additional improvements are necessary and I plan to continue with efforts in this direction.

As for the obtained results, I focused on the investigation of the fragmentation mechanism of the furan molecule in three charge states. It has been shown that preceding ionization of the molecule leads to divergent fragmentation patterns. Apart from evident production of ionized

species, the most prevalent products differed in composition. Dynamics of the fragmentation of the neutral furan is dominated by channels HCCH + H_2CCO and CO + H_2CCCH$_2$ for lower energies and by H_2 + CO + HCCCH for higher energies. On the other hand, the most abundant channels in the case of singly ionized furan were c-H$_3$C$_3^+$ + HCO for lower energies and c-H$_3$C$_3^+$ + CO + H and HCCCH$^+$ + CO + 2H for higher energies. Similarly to the furan cation, furan dication fragments to c-H$_3$C$_3^+$ + HCO$^+$ and c-H$_3$C$_3^+$ + CO + H$^+$ with the highest probability. The frequency of trajectories finishing with an isomer of furan decreased when the molecule is ionized. All three cases of charge states showed that at low energies, if at all, isomerization takes place late in the dynamics. Hence, provided longer simulation times the system could potentially undergo fragmentation. The mechanism of skeleton fragmentation differs with ionization as well. Decomposition in the neutral case requires prior hydrogen transfer. Fragmentation of singly ionized furan relies only on the ring cleavage and formation of a metastable complex. Then again, skeleton fragmentation of furan dication proceeds through C-O bond scission and rotation around C$_\alpha$-C$_\beta$ bond. Finally, H and H_2 loss processes were extensively studied due to their abundant occurrence at higher energies.

Theoretical predictions presented in my dissertation were compared with previously published studies, as well as with results of recently performed experiments. Consequently, novel theoretical methodology could be verified and employed to support the interpretation of the measured data. Investigation of the neutral furan decomposition showed channels and mechanisms of skeleton fragmentation in accordance with previous works. A new insight relied on demonstration of multifragmentation processes. As for the furan cation, a direct comparison between theory and experiment was possible owing to the new PEPICO measurements. I concluded that theoretical breakdown curves mostly maintain the shape of experimental curves. Moreover, analogies between measured Appearance Energies and calculated energy barriers for certain pathways confirmed the most likely mechanisms of decomposition. Another important outcome of my work relied on the determination of the energy transfer function based on the comparison between reproduced theoretical and measured mass spectra. Finally, coincidence measurements of ionic fragments produced by ion-furan collisions allowed for qualitative comparison and first elucidation of the furan dication decomposition mechanism. Moreover, an explanation for the observation of the metastable furan dication, with a lifetime larger than the time needed by the molecule to reach the detector, was proposed.

As a way of complementing the present work, further studies on the furan fragmentation processes could deal with the excited state behaviour and non-adiabatic effects - essential aspects of electron transfer processes, heterolytic dissociation and many recombination reactions [104]. Such features as the excited state lifetime and deactivating pathways may differ significantly from the properties of thermally activated systems. Therefore, a detailed analysis of the excited state dynamics with methods like Time-dependent Density Functional Theory [105] or trajectory surface hopping [106] might provide some valuable, new information. Moreover, several recent studies [107], [108] focused on the fragmentation of fullerenes and Polycyclic Aromatic Hydrocarbons induced by low energy collisions with heavy particles and displayed

evidence of non-statistical fragmentation. In this mechanism, the excess energy is not redistributed over internal degrees of freedom, but rather single atoms are knocked out few femtoseconds after the collision. Such processes have not been investigated in the present work, however, due to significantly smaller size of the target molecule, non-statistical fragmentation is expected to play a minor role in the decomposition of furan.

Appendix A

M$_3$C fragments database

This appendix presents the collection of possible fragments, which were taken as the input database for the M$_3$C calculations of furan. Molecules are sorted by the increasing number of atoms. The .rxyz files containing the electronic energy, geometry in an xyz format, vibrational frequencies, symmetry of the wave function and molecular symmetry of every molecule presented here are available at an open-access repository [109]. The naming of the molecules corresponds to the following scheme: <stoichiometry>.q<charge>.m<multiplicity>-<id>.

H	
1	2
H.q0.m2-2	H.q1.m1-1
2-S (SO3)	1-S (SO3)

C			
1	2	3	4
C.q0.m1-2	C.q0.m3-1	C.q1.m2-2	C.q1.m4-1
1-D (SO3)	3-P (SO3)	2-P (SO3)	4-P (SO3)

O			
1	2	3	4
O.q0.m1-2	O.q0.m3-1	O.q1.m2-2	O.q1.m4-1
1-D (SO3)	3-P (SO3)	2-D (SO3)	4-S (SO3)

H₂	
1 H2.q0.m1-2 1-SGG (D*H)	2 H2.q1.m2-1 2-SGG (D*H)

HC			
1 HC.q0.m2-1 2-PI (C*V)	2 HC.q0.m4-24 4-SG (C*V)	3 HC.q1.m1-1 1-SG (C*V)	4 HC.q1.m3-1 3-PI (C*V)
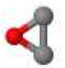
HO		
1 HO.q0.m2-2 2-PI (C*V)	2 HO.q1.m1-1 1-SG (C*V)	3 HO.q1.m3-1 3-SG (C*V)

C₂			
1 C2.q0.m1-3 1-SGG (D*H)	2 C2.q0.m3-2 3-PIU (D*H)	3 C2.q1.m2-4 2-PIU (D*H)	4 C2.q1.m4-1 4-SGG (D*H)

CO			
1 CO.q0.m1-2 1-SG (C*V)	2 CO.q0.m3-2 3-PI (C*V)	3 CO.q1.m2-3 2-SG (C*V)	4 CO.q1.m4-8 4-PI (C*V)

H$_3$
1
H3.q1.m1-7
1-A1 (C2V)

H$_2$C				
1	2	3	4	5
H2C.q0.m1-1	H2C.q0.m3-7	H2C.q0.m3-9	H2C.q1.m2-18	H2C.q1.m4-1
1-A1 (C2V)	3-B1 (C2V)	3-A2 (C2V)	2-A1 (C2V)	4-A2 (C2V)

H$_2$O		
1	2	3
H2O.q0.m1-2	H2O.q1.m2-5	H2O.q1.m2-6
1-A1 (C2V)	2-B1 (C2V)	2-B1 (C2V)

HC$_2$				
1	2	3	4	5
HC2.q0.m2-1	HC2.q0.m2-3	HC2.q0.m4-1	HC2.q1.m1-2	HC2.q1.m3-1
2-SG (C*V)	2-A1 (C2V)	4-A" (CS)	1-A' (CS)	3-PI (C*V)

HCO					
1	2	3	4	5	6
HCO.q0.m2-2	HCO.q0.m2-7	HCO.q0.m4-12	HCO.q1.m1-1	HCO.q1.m1-2	HCO.q1.m3-2
2-A' (CS)	2-A' (CS)	4-A" (CS)	1-SG (C*V)	1-SG (C*V)	3-A' (CS)
7					
HCO.q1.m3-3					
3-A' (CS)					

C₃

1	2	3	4	5	6
C3.q0.m1-1	C3.q0.m3-1	C3.q0.m3-3	C3.q1.m2-1	C3.q1.m2-2	C3.q1.m4-3
1-SGG (D*H)	3-A1′ (D3H)	3-PIG (D*H)	2-B2 (C2V)	2-A′ (CS)	4-PIU (D*H)

7
C3.q1.m4-4
4-A1′ (D3H)

C₂O

1	2	3	4	5
C2O.q0.m1-2	C2O.q0.m1-3	C2O.q0.m3-2	C2O.q1.m2-1	C2O.q1.m4-2
1-SG (C*V)	1-A1 (C2V)	3-SG (C*V)	2-PI (C*V)	4-SG (C*V)

H₃C

1	2	3
H3C.q0.m2-1	H3C.q1.m1-1	H3C.q1.m3-1
2-A2″ (D3H)	1-A1′ (D3H)	3-A″ (CS)

H₂C₂

1	2	3	4	5	6
H2C2.q0.m1-2	H2C2.q0.m1-3	H2C2.q0.m3-1	H2C2.q0.m3-2	H2C2.q0.m3-4	H2C2.q1.m2-1
1-SG (C*V)	1-A1 (C2V)	3-B2 (C2V)	3-AU (C2H)	3-B2 (C2V)	2-PIU (D*H)
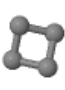
7	8	9	10
H2C2.q1.m2-2	H2C2.q1.m4-2	H2C2.q1.m4-3	H2C2.q1.m4-4
2-A′ (CS)	4-BG (C2H)	4-A2 (C2V)	4-A2 (C2V)

H₂CO					
1 H2CO.q0.m1-1 1-A1 (C2V)	2 H2CO.q0.m1-3 1-A1 (C2V)	3 H2CO.q0.m1-4 1-A′ (CS)	4 H2CO.q0.m3-4 3-A″ (CS)	5 H2CO.q1.m2-3 2-A′ (CS)	6 H2CO.q1.m2-5 2-B2 (C2V)
7 H2CO.q1.m4-1 4-A″ (CS)	8 H2CO.q1.m4-3 4-A (C1)				

HC₃					
1 HC3.q0.m2-1 2-A′ (CS)	2 HC3.q0.m2-2 2-B2 (C2V)	3 HC3.q0.m4-16 4-SG (C*V)	4 HC3.q0.m4-18 4-A″ (CS)	5 HC3.q1.m1-1 1-A1 (C2V)	6 HC3.q1.m1-2 1-A1 (C2V)
7 HC3.q1.m1-3 1-SG (C*V)	8 HC3.q1.m3-1 3-PI (C*V)	9 HC3.q1.m3-2 3-B2 (C2V)			

HC₂O					
1 HC2O.q0.m2-2 2-A″ (CS)	2 HC2O.q0.m2-5 2-A″ (CS)	3 HC2O.q0.m4-6 4-A″ (CS)	4 HC2O.q0.m4-8 4-A (C1)	5 HC2O.q0.m4-13 4-A″ (CS)	6 HC2O.q0.m4-14 4-A″ (CS)
7 HC2O.q0.m4-16 4-A″ (CS)	8 HC2O.q1.m1-1 1-A′ (CS)	9 HC2O.q1.m1-2 1-A′ (CS)	10 HC2O.q1.m1-3 1-A′ (CS)	11 HC2O.q1.m1-4 1-A (C1)	12 HC2O.q1.m1-5 1-A′ (CS)
13 HC2O.q1.m3-1 3-A″ (CS)	14 HC2O.q1.m3-2 3-A″ (CS)	15 HC2O.q1.m3-4 3-A″ (CS)			

C₄					
1 C4.q0.m1-1 1-SGG (D*H)	2 C4.q0.m1-3 1-AG (D2H)	3 C4.q0.m3-1 3-SGG (D*H)	4 C4.q0.m3-2 3-B1 (C2V)	5 C4.q0.m3-5 3-A1 (D2D)	6 C4.q1.m2-1 2-PIG (D*H)
7 C4.q1.m2-2 2-A' (CS)	8 C4.q1.m4-1 4-B3U (D2H)	9 C4.q1.m4-2 4-A2 (C2V)			

C₃O					
1 C3O.q0.m1-3 1-A' (CS)	2 C3O.q0.m1-4 1-SG (C*V)	3 C3O.q0.m1-5 1-SG (C*V)	4 C3O.q0.m3-1 3-A' (CS)	5 C3O.q1.m2-2 2-SG (C*V)	6 C3O.q1.m2-3 2-SG (C*V)
7 C3O.q1.m2-4 2-A (C1)	8 C3O.q1.m4-4 4-A2 (C2V)	9 C3O.q1.m4-5 4-A (C1)			

H₄
1 H4.q1.m2-1 2-A1 (C2V)

H₄C	
1 H4C.q0.m1-1 1-A1 (TD)	2 H4C.q1.m2-1 2-B2 (D2D)

H₃C₂					
1 H3C2.q0.m2-1 2-A" (CS)	2 H3C2.q0.m2-2 2-A' (CS)	3 H3C2.q0.m4-8 4-A1 (C3V)	4 H3C2.q0.m4-9 4-A" (CS)	5 H3C2.q1.m1-1 1-A1 (C3V)	6 H3C2.q1.m1-2 1-A1 (C2V)
7 H3C2.q1.m3-2 3-A" (CS)	8 H3C2.q1.m3-3 3-A" (CS)				

H₃CO				
1 H3CO.q0.m2-1 2-A' (CS)	2 H3CO.q0.m2-2 2-A (C1)	3 H3CO.q1.m1-3 1-A' (CS)	4 H3CO.q1.m3-2 3-A" (CS)	5 H3CO.q1.m3-8 3-A" (CS)

H₂C₃					
1 H2C3.q0.m1-2 1-A1 (C2V)	2 H2C3.q0.m1-3 1-AG (C2H)	3 H2C3.q0.m1-4 1-A1 (C2V)	4 H2C3.q0.m1-5 1-A (C2)	5 H2C3.q0.m3-1 3-SGG (D*H)	6 H2C3.q0.m3-2 3-A" (CS)
7 H2C3.q0.m3-3 3-A" (CS)	8 H2C3.q0.m3-4 3-B2 (C2V)	9 H2C3.q0.m3-5 3-A (C1)	10 H2C3.q1.m2-1 2-PIG (D*H)	11 H2C3.q1.m2-2 2-A' (CS)	12 H2C3.q1.m2-3 2-A1 (C2V)
13 H2C3.q1.m4-1 4-A2 (C2V)	14 H2C3.q1.m4-2 4-A (C1)	15 H2C3.q1.m4-4 4-A2 (C2V)	16 H2C3.q1.m4-5 4-A" (CS)		

H₂C₂O					
1 H2C2O.q0.m1-4 1-A′ (CS)	2 H2C2O.q0.m1-5 1-A1 (C2V)	3 H2C2O.q0.m1-6 1-A (C1)	4 H2C2O.q0.m1-7 1-A (C1)	5 H2C2O.q0.m3-5 3-A″ (CS)	6 H2C2O.q1.m2-2 2-A (C1)
7 H2C2O.q1.m2-3 2-A (C1)	8 H2C2O.q1.m4-4 4-A″ (CS)	9 H2C2O.q1.m4-5 4-A″ (CS)	10 H2C2O.q1.m4-6 4-A″ (CS)	11 H2C2O.q1.m4-8 4-A″ (CS)	

HC₄					
1 HC4.q0.m2-1 2-A′ (CS)	2 HC4.q0.m2-2 2-A (C1)	3 HC4.q0.m2-5 2-A′ (CS)	4 HC4.q0.m2-6 2-B1 (C2V)	5 HC4.q0.m4-1 4-A (C1)	6 HC4.q0.m4-2 4-A″ (CS)
7 HC4.q0.m4-3 4-A″ (CS)	8 HC4.q0.m4-4 4-A″ (CS)	9 HC4.q0.m4-5 4-A″ (CS)	10 HC4.q1.m1-1 1-A1 (C2V)	11 HC4.q1.m1-3 1-A′ (CS)	12 HC4.q1.m1-4 1-SG (C*V)
13 HC4.q1.m1-5 1-A1 (C2V)	14 HC4.q1.m3-3 3-A″ (CS)	15 HC4.q1.m3-4 3-A2 (C2V)	16 HC4.q1.m3-5 3-A″ (CS)	17 HC4.q1.m3-6 3-A″ (CS)	

HC₃O					
1 HC3O.q0.m2-1 2-A′ (CS)	2 HC3O.q0.m4-1 4-A (C1)	3 HC3O.q1.m1-1 1-A (C1)	4 HC3O.q1.m1-2 1-A′ (CS)	5 HC3O.q1.m1-3 1-SG (C*V)	6 HC3O.q1.m3-1 3-A′ (CS)
7 HC3O.q1.m3-2 3-A (C1)					

C₄O

1	2	3	4	5	6
C4O.q0.m1-2	C4O.q0.m1-3	C4O.q0.m1-4	C4O.q0.m1-5	C4O.q0.m3-2	C4O.q1.m2-1
1-A' (CS)	1-A1 (C2V)	1-A' (CS)	1-A1 (C2V)	3-SG (C*V)	2-A' (CS)

H₄C₂

1	2	3	4	5	6
H4C2.q0.m1-3	H4C2.q0.m1-4	H4C2.q0.m3-4	H4C2.q0.m3-5	H4C2.q1.m2-1	H4C2.q1.m2-6
1-A (C1)	1-AG (D2H)	3-A" (CS)	3-A1 (D2D)	2-A' (CS)	2-B3 (D2)
7					
H4C2.q1.m4-1					
4-A (C1)					

H₄CO

1	2
H4CO.q0.m1-6	H4CO.q1.m2-3
1-A' (CS)	2-A" (CS)

H₃C₃

1	2	3	4	5	6
H3C3.q0.m2-1	H3C3.q0.m2-2	H3C3.q0.m2-3	H3C3.q0.m4-1	H3C3.q0.m4-2	H3C3.q1.m1-1
2-B1 (C2V)	2-A' (CS)	2-A" (CS)	4-A (C1)	4-A" (CS)	1-A1' (D3H)
7	8	9	10	11	
H3C3.q1.m1-3	H3C3.q1.m1-9	H3C3.q1.m3-1	H3C3.q1.m3-2	H3C3.q1.m3-3	
1-A' (CS)	1-A' (CS)	3-A" (CS)	3-A (C1)	3-A' (CS)	
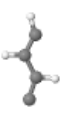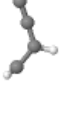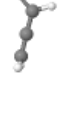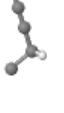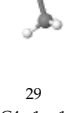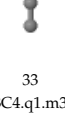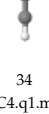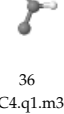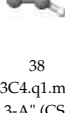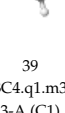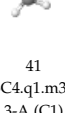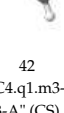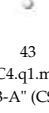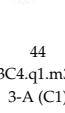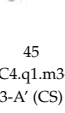
H₃C₂O					
1 H3C2O.q0.m2-1 2-A (C1)	2 H3C2O.q0.m4-3 4-A (C1)	3 H3C2O.q0.m4-4 4-A (C1)	4 H3C2O.q1.m1-1 1-A1 (C3V)	5 H3C2O.q1.m1-2 1-A' (CS)	6 H3C2O.q1.m1-4 1-A' (CS)
7 H3C2O.q1.m1-5 1-A' (CS)	8 H3C2O.q1.m1-6 1-A' (CS)	9 H3C2O.q1.m3-2 3-A" (CS)			
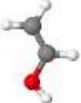
H₂C₄					
1 H2C4.q0.m1-1 1-SG (C*V)	2 H2C4.q0.m1-2 1-A' (CS)	3 H2C4.q0.m1-4 1-A (C2)	4 H2C4.q0.m1-5 1-A1 (C2V)	5 H2C4.q0.m1-7 1-A1 (C2V)	6 H2C4.q0.m1-8 1-A1 (C2V)
7 H2C4.q0.m1-9 1-AG (C2H)	8 H2C4.q0.m3-2 3-A2 (C2V)	9 H2C4.q0.m3-3 3-AU (CI)	10 H2C4.q0.m3-4 3-A (C1)	11 H2C4.q0.m3-5 3-A (C1)	12 H2C4.q0.m3-7 3-A (C1)
13 H2C4.q0.m3-9 3-A2 (C2V)	14 H2C4.q0.m3-10 3-A2 (C2V)	15 H2C4.q0.m3-11 3-A (C1)	16 H2C4.q1.m2-2 2-A2 (C2V)	17 H2C4.q1.m2-3 2-B1 (C2V)	18 H2C4.q1.m2-4 2-A (C1)
19 H2C4.q1.m2-7 2-A" (CS)	20 H2C4.q1.m2-9 2-AG (C2H)	21 H2C4.q1.m4-1 4-A" (CS)	22 H2C4.q1.m4-2 4-B1 (C2V)	23 H2C4.q1.m4-4 4-A2 (C2V)	24 H2C4.q1.m4-5 4-A (C1)
25 H2C4.q1.m4-6 4-A (C1)	26 H2C4.q1.m4-7 4-A" (CS)	27 H2C4.q1.m4-8 4-A (C1)	28 H2C4.q1.m4-9 4-A2 (C2V)		

H₂C₃O

1	2	3	4
H2C3O.q0.m1-1	H2C3O.q0.m1-2	H2C3O.q0.m3-1	H2C3O.q1.m4-3
1-A' (CS)	1-A' (CS)	3-A (C1)	4-A (C1)

HC₄O

1	2	3	4	5	6
HC4O.q0.m2-1	HC4O.q1.m1-1	HC4O.q1.m1-2	HC4O.q1.m1-3	HC4O.q1.m1-6	HC4O.q1.m1-7
2-A" (CS)	1-A' (CS)	1-A' (CS)	1-A (C1)	1-A' (CS)	1-A (C1)

H₄C₃

1	2	3	4	5	6
H4C3.q0.m1-1	H4C3.q0.m1-2	H4C3.q0.m1-3	H4C3.q0.m1-4	H4C3.q0.m1-5	H4C3.q0.m3-2
1-A (C1)	1-A1 (C2V)	1-A (C1)	1-A1 (C3V)	1-A1 (C2V)	3-A (C1)

7	8	9	10	11	12
H4C3.q0.m3-4	H4C3.q0.m3-5	H4C3.q0.m3-6	H4C3.q0.m3-7	H4C3.q1.m2-1	H4C3.q1.m2-2
3-A (C1)	3-B1 (C2V)	3-A" (CS)	3-A" (CS)	2-A (C1)	2-A (C1)

13	14	15	16	17	18
H4C3.q1.m2-3	H4C3.q1.m2-4	H4C3.q1.m2-6	H4C3.q1.m4-1	H4C3.q1.m4-2	H4C3.q1.m4-3
2-A" (CS)	2-A' (CS)	2-B (C2)	4-A" (CS)	4-B2 (C2V)	4-A" (CS)

19	20	21
H4C3.q1.m4-4	H4C3.q1.m4-5	H4C3.q1.m4-6
4-A (C1)	4-A" (CS)	4-B (C2)

H$_3$C$_4$

1	2	3	4	5	6
H3C4.q0.m2-2	H3C4.q0.m2-3	H3C4.q0.m2-4	H3C4.q0.m2-5	H3C4.q0.m2-7	H3C4.q0.m2-8
2-B2 (C2V)	2-A (C1)	2-A' (CS)	2-A' (CS)	2-A (C1)	2-A (C1)
7	8	9	10	11	12
H3C4.q0.m2-10	H3C4.q0.m2-12	H3C4.q0.m2-13	H3C4.q0.m2-14	H3C4.q0.m4-1	H3C4.q0.m4-2
2-A (C1)	2-A" (CS)	2-A" (CS)	2-A (C1)	4-A1 (C3V)	4-A" (CS)
13	14	15	16	17	18
H3C4.q0.m4-3	H3C4.q0.m4-4	H3C4.q0.m4-5	H3C4.q0.m4-6	H3C4.q0.m4-7	H3C4.q0.m4-8
4-A" (CS)	4-A" (CS)	4-A (C1)	4-A (C1)	4-A" (CS)	4-A" (CS)
19	20	21	22	23	24
H3C4.q0.m4-9	H3C4.q0.m4-10	H3C4.q0.m4-12	H3C4.q0.m4-13	H3C4.q0.m4-14	H3C4.q1.m1-1
4-A (C1)	4-A (C1)	4-B2 (C2V)	4-A' (CS)	4-A" (CS)	1-A1 (C3V)
25	26	27	28	29	30
H3C4.q1.m1-2	H3C4.q1.m1-3	H3C4.q1.m1-5	H3C4.q1.m1-7	H3C4.q1.m1-10	H3C4.q1.m1-11
1-A1 (C2V)	1-A (C1)	1-A' (CS)	1-A (C1)	1-A' (CS)	1-A (C1)
31	32	33	34	35	36
H3C4.q1.m1-13	H3C4.q1.m1-15	H3C4.q1.m3-1	H3C4.q1.m3-2	H3C4.q1.m3-3	H3C4.q1.m3-4
1-A1 (C2V)	1-A (C1)	3-A" (CS)	3-A2 (C2V)	3-A" (CS)	3-A" (CS)
37	38	39	40	41	42
H3C4.q1.m3-5	H3C4.q1.m3-7	H3C4.q1.m3-8	H3C4.q1.m3-10	H3C4.q1.m3-11	H3C4.q1.m3-12
3-A" (CS)	3-A" (CS)	3-A (C1)	3-A (C1)	3-A (C1)	3-A" (CS)
43	44	45			
H3C4.q1.m3-13	H3C4.q1.m3-14	H3C4.q1.m3-15			
3-A" (CS)	3-A (C1)	3-A' (CS)			

H₄C₂O			
1 H4C2O.q0.m1-3 1-A′ (CS)	2 H4C2O.q0.m1-5 1-A (C1)	3 H4C2O.q0.m1-9 1-A′ (CS)	4 H4C2O.q0.m1-10 1-A′ (CS)
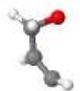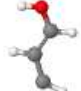
H₂C₄O					
1 H2C4O.q0.m1-1 1-A (C1)	2 H2C4O.q0.m1-2 1-A (C1)	3 H2C4O.q1.m2-1 2-A (C1)	4 H2C4O.q1.m2-2 2-A" (CS)	5 H2C4O.q1.m2-4 2-A (C1)	6 H2C4O.q1.m2-5 2-A (C1)
7 H2C4O.q1.m2-6 2-A (C1)	8 H2C4O.q1.m4-1 4-A (C1)				
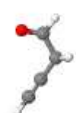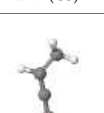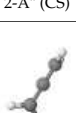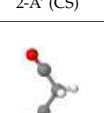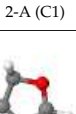
H₃C₃O			
1 H3C3O.q1.m1-1 1-A′ (CS)	2 H3C3O.q1.m1-2 1-A′ (CS)	3 H3C3O.q1.m1-5 1-A′ (CS)	4 H3C3O.q1.m1-6 1-A′ (CS)

H₃C₄O					
1 H3C4O.q0.m2-1 2-A" (CS)	2 H3C4O.q0.m2-2 2-A (C1)	3 H3C4O.q1.m1-1 1-A (C1)	4 H3C4O.q1.m1-2 1-A (C1)	5 H3C4O.q1.m1-3 1-A (C1)	6 H3C4O.q1.m1-4 1-A (C1)
7 H3C4O.q1.m1-5 1-A (C1)					

H₄C₄					
1 H4C4.q0.m1-1 1-A′ (CS)	2 H4C4.q0.m1-2 1-A (C1)	3 H4C4.q0.m1-3 1-A (C1)	4 H4C4.q0.m1-4 1-A1 (C2V)	5 H4C4.q0.m1-5 1-A (C1)	6 H4C4.q0.m1-6 1-A′ (CS)
7 H4C4.q0.m1-7 1-A′ (CS)	8 H4C4.q0.m1-11 1-A (C1)	9 H4C4.q0.m1-12 1-A′ (CS)	10 H4C4.q0.m1-13 1-AG (D2H)	11 H4C4.q0.m1-14 1-A (C1)	12 H4C4.q0.m1-15 1-A′ (CS)
13 H4C4.q0.m1-17 1-A′ (CS)	14 H4C4.q0.m1-18 1-A1 (TD)	15 H4C4.q0.m1-19 1-AG (D2H)	16 H4C4.q0.m3-1 3-A″ (CS)	17 H4C4.q0.m3-3 3-A (C1)	18 H4C4.q0.m3-4 3-A (C1)
19 H4C4.q0.m3-5 3-A (C1)	20 H4C4.q0.m3-6 3-A″ (CS)	21 H4C4.q0.m3-7 3-BU (C2H)	22 H4C4.q0.m3-8 3-A (C1)	23 H4C4.q0.m3-9 3-A (C1)	24 H4C4.q0.m3-10 3-A (C1)
25 H4C4.q0.m3-12 3-A (C1)	26 H4C4.q0.m3-13 3-AG (CI)	27 H4C4.q0.m3-14 3-A″ (CS)	28 H4C4.q0.m3-15 3-A2 (C2V)	29 H4C4.q0.m3-16 3-B2 (C2V)	30 H4C4.q0.m3-17 3-A (C1)
31 H4C4.q0.m3-18 3-A″ (CS)	32 H4C4.q0.m3-19 3-A1 (D2D)	33 H4C4.q1.m2-1 2-A (C1)	34 H4C4.q1.m2-2 2-A″ (CS)	35 H4C4.q1.m2-3 2-A (C1)	36 H4C4.q1.m2-4 2-B1 (C2V)
37 H4C4.q1.m2-5 2-A (C1)	38 H4C4.q1.m2-6 2-A″ (CS)	39 H4C4.q1.m2-7 2-A (C1)	40 H4C4.q1.m2-8 2-A′ (CS)	41 H4C4.q1.m2-9 2-A (C1)	42 H4C4.q1.m2-10 2-A (C1)
43 H4C4.q1.m2-11 2-A (C1)	44 H4C4.q1.m2-12 2-A″ (CS)	45 H4C4.q1.m2-13 2-B2G (D2H)	46 H4C4.q1.m2-14 2-A (C1)	47 H4C4.q1.m2-15 2-A′ (CS)	48 H4C4.q1.m2-17 2-BU (C2H)

H₄C₄ (*Continued from previous page*)					
49 H4C4.q1.m2-18 2-A1 (D2D)	50 H4C4.q1.m2-19 2-B2 (D2)	51 H4C4.q1.m4-1 4-A (C1)	52 H4C4.q1.m4-2 4-A (C1)	53 H4C4.q1.m4-3 4-A (C1)	54 H4C4.q1.m4-4 4-A (C1)
55 H4C4.q1.m4-5 4-A" (CS)	56 H4C4.q1.m4-6 4-A (C1)	57 H4C4.q1.m4-7 4-AU (C2H)	58 H4C4.q1.m4-8 4-A (C1)	59 H4C4.q1.m4-9 4-A" (CS)	60 H4C4.q1.m4-10 4-A (C1)
61 H4C4.q1.m4-11 4-A (C1)	62 H4C4.q1.m4-12 4-A" (CS)	63 H4C4.q1.m4-13 4-AU (C2H)	64 H4C4.q1.m4-14 4-A (C1)	65 H4C4.q1.m4-15 4-B2 (C2V)	66 H4C4.q1.m4-16 4-A2 (C2V)
67 H4C4.q1.m4-17 4-B1 (C2V)	68 H4C4.q1.m4-18 4-A (C1)	69 H4C4.q1.m4-19 4-B3 (D2)			

H₄C₃O					
1 H4C3O.q0.m1-2 1-A (C1)	2 H4C3O.q0.m1-3 1-A (C1)	3 H4C3O.q0.m1-4 1-A (C1)	4 H4C3O.q0.m3-2 3-A (C1)	5 H4C3O.q1.m2-2 2-A (C1)	6 H4C3O.q1.m2-4 2-A" (CS)
7 H4C3O.q1.m4-1 4-A (C1)	8 H4C3O.q1.m4-2 4-A (C1)	9 H4C3O.q1.m4-3 4-A (C1)			

C₄H₄O					
1 C4H4O.q0.m1-1 1-A′ (CS)	2 C4H4O.q0.m1-2 1-A1 (C2V)	3 C4H4O.q0.m1-3 1-A′ (CS)	4 C4H4O.q0.m1-4 1-A1 (C2V)	5 C4H4O.q0.m1-5 1-A′ (CS)	6 C4H4O.q0.m1-6 1-A′ (CS)
7 C4H4O.q0.m1-7 1-A (C1)	8 C4H4O.q0.m1-8 1-A′ (CS)	9 C4H4O.q0.m1-9 1-A′ (CS)	10 C4H4O.q0.m1-10 1-A′ (CS)	11 C4H4O.q0.m1-11 1-A′ (CS)	12 C4H4O.q0.m1-12 1-A′ (CS)
13 C4H4O.q0.m1-13 1-A′ (CS)	14 C4H4O.q0.m1-14 1-A′ (CS)	15 C4H4O.q0.m1-15 1-A (C1)	16 C4H4O.q0.m1-16 1-A (C1)	17 C4H4O.q0.m1-17 1-A′ (CS)	18 C4H4O.q0.m1-18 1-A′ (CS)
19 C4H4O.q0.m1-19 1-A′ (CS)	20 C4H4O.q0.m1-20 1-A′ (CS)	21 C4H4O.q0.m1-21 1-A′ (CS)	22 C4H4O.q1.m2-1 2-A′ (CS)	23 C4H4O.q1.m2-2 2-A (C1)	24 C4H4O.q1.m2-3 2-A2 (C2V)
25 C4H4O.q1.m2-4 2-A′ (CS)	26 C4H4O.q1.m2-5 2-A" (CS)	27 C4H4O.q1.m2-6 2-A (C1)	28 C4H4O.q1.m2-7 2-A′ (CS)	29 C4H4O.q1.m2-8 2-A" (CS)	30 C4H4O.q1.m2-9 2-A" (CS)
31 C4H4O.q1.m2-10 2-A′ (CS)	32 C4H4O.q1.m2-11 2-A (C1)	33 C4H4O.q1.m2-12 2-A (C1)	34 C4H4O.q1.m2-13 2-A (C1)	35 C4H4O.q1.m2-14 2-A′ (CS)	36 C4H4O.q1.m2-15 2-A (C1)
37 C4H4O.q1.m2-16 2-A (C1)	38 C4H4O.q1.m2-19 2-A′ (CS)	39 C4H4O.q1.m2-20 2-A (C1)			

Appendix B

M₃C input file

The following code presents the input file of M₃C calculations for the singly ionized furan. The results of this simulation were presented in Chapter 5.2.3.

```
 1   BEGIN  EXCITATION_ENERGY_SCAN
 2   excitationEnergy  =  0:10:21  # dE = 0.5 eV
 3   END  EXCITATION_ENERGY_SCAN
 4
 5   BEGIN  GOPTIONS
 6   systemRadius  =  13.0
 7   overlappingRadius  =  0.4
 8
 9   useRandomWalkers  =  FALSE
10   randomWalkStepRadius  =  1.0
11
12   useZPECorrection  =  TRUE
13   useSpinConservationRules  =  FALSE
14
15   angularMomentumCouplingScheme  =  JJL
16   structureSamplingMethod  =  SEQUENTIAL
17   END  GOPTIONS
18
19   BEGIN  MARKOV_CHAIN
20   task  =  V,T,R,5*S:0,V,T,R,5*S:1:−1
21   burnInFraction  =  0.1
22
23   reactives  =  C4H4Op(d3)
24   excitationEnergy  =  4.0
25
26   tracking  =  none
27   numberOfEvents  =  200000
28   numberOfExperiments  =  500
29   historyFileFrequency  =  500
30
31   geometryHistoryFilePrefix = geom
32   energyHistoryFile  =  C4H4O.q1.energy.dat
33   weightHistoryFile  =  C4H4O.q1.weight.dat
34   JHistoryFile  =  C4H4O.q1.J.dat
35   histogramFile  =  C4H4O.q1.histogram.dat
36   END  MARKOV_CHAIN
37
38   BEGIN  FRAGMENTS_DATABASE
39
40   store  =  /home/eerd/Furan_M3Cv2.0/new5_rxyz
41   reference  =  C4H4Op(d3)
42
```

#	Label	Z	M	WL	SYM	geomFile	Eelec		maxVib	
43	#——									
44	# Label	Z	M	WL	SYM	geomFile	Eelec		maxVib	
45	#——									
46	H(d2)	0	2	1	1	H.q0.m2−2.rxyz	−13.667114	#		SO3(2−S)
47	C(s2)	0	1	5	1	C.q0.m1−2.rxyz	−1028.370642	#		SO3(1−D)
48	C(t1)	0	3	3	1	C.q0.m3−1.rxyz	−1030.149091	#		SO3(3−P)
49	O(s2)	0	1	5	1	O.q0.m1−2.rxyz	−2040.552863	#		SO3(1−D)
50	O(t1)	0	3	3	1	O.q0.m3−1.rxyz	−2043.300455	#		SO3(3−P)
51	H2(s2)	0	1	1	2	H2.q0.m1−2.rxyz	−32.097788	H(d2)+H(d2)	#	4.76	D*H(1−SGG)
52	HC(d1)	0	2	2	1	HC.q0.m2−1.rxyz	−1047.478280	H(d2)+C(t1)	#	3.66	C*V(2−PI)
53	HC(q24)	0	4	1	1	HC.q0.m4−24.rxyz	−1046.582374	H(d2)+C(t1)	#	2.77	C*V(4−SG)
54	HO(d2)	0	2	2	1	HO.q0.m2−2.rxyz	−2061.601014	H(d2)+O(t1)	#	4.63	C*V(2−PI)
55	C2(s3)	0	1	1	2	C2.q0.m1−3.rxyz	−2065.388103	C(t1)+C(t1)	#	5.09	D*H(1−SGG)
56	C2(t2)	0	3	2	2	C2.q0.m3−2.rxyz	−2066.382008	C(t1)+C(t1)	#	6.08	D*H(3−PIU)

57	CO(s2)	0	1	1	1	CO.q0.m1−2.rxyz	−3084.385908	C(t1)+O(t1)	#	10.94	C∗V(1−SG)
58	CO(t2)	0	3	2	1	CO.q0.m3−2.rxyz	−3078.539149	C(t1)+O(t1)	#	5.09	C∗V(3−PI)
59	H2C(s1)	0	1	1	2	H2C.q0.m1−2.rxyz	−1065.237570	H2(s2)+C(t1)	#	2.99	C2V(1−A1)
60	H2C(t7)	0	3	1	2	H2C.q0.m3−7.rxyz	−1065.764739	H2(s2)+C(t1)	#	3.52	C2V(3−B1)
61	H2C(t9)	0	3	1	2	H2C.q0.m3−9.rxyz	−1062.565811	H2(s2)+C(t1)	#	0.32	C2V(3−A2)
62	H2O(s2)	0	1	1	2	H2O.q0.m1−2.rxyz	−2080.543368	H2(s2)+O(t1)	#	5.15	C2V(1−A1)
63	HC2(d1)	0	2	1	1	HC2.q0.m2−1.rxyz	−2085.234915	H(d2)+C2(t2)	#	5.19	C∗V(2−SG)
64	HC2(d3)	0	2	1	2	HC2.q0.m2−3.rxyz	−2084.226879	H(d2)+C2(t2)	#	4.18	C2V(2−A1)
65	HC2(q1)	0	4	1	1	HC2.q0.m4−1.rxyz	−2081.632608	H(d2)+C2(t2)	#	1.58	CS(4−A")
66	HCO(d2)	0	2	1	1	HCO.q0.m2−2.rxyz	−3097.317862	H(d2)+CO(t2)	#	5.11	CS(2−A')
67	HCO(d7)	0	2	1	1	HCO.q0.m2−7.rxyz	−3099.142127	H(d2)+CO(s2)	#	1.09	CS(2−A')
68	HCO(q12)	0	4	1	1	HCO.q0.m4−12.rxyz	−3094.144308	H(d2)+CO(t2)	#	1.94	CS(4−A")
69	C3(s1)	0	1	1	6	C3.q0.m1−1.rxyz	−3104.192084	C(t1)+C2(t2)	#	7.66	D∗H(1−SGG)
70	C3(t1)	0	3	1	6	C3.q0.m3−1.rxyz	−3103.356704	C(t1)+C2(t2)	#	6.83	D3H(3−A1′)
71	C3(t3)	0	3	2	2	C3.q0.m3−3.rxyz	−3101.996725	C(t1)+C2(t2)	#	5.47	D∗H(3−PIG)
72	C2O(s2)	0	1	1	1	C2O.q0.m1−2.rxyz	−4116.133213	C(t1)+CO(s2)	#	1.60	C∗V(1−SG)
73	C2O(s3)	0	1	1	2	C2O.q0.m1−3.rxyz	−4115.306606	C(t1)+CO(s2)	#	0.77	C2V(1−A1)
74	C2O(t2)	0	3	1	1	C2O.q0.m3−2.rxyz	−4117.219022	C(t1)+CO(s2)	#	2.68	C∗V(3−SG)
75	H3C(d1)	0	2	1	6	H3C.q0.m2−1.rxyz	−1084.515305	H2(s2)+HC(d1)	#	4.94	D3H(2−A2")
76	H2C2(s2)	0	1	1	1	H2C2.q0.m1−2.rxyz	−2104.982786	H(d2)+HC2(d1)	#	6.08	C∗V(1−SG)
77	H2C2(s3)	0	1	1	2	H2C2.q0.m1−3.rxyz	−2103.110538	H(d2)+HC2(d1)	#	4.21	C2V(1−A1)
78	H2C2(t1)	0	3	1	2	H2C2.q0.m3−1.rxyz	−2101.052209	H(d2)+HC2(d1)	#	2.15	C2V(3−B2)
79	H2C2(t2)	0	3	1	2	H2C2.q0.m3−2.rxyz	−2100.723310	H(d2)+HC2(d1)	#	1.82	C2H(3−AU)
80	H2C2(t4)	0	3	1	2	H2C2.q0.m3−4.rxyz	−2101.216995	H(d2)+HC2(d1)	#	2.31	C2V(3−B2)
81	H2CO(s1)	0	1	1	2	H2CO.q0.m1−1.rxyz	−3116.843626	H2(s2)+CO(s2)	#	0.36	C2V(1−A1)
82	H2CO(s3)	0	1	1	2	H2CO.q0.m1−3.rxyz	−3109.932451	HC(d1)+HO(d2)	#	0.85	C2V(1−A1)
83	H2CO(s4)	0	1	1	1	H2CO.q0.m1−4.rxyz	−3114.565682	H(d2)+HCO(d7)	#	1.76	CS(1−A')
84	H2CO(t4)	0	3	1	1	H2CO.q0.m3−4.rxyz	−3113.908267	H(d2)+HCO(d7)	#	1.10	CS(3−A")
85	HC3(d1)	0	2	1	1	HC3.q0.m2−1.rxyz	−3121.463520	H(d2)+C3(s1)	#	3.60	CS(2−A')
86	HC3(d2)	0	2	1	2	HC3.q0.m2−2.rxyz	−3121.481650	H(d2)+C3(s1)	#	3.62	C2V(2−B2)
87	HC3(q16)	0	4	1	1	HC3.q0.m4−16.rxyz	−3120.091298	H(d2)+C3(s1)	#	2.23	C∗V(4−SG)
88	HC3(q18)	0	4	1	1	HC3.q0.m4−18.rxyz	−3118.684622	H(d2)+C3(s1)	#	0.83	CS(4−A")
89	HC2O(d2)	0	2	1	1	HC2O.q0.m2−2.rxyz	−4135.429877	HC(d1)+CO(s2)	#	3.57	CS(2−A')
90	HC2O(d5)	0	2	1	1	HC2O.q0.m2−5.rxyz	−4133.003853	HC(d1)+CO(s2)	#	1.14	CS(2−A')
91	HC2O(q6)	0	4	1	1	HC2O.q0.m4−6.rxyz	−4130.479318	H(d2)+C2O(s2)	#	0.68	CS(4−A")
92	HC2O(q8)	0	4	1	1	HC2O.q0.m4−8.rxyz	−4130.099054	H(d2)+C2O(s2)	#	0.30	C1(4−A)
93	HC2O(q13)	0	4	1	1	HC2O.q0.m4−13.rxyz	−4130.580540	H(d2)+C2O(s2)	#	0.78	CS(4−A")
94	HC2O(q14)	0	4	1	1	HC2O.q0.m4−14.rxyz	−4132.954431	HC(d1)+CO(s2)	#	1.09	CS(4−A")
95	HC2O(q16)	0	4	1	1	HC2O.q0.m4−16.rxyz	−4130.086184	H(d2)+C2O(s2)	#	0.29	CS(4−A")
96	C4(s1)	0	1	1	2	C4.q0.m1−1.rxyz	−4138.951566	C(t1)+C3(s1)	#	4.61	D∗H(1−SGG)
97	C4(s3)	0	1	1	4	C4.q0.m1−3.rxyz	−4139.021954	C(t1)+C3(s1)	#	4.68	D2H(1−AG)
98	C4(t1)	0	3	1	2	C4.q0.m3−1.rxyz	−4139.723603	C(t1)+C3(s1)	#	5.38	D∗H(3−SGG)
99	C4(t2)	0	3	1	2	C4.q0.m3−2.rxyz	−4138.150510	C(t1)+C3(s1)	#	3.81	C2V(3−B1)
100	C4(t5)	0	3	1	4	C4.q0.m3−5.rxyz	−4137.870781	C(t1)+C3(s1)	#	3.53	D2D(3−A1)
101	C3O(s3)	0	1	1	1	C3O.q0.m1−3.rxyz	−5150.874006	C2(t2)+CO(s2)	#	0.11	CS(1−A')
102	C3O(s4)	0	1	1	1	C3O.q0.m1−4.rxyz	−5150.554249	C2(s3)+CO(s2)	#	0.78	C∗V(1−SG)
103	C3O(s5)	0	1	1	1	C3O.q0.m1−5.rxyz	−5155.225939	C2(t2)+CO(s2)	#	4.46	C∗V(1−SG)
104	C3O(t1)	0	3	1	1	C3O.q0.m3−1.rxyz	−5152.236992	C2(t2)+CO(s2)	#	1.47	CS(3−A')
105	H4C(s1)	0	1	1	12	H4C.q0.m1−1.rxyz	−1102.985717	H(d2)+H3C(d1)	#	4.80	TD(1−A1)
106	H3C2(d1)	0	2	1	1	H3C2.q0.m2−1.rxyz	−2118.467253	H2(s2)+HC2(d1)	#	1.13	CS(2−A")
107	H3C2(d2)	0	2	1	1	H3C2.q0.m2−2.rxyz	−2120.556900	H(d2)+H2C2(s2)	#	1.91	CS(2−A')
108	H3C2(q8)	0	4	1	3	H3C2.q0.m4−8.rxyz	−2116.944015	H(d2)+H2C2(s3)	#	0.17	C3V(4−A1)
109	H3C2(q9)	0	4	1	1	H3C2.q0.m4−9.rxyz	−2117.310373	H(d2)+H2C2(s3)	#	0.53	CS(4−A")
110	H3CO(d1)	0	2	1	1	H3CO.q0.m2−1.rxyz	−3131.820663	H2(s2)+HCO(d7)	#	0.58	CS(2−A')
111	H3CO(d2)	0	2	1	1	H3CO.q0.m2−2.rxyz	−3132.100672	H2(s2)+HCO(d7)	#	0.86	C1(2−A)
112	H2C3(s2)	0	1	1	2	H2C3.q0.m1−2.rxyz	−3139.846584	H2(s2)+C3(s1)	#	3.56	C2V(1−A1)
113	H2C3(s3)	0	1	1	2	H2C3.q0.m1−3.rxyz	−3138.896382	H2(s2)+C3(s1)	#	2.61	C2H(1−AG)
114	H2C3(s4)	0	1	1	1	H2C3.q0.m1−4.rxyz	−3139.322057	H2(s2)+C3(s1)	#	3.03	C2V(1−A1)
115	H2C3(s5)	0	1	1	2	H2C3.q0.m1−5.rxyz	−3138.897037	H2(s2)+C3(s1)	#	2.61	C2(1−A)
116	H2C3(t2)	0	3	1	1	H2C3.q0.m3−2.rxyz	−3136.860097	H2(s2)+C3(s1)	#	0.57	CS(3−A")
117	H2C3(t3)	0	3	1	1	H2C3.q0.m3−3.rxyz	−3138.055634	H2(s2)+C3(s1)	#	1.77	CS(3−A")
118	H2C3(t4)	0	3	1	2	H2C3.q0.m3−4.rxyz	−3136.757974	H2(s2)+C3(s1)	#	0.47	C2V(3−B2)
119	H2C3(t5)	0	3	1	1	H2C3.q0.m3−5.rxyz	−3137.625178	H2(s2)+C3(s1)	#	1.34	C1(3−A)
120	H2C2O(s4)	0	1	1	1	H2C2O.q0.m1−4.rxyz	−4150.125582	H2C(s1)+CO(s2)	#	0.50	CS(1−A')
121	H2C2O(s5)	0	1	1	2	H2C2O.q0.m1−5.rxyz	−4153.863118	H2C(t7)+CO(s2)	#	3.71	C2V(1−A1)
122	H2C2O(s6)	0	1	1	1	H2C2O.q0.m1−6.rxyz	−4152.257034	H2C(t7)+CO(s2)	#	2.11	C1(1−A)
123	H2C2O(s7)	0	1	1	1	H2C2O.q0.m1−7.rxyz	−4150.071871	H2C(s1)+CO(s2)	#	0.45	C1(1−A)
124	H2C2O(t5)	0	3	1	1	H2C2O.q0.m3−5.rxyz	−4151.612634	H2C(t7)+CO(s2)	#	1.46	CS(3−A")
125	HC4(d1)	0	2	1	1	HC4.q0.m2−1.rxyz	−4158.322644	H(d2)+C4(t1)	#	4.93	CS(2−A")
126	HC4(d2)	0	2	1	1	HC4.q0.m2−2.rxyz	−4156.788760	H(d2)+C4(t1)	#	3.40	C1(2−A)
127	HC4(d5)	0	2	1	1	HC4.q0.m2−5.rxyz	−4156.002094	H(d2)+C4(t1)	#	2.61	CS(2−A')
128	HC4(d6)	0	2	1	2	HC4.q0.m2−6.rxyz	−4156.916497	H(d2)+C4(t1)	#	3.53	C2V(2−B1)
129	HC4(q1)	0	4	1	1	HC4.q0.m4−1.rxyz	−4154.587179	H(d2)+C4(t1)	#	1.20	C1(4−A)
130	HC4(q2)	0	4	1	1	HC4.q0.m4−2.rxyz	−4154.587224	H(d2)+C4(t1)	#	1.20	CS(4−A")
131	HC4(q3)	0	4	1	1	HC4.q0.m4−3.rxyz	−4154.646601	H(d2)+C4(t1)	#	1.26	CS(4−A")
132	HC4(q4)	0	4	1	1	HC4.q0.m4−4.rxyz	−4155.175823	H(d2)+C4(t1)	#	1.79	CS(4−A")
133	HC4(q5)	0	4	1	1	HC4.q0.m4−5.rxyz	−4155.687064	H(d2)+C4(t1)	#	2.30	CS(4−A")
134	HC3O(d1)	0	2	1	1	HC3O.q0.m2−1.rxyz	−5169.766105	HC2(d1)+CO(s2)	#	0.15	CS(2−A')
135	HC3O(q1)	0	4	1	1	HC3O.q0.m4−1.rxyz	−5167.828815	HC2(q1)+CO(s2)	#	1.81	C1(4−A)
136	C4O(s2)	0	1	1	1	C4O.q0.m1−2.rxyz	−6184.266574	C2(t2)+C2O(t2)	#	0.67	CS(1−A')
137	C4O(s3)	0	1	1	2	C4O.q0.m1−3.rxyz	−6185.014804	C2(t2)+C2O(t2)	#	1.41	C2V(1−A1)

138	C4O(s4)	0	1	1	1	C4O.q0.m1−4.rxyz	−6189.620301	CO(s2)+C3(s1)	#	1.04	CS(1−A′)
139	C4O(s5)	0	1	1	2	C4O.q0.m1−5.rxyz	−6189.235058	CO(s2)+C3(s1)	#	0.66	C2V(1−A1)
140	C4O(t2)	0	3	1	1	C4O.q0.m3−2.rxyz	−6190.318781	CO(s2)+C3(s1)	#	1.74	C∗V(3−SG)
141	H4C2(s3)	0	1	1	1	H4C2.q0.m1−3.rxyz	−2135.945696	H2(s2)+H2C2(s3)	#	0.74	C1(1−A)
142	H4C2(s4)	0	1	1	4	H4C2.q0.m1−4.rxyz	−2139.238560	H2(s2)+H2C2(s2)	#	2.16	D2H(1−AG)
143	H4C2(t4)	0	3	1	1	H4C2.q0.m3−4.rxyz	−2136.158317	H2(s2)+H2C2(s3)	#	0.95	CS(3−A″)
144	H4C2(t5)	0	3	1	4	H4C2.q0.m3−5.rxyz	−2136.457431	H2(s2)+H2C2(s3)	#	1.25	D2D(3−A1)
145	H4CO(s6)	0	1	1	1	H4CO.q0.m1−6.rxyz	−3150.127252	H2(s2)+H2CO(s1)	#	1.19	CS(1−A′)
146	H3C3(d1)	0	2	1	2	H3C3.q0.m2−1.rxyz	−3157.603798	H2(s2)+HC3(d2)	#	4.02	C2V(2−B1)
147	H3C3(d2)	0	2	1	1	H3C3.q0.m2−2.rxyz	−3156.146261	H2(s2)+HC3(d2)	#	2.57	CS(2−A′)
148	H3C3(d3)	0	2	1	1	H3C3.q0.m2−3.rxyz	−3155.503736	H2(s2)+HC3(d2)	#	1.92	CS(2−A″)
149	H3C3(q1)	0	4	1	1	H3C3.q0.m4−1.rxyz	−3152.801034	H(d2)+H2C3(s5)	#	0.24	C1(4−A)
150	H3C3(q2)	0	4	1	1	H3C3.q0.m4−2.rxyz	−3153.855028	H2(s2)+HC3(d2)	#	0.28	CS(4−A″)
151	H3C2O(d1)	0	2	1	1	H3C2O.q0.m2−1.rxyz	−4168.328380	H(d2)+H2C2O(s5)	#	0.80	C1(2−A)
152	H3C2O(q3)	0	4	1	1	H3C2O.q0.m4−3.rxyz	−4165.408908	H(d2)+H2C2O(t5)	#	0.13	C1(4−A)
153	H3C2O(q4)	0	4	1	1	H3C2O.q0.m4−4.rxyz	−4164.377623	HC(d1)+H2CO(s1)	#	0.06	C1(4−A)
154	H2C4(s1)	0	1	1	1	H2C4.q0.m1−1.rxyz	−4177.793847	H(d2)+HC4(d1)	#	5.80	C∗V(1−SG)
155	H2C4(s2)	0	1	1	1	H2C4.q0.m1−2.rxyz	−4175.019761	H(d2)+HC4(d1)	#	3.03	CS(1−A′)
156	H2C4(s4)	0	1	1	2	H2C4.q0.m1−4.rxyz	−4174.480945	H(d2)+HC4(d1)	#	2.49	C2(1−A)
157	H2C4(s5)	0	1	1	2	H2C4.q0.m1−5.rxyz	−4173.383518	H(d2)+HC4(d1)	#	1.39	C2V(1−A1)
158	H2C4(s7)	0	1	1	2	H2C4.q0.m1−7.rxyz	−4174.687846	H(d2)+HC4(d1)	#	2.70	C2V(1−A1)
159	H2C4(s8)	0	1	1	2	H2C4.q0.m1−8.rxyz	−4176.002170	H(d2)+HC4(d1)	#	4.01	C2V(1−A1)
160	H2C4(s9)	0	1	1	2	H2C4.q0.m1−9.rxyz	−4175.008459	H(d2)+HC4(d1)	#	3.02	C2H(1−AG)
161	H2C4(t2)	0	3	1	2	H2C4.q0.m3−2.rxyz	−4174.370468	H(d2)+HC4(d1)	#	2.38	C2V(3−A2)
162	H2C4(t3)	0	3	1	1	H2C4.q0.m3−3.rxyz	−4174.384188	H(d2)+HC4(d1)	#	2.39	CI(3−AU)
163	H2C4(t4)	0	3	1	1	H2C4.q0.m3−4.rxyz	−4174.510965	H(d2)+HC4(d1)	#	2.52	C1(3−A)
164	H2C4(t5)	0	3	1	1	H2C4.q0.m3−5.rxyz	−4171.053240	H2(s2)+C4(s1)	#	0.00	C1(3−A)
165	H2C4(t7)	0	3	1	1	H2C4.q0.m3−7.rxyz	−4173.726230	H(d2)+HC4(d1)	#	1.74	C1(3−A)
166	H2C4(t9)	0	3	1	2	H2C4.q0.m3−9.rxyz	−4174.251610	H(d2)+HC4(d1)	#	2.26	C2V(3−A2)
167	H2C4(t10)	0	3	1	2	H2C4.q0.m3−10.rxyz	−4174.090018	H(d2)+HC4(d1)	#	2.10	C2V(3−A2)
168	H2C4(t11)	0	3	1	1	H2C4.q0.m3−11.rxyz	−4173.705928	H(d2)+HC4(d1)	#	1.72	C1(3−A)
169	H2C3O(s1)	0	1	1	1	H2C3O.q0.m1−1.rxyz	−5187.325416	H2(s2)+C3O(s5)	#	0.00	CS(1−A′)
170	H2C3O(s2)	0	1	1	1	H2C3O.q0.m1−2.rxyz	−5187.557447	H2C2(s3)+CO(s2)	#	0.06	CS(1−A′)
171	H2C3O(t1)	0	3	1	1	H2C3O.q0.m3−1.rxyz	−5185.195799	H2C2(t2)+CO(s2)	#	0.09	C1(3−A)
172	HC4O(d1)	0	2	1	1	HC4O.q0.m2−1.rxyz	−6203.609844	HCO(d7)+C3(s1)	#	0.28	CS(2−A″)
173	H4C3(s1)	0	1	1	1	H4C3.q0.m1−1.rxyz	−3172.745703	H2(s2)+H2C3(s2)	#	0.80	C1(1−A)
174	H4C3(s2)	0	1	1	2	H4C3.q0.m1−2.rxyz	−3174.327747	H2(s2)+H2C3(s2)	#	2.38	C2V(1−A1)
175	H4C3(s3)	0	1	1	1	H4C3.q0.m1−3.rxyz	−3175.444848	H2(s2)+H2C3(s2)	#	3.50	C1(1−A)
176	H4C3(s4)	0	1	1	3	H4C3.q0.m1−4.rxyz	−3175.375379	H2(s2)+H2C3(s2)	#	3.43	C3V(1−A1)
177	H4C3(s5)	0	1	1	2	H4C3.q0.m1−5.rxyz	−3172.414211	H2(s2)+H2C3(s2)	#	0.47	C2V(1−A1)
178	H4C3(t2)	0	3	1	1	H4C3.q0.m3−2.rxyz	−3173.303796	H2(s2)+H2C3(s2)	#	1.36	C1(3−A)
179	H4C3(t4)	0	3	1	1	H4C3.q0.m3−4.rxyz	−3173.203069	H2(s2)+H2C3(s2)	#	1.26	C1(3−A)
180	H4C3(t5)	0	3	1	2	H4C3.q0.m3−5.rxyz	−3171.840208	H2(s2)+H2C3(s4)	#	0.42	C2V(3−B1)
181	H4C3(t6)	0	3	1	1	H4C3.q0.m3−6.rxyz	−3171.550572	H2(s2)+H2C3(s4)	#	0.13	CS(3−A″)
182	H4C3(t7)	0	3	1	1	H4C3.q0.m3−7.rxyz	−3173.183024	H2(s2)+H2C3(s2)	#	1.24	CS(3−A″)
183	H4C2O(s3)	0	1	1	1	H4C2O.q0.m1−3.rxyz	−4184.975242	H2(s2)+H2C2O(s6)	#	0.62	CS(1−A′)
184	H4C2O(s5)	0	1	1	1	H4C2O.q0.m1−5.rxyz	−4185.138626	H2(s2)+H2C2O(s6)	#	0.78	C1(1−A)
185	H4C2O(s9)	0	1	1	1	H4C2O.q0.m1−9.rxyz	−4186.899422	H2(s2)+H2C2O(s5)	#	0.94	CS(1−A′)
186	H4C2O(s10)	0	1	1	1	H4C2O.q0.m1−10.rxyz	−4186.838928	H2(s2)+H2C2O(s5)	#	0.88	CS(1−A′)
187	H3C4(d2)	0	2	1	2	H3C4.q0.m2−2.rxyz	−4193.773129	H(d2)+H2C4(s1)	#	2.31	C2V(2−B2)
188	H3C4(d3)	0	2	1	1	H3C4.q0.m2−3.rxyz	−4192.451080	H(d2)+H2C4(s1)	#	0.99	C1(2−A)
189	H3C4(d4)	0	2	1	1	H3C4.q0.m2−4.rxyz	−4191.070697	H2(s2)+HC4(d1)	#	0.65	CS(2−A′)
190	H3C4(d5)	0	2	1	1	H3C4.q0.m2−5.rxyz	−4193.087036	H(d2)+H2C4(s1)	#	1.63	CS(2−A′)
191	H3C4(d7)	0	2	1	1	H3C4.q0.m2−7.rxyz	−4192.399740	H(d2)+H2C4(s1)	#	0.94	C1(2−A)
192	H3C4(d8)	0	2	1	1	H3C4.q0.m2−8.rxyz	−4190.745867	H2(s2)+HC4(d1)	#	0.33	C1(2−A)
193	H3C4(d10)	0	2	1	1	H3C4.q0.m2−10.rxyz	−4192.070388	H(d2)+H2C4(s1)	#	0.61	C1(2−A)
194	H3C4(d12)	0	2	1	1	H3C4.q0.m2−12.rxyz	−4191.940670	H(d2)+H2C4(s1)	#	0.48	CS(2−A″)
195	H3C4(d13)	0	2	1	1	H3C4.q0.m2−13.rxyz	−4192.115264	H(d2)+H2C4(s1)	#	0.65	CS(2−A″)
196	H3C4(d14)	0	2	1	1	H3C4.q0.m2−14.rxyz	−4191.320108	H2(s2)+HC4(d1)	#	0.90	C1(2−A)
197	H3C4(q1)	0	4	1	3	H3C4.q0.m4−1.rxyz	−4190.495760	H2(s2)+HC4(d1)	#	0.08	C3V(4−A1)
198	H3C4(q2)	0	4	1	1	H3C4.q0.m4−2.rxyz	−4191.374512	H2(s2)+HC4(d1)	#	0.95	CS(4−A″)
199	H3C4(q3)	0	4	1	1	H3C4.q0.m4−3.rxyz	−4189.887720	H(d2)+H2C4(s8)	#	0.22	CS(4−A″)
200	H3C4(q4)	0	4	1	1	H3C4.q0.m4−4.rxyz	−4189.415260	HC2(d3)+H2C2(s2)	#	0.21	CS(4−A″)
201	H3C4(q5)	0	4	1	1	H3C4.q0.m4−5.rxyz	−4190.500637	H2(s2)+HC4(d1)	#	0.08	C1(4−A)
202	H3C4(q6)	0	4	1	1	H3C4.q0.m4−6.rxyz	−4188.913741	H2(s2)+HC4(d2)	#	0.03	C1(4−A)
203	H3C4(q7)	0	4	1	1	H3C4.q0.m4−7.rxyz	−4189.904618	H(d2)+H2C4(s8)	#	0.24	CS(4−A″)
204	H3C4(q8)	0	4	1	1	H3C4.q0.m4−8.rxyz	−4189.266429	HC2(d3)+H2C2(s2)	#	0.06	CS(4−A″)
205	H3C4(q9)	0	4	1	1	H3C4.q0.m4−9.rxyz	−4188.690826	H(d2)+H2C4(s1)	#	0.00	C1(4−A)
206	H3C4(q10)	0	4	1	1	H3C4.q0.m4−10.rxyz	−4189.041321	H2(s2)+HC4(d6)	#	0.03	C1(4−A)
207	H3C4(q12)	0	4	1	2	H3C4.q0.m4−12.rxyz	−4191.168203	H2(s2)+HC4(d1)	#	0.75	C2V(4−B2)
208	H3C4(q13)	0	4	1	1	H3C4.q0.m4−13.rxyz	−4189.598874	HC2(d3)+H2C2(s2)	#	0.39	CS(4−A′)
209	H3C4(q14)	0	4	1	1	H3C4.q0.m4−14.rxyz	−4190.062736	H(d2)+H2C4(s8)	#	0.39	CS(4−A″)
210	H2C4O(s1)	0	1	1	1	H2C4O.q0.m1−1.rxyz	−6224.306012	CO(s2)+H2C3(s2)	#	0.07	C1(1−A)
211	H2C4O(s2)	0	1	1	1	H2C4O.q0.m1−2.rxyz	−6223.240326	CO(s2)+H2C3(t3)	#	0.80	C1(1−A)
212	H4C4(s1)	0	1	1	1	H4C4.q0.m1−1.rxyz	−4209.761177	H2(s2)+H2C4(s8)	#	1.66	CS(1−A′)
213	H4C4(s2)	0	1	1	1	H4C4.q0.m1−2.rxyz	−4209.401139	H2(s2)+H2C4(s8)	#	1.30	C1(1−A)
214	H4C4(s3)	0	1	1	1	H4C4.q0.m1−3.rxyz	−4210.311366	H2C2(s2)+H2C2(s2)	#	0.35	C1(1−A)
215	H4C4(s4)	0	1	1	2	H4C4.q0.m1−4.rxyz	−4210.873757	H2C2(s2)+H2C2(s2)	#	0.91	C2V(1−A1)
216	H4C4(s5)	0	1	1	1	H4C4.q0.m1−5.rxyz	−4208.803837	H2(s2)+H2C4(s8)	#	0.70	C1(1−A)
217	H4C4(s6)	0	1	1	1	H4C4.q0.m1−6.rxyz	−4211.871901	H2C2(s2)+H2C2(s2)	#	1.91	CS(1−A′)
218	H4C4(s7)	0	1	1	1	H4C4.q0.m1−7.rxyz	−4207.896154	H(d2)+H3C4(d2)	#	0.46	CS(1−A′)

#	Label					File	Energy	Products		Value	Symmetry
219	H4C4(s11)	0	1	1	1	H4C4.q0.m1−11.rxyz	−4209.422413	H2(s2)+H2C4(s8)	#	1.32	C1(1−A)
220	H4C4(s12)	0	1	1	1	H4C4.q0.m1−12.rxyz	−4209.822436	H2(s2)+H2C4(s8)	#	1.72	CS(1−A′)
221	H4C4(s13)	0	1	1	4	H4C4.q0.m1−13.rxyz	−4210.179391	H2C2(s2)+H2C2(s2)	#	0.21	D2H(1−AG)
222	H4C4(s14)	0	1	1	1	H4C4.q0.m1−14.rxyz	−4209.821508	H2(s2)+H2C4(s8)	#	1.72	C1(1−A)
223	H4C4(s15)	0	1	1	1	H4C4.q0.m1−15.rxyz	−4209.510619	H2(s2)+H2C4(s8)	#	1.41	CS(1−A′)
224	H4C4(s17)	0	1	1	1	H4C4.q0.m1−17.rxyz	−4208.762721	H2(s2)+H2C4(s8)	#	0.66	CS(1−A′)
225	H4C4(s18)	0	1	1	12	H4C4.q0.m1−18.rxyz	−4209.090638	H2(s2)+H2C4(s8)	#	0.99	TD(1−A1)
226	H4C4(s19)	0	1	1	4	H4C4.q0.m1−19.rxyz	−4211.717303	H2C2(s2)+H2C2(s2)	#	1.75	D2H(1−AG)
227	H4C4(t1)	0	3	1	1	H4C4.q0.m3−1.rxyz	−4208.276491	H2(s2)+H2C4(s8)	#	0.18	CS(3−A")
228	H4C4(t3)	0	3	1	1	H4C4.q0.m3−3.rxyz	−4208.082033	H(d2)+H3C4(d2)	#	0.64	C1(3−A)
229	H4C4(t4)	0	3	1	1	H4C4.q0.m3−4.rxyz	−4209.237784	H2(s2)+H2C4(s8)	#	1.14	C1(3−A)
230	H4C4(t5)	0	3	1	1	H4C4.q0.m3−5.rxyz	−4208.641887	H2(s2)+H2C4(s8)	#	0.54	C1(3−A)
231	H4C4(t6)	0	3	1	1	H4C4.q0.m3−6.rxyz	−4209.462840	H2(s2)+H2C4(s8)	#	1.36	CS(3−A")
232	H4C4(t7)	0	3	1	2	H4C4.q0.m3−7.rxyz	−4208.519539	H2(s2)+H2C4(s8)	#	0.42	C2H(3−BU)
233	H4C4(t8)	0	3	1	1	H4C4.q0.m3−8.rxyz	−4207.643831	H(d2)+H3C4(d2)	#	0.20	C1(3−A)
234	H4C4(t9)	0	3	1	1	H4C4.q0.m3−9.rxyz	−4207.060731	H2(s2)+H2C4(s7)	#	0.28	C1(3−A)
235	H4C4(t10)	0	3	1	1	H4C4.q0.m3−10.rxyz	−4206.261014	H2C2(s3)+H2C2(s3)	#	0.04	C1(3−A)
236	H4C4(t12)	0	3	1	1	H4C4.q0.m3−12.rxyz	−4208.077045	H(d2)+H3C4(d2)	#	0.64	C1(3−A)
237	H4C4(t13)	0	3	1	1	H4C4.q0.m3−13.rxyz	−4209.923557	H2(s2)+H2C4(s1)	#	0.03	CI(3−AG)
238	H4C4(t14)	0	3	1	1	H4C4.q0.m3−14.rxyz	−4208.979626	H2(s2)+H2C4(s8)	#	0.88	CS(3−A")
239	H4C4(t15)	0	3	1	2	H4C4.q0.m3−15.rxyz	−4208.881537	H2(s2)+H2C4(s8)	#	0.78	C2V(3−A2)
240	H4C4(t16)	0	3	1	2	H4C4.q0.m3−16.rxyz	−4207.808144	H(d2)+H3C4(d2)	#	0.37	C2V(3−B2)
241	H4C4(t17)	0	3	1	1	H4C4.q0.m3−17.rxyz	−4207.491125	H(d2)+H3C4(d2)	#	0.05	C1(3−A)
242	H4C4(t18)	0	3	1	1	H4C4.q0.m3−18.rxyz	−4207.880328	H(d2)+H3C4(d2)	#	0.44	CS(3−A")
243	H4C4(t19)	0	3	1	4	H4C4.q0.m3−19.rxyz	−4210.245244	H2C2(s2)+H2C2(s2)	#	0.28	D2D(3−A1)
244	H4C3O(s2)	0	1	1	1	H4C3O.q0.m1−2.rxyz	−5222.571661	H2C2(s2)+H2CO(s1)	#	0.75	C1(1−A)
245	H4C3O(s3)	0	1	1	1	H4C3O.q0.m1−3.rxyz	−5221.924489	H2C2(s2)+H2CO(s1)	#	0.10	C1(1−A)
246	H4C3O(s4)	0	1	1	1	H4C3O.q0.m1−4.rxyz	−5220.510159	H2O(s2)+H2C3(s2)	#	0.12	C1(1−A)
247	H4C3O(t2)	0	3	1	1	H4C3O.q0.m3−2.rxyz	−5220.509611	H2O(s2)+H2C3(s2)	#	0.12	C1(3−A)
248	H3C4O(d1)	0	2	1	1	H3C4O.q0.m2−1.rxyz	−6241.279136	CO(s2)+H3C3(d2)	#	0.75	CS(2−A")
249	H3C4O(d2)	0	2	1	1	H3C4O.q0.m2−2.rxyz	−6241.939296	CO(s2)+H3C3(d2)	#	1.41	C1(2−A)
250	C4H4O(s1)	0	1	1	1	C4H4O.q0.m1−1.rxyz	−6260.102121	CO(s2)+H4C3(s3)	#	0.27	CS(1−A′)
251	C4H4O(s2)	0	1	1	2	C4H4O.q0.m1−2.rxyz	−6259.753929	H2C2(s2)+H2C2O(s5)	#	0.91	C2V(1−A1)
252	C4H4O(s3)	0	1	1	1	C4H4O.q0.m1−3.rxyz	−6259.000480	H2C2(s2)+H2C2O(s5)	#	0.15	CS(1−A′)
253	C4H4O(s4)	0	1	1	2	C4H4O.q0.m1−4.rxyz	−6261.012550	CO(s2)+H4C3(s3)	#	1.18	C2V(1−A1)
254	C4H4O(s5)	0	1	1	1	C4H4O.q0.m1−5.rxyz	−6259.879602	CO(s2)+H4C3(s3)	#	0.05	CS(1−A′)
255	C4H4O(s6)	0	1	1	1	C4H4O.q0.m1−6.rxyz	−6259.388636	H2C2(s2)+H2C2O(s5)	#	0.54	CS(1−A′)
256	C4H4O(s7)	0	1	1	1	C4H4O.q0.m1−7.rxyz	−6259.910881	CO(s2)+H4C3(s3)	#	0.08	C1(1−A)
257	C4H4O(s8)	0	1	1	1	C4H4O.q0.m1−8.rxyz	−6260.042473	H4C3(s3)	#	0.21	CS(1−A′)
258	C4H4O(s9)	0	1	1	1	C4H4O.q0.m1−9.rxyz	−6258.526658	H2O(s2)+H2C4(s1)	#	0.19	CS(1−A′)
259	C4H4O(s10)	0	1	1	1	C4H4O.q0.m1−10.rxyz	−6260.231006	CO(s2)+H4C3(s3)	#	0.40	CS(1−A′)
260	C4H4O(s11)	0	1	1	1	C4H4O.q0.m1−11.rxyz	−6259.660457	H2C2(s2)+H2C2O(s5)	#	0.81	CS(1−A′)
261	C4H4O(s12)	0	1	1	1	C4H4O.q0.m1−12.rxyz	−6259.636896	H2C2(s2)+H2C2O(s5)	#	0.79	CS(1−A′)
262	C4H4O(s13)	0	1	1	1	C4H4O.q0.m1−13.rxyz	−6258.938633	H2C2(s2)+H2C2O(s5)	#	0.09	CS(1−A′)
263	C4H4O(s14)	0	1	1	1	C4H4O.q0.m1−14.rxyz	−6259.000481	H2C2(s2)+H2C2O(s5)	#	0.15	CS(1−A′)
264	C4H4O(s15)	0	1	1	1	C4H4O.q0.m1−15.rxyz	−6259.525173	H2C2(s2)+H2C2O(s5)	#	0.68	C1(1−A)
265	C4H4O(s16)	0	1	1	1	C4H4O.q0.m1−16.rxyz	−6259.656077	H2C2(s2)+H2C2O(s5)	#	0.81	C1(1−A)
266	C4H4O(s17)	0	1	1	1	C4H4O.q0.m1−17.rxyz	−6259.977553	CO(s2)+H4C3(s3)	#	0.15	CS(1−A′)
267	C4H4O(s18)	0	1	1	1	C4H4O.q0.m1−18.rxyz	−6260.102123	CO(s2)+H4C3(s3)	#	0.27	CS(1−A′)
268	C4H4O(s19)	0	1	1	1	C4H4O.q0.m1−19.rxyz	−6258.518900	H2O(s2)+H2C4(s1)	#	0.18	CS(1−A′)
269	C4H4O(s20)	0	1	1	1	C4H4O.q0.m1−20.rxyz	−6258.522608	H2O(s2)+H2C4(s1)	#	0.19	CS(1−A′)
270	C4H4O(s21)	0	1	1	1	C4H4O.q0.m1−21.rxyz	−6259.636894	H2C2(s2)+H2C2O(s5)	#	0.79	CS(1−A′)
271	Hp(s1)	1	1	1	1	H.q1.m1−1.rxyz	0.000000		#		SO3(1−S)
272	Cp(d2)	1	2	3	1	C.q1.m2−2.rxyz	−1018.600064		#		SO3(2−P)
273	Cp(q1)	1	4	3	1	C.q1.m4−1.rxyz	−1013.303219		#		SO3(4−P)
274	Op(d2)	1	2	5	1	O.q1.m2−2.rxyz	−2025.260550		#		SO3(2−D)
275	Op(q1)	1	4	1	1	O.q1.m4−1.rxyz	−2029.166170		#		SO3(4−S)
276	H2p(d1)	1	2	1	2	H2.q1.m2−1.rxyz	−16.585221	H(d2)+Hp(s1)	#	2.92	D*H(2−SGG)
277	HCp(s1)	1	1	1	1	HC.q1.m1−1.rxyz	−1036.475136	H(d2)+Cp(d2)	#	4.21	C*V(1−SG)
278	HCp(t1)	1	3	2	1	HC.q1.m3−1.rxyz	−1035.567104	H(d2)+Cp(d2)	#	3.30	C*V(3−PI)
279	HOp(s1)	1	1	1	1	HO.q1.m1−1.rxyz	−2045.348655	Hp(s1)+O(t1)	#	2.05	C*V(1−SG)
280	HOp(t1)	1	3	1	1	HO.q1.m3−1.rxyz	−2048.357479	Hp(s1)+O(t1)	#	5.06	C*V(3−SG)
281	C2p(d4)	1	2	2	2	C2.q1.m2−4.rxyz	−2053.047582	C(t1)+Cp(d2)	#	4.30	D*H(2−PIU)
282	C2p(q1)	1	4	1	2	C2.q1.m4−1.rxyz	−2054.470276	C(t1)+Cp(d2)	#	5.72	D*H(4−SGG)
283	COp(d3)	1	2	1	1	CO.q1.m2−3.rxyz	−3070.194119	Cp(d2)+O(t1)	#	8.29	C*V(2−SG)
284	COp(q8)	1	4	2	1	CO.q1.m4−8.rxyz	−3063.496256	Cp(d2)+O(t1)	#	1.60	C*V(4−PI)
285	H3p(s7)	1	1	1	2	H3.q1.m1−7.rxyz	−36.632656	Hp(s1)+H2(s2)	#	4.53	C2V(1−A1)
286	H2Cp(d18)	1	2	1	2	H2C.q1.m2−18.rxyz	−1055.339604	H2(s2)+Cp(d2)	#	4.64	C2V(2−A1)
287	H2Cp(q1)	1	4	1	1	H2C.q1.m4−1.rxyz	−1051.457390	H2(s2)+Cp(d2)	#	0.76	C2V(4−A2)
288	H2Op(d5)	1	2	1	2	H2O.q1.m2−5.rxyz	−2067.865483	H(d2)+HOp(t1)	#	5.84	C2V(2−B1)
289	H2Op(d6)	1	2	1	2	H2O.q1.m2−6.rxyz	−2067.495738	H(d2)+HOp(t1)	#	5.47	C2V(2−B1)
290	HC2p(s2)	1	1	1	1	HC2.q1.m1−2.rxyz	−2072.204246	H(d2)+C2p(q1)	#	4.07	CS(1−A′)
291	HC2p(t1)	1	3	2	1	HC2.q1.m3−1.rxyz	−2073.686480	H(d2)+C2p(q1)	#	5.55	C*V(3−PI)
292	HCOp(s1)	1	1	1	1	HCO.q1.m1−1.rxyz	−3090.717181	Hp(s1)+CO(s2)	#	6.33	C*V(1−SG)
293	HCOp(s2)	1	1	1	1	HCO.q1.m1−2.rxyz	−3089.018828	Hp(s1)+CO(s2)	#	4.63	C*V(1−SG)
294	HCOp(t2)	1	3	1	1	HCO.q1.m3−2.rxyz	−3084.951675	Hp(s1)+CO(s2)	#	0.57	CS(3−A′)
295	HCOp(t3)	1	3	1	1	HCO.q1.m3−3.rxyz	−3085.130738	Hp(s1)+CO(s2)	#	0.74	CS(3−A′)
296	C3p(d1)	1	2	1	2	C3.q1.m2−1.rxyz	−3092.280087	Cp(d2)+C2(t2)	#	7.30	C2V(2−B2)
297	C3p(d2)	1	2	1	1	C3.q1.m2−2.rxyz	−3092.045156	Cp(d2)+C2(t2)	#	7.06	CS(2−A′)
298	C3p(q3)	1	4	2	2	C3.q1.m4−3.rxyz	−3090.591166	Cp(d2)+C2(t2)	#	5.61	D*H(4−PIU)
299	C3p(q4)	1	4	1	6	C3.q1.m4−4.rxyz	−3091.639940	Cp(d2)+C2(t2)	#	6.66	D3H(4−A1′)

300	C2Op(d1)	1	2	2	1	C2O.q1.m2−1.rxyz	−4104.357894	Cp(d2)+CO(s2)	#	1.37	C*V(2−PI)
301	C2Op(q2)	1	4	1	1	C2O.q1.m4−2.rxyz	−4105.663626	Cp(d2)+CO(s2)	#	2.68	C*V(4−SG)
302	H4p(d1)	1	2	1	2	H4.q1.m2−1.rxyz	−50.771232	H(d2)+H3p(s7)	#	0.47	C2V(2−A1)
303	H3Cp(s1)	1	1	1	6	H3C.q1.m1−1.rxyz	−1074.618094	H(d2)+H2Cp(d18)	#	5.61	D3H(1−A1′)
304	H3Cp(t1)	1	3	1	1	H3C.q1.m3−1.rxyz	−1071.017296	H(d2)+H2Cp(d18)	#	2.01	CS(3−A″)
305	H2C2p(d1)	1	2	2	2	H2C2.q1.m2−1.rxyz	−2093.702078	H(d2)+HC2p(t1)	#	6.35	D*H(2−PIU)
306	H2C2p(d2)	1	2	1	1	H2C2.q1.m2−2.rxyz	−2091.809253	H(d2)+HC2p(t1)	#	4.46	CS(2−A′)
307	H2C2p(q2)	1	4	1	2	H2C2.q1.m4−2.rxyz	−2090.207233	H(d2)+HC2p(t1)	#	2.85	C2H(4−BG)
308	H2C2p(q3)	1	4	1	2	H2C2.q1.m4−3.rxyz	−2090.548560	H(d2)+HC2p(t1)	#	3.19	C2V(4−A2)
309	H2C2p(q4)	1	4	1	2	H2C2.q1.m4−4.rxyz	−2090.265931	H(d2)+HC2p(t1)	#	2.91	C2V(4−A2)
310	H2COp(d3)	1	2	1	1	H2CO.q1.m2−3.rxyz	−3105.479226	H(d2)+HCOp(s1)	#	1.09	CS(2−A′)
311	H2COp(d5)	1	2	1	2	H2CO.q1.m2−5.rxyz	−3103.296782	H(d2)+HCOp(s2)	#	0.61	C2V(2−B2)
312	H2COp(q1)	1	4	1	1	H2CO.q1.m4−1.rxyz	−3100.775774	Cp(d2)+H2O(s2)	#	1.63	CS(4−A″)
313	H2COp(q3)	1	4	1	1	H2CO.q1.m4−3.rxyz	−3100.339343	Cp(d2)+H2O(s2)	#	1.20	C1(4−A)
314	HC3p(s1)	1	1	1	2	HC3.q1.m1−1.rxyz	−3109.736543	H(d2)+C3p(d1)	#	3.79	C2V(1−A1)
315	HC3p(s2)	1	1	1	2	HC3.q1.m1−2.rxyz	−3109.736537	H(d2)+C3p(d1)	#	3.79	C2V(1−A1)
316	HC3p(s3)	1	1	1	1	HC3.q1.m1−3.rxyz	−3112.161925	H(d2)+C3p(d1)	#	6.21	C*V(1−SG)
317	HC3p(t1)	1	3	2	1	HC3.q1.m3−1.rxyz	−3110.621832	H(d2)+C3p(d1)	#	4.67	C*V(3−PI)
318	HC3p(t2)	1	3	1	2	HC3.q1.m3−2.rxyz	−3111.285088	H(d2)+C3p(d1)	#	5.34	C2V(3−B2)
319	HC2Op(s1)	1	1	1	1	HC2O.q1.m1−1.rxyz	−4121.973057	C(t1)+HCOp(s1)	#	1.11	CS(1−A′)
320	HC2Op(s2)	1	1	1	1	HC2O.q1.m1−2.rxyz	−4120.216950	HCp(t1)+CO(s2)	#	0.26	CS(1−A′)
321	HC2Op(s3)	1	1	1	1	HC2O.q1.m1−3.rxyz	−4124.295153	C(t1)+HCOp(s1)	#	3.43	CS(1−A′)
322	HC2Op(s4)	1	1	1	1	HC2O.q1.m1−4.rxyz	−4122.138572	C(t1)+HCOp(s1)	#	1.27	C1(1−A)
323	HC2Op(s5)	1	1	1	1	HC2O.q1.m1−5.rxyz	−4123.233575	C(t1)+HCOp(s1)	#	2.37	CS(1−A′)
324	HC2Op(t1)	1	3	1	1	HC2O.q1.m3−1.rxyz	−4122.110160	C(t1)+HCOp(s1)	#	1.24	CS(3−A″)
325	HC2Op(t2)	1	3	1	1	HC2O.q1.m3−2.rxyz	−4121.898404	C(t1)+HCOp(s1)	#	1.03	CS(3−A″)
326	HC2Op(t4)	1	3	1	1	HC2O.q1.m3−4.rxyz	−4122.545145	C(t1)+HCOp(s1)	#	1.68	CS(3−A″)
327	C4p(d1)	1	2	2	2	C4.q1.m2−1.rxyz	−4128.427168	Cp(d2)+C3(s1)	#	5.64	D*H(2−PIG)
328	C4p(d2)	1	2	1	1	C4.q1.m2−2.rxyz	−4128.147757	Cp(d2)+C3(s1)	#	5.36	CS(2−A′)
329	C4p(q1)	1	4	1	4	C4.q1.m4−1.rxyz	−4127.823323	Cp(d2)+C3(s1)	#	5.03	D2H(4−B3U)
330	C4p(q2)	1	4	1	2	C4.q1.m4−2.rxyz	−4127.279733	Cp(d2)+C3(s1)	#	4.49	C2V(4−A2)
331	C3Op(d2)	1	2	1	1	C3O.q1.m2−2.rxyz	−5140.364237	C2p(q1)+CO(s2)	#	1.51	C*V(2−SG)
332	C3Op(d3)	1	2	1	1	C3O.q1.m2−3.rxyz	−5144.172766	C2p(q1)+CO(s2)	#	5.32	C*V(2−SG)
333	C3Op(d4)	1	2	1	1	C3O.q1.m2−4.rxyz	−5139.751725	C2p(q1)+CO(s2)	#	0.90	C1(2−A)
334	C3Op(q4)	1	4	1	2	C3O.q1.m4−4.rxyz	−5140.161008	C2p(q1)+CO(s2)	#	1.30	C2V(4−A2)
335	C3Op(q5)	1	4	1	1	C3O.q1.m4−5.rxyz	−5140.481765	C2p(q1)+CO(s2)	#	1.63	C1(4−A)
336	H4Cp(d1)	1	2	1	4	H4C.q1.m2−1.rxyz	−1090.288860	H(d2)+H3Cp(s1)	#	2.00	D2D(2−B2)
337	H3C2p(s1)	1	1	1	3	H3C2.q1.m1−1.rxyz	−2109.777475	H(d2)+H2C2p(d1)	#	2.41	C3V(1−A1)
338	H3C2p(s2)	1	1	1	2	H3C2.q1.m1−2.rxyz	−2111.824893	H(d2)+H2C2p(d1)	#	4.46	C2V(1−A1)
339	H3C2p(t2)	1	3	1	1	H3C2.q1.m3−2.rxyz	−2109.963286	H(d2)+H2C2p(d1)	#	2.59	CS(3−A″)
340	H3C2p(t3)	1	3	1	1	H3C2.q1.m3−3.rxyz	−2107.878030	H(d2)+H2C2p(d1)	#	0.51	CS(3−A″)
341	H3COp(s3)	1	1	1	1	H3CO.q1.m1−3.rxyz	−3121.047337	H3p(s7)+CO(s2)	#	0.03	CS(1−A′)
342	H3COp(t2)	1	3	1	1	H3CO.q1.m3−2.rxyz	−3120.637235	H(d2)+H2COp(d3)	#	1.49	CS(3−A″)
343	H3COp(t8)	1	3	1	1	H3CO.q1.m3−8.rxyz	−3120.496623	H(d2)+H2COp(d3)	#	1.35	CS(3−A″)
344	H2C3p(d1)	1	2	2	2	H2C3.q1.m2−1.rxyz	−3130.539108	H(d2)+HC3p(s3)	#	4.71	D*H(2−PIG)
345	H2C3p(d2)	1	2	1	1	H2C3.q1.m2−2.rxyz	−3128.978905	H(d2)+HC3p(s3)	#	3.15	CS(2−A′)
346	H2C3p(d3)	1	2	1	2	H2C3.q1.m2−3.rxyz	−3130.707428	H(d2)+HC3p(s3)	#	4.88	C2V(2−A1)
347	H2C3p(q1)	1	4	1	2	H2C3.q1.m4−1.rxyz	−3127.539259	H(d2)+HC3p(s3)	#	1.71	C2V(4−A2)
348	H2C3p(q2)	1	4	1	2	H2C3.q1.m4−2.rxyz	−3127.956762	H(d2)+HC3p(s3)	#	2.13	C1(4−A)
349	H2C3p(q4)	1	4	1	2	H2C3.q1.m4−4.rxyz	−3126.590137	H(d2)+HC3p(s3)	#	0.76	C2V(4−A2)
350	H2C3p(q5)	1	4	1	1	H2C3.q1.m4−5.rxyz	−3126.438218	H(d2)+HC3p(s3)	#	0.61	CS(4−A″)
351	H2C2Op(d2)	1	2	1	1	H2C2O.q1.m2−2.rxyz	−4142.389598	H2Cp(d18)+CO(s2)	#	2.66	C1(2−A)
352	H2C2Op(d3)	1	2	1	1	H2C2O.q1.m2−3.rxyz	−4144.194004	H2Cp(d18)+CO(s2)	#	4.47	C1(2−A)
353	H2C2Op(q4)	1	4	1	1	H2C2O.q1.m4−4.rxyz	−4139.158811	HC(d1)+HCOp(s1)	#	0.96	CS(4−A″)
354	H2C2Op(q5)	1	4	1	1	H2C2O.q1.m4−5.rxyz	−4139.415957	HC(d1)+HCOp(s1)	#	1.22	CS(4−A″)
355	H2C2Op(q6)	1	4	1	1	H2C2O.q1.m4−6.rxyz	−4139.693669	HC(d1)+HCOp(s1)	#	1.50	CS(4−A″)
356	H2C2Op(q8)	1	4	1	1	H2C2O.q1.m4−8.rxyz	−4140.150401	H2Cp(d18)+CO(s2)	#	0.42	CS(4−A″)
357	HC4p(s1)	1	1	1	2	HC4.q1.m1−1.rxyz	−4147.382699	C(t1)+HC3p(s3)	#	5.07	C2V(1−A1)
358	HC4p(s3)	1	1	1	1	HC4.q1.m1−3.rxyz	−4146.442738	C(t1)+HC3p(s3)	#	4.13	CS(1−A′)
359	HC4p(s4)	1	1	1	1	HC4.q1.m1−4.rxyz	−4147.414890	C(t1)+HC3p(s3)	#	5.10	C*V(1−SG)
360	HC4p(s5)	1	1	1	2	HC4.q1.m1−5.rxyz	−4146.382843	C(t1)+HC3p(s3)	#	4.07	C2V(1−A1)
361	HC4p(t3)	1	3	1	1	HC4.q1.m3−3.rxyz	−4146.538043	C(t1)+HC3p(s3)	#	4.23	CS(3−A″)
362	HC4p(t4)	1	3	1	2	HC4.q1.m3−4.rxyz	−4146.291846	C(t1)+HC3p(s3)	#	3.98	C2V(3−A2)
363	HC4p(t5)	1	3	1	1	HC4.q1.m3−5.rxyz	−4146.538028	C(t1)+HC3p(s3)	#	4.23	CS(3−A″)
364	HC4p(t6)	1	3	1	1	HC4.q1.m3−6.rxyz	−4146.662846	C(t1)+HC3p(s3)	#	4.35	CS(3−A″)
365	HC3Op(s1)	1	1	1	1	HC3O.q1.m1−1.rxyz	−5160.834652	HC2p(t1)+CO(s2)	#	2.76	C1(1−A)
366	HC3Op(s2)	1	1	1	1	HC3O.q1.m1−2.rxyz	−5161.865620	HC2p(t1)+CO(s2)	#	3.79	CS(1−A′)
367	HC3Op(s3)	1	1	1	1	HC3O.q1.m1−3.rxyz	−5164.304223	HC2p(t1)+CO(s2)	#	6.23	C*V(1−SG)
368	HC3Op(t1)	1	3	1	1	HC3O.q1.m3−1.rxyz	−5159.346104	HC2p(t1)+CO(s2)	#	1.27	CS(3−A′)
369	HC3Op(t2)	1	3	1	1	HC3O.q1.m3−2.rxyz	−5159.196692	HC2p(t1)+CO(s2)	#	1.12	C1(3−A)
370	C4Op(d1)	1	2	1	1	C4O.q1.m2−1.rxyz	−6179.525308	CO(s2)+C3p(d1)	#	2.86	CS(2−A′)
371	H4C2p(d1)	1	2	1	1	H4C2.q1.m2−1.rxyz	−2124.041604	H2(s2)+H2C2p(d2)	#	0.13	CS(2−A′)
372	H4C2p(d6)	1	2	1	4	H4C2.q1.m2−6.rxyz	−2128.892769	H2(s2)+H2C2p(d1)	#	3.09	D2(2−B3)
373	H4C2p(q1)	1	4	1	1	H4C2.q1.m4−1.rxyz	−2123.561926	H(d2)+	#	0.12	C1(4−A)
374	H4COp(d3)	1	2	1	1	H4CO.q1.m2−3.rxyz	−3139.418728	H2(s2)+H2COp(d3)	#	1.84	CS(2−A″)
375	H3C3p(s1)	1	1	1	6	H3C3.q1.m1−1.rxyz	−3150.021178	H(d2)+H2C3p(d3)	#	5.65	D3H(1−A1′)
376	H3C3p(s3)	1	1	1	1	H3C3.q1.m1−3.rxyz	−3146.915732	H(d2)+H2C3p(d3)	#	2.54	CS(1−A′)
377	H3C3p(s9)	1	1	2	1	H3C3.q1.m1−9.rxyz	−3148.923926	H(d2)+H2C3p(d3)	#	4.55	CS(1−A′)
378	H3C3p(t1)	1	3	1	1	H3C3.q1.m3−1.rxyz	−3145.784259	H(d2)+H2C3p(d3)	#	1.41	CS(3−A′)
379	H3C3p(t2)	1	3	1	1	H3C3.q1.m3−2.rxyz	−3144.706435	H(d2)+H2C3p(d3)	#	0.33	C1(3−A)
380	H3C3p(t3)	1	3	1	1	H3C3.q1.m3−3.rxyz	−3145.888564	H(d2)+H2C3p(d3)	#	1.51	CS(3−A′)

381	H3C2Op(s1)	1	1	1	3	H3C2O.q1.m1−1.rxyz	−4162.518505	H3Cp(s1)+CO(s2)	#	3.51	C3V(1−A1)
382	H3C2Op(s2)	1	1	1	1	H3C2O.q1.m1−2.rxyz	−4157.002116	H2C(t7)+HCOp(s1)	#	0.52	CS(1−A′)
383	H3C2Op(s4)	1	1	1	1	H3C2O.q1.m1−4.rxyz	−4157.922363	H(d2)+H2C2Op(d3)	#	0.06	CS(1−A′)
384	H3C2Op(s5)	1	1	1	1	H3C2O.q1.m1−5.rxyz	−4160.058913	H3Cp(s1)+CO(s2)	#	1.05	CS(1−A′)
385	H3C2Op(s6)	1	1	1	1	H3C2O.q1.m1−6.rxyz	−4160.813824	H3Cp(s1)+CO(s2)	#	1.81	CS(1−A′)
386	H3C2Op(t2)	1	3	1	1	H3C2O.q1.m3−2.rxyz	−4159.101114	H3Cp(s1)+CO(s2)	#	0.10	CS(3−A″)
387	H2C4p(d2)	1	2	1	2	H2C4.q1.m2−2.rxyz	−4163.312914	H(d2)+HC4p(s4)	#	2.23	C2V(2−A2)
388	H2C4p(d3)	1	2	1	2	H2C4.q1.m2−3.rxyz	−4166.211464	H(d2)+HC4p(s4)	#	5.13	C2V(2−B1)
389	H2C4p(d4)	1	2	1	1	H2C4.q1.m2−4.rxyz	−4165.296177	H(d2)+HC4p(s4)	#	4.21	C1(2−A)
390	H2C4p(d7)	1	2	1	1	H2C4.q1.m2−7.rxyz	−4165.749950	H(d2)+HC4p(s4)	#	4.67	CS(2−A″)
391	H2C4p(d9)	1	2	1	2	H2C4.q1.m2−9.rxyz	−4166.637317	H(d2)+HC4p(s4)	#	5.56	C2H(2−AG)
392	H2C4p(q1)	1	4	1	1	H2C4.q1.m4−1.rxyz	−4163.851070	H(d2)+HC4p(s4)	#	2.77	CS(4−A″)
393	H2C4p(q2)	1	4	1	2	H2C4.q1.m4−2.rxyz	−4165.183449	H(d2)+HC4p(s4)	#	4.10	C2V(4−B1)
394	H2C4p(q4)	1	4	1	2	H2C4.q1.m4−4.rxyz	−4164.684310	H(d2)+HC4p(s4)	#	3.60	C2V(4−A2)
395	H2C4p(q5)	1	4	1	1	H2C4.q1.m4−5.rxyz	−4160.918679	C(t1)+H2C3p(d3)	#	0.06	C1(4−A)
396	H2C4p(q6)	1	4	1	1	H2C4.q1.m4−6.rxyz	−4163.844843	H(d2)+HC4p(s4)	#	2.76	C1(4−A)
397	H2C4p(q7)	1	4	1	1	H2C4.q1.m4−7.rxyz	−4164.150404	H(d2)+HC4p(s4)	#	3.07	CS(4−A″)
398	H2C4p(q8)	1	4	1	1	H2C4.q1.m4−8.rxyz	−4164.454721	H(d2)+HC4p(s4)	#	3.37	C1(4−A)
399	H2C4p(q9)	1	4	1	2	H2C4.q1.m4−9.rxyz	−4164.024964	H(d2)+HC4p(s4)	#	2.94	C2V(4−A2)
400	H2C3Op(q3)	1	4	1	1	H2C3O.q1.m4−3.rxyz	−5171.490564	H2Cp(d18)+C2O(s2)	#	0.02	C1(4−A)
401	HC4Op(s1)	1	1	1	1	HC4O.q1.m1−1.rxyz	−6198.625165	CO(s2)+HC3p(s3)	#	2.08	CS(1−A′)
402	HC4Op(s2)	1	1	1	1	HC4O.q1.m1−2.rxyz	−6194.570185	C(t1)+HC3Op(s3)	#	0.12	CS(1−A′)
403	HC4Op(s3)	1	1	1	1	HC4O.q1.m1−3.rxyz	−6194.243864	CO(s2)+HC3p(s1)	#	0.12	C1(1−A)
404	HC4Op(s6)	1	1	1	1	HC4O.q1.m1−6.rxyz	−6196.543504	CO(s2)+HC3p(t2)	#	0.87	CS(1−A′)
405	HC4Op(s7)	1	1	1	1	HC4O.q1.m1−7.rxyz	−6192.642583	HCOp(s2)+C3(t1)	#	0.27	C1(1−A)
406	H4C3p(d1)	1	2	1	1	H4C3.q1.m2−1.rxyz	−3164.567164	H(d2)+H3C3p(s1)	#	0.88	C1(2−A)
407	H4C3p(d2)	1	2	1	1	H4C3.q1.m2−2.rxyz	−3164.776746	H(d2)+H3C3p(s1)	#	1.09	C1(2−A)
408	H4C3p(d3)	1	2	1	1	H4C3.q1.m2−3.rxyz	−3162.954141	H2(s2)+H2C3p(d3)	#	0.15	CS(2−A″)
409	H4C3p(d4)	1	2	1	1	H4C3.q1.m2−4.rxyz	−3164.472414	H(d2)+H3C3p(s1)	#	0.78	CS(2−A′)
410	H4C3p(d6)	1	2	1	2	H4C3.q1.m2−6.rxyz	−3164.472414	H(d2)+H3C3p(s1)	#	0.78	C2(2−B)
411	H4C3p(q1)	1	4	1	1	H4C3.q1.m4−1.rxyz	−3161.753281	H2(s2)+H2C3p(d2)	#	0.68	CS(4−A″)
412	H4C3p(q2)	1	4	1	2	H4C3.q1.m4−2.rxyz	−3162.740820	H2(s2)+H2C3p(d1)	#	0.10	C2V(4−B2)
413	H4C3p(q3)	1	4	1	1	H4C3.q1.m4−3.rxyz	−3161.515806	H2(s2)+H2C3p(d2)	#	0.44	CS(4−A″)
414	H4C3p(q4)	1	4	1	1	H4C3.q1.m4−4.rxyz	−3162.606689	H(d2)+H3C3p(s9)	#	0.02	C1(4−A)
415	H4C3p(q5)	1	4	1	1	H4C3.q1.m4−5.rxyz	−3161.194663	H2(s2)+H2C3p(d2)	#	0.12	CS(4−A″)
416	H4C3p(q6)	1	4	1	2	H4C3.q1.m4−6.rxyz	−3161.702336	H2(s2)+H2C3p(d2)	#	0.63	C2(4−B)
417	H3C4p(s1)	1	1	1	3	H3C4.q1.m1−1.rxyz	−4183.779001	H(d2)+H2C4p(d9)	#	3.47	C3V(1−A1)
418	H3C4p(s2)	1	1	1	2	H3C4.q1.m1−2.rxyz	−4185.752393	H(d2)+H2C4p(d9)	#	5.45	C2V(1−A1)
419	H3C4p(s3)	1	1	1	1	H3C4.q1.m1−3.rxyz	−4182.647615	H(d2)+H2C4p(d9)	#	2.34	C1(1−A)
420	H3C4p(s5)	1	1	1	1	H3C4.q1.m1−5.rxyz	−4184.785199	H(d2)+H2C4p(d9)	#	4.48	CS(1−A′)
421	H3C4p(s7)	1	1	1	1	H3C4.q1.m1−7.rxyz	−4184.234426	H(d2)+H2C4p(d9)	#	3.93	C1(1−A)
422	H3C4p(s10)	1	1	1	1	H3C4.q1.m1−10.rxyz	−4180.551637	H(d2)+H2C4p(d9)	#	0.25	CS(1−A′)
423	H3C4p(s11)	1	1	1	1	H3C4.q1.m1−11.rxyz	−4180.573191	H(d2)+H2C4p(d9)	#	0.27	C1(1−A)
424	H3C4p(s13)	1	1	1	2	H3C4.q1.m1−13.rxyz	−4184.804281	H(d2)+H2C4p(d9)	#	4.50	C2V(1−A1)
425	H3C4p(s15)	1	1	1	1	H3C4.q1.m1−15.rxyz	−4184.274931	H(d2)+H2C4p(d9)	#	3.97	C1(1−A)
426	H3C4p(t1)	1	3	1	1	H3C4.q1.m3−1.rxyz	−4182.032425	H(d2)+H2C4p(d9)	#	1.73	CS(3−A″)
427	H3C4p(t2)	1	3	1	2	H3C4.q1.m3−2.rxyz	−4184.392526	H(d2)+H2C4p(d9)	#	4.09	C2V(3−A2)
428	H3C4p(t3)	1	3	1	1	H3C4.q1.m3−3.rxyz	−4182.744498	H(d2)+H2C4p(d9)	#	2.44	CS(3−A″)
429	H3C4p(t4)	1	3	1	1	H3C4.q1.m3−4.rxyz	−4181.582626	H(d2)+H2C4p(d9)	#	1.28	CS(3−A″)
430	H3C4p(t5)	1	3	1	1	H3C4.q1.m3−5.rxyz	−4184.083303	H(d2)+H2C4p(d9)	#	3.78	CS(3−A″)
431	H3C4p(t7)	1	3	1	1	H3C4.q1.m3−7.rxyz	−4183.745815	H(d2)+H2C4p(d9)	#	3.44	CS(3−A″)
432	H3C4p(t8)	1	3	1	1	H3C4.q1.m3−8.rxyz	−4180.820135	H(d2)+H2C4p(d9)	#	0.52	C1(3−A)
433	H3C4p(t10)	1	3	1	1	H3C4.q1.m3−10.rxyz	−4182.420230	H(d2)+H2C4p(d9)	#	2.12	C1(3−A)
434	H3C4p(t11)	1	3	1	1	H3C4.q1.m3−11.rxyz	−4181.605034	H(d2)+H2C4p(d9)	#	1.30	C1(3−A)
435	H3C4p(t12)	1	3	1	1	H3C4.q1.m3−12.rxyz	−4183.433032	H(d2)+H2C4p(d9)	#	3.13	CS(3−A″)
436	H3C4p(t13)	1	3	1	1	H3C4.q1.m3−13.rxyz	−4182.214560	H(d2)+H2C4p(d9)	#	1.91	CS(3−A″)
437	H3C4p(t14)	1	3	1	1	H3C4.q1.m3−14.rxyz	−4182.184756	H(d2)+H2C4p(d9)	#	1.88	C1(3−A)
438	H3C4p(t15)	1	3	1	1	H3C4.q1.m3−15.rxyz	−4181.772141	H(d2)+H2C4p(d9)	#	1.47	CS(3−A′)
439	H3C3Op(s1)	1	1	1	1	H3C3O.q1.m1−1.rxyz	−5195.202750	H3C2p(t2)+CO(s2)	#	0.85	CS(1−A′)
440	H3C3Op(s2)	1	1	1	1	H3C3O.q1.m1−2.rxyz	−5198.096938	H2(s2)+HC3Op(s3)	#	1.69	CS(1−A′)
441	H3C3Op(s5)	1	1	1	1	H3C3O.q1.m1−5.rxyz	−5197.675208	H2(s2)+HC3Op(s3)	#	1.27	CS(1−A′)
442	H3C3Op(s6)	1	1	1	1	H3C3O.q1.m1−6.rxyz	−5197.675210	H2(s2)+HC3Op(s3)	#	1.27	CS(1−A′)
443	H2C4Op(d1)	1	2	1	1	H2C4O.q1.m2−1.rxyz	−6211.029970	CO(s2)+H2C3p(q4)	#	0.05	C1(2−A)
444	H2C4Op(d2)	1	2	1	1	H2C4O.q1.m2−2.rxyz	−6211.029970	CO(s2)+H2C3p(q4)	#	0.05	CS(2−A″)
445	H2C4Op(d4)	1	2	1	1	H2C4O.q1.m2−4.rxyz	−6211.029970	CO(s2)+H2C3p(q4)	#	0.05	C1(2−A)
446	H2C4Op(d5)	1	2	1	1	H2C4O.q1.m2−5.rxyz	−6211.029970	CO(s2)+H2C3p(q4)	#	0.05	C1(2−A)
447	H2C4Op(d6)	1	2	1	1	H2C4O.q1.m2−6.rxyz	−6211.029970	CO(s2)+H2C3p(q4)	#	0.05	CS(2−A″)
448	H2C4Op(q1)	1	4	1	1	H2C4O.q1.m4−1.rxyz	−6214.214654	CO(s2)+H2C3p(d2)	#	0.85	C1(4−A)
449	H4C4p(d1)	1	2	1	1	H4C4.q1.m2−1.rxyz	−4199.981298	H(d2)+H3C4p(s2)	#	0.56	C1(2−A)
450	H4C4p(d2)	1	2	1	1	H4C4.q1.m2−2.rxyz	−4201.883229	H(d2)+H3C4p(s2)	#	2.46	CS(2−A″)
451	H4C4p(d3)	1	2	1	1	H4C4.q1.m2−3.rxyz	−4201.746386	H(d2)+H3C4p(s2)	#	2.33	C1(2−A)
452	H4C4p(d4)	1	2	1	2	H4C4.q1.m2−4.rxyz	−4202.874576	H(d2)+H3C4p(s2)	#	3.46	C2V(2−B1)
453	H4C4p(d5)	1	2	1	1	H4C4.q1.m2−5.rxyz	−4199.552871	H(d2)+H3C4p(s2)	#	0.13	C1(2−A)
454	H4C4p(d6)	1	2	1	1	H4C4.q1.m2−6.rxyz	−4202.617769	H(d2)+H3C4p(s2)	#	3.20	CS(2−A″)
455	H4C4p(d7)	1	2	1	1	H4C4.q1.m2−7.rxyz	−4200.520881	H(d2)+H3C4p(s2)	#	1.10	C1(2−A)
456	H4C4p(d8)	1	2	1	1	H4C4.q1.m2−8.rxyz	−4201.111169	H(d2)+H3C4p(s2)	#	1.69	CS(2−A′)
457	H4C4p(d9)	1	2	1	1	H4C4.q1.m2−9.rxyz	−4198.349090	H2(s2)+H2C4p(d3)	#	0.04	C1(2−A)
458	H4C4p(d10)	1	2	1	1	H4C4.q1.m2−10.rxyz	−4198.349088	H2(s2)+H2C4p(d3)	#	0.04	C1(2−A)
459	H4C4p(d11)	1	2	1	1	H4C4.q1.m2−11.rxyz	−4199.471006	H(d2)+H3C4p(s2)	#	0.05	C1(2−A)
460	H4C4p(d12)	1	2	1	1	H4C4.q1.m2−12.rxyz	−4200.414074	H(d2)+H3C4p(s2)	#	0.99	CS(2−A″)
461	H4C4p(d13)	1	2	1	4	H4C4.q1.m2−13.rxyz	−4202.486088	H(d2)+H3C4p(s2)	#	3.07	D2H(2−B2G)

462	H4C4p(d14)	1	2	1	1	H4C4.q1.m2−14.rxyz	−4201.626865	H(d2)+H3C4p(s2)	#	2.21	C1(2−A)
463	H4C4p(d15)	1	2	1	1	H4C4.q1.m2−15.rxyz	−4201.111168	H(d2)+H3C4p(s2)	#	1.69	CS(2−A′)
464	H4C4p(d17)	1	2	1	1	H4C4.q1.m2−17.rxyz	−4199.757591	H(d2)+H3C4p(s2)	#	0.34	C2H(2−BU)
465	H4C4p(d18)	1	2	1	4	H4C4.q1.m2−18.rxyz	−4201.140000	H(d2)+H3C4p(s2)	#	1.72	D2D(2−A1)
466	H4C4p(d19)	1	2	1	4	H4C4.q1.m2−19.rxyz	−4202.794899	H(d2)+H3C4p(s2)	#	3.38	D2(2−B2)
467	H4C4p(q1)	1	4	1	1	H4C4.q1.m4−1.rxyz	−4198.156437	H(d2)+H3C4p(t2)	#	0.10	C1(4−A)
468	H4C4p(q2)	1	4	1	1	H4C4.q1.m4−2.rxyz	−4199.159433	H2(s2)+H2C4p(d9)	#	0.42	C1(4−A)
469	H4C4p(q3)	1	4	1	1	H4C4.q1.m4−3.rxyz	−4197.261950	H(d2)+H3C4p(t12)	#	0.16	C1(4−A)
470	H4C4p(q4)	1	4	1	1	H4C4.q1.m4−4.rxyz	−4199.750983	H(d2)+H3C4p(s2)	#	0.33	C1(4−A)
471	H4C4p(q5)	1	4	1	1	H4C4.q1.m4−5.rxyz	−4197.070282	HC2(d1)+H3C2p(s2)	#	0.01	CS(4−A″)
472	H4C4p(q6)	1	4	1	1	H4C4.q1.m4−6.rxyz	−4199.293140	H2(s2)+H2C4p(d9)	#	0.56	C1(4−A)
473	H4C4p(q7)	1	4	1	2	H4C4.q1.m4−7.rxyz	−4199.741269	H(d2)+H3C4p(s2)	#	0.32	C2H(4−AU)
474	H4C4p(q8)	1	4	1	1	H4C4.q1.m4−8.rxyz	−4197.849348	H2(s2)+H2C4p(d7)	#	0.00	C1(4−A)
475	H4C4p(q9)	1	4	1	1	H4C4.q1.m4−9.rxyz	−4197.243924	H(d2)+H3C4p(t12)	#	0.14	CS(4−A″)
476	H4C4p(q10)	1	4	1	1	H4C4.q1.m4−10.rxyz	−4196.642011	HC(q24)+H3C3p(s1)	#	0.04	C1(4−A)
477	H4C4p(q11)	1	4	1	1	H4C4.q1.m4−11.rxyz	−4197.250344	H(d2)+H3C4p(t12)	#	0.15	C1(4−A)
478	H4C4p(q12)	1	4	1	1	H4C4.q1.m4−12.rxyz	−4198.956395	H2(s2)+H2C4p(d9)	#	0.22	CS(4−A″)
479	H4C4p(q13)	1	4	1	2	H4C4.q1.m4−13.rxyz	−4199.136773	H2(s2)+H2C4p(d9)	#	0.40	C2H(4−AU)
480	H4C4p(q14)	1	4	1	1	H4C4.q1.m4−14.rxyz	−4198.827197	H2(s2)+H2C4p(d9)	#	0.09	C1(4−A)
481	H4C4p(q15)	1	4	1	2	H4C4.q1.m4−15.rxyz	−4199.016424	H2(s2)+H2C4p(d9)	#	0.28	C2V(4−B2)
482	H4C4p(q16)	1	4	1	2	H4C4.q1.m4−16.rxyz	−4198.442984	H2(s2)+H2C4p(d3)	#	0.13	C2V(4−A2)
483	H4C4p(q17)	1	4	1	2	H4C4.q1.m4−17.rxyz	−4198.015534	H(d2)+H3C4p(s15)	#	0.07	C2V(4−B1)
484	H4C4p(q18)	1	4	1	1	H4C4.q1.m4−18.rxyz	−4198.956365	H2(s2)+H2C4p(d9)	#	0.22	C1(4−A)
485	H4C4p(q19)	1	4	1	4	H4C4.q1.m4−19.rxyz	−4199.779816	H(d2)+H3C4p(s2)	#	0.36	D2(4−B3)
486	H4C3Op(d2)	1	2	1	1	H4C3O.q1.m2−2.rxyz	−5210.851679	H2C2p(d1)+H2CO(s1)	#	0.31	C1(2−A)
487	H4C3Op(d4)	1	2	1	1	H4C3O.q1.m2−4.rxyz	−5214.059844	CO(s2)+H4C2p(d6)	#	0.78	CS(2−A″)
488	H4C3Op(q1)	1	4	1	1	H4C3O.q1.m4−1.rxyz	−5209.874929	H3C2(d2)+HCOp(s2)	#	0.30	C1(4−A)
489	H4C3Op(q2)	1	4	1	1	H4C3O.q1.m4−2.rxyz	−5208.779730	H2C2p(d2)+H2CO(s1)	#	0.13	C1(4−A)
490	H4C3Op(q3)	1	4	1	1	H4C3O.q1.m4−3.rxyz	−5210.772550	H2C2p(d1)+H2CO(s1)	#	0.23	C1(4−A)
491	H3C4Op(s1)	1	1	1	1	H3C4O.q1.m1−1.rxyz	−6232.352229	CO(s2)+H3C3p(s3)	#	1.05	C1(1−A)
492	H3C4Op(s2)	1	1	1	1	H3C4O.q1.m1−2.rxyz	−6232.254464	CO(s2)+H3C3p(s3)	#	0.95	C1(1−A)
493	H3C4Op(s3)	1	1	1	1	H3C4O.q1.m1−3.rxyz	−6231.249319	H2(s2)+HC4Op(s1)	#	0.53	C1(1−A)
494	H3C4Op(s4)	1	1	1	1	H3C4O.q1.m1−4.rxyz	−6234.138858	CO(s2)+H3C3p(s9)	#	0.83	C1(1−A)
495	H3C4Op(s5)	1	1	1	1	H3C4O.q1.m1−5.rxyz	−6234.580982	CO(s2)+H3C3p(s1)	#	0.17	C1(1−A)
496	C4H4Op(d1)	1	2	1	1	C4H4O.q1.m2−1.rxyz	−6250.401041	HCO(d7)+H3C3p(s1)	#	1.24	CS(2−A′)
497	C4H4Op(d2)	1	2	1	1	C4H4O.q1.m2−2.rxyz	−6251.024034	H2C2(s2)+H2C2Op(d3)	#	1.85	C1(2−A)
498	C4H4Op(d3)	1	2	1	2	C4H4O.q1.m2−3.rxyz	−6252.230613	H2C2(s2)+H2C2Op(d3)	#	3.05	C2V(2−A2)
499	C4H4Op(d4)	1	2	1	1	C4H4O.q1.m2−4.rxyz	−6249.928268	H2C2(s2)+H2C2Op(d3)	#	0.75	CS(2−A′)
500	C4H4Op(d5)	1	2	1	1	C4H4O.q1.m2−5.rxyz	−6250.626673	HCO(d7)+H3C3p(s1)	#	1.46	CS(2−A″)
501	C4H4Op(d6)	1	2	1	1	C4H4O.q1.m2−6.rxyz	−6250.027479	H2C2(s2)+H2C2Op(d3)	#	0.85	C1(2−A)
502	C4H4Op(d7)	1	2	1	1	C4H4O.q1.m2−7.rxyz	−6251.359739	H2C2(s2)+H2C2Op(d3)	#	2.18	CS(2−A′)
503	C4H4Op(d8)	1	2	1	1	C4H4O.q1.m2−8.rxyz	−6249.560369	HCO(d7)+H3C3p(s1)	#	0.40	CS(2−A″)
504	C4H4Op(d9)	1	2	1	1	C4H4O.q1.m2−9.rxyz	−6252.200165	H2C2(s2)+H2C2Op(d3)	#	3.02	CS(2−A″)
505	C4H4Op(d10)	1	2	1	1	C4H4O.q1.m2−10.rxyz	−6250.736228	HCO(d7)+H3C3p(s1)	#	1.57	CS(2−A′)
506	C4H4Op(d11)	1	2	1	1	C4H4O.q1.m2−11.rxyz	−6250.388866	H2C2(s2)+H2C2Op(d3)	#	1.21	C1(2−A)
507	C4H4Op(d12)	1	2	1	1	C4H4O.q1.m2−12.rxyz	−6250.469588	H2C2(s2)+H2C2Op(d3)	#	1.29	C1(2−A)
508	C4H4Op(d13)	1	2	1	1	C4H4O.q1.m2−13.rxyz	−6250.453165	H2C2(s2)+H2C2Op(d3)	#	1.28	C1(2−A)
509	C4H4Op(d14)	1	2	1	1	C4H4O.q1.m2−14.rxyz	−6249.709468	H2C2(s2)+H2C2Op(d3)	#	0.53	CS(2−A′)
510	C4H4Op(d15)	1	2	1	1	C4H4O.q1.m2−15.rxyz	−6251.097207	H2C2(s2)+H2C2Op(d3)	#	1.92	C1(2−A)
511	C4H4Op(d16)	1	2	1	1	C4H4O.q1.m2−16.rxyz	−6251.078759	HCO(d7)+H3C3p(s1)	#	1.92	C1(2−A)
512	C4H4Op(d19)	1	2	1	1	C4H4O.q1.m2−19.rxyz	−6250.169761	H2C2(s2)+H2C2Op(d3)	#	0.99	CS(2−A′)
513	C4H4Op(d20)	1	2	1	1	C4H4O.q1.m2−20.rxyz	−6250.605822	H2C2(s2)+H2C2Op(d3)	#	1.43	C1(2−A)

```
514   #----------------------------------------------------------------------------
515   END FRAGMENTS_DATABASE
516
517   BEGIN EXPERIMENTAL_BRANCHING_RATIOS
518   error = absolute
519   diagram = S.vs.E
520   #------------------------------------------------
521   #  Channel      BR     error    q/n
522   #------------------------------------------------
523   Hp        0.0      0.0      1.0
524   H2p       0.0      0.0      2.0
525   H3p       0.0      0.0      3.0
526   Cp        0.0      0.0     12.0
527   HCp       0.0      0.0     13.0
528   H2Cp      0.0      0.0     14.0
529   H3Cp      0.0      0.0     15.0
530   H4Cp      0.0      0.0     16.0
531   HOp       0.0      0.0     17.0
532   H2Op      0.0      0.0     18.0
533   H3Op      0.0      0.0     19.0
534   H4Op      0.0      0.0     20.0
535   C2p       3.70     0.0     24.0
536   HC2p      1.88     0.0     25.0
537   H2C2p     1.56     0.0     26.0
538   H3C2p     0.27     0.0     27.0
539   COp       2.71     0.0     28.0
540   HCOp      9.49     0.0     29.0
541   H2COp     0.0      0.0     30.0
542   H3COp     0.0      0.0     31.0
```

```
543   H4COp        0.0        0.0      32.0
544   C3p          2.17       0.0      36.0
545   HC3p         4.10       0.0      37.0
546   H2C3p        7.50       0.0      38.0
547   H3C3p       19.49       0.0      39.0
548   H4C3p        2.23       0.0      40.0
549   HC2Op        0.62       0.0      41.0
550   H2C2Op       1.45       0.0      42.0
551   H3C2Op       0.0        0.0      43.0
552   H4C2Op       0.0        0.0      44.0
553   C4p          0.0        0.0      48.0
554   HC4p         0.0        0.0      49.0
555   H2C4p        0.0        0.0      50.0
556   H3C4p        0.06       0.0      51.0
557   H4C4p        0.14       0.0      52.0
558   HC3Op        0.20       0.0      53.0
559   H2C3Op       0.04       0.0      54.0
560   H3C3Op       0.0        0.0      55.0
561   H4C3Op       0.0        0.0      56.0
562   C4Op         0.0        0.0      64.0
563   HC4Op        0.0        0.0      65.0
564   H2C4Op       0.09       0.0      66.0
565   H3C4Op       0.13       0.0      67.0
566   C4H4Op      40.33       0.0      68.0
567   #-------------------------------------------
568
569   END EXPERIMENTAL_BRANCHING_RATIOS
570
571   BEGIN FIT_BRANCHING_RATIOS
572   method = NNLS
573   basis = 60,60
574   eDistfile = O6.edist.dat
575   BRfile = O6.fitBR.dat
576   END FIT_BRANCHING_RATIOS
```

Bibliography

[1] M. Dampc and M. Zubek, "Dissociation and fragmentation of furan by electron impact", *International Journal of Mass Spectrometry*, vol. 277, no. 1-3, pp. 52–56, 2008. DOI: `10.1016/j.ijms.2008.04.010`.

[2] M. Dampc, I. Linert, and M. Zubek, "Ionization and fragmentation of furan molecules by electron collisions", *Journal of Physics B: Atomic, Molecular and Optical Physics*, vol. 48, no. 16, p. 165 202, 2015. DOI: `10.1088/0953-4075/48/16/165202`.

[3] Z. D. Pešić, D. Rolles, I. Dumitriu, and N. Berrah, "Fragmentation dynamics of gas-phase furan following *K*-shell ionization", *Physical Review A*, vol. 82, no. 1, p. 013 401, 2010. DOI: `10.1103/PhysRevA.82.013401`.

[4] M. K. Akalın and S. Karagöz, "Analytical pyrolysis of biomass using gas chromatography coupled to mass spectrometry", *TrAC Trends in Analytical Chemistry*, vol. 61, pp. 11 –16, 2014. DOI: `10.1016/j.trac.2014.06.006`.

[5] F. M. Kerton and N. Yan, *9.7.3 pyrolysis*, 2017.

[6] J. Laskin and C. Lifshitz, "Kinetic energy release distributions in mass spectrometry", *Journal of Mass Spectrometry*, vol. 36, no. 5, pp. 459–478, 2001. DOI: `10.1002/jms.164`.

[7] J. de Vries, R. Hoekstra, R. Morgenstern, and T. Schlathölter, "C^{q+}-induced excitation and fragmentation of uracil: effects of the projectile electronic structure", *Journal of Physics B: Atomic, Molecular and Optical Physics*, vol. 35, no. 21, p. 4373, 2002. DOI: `10.1088/0953-4075/35/21/304`.

[8] M. C. Bacchus-Montabonel, M. Łabuda, Y. S. Tergiman, and J. E. Sienkiewicz, "Theoretical treatment of charge-transfer processes induced by collision of C^{q+} ions with uracil", *Physical Review A*, vol. 72, p. 052 706, 5 2005. DOI: `10.1103/PhysRevA.72.052706`.

[9] T. Ridley, K. P. Lawley, M. H. Al-Kahali, and R. J. Donovan, "Determination of the first ionization energy of furan (C_4H_4O) from an extrapolation of two *n*d Rydberg series observed in the mass-resolved (2+1) resonance enhanced multiphoton ionization spectrum", *Chemical Physics Letters*, vol. 390, no. 4, pp. 376 –379, 2004. DOI: `10.1016/j.cplett.2004.04.052`.

[10] P. R. Nelson, C. A. F. Kee Fung, J. B. Sedgwick, G. C. Shields, L. E. Abbey, and T. F. Moran, "Doubly charged ion mass spectra of alkyl-substituted furans and pyrroles", *Organic Mass Spectrometry*, vol. 22, no. 7, pp. 389–399, 1987. DOI: `10.1002/oms.1210220703`.

[11] E. Rennie, C. Johnson, J. Parker, D. Holland, D. Shaw, M. MacDonald, M. Hayes, and L. Shpinkova, "A study of the spectroscopic and thermodynamic properties of furan by means of photoabsorption, photoelectron and photoion spectroscopy", *Chemical Physics*, vol. 236, no. 1-3, pp. 365–385, 1998. DOI: 10.1016/S0301-0104(98)00229-8.

[12] L. Wei, C. Tang, X. Man, X. Jiang, and Z. Huang, "High-temperature ignition delay times and kinetic study of furan", *Energy and Fuels*, vol. 26, no. 4, pp. 2075–2081, 2012. DOI: 10.1021/ef300336y.

[13] J. P. Mathews and A. L. Chaffee, "The molecular representations of coal – a review", *Fuel*, vol. 96, pp. 1–14, 2012. DOI: 10.1016/j.fuel.2011.11.025.

[14] J. Sperry and D. Wright, "Furans thiophenes and related heterocycles in drug discovery", *Current Opinion in Drug Discovery Development*, vol. 8, pp. 723–740, 2006. DOI: 10.1002/chin.200615242.

[15] D. G. Hatzinikolaou, V. Lagesson, A. J. Stavridou, A. E. Pouli, L. Lagesson-Andrasko, and J. C. Stavrides, "Analysis of the Gas Phase of Cigarette Smoke by Gas Chromatography Coupled with UV-Diode Array Detection", *Analytical Chemistry*, vol. 78, no. 13, pp. 4509–4516, 2006. DOI: 10.1021/ac052004y.

[16] S. Moro, J. K. Chipman, J.-W. Wegener, C. Hamberger, W. Dekant, and A. Mally, "Furan in heat-treated foods: Formation, exposure, toxicity, and aspects of risk assessment", *Molecular Nutrition & Food Research*, vol. 56, no. 8, pp. 1197–1211, 2012. DOI: 10.1002/mnfr.201200093.

[17] J. Ward, "DNA Damage Produced by Ionizing Radiation in Mammalian Cells: Identities, Mechanisms of Formation and Reparability", *Progress in Nucleic Acid Research and Molecular Biology*, vol. 35, pp. 95–125, 1988. DOI: 10.1016/S0079-6603(08)60611-X.

[18] K. K. Khanna and S. P. Jackson, "DNA double-strand breaks: signaling, repair and the cancer connection", *Nature Genetics*, vol. 27, pp. 247–254, 2001. DOI: 10.1038/85798.

[19] B. D. Michael and P. O'Neill, "A sting in the tail of electron tracks", *Science*, vol. 287, no. 5458, pp. 1603–1604, 2000. DOI: 10.1126/science.287.5458.1603.

[20] L. Sanche, "Low energy electron-driven damage in biomolecules", *The European Physical Journal D - Atomic, Molecular, Optical and Plasma Physics*, vol. 35, no. 2, pp. 367–390, 2005. DOI: 10.1140/epjd/e2005-00206-6.

[21] B. Balasubramanian, W. K. Pogozelski, and T. D. Tullius, "DNA strand breaking by the hydroxyl radical is governed by the accessible surface areas of the hydrogen atoms of the DNA backbone", *Proceedings of the National Academy of Sciences*, vol. 95, no. 17, pp. 9738–9743, 1998. DOI: 10.1073/pnas.95.17.9738.

[22] M. A. Grela, V. T. Amorebieta, and A. J. Colussi, "Very low pressure pyrolysis of furan, 2-methylfuran, and 2,5-dimethylfuran. The stability of the furan ring", *Journal of Physical Chemistry*, vol. 89, no. 1, pp. 38–41, 1985. DOI: 10.1021/j100247a011.

[23] A. Lifshitz, M. Bidani, and S. Bidani, "Thermal Reactions of Cyclic Ethers at High Temperatures. 3. Pyrolysis of Furan behind Reflected Shocks", *The Journal of Physical Chemistry*, vol. 90, pp. 5373–5377, 1986. DOI: `10.1021/j100412a096`.

[24] P. P. Organ and J. C. Mackie, "Kinetics Pyrolysis Furan", *Journal of the Chemical Society, Faraday Transactions*, vol. 87, no. 6, pp. 815–823, 1991. DOI: `10.1039/FT9918700815`.

[25] D. Fulle, A. Dib, J. H. Kiefer, Q. Zhang, J. Yao, and R. D. Kern, "Pyrolysis of furan at low pressures: Vibrational relaxation, unimolecular dissociation, and incubation times", *Journal of Physical Chemistry A*, vol. 102, no. 38, pp. 7480–7486, 1998. DOI: `10.1021/jp9823042`.

[26] R. Liu, X. Zhou, and L. Zhai, "Theoretical investigation of unimolecular decomposition channels of furan", *Journal of computational chemistry*, vol. 19, no. 2, pp. 240–249, 1998. DOI: `10.1002/(SICI)1096-987X(19980130)19:2<240::AID-JCC17>3.0.CO; 2-L`.

[27] O. Sorkhabi, F. Qi, A. H. Rizvi, and A. G. Suits, "Ultraviolet photodissociation of furan probed by tunable synchrotron radiation", *Journal of Chemical Physics*, vol. 111, no. 1, pp. 100–107, 1999. DOI: `10.1063/1.479257`.

[28] K. Sendt, G. B. Bacskay, and J. C. Mackie, "Pyrolysis of Furan : Ab Initio Quantum Chemical and Kinetic Modeling Studies", *Journal of Physical Chemistry A*, vol. 104, pp. 1861–1875, 2000. DOI: `10.1021/jp993537b`.

[29] A. Vasiliou, M. R. Nimlos, J. W. Daily, and G. B. Ellison, "Thermal decomposition of furan generates propargyl radicals", *Journal of Physical Chemistry A*, vol. 113, no. 30, pp. 8540–8547, 2009. DOI: `10.1021/jp903401h`.

[30] Z. Tian, T. Yuan, R. Fournet, P. A. Glaude, B. Sirjean, F. Battin-Leclerc, K. Zhang, and F. Qi, "An experimental and kinetic investigation of premixed furan/oxygen/argon flames", *Combustion and Flame*, vol. 158, no. 4, pp. 756–773, 2011. DOI: `10.1016/j.combustflame.2010.12.022`.

[31] K. N. Urness, Q. Guan, A. Golan, J. W. Daily, M. R. Nimlos, J. F. Stanton, M. Ahmed, G. B. Ellison, K. N. Urness, Q. Guan, A. Golan, J. W. Daily, and M. R. Nimlos, "Pyrolysis of furan in a microreactor Pyrolysis of furan in a microreactor", *Journal of Chemical Physics*, vol. 139, p. 124 305, 2013. DOI: `10.1063/1.4821600`.

[32] Z. Cheng, Y. Tan, L. Wei, L. Xing, J. Yang, L. Zhang, Y. Guan, B. Yan, G. Chen, and D. Y. Leung, "Experimental and kinetic modeling studies of furan pyrolysis: Fuel decomposition and aromatic ring formation", *Fuel*, vol. 206, pp. 239–247, 2017. DOI: `10.1016/j.fuel.2017.05.090`.

[33] P. Derrick, L. Åsbrink, O. Edqvist, B.-. Jonsson, and E. Lindholm, "Rydberg series in small molecules: X. photoelectron spectroscopy and electronic structure of furan", *International Journal of Mass Spectrometry and Ion Physics*, vol. 6, no. 3, pp. 161 –175, 1971. DOI: `https://doi.org/10.1016/0020-7381(71)80001-3`.

[34] J. M. Tedder and P. H. Vidaud, "Charge-exchange mass spectra of thiophene, pyrrole and furan", *Journal of the Chemical Society, Faraday Transactions 2: Molecular and Chemical Physics*, vol. 76, pp. 1516–1522, 0 1980. DOI: 10.1039/F29807601516.

[35] D. H. Williams, R. G. Cooks, J. Ronayne, and S. Tam, "Studies in mass spectrometry. Part XXVII. The decomposition of furan, thiophen and deuterated analogues under electron impact", *Tetrahedron Letters*, vol. 9, no. 14, pp. 1777 –1780, 1968. DOI: 10.1016/S0040-4039(01)99049-5.

[36] J. L. Holmes and J. K. Terlouw, "Structures of $[C_4H_4O]^+$ ions produced from 2- and 4-pyrone", *Journal of the American Chemical Society*, vol. 101, no. 17, pp. 4973–4975, 1979. DOI: 10.1021/ja00511a029.

[37] P. C. Burgers, J. L. Holmes, F. P. Lossing, A. A. Mommers, F. R. Povel, and J. K. Terlouw, "Isomeric and tautomeric $[C_4H_4O]^+$ ions; their thermochemistry and collisionally induced fragmentation characteristics", *Canadian Journal of Chemistry*, vol. 60, no. 17, pp. 2246–2255, 1982. DOI: 10.1139/v82-319.

[38] G. D. Willett and T. Baer, "Thermochemistry and Dissociation Dynamics of State-Selected C_4H_4X Ions.", *Journal of the American Chemical Society*, vol. 102, no. 22, pp. 6769–6773, 1980. DOI: 10.1021/ja00542a017.

[39] E. E. Rennie, L. Cooper, C. A. Johnson, J. E. Parker, R. A. Mackie, L. G. Shpinkova, D. M. Holland, D. A. Shaw, and M. A. Hayes, "A study of the unimolecular decomposition of internal-energy-selected furan molecular ions by threshold-photoelectron-photoion coincidence spectroscopy", *Chemical Physics*, vol. 263, no. 1, pp. 149–165, 2001. DOI: 10.1016/S0301-0104(00)00346-3.

[40] G. Wu and A. J. Stace, "IRMPD study of the furan cation in an ion trap: Evidence of the extreme effect a competitive shift can have on reaction pathway", *Chemical Physics Letters*, vol. 412, no. 1-3, pp. 1–4, 2005. DOI: 10.1016/j.cplett.2005.06.083.

[41] M. Al–Kahali, T Ridley, K. P. Lawley, and R. J. Donovan, "On the Fragmentation of Furan Molecule and Its Dependence on the Laser Wavelength", *The Arabian Journal for Science and Engineering*, vol. 33, no. 1A, pp. 51–54, 2008.

[42] M. Winfough, K. Voronova, G. Muller, G. Laguisma, B. Sztáray, A. Bodi, and G. Meloni, "Furfural: The Unimolecular Dissociative Photoionization Mechanism of the Simplest Furanic Aldehyde", *Journal of Physical Chemistry A*, vol. 121, no. 18, pp. 3401–3410, 2017. DOI: 10.1021/acs.jpca.7b01185.

[43] M. Born and R. Oppenheimer, "Zur Quantentheorie der Molekeln", *Annalen der Physik*, vol. 389, no. 20, pp. 457–484, 1927. DOI: 10.1002/andp.19273892002.

[44] I. Mayer, *Simple Theorems, Proofs, and Derivations in Quantum Chemistry*. Springer, Boston, MA, 2003. DOI: 10.1007/978-1-4757-6519-9.

[45] P. Hohenberg and W. Kohn, "Inhomogeneous electron gas", *Physical Review*, vol. 136, B864–B871, 1964. DOI: 10.1103/PhysRev.136.B864.

[46] W. Kohn and L. J. Sham, "Self-consistent equations including exchange and correlation effects", *Physical Review*, vol. 140, A1133–A1138, 4A 1965. DOI: 10.1103/PhysRev.140.A1133.

[47] C. A. Ullrich, *Time-Dependent Density-Functional Theory*. Oxford University Press, 2012, ISBN: 9780199563029.

[48] W. Kohn and L. J. Sham, "Quantum density oscillations in an inhomogeneous electron gas", *Physical Review*, vol. 137, A1697–A1705, 1965. DOI: 10.1103/PhysRev.137.A1697.

[49] D. M. Ceperley and B. J. Alder, "Ground state of the electron gas by a stochastic method", *Physical Review Letters*, vol. 45, pp. 566–569, 7 1980. DOI: 10.1103/PhysRevLett.45.566.

[50] J. P. Perdew and Y. Wang, "Accurate and simple analytic representation of the electron-gas correlation energy", *Physical Review B*, vol. 45, pp. 13 244–13 249, 23 1992. DOI: 10.1103/PhysRevB.45.13244.

[51] C. Attaccalite, S. Moroni, P. Gori-Giorgi, and G. B. Bachelet, "Correlation energy and spin polarization in the 2d electron gas", *Physical Review Letters*, vol. 88, p. 256 601, 25 2002. DOI: 10.1103/PhysRevLett.88.256601.

[52] A. D. Becke, "Density-functional exchange-energy approximation with correct asymptotic behavior", *Physical Review A*, vol. 38, pp. 3098–3100, 6 1988. DOI: 10.1103/PhysRevA.38.3098.

[53] C. Lee, W. Yang, and R. G. Parr, "Development of the colle-salvetti correlation-energy formula into a functional of the electron density", *Physical Review B*, vol. 37, pp. 785–789, 2 1988. DOI: 10.1103/PhysRevB.37.785.

[54] J. P. Perdew, K. Burke, and M. Ernzerhof, "Generalized gradient approximation made simple", *Physical Review Letters*, vol. 77, pp. 3865–3868, 18 1996. DOI: 10.1103/PhysRevLett.77.3865.

[55] J. P. Perdew, M. Ernzerhof, and K. Burke, "Rationale for mixing exact exchange with density functional approximations", *The Journal of Chemical Physics*, vol. 105, no. 22, pp. 9982–9985, 1996. DOI: 10.1063/1.472933.

[56] A. D. Becke, "A new inhomogeneity parameter in density-functional theory", *The Journal of Chemical Physics*, vol. 109, no. 6, pp. 2092–2098, 1998. DOI: 10.1063/1.476722.

[57] J. W. Finley and P. E. Stephens, "Density functional theory calculations of molecular structures and harmonic vibrational frequencies using hybrid density functionals", *Journal of Molecular Structure: THEOCHEM*, vol. 357, pp. 225–235, 1995. DOI: 10.1016/0166-1280(95)04333-8.

[58] V. N. Staroverov, G. E. Scuseria, J. Tao, and J. P. Perdew, "Comparative assessment of a new nonempirical density functional: Molecules and hydrogen-bonded complexes", *Journal of Chemical Physics*, vol. 119, p. 12 129, 2004. DOI: 10.1063/1.1795692.

[59] J. Tirado-Rives and W. L. Jorgensen, "Performance of B3LYP density functional methods for a large set of organic molecules", *Journal of Chemical Theory and Computation*, vol. 4, pp. 297–306, 2008. DOI: `10.1021/ct700248k`.

[60] A. Leach, *Molecular Modelling: Principles and Applications*, Second edition. Pearson Education Limited, 2001, ch. 5, ISBN: 978-0-582-38210-7.

[61] M. J. Frisch, G. W. Trucks, H. B. Schlegel, G. E. Scuseria, M. A. Robb, J. R. Cheeseman, G. Scalmani, V. Barone, G. A. Petersson, H. Nakatsuji, X. Li, M. Caricato, A. V. Marenich, J. Bloino, B. G. Janesko, R. Gomperts, B. Mennucci, H. P. Hratchian, J. V. Ortiz, A. F. Izmaylov, J. L. Sonnenberg, D. Williams-Young, F. Ding, F. Lipparini, F. Egidi, J. Goings, B. Peng, A. Petrone, T. Henderson, D. Ranasinghe, V. G. Zakrzewski, J. Gao, N. Rega, G. Zheng, W. Liang, M. Hada, M. Ehara, K. Toyota, R. Fukuda, J. Hasegawa, M. Ishida, T. Nakajima, Y. Honda, O. Kitao, H. Nakai, T. Vreven, K. Throssell, J. A. Montgomery Jr., J. E. Peralta, F. Ogliaro, M. J. Bearpark, J. J. Heyd, E. N. Brothers, K. N. Kudin, V. N. Staroverov, T. A. Keith, R. Kobayashi, J. Normand, K. Raghavachari, A. P. Rendell, J. C. Burant, S. S. Iyengar, J. Tomasi, M. Cossi, J. M. Millam, M. Klene, C. Adamo, R. Cammi, J. W. Ochterski, R. L. Martin, K. Morokuma, O. Farkas, J. B. Foresman, and D. J. Fox, *Gaussian~09 Revision E.01*, Gaussian Inc. Wallingford CT, 2016.

[62] X. Li and M. J. Frisch, "Energy-represented direct inversion in the iterative subspace within a hybrid geometry optimization method", *Journal of Chemical Theory and Computation*, vol. 2, no. 3, pp. 835–839, 2006. DOI: `10.1021/ct050275a`.

[63] W. C. Swope, H. C. Andersen, P. H. Berens, and K. R. Wilson, "A computer simulation method for the calculation of equilibrium constants for the formation of physical clusters of molecules: Application to small water clusters", *The Journal of Chemical Physics*, vol. 76, no. 1, pp. 637–649, 1982. DOI: `10.1063/1.442716`.

[64] C. Runge, "Ueber die numerische auflösung von differentialgleichungen", *Mathematische Annalen*, vol. 46, no. 2, pp. 167–178, 1895. DOI: `10.1007/BF01446807`.

[65] A. B. Pacheco, S. M. Dietrick, P. S. Stevens, and S. S. Iyengar, ""Pump-Probe" Atom-Centered Density Matrix Propagation Studies To Gauge Anharmonicity and Energy Repartitioning in Atmospheric Reactive Adducts: Case Study of the OH + Isoprene and OH + Butadiene Reaction Intermediates", *Journal of Physical Chemistry A*, vol. 116, no. 16, pp. 4108–4128, 2012. DOI: `10.1021/jp212330e`.

[66] R. Car and M. Parrinello, "Unified approach for molecular dynamics and density-functional theory", *Physical Review Letters*, vol. 55, pp. 2471–2474, 22 1985. DOI: `10.1103/PhysRevLett.55.2471`.

[67] D. Marx and J. Hutter, *Ab Initio Molecular Dynamics: Basic Theory and Advanced Methods*. Cambridge University Press, 2009. DOI: `10.1017/CBO9780511609633`.

[68] H. B. Schlegel, J. M. Millam, S. S. Iyengar, G. A. Voth, A. D. Daniels, G. E. Scuseria, and M. J. Frisch, "Ab initio molecular dynamics: Propagating the density matrix with Gaussian orbitals", *Journal of Chemical Physics*, vol. 114, no. 22, pp. 9758–9763, 2001. DOI: `10.1063/1.1372182`.

[69] S. S. Iyengar, H. B. Schlegel, J. M. Millam, G. A. Voth, G. E. Scuseria, and M. J. Frisch, "Ab initio molecular dynamics: Propagating the density matrix with Gaussian orbitals. II. Generalizations based on mass-weighting, idempotency, energy conservation and choice of initial conditions", *Journal of Chemical Physics*, vol. 115, no. 22, pp. 10 291–10 302, 2001. DOI: `10.1063/1.1416876`.

[70] H. B. Schlegel, S. S. Iyengar, X. Li, J. M. Millam, G. A. Voth, G. E. Scuseria, and M. J. Frisch, "Ab initio molecular dynamics: Propagating the density matrix with Gaussian orbitals. III. Comparison with Born-Oppenheimer dynamics", *Journal of Chemical Physics*, vol. 117, no. 19, pp. 8694–8704, 2002. DOI: `10.1063/1.1514582`.

[71] R. McWeeny, "Some recent advances in density matrix theory", *Reviews of Modern Physics*, vol. 32, pp. 335–369, 2 1960. DOI: `10.1103/RevModPhys.32.335`.

[72] S. S. Iyengar, H. B. Schlegel, G. A. Voth, J. M. Millam, G. E. Scuseria, and M. J. Frisch, "Ab initio molecular dynamics: Propagating the density matrix with gaussian orbitals. IV. Formal analysis of the deviations from born-oppenheimer dynamics", *Israel Journal of Chemistry*, vol. 42, no. 2-3, pp. 191–202, 2002. DOI: `10.1560/GLW2-8NVQ-4N6T-6C92`.

[73] T. Schlick, *Molecular Modeling and Simulation: An Interdisciplinary Guide*, 2nd ed. Springer-Verlag New York, 2010. DOI: `10.1007/978-1-4419-6351-2`.

[74] D. H. Gross and P.-A. Hervieux, "Statistical fragmentation of hot atomic metal clusters", *Zeitschrift für Physik D Atoms, Molecules and Clusters*, vol. 35, no. 1, pp. 27–42, 1995. DOI: `10.1007/BF01439980`.

[75] G. Martinet, S. Díaz-Tendero, M. Chabot, K. Wohrer, S. Della Negra, F. Mezdari, H. Hamrita, P. Désesquelles, A. Le Padellec, D. Gardés, L. Lavergne, G. Lalu, X. Grave, J. F. Ciavelin, P.-A. Hervieux, M. Alcamí, and F. Martín, "Fragmentation of highly excited small neutral carbon clusters", *Physical Review Letters*, vol. 93, no. 6, pp. 1–4, 2004. DOI: `10.1103/PhysRevLett.93.063401`.

[76] S. Díaz-Tendero, P.-A. Hervieux, M. Alcamí, and F. Martín, "Statistical fragmentation of small neutral carbon clusters", *Physical Review A*, vol. 71, no. 3, p. 033 202, 2005. DOI: `10.1103/PhysRevA.71.033202`.

[77] S. Díaz-Tendero, G. Sánchez, M. Alcamí, F. Martín, P.-A. Hervieux, M. Chabot, G. Martinet, P. Désesquelles, F. Mezdari, K. Wohrer-Béroff, S. D. Negra, H. Hamrita, A. LePadellec, and L. Montagnon, "Fragmentation of small neutral carbon clusters", *International Journal of Mass Spectrometry*, vol. 252, no. 2, pp. 126–132, 2006. DOI: `10.1016/j.ijms.2005.12.055`.

[78] N. F. Aguirre, S. Díaz-Tendero, P.-A. Hervieux, M. Alcamí, and F. Martín, "M$_3$C: A Computational Approach To Describe Statistical Fragmentation of Excited Molecules and Clusters", *Journal of Chemical Theory and Computation*, vol. 13, pp. 992–1009, 2017. DOI: `10.1021/acs.jctc.6b00984`.

[79] J. Jellinek and D. H. Li, "Separation of the energy of overall rotation in any n-body system", *Physical Review Letters*, vol. 62, pp. 241–244, 3 1989. DOI: `10.1103/PhysRevLett.62.241`.

[80]   N. Metropolis, A. W. Rosenbluth, M. N. Rosenbluth, A. H. Teller, and E. Teller, "Equation of state calculations by fast computing machines", *The Journal of Chemical Physics*, vol. 21, no. 6, pp. 1087–1092, 1953. DOI: 10.1063/1.1699114.

[81]   C. R. d. Oliveira and T. Werlang, "Ergodic hypothesis in classical statistical mechanics", *Revista Brasileira de Ensino de Física*, vol. 29, pp. 189–201, 2 2007. DOI: 10.1590/S1806-11172007000200003.

[82]   P. Atkins and R. Friedman, *Molecular Quantum Mechanics*. Oxford University Press, 2005, ISBN: 0–19–927498–3.

[83]   G. Schaftenaar and J. Noordik, "Molden: A pre- and post-processing program for molecular and electronic structures", *Journal of Computer-Aided Molecular Design*, vol. 14, pp. 123–134, 2000. DOI: 10.1023/A:100819380.

[84]   J. P. Sánchez, N. F. Aguirre, S. Díaz-Tendero, F. Martín, and M. Alcamí, "Structure, Ionization, and Fragmentation of Neutral and Positively Charged Hydrogenated Carbon Clusters: $C_nH_m^{q+}$ (n = 1-5, m = 1-4, q = 0-3)", *Journal of Physical Chemistry A*, vol. 120, no. 4, pp. 588–605, 2016. DOI: 10.1021/acs.jpca.5b10143.

[85]   A. M. Mebel and A. D. Bandrauk, "Theoretical study of unimolecular decomposition of allene cations", *Journal of Chemical Physics*, vol. 129, no. 22, 2008. DOI: 10.1063/1.3037204.

[86]   K. Shen, Y. Fu, J. N. Li, L. Liu, and Q. X. Guo, "What are the pK_a values of C-H bonds in aromatic heterocyclic compounds in DMSO?", *Tetrahedron*, vol. 63, no. 7, pp. 1568–1576, 2007. DOI: 10.1016/j.tet.2006.12.032.

[87]   E. Kukk, D. T. Ha, Y. Wang, D. G. Piekarski, S. Díaz-Tendero, K. Kooser, E. Itälä, H. Levola, M. Alcamí, E. Rachlew, and F. Martín, "Internal energy dependence in x-ray-induced molecular fragmentation: An experimental and theoretical study of thiophene", *Physical Review A - Atomic, Molecular, and Optical Physics*, vol. 91, no. 4, pp. 1–7, 2015. DOI: 10.1103/PhysRevA.91.043417.

[88]   R. Dennington, T. A. Keith, and J. M. Millam, *Gaussview Version 5*, Semichem Inc. Shawnee Mission KS, 2009.

[89]   L. Chen, S. Martin, J. Bernard, and R. Brédy, "Direct measurement of internal energy of fragmented C_{60}", *Physical Review Letters*, vol. 98, no. 19, pp. 6–9, 2007. DOI: 10.1103/PhysRevLett.98.193401.

[90]   S. Maclot, R. Delaunay, D. Piekarski, A. Domaracka, B. Huber, L. Adoui, F. Martín, M. Alcamí, L. Avaldi, P. Bolognesi, and P. Rousseau, "Determination of Energy-Transfer Distributions in Ionizing Ion-Molecule Collisions", *Physical Review Letters*, vol. 073201, pp. 1–6, 2016. DOI: 10.1103/PhysRevLett.117.073201.

[91]   T. Chen, M. Gatchell, M. H. Stockett, J. D. Alexander, Y. Zhang, P. Rousseau, A. Domaracka, S. MacLot, R. Delaunay, L. Adoui, B. A. Huber, T. Schlathölter, H. T. Schmidt, H. Cederquist, and H. Zettergren, "Absolute fragmentation cross sections in atom-molecule

collisions: Scaling laws for non-statistical fragmentation of polycyclic aromatic hydro-carbon molecules", *Journal of Chemical Physics*, vol. 140, no. 22, 2014. DOI: `10.1063/1.4881603`.

[92] P.-A. Hervieux, B. Zarour, J. Hanssen, M. Politis, and F. Martín, " Fragmentation in collisions of Na^{9+} clusters with Cs atoms", *Journal of Physics B*, no. 34, pp. 3331–3355, 2001. DOI: `10.1088/0953-4075/34/16/310`.

[93] P.-A. Hervieux, L. F. Ruiz, S. Díaz-Tendero, M. Alcamí, B. Zarour, M. F. Politis, J. Hanssen, and F. Martín, "Charge Transfer and Evaporation in Low Energy Collisions of Metal Clusters and Fullerenes with Atomic Targets", *Physica Scripta*, vol. 110, p. 308, 2004. DOI: `10.1238/Physica.Topical.110a00308`.

[94] C. L. Lawson and R. J. Hanson, *Solving Least Squares Problems*. Prentice-Hall, 1987.

[95] S. Wu, H. Yang, J. Hu, D. Shen, H. Zhang, and R. Xiao, "Pyrolysis of furan and its derivatives at 1100°C: PAH products and DFT study", *Journal of Analytical and Applied Pyrolysis*, vol. 120, pp. 252–257, 2016. DOI: `10.1016/j.jaap.2016.05.013`.

[96] P. Bolognesi, *et al*, Private Communication.

[97] P. Rousseau, *et al*, Private Communication.

[98] S. Maclot, D. G. Piekarski, R. Delaunay, A. Domaracka, A. Méry, V. Vizcaino, J.-Y. Chesnel, F. Martín, M. Alcamí, B. A. Huber, L. Adoui, P. Rousseau, and S. Díaz-Tendero, "Stability of the glycine cation in the gas phase after interaction with multiply charged ions", *The European Physical Journal D*, vol. 68, no. 6, p. 149, 2014. DOI: `10.1140/epjd/e2014-40819-x`.

[99] J. Daligault, F. Chandezon, C. Guet, B. A. Huber, and S. Tomita, "Energy transfer in collisions of metal clusters with multiply charged ions", *Physical Review A*, vol. 66, p. 033 205, 3 2002. DOI: `10.1103/PhysRevA.66.033205`.

[100] T. Bergen, X. Biquard, A. Brenac, F. Chandezon, B. A. Huber, D. Jalabert, H. Lebius, M. Maurel, E. Monnand, J. Opitz, A. Pesnelle, B. Pras, C. Ristori, and J. C. Rocco, "Multiply charged cluster ion crossed-beam apparatus: Multi-ionization of clusters by ion impact", *Review of Scientific Instruments*, vol. 70, no. 8, pp. 3244–3253, 1999. DOI: `10.1063/1.1149900`.

[101] J. H. D. Eland, "Dynamics of Fragmentation Reactions From Peak Shapes in Multiparticle Coincidence Experiments", *Laser Chemistry*, vol. 11, pp. 259–263, 1991. DOI: `dx.doi.org/10.1155/LC.11.259`.

[102] T. A. Field and J. H. Eland, "Lifetimes of metastable molecular doubly charged ions", *Chemical Physics Letters*, vol. 211, no. 4,5, pp. 436–442, 1993. DOI: `10.1016/0168-583X(94)00757-8`.

[103] M. Alagia, P. Candori, S. Falcinelli, M. Lavollée, F. Pirani, R. Richter, S. Stranges, and F. Vecchiocattivi, "Double Photoionization of CO_2 Molecules in the 34-50 eV Energy Range", *Journal of Physical Chemistry A*, vol. 113, pp. 14 755–14 759, 2009. DOI: `10.1021/jp9048988`.

[104]   A. W. Jasper, C. Zhu, S. Nangia, and D. G. Truhlar, "Introductory lecture: Nonadiabatic effects in chemical dynamics", *Faraday Discussions*, vol. 127, pp. 1–22, 2004. DOI: `10.1039/b405601a`.

[105]   I. Tavernelli, U. F. Röhrig, and U. Rothlisberger, "Molecular dynamics in electronically excited states using time-dependent density functional theory", *Molecular Physics*, vol. 103, no. 6-8, pp. 963–981, 2005. DOI: `10.1080/00268970512331339378`.

[106]   J. C. Tully and R. K. Preston, "Trajectory Surface Hopping Approach to Nonadiabatic Molecular Collisions: The Reaction of H^+ with D_2", *The Journal of Chemical Physics*, vol. 55, no. 2, pp. 562–572, 1971. DOI: `10.1063/1.1675788`.

[107]   M. Gatchell, M. Stockett, P. Rousseau, T. Chen, K. Kulyk, H. Schmidt, J. Chesnel, A. Domaracka, A. Méry, S. Maclot, L. Adoui, K. Støchkel, P. Hvelplund, Y. Wang, M. Alcamí, B. Huber, F. Martín, H. Zettergren, and H. Cederquist, "Non-statistical fragmentation of pahs and fullerenes in collisions with atoms", *International Journal of Mass Spectrometry*, vol. 365-366, pp. 260 –265, 2014. DOI: `https://doi.org/10.1016/j.ijms.2013.12.013`.

[108]   M. H. Stockett, H. Zettergren, L. Adoui, J. D. Alexander, U. Bērzeņiš, T. Chen, M. Gatchell, N. Haag, B. A. Huber, P. Hvelplund, A. Johansson, H. A. B. Johansson, K. Kulyk, S. Rosén, P. Rousseau, K. Støchkel, H. T. Schmidt, and H. Cederquist, "Nonstatistical fragmentation of large molecules", *Physical Review A*, vol. 89, p. 032 701, 3 2014. DOI: `10.1103/PhysRevA.89.032701`.

[109]   *M₃C fragment database*, [Accessed 8-April-2019]. [Online]. Available: `https://github.com/nfaguirrec/M3C-store`.